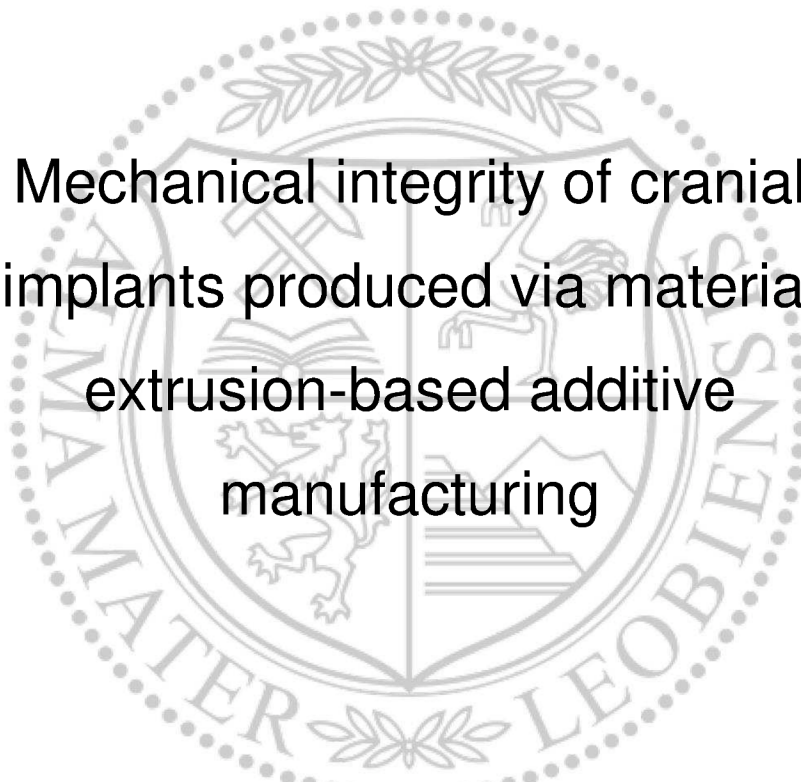




Materials Science and Testing of Polymers

Doctoral Thesis



Mechanical integrity of cranial
implants produced via material
extrusion-based additive
manufacturing

Dipl.-Ing. Sandra Petersmann, BSc

Leoben, October 2022



EIDESSTATTLICHE ERKLÄRUNG

Ich erkläre an Eides statt, dass ich diese Arbeit selbständig verfasst, andere als die angegebenen Quellen und Hilfsmittel nicht benutzt, und mich auch sonst keiner unerlaubten Hilfsmittel bedient habe.

Ich erkläre, dass ich die Richtlinien des Senats der Montanuniversität Leoben zu "Gute wissenschaftliche Praxis" gelesen, verstanden und befolgt habe.

Weiters erkläre ich, dass die elektronische und gedruckte Version der eingereichten wissenschaftlichen Abschlussarbeit formal und inhaltlich identisch sind.

Datum 20.10.2022

A handwritten signature in blue ink, appearing to read 'S. Petersmann', written over a horizontal line.

Unterschrift Verfasser/in
Sandra Petersmann

Sandra Petersmann

Dissertation

Mechanical integrity of cranial implants produced via material extrusion-based additive manufacturing

October 2022

This cumulative Dissertation was authored by

Dipl.-Ing. Sandra Petersmann, BSc.

born 20. June 1994

in Villach (Carinthia, Austria)

Materials Science and Testing of Polymers

Department Polymer Engineering and Science, Montanuniversitaet Leoben

You never fail until you stop trying

Albert Einstein

Preamble

Acknowledgement

The research work of this thesis was performed at the Montanuniversitaet Leoben - Materials Science and Testing of Polymers within the framework of two funded projects: CAMed (COMET K-Project 871132), which is funded by the Austrian Federal Ministry of Transport, Innovation and Technology (BMVIT), Austrian Federal Ministry of Digital and Economic Affairs (BMDW), and the Styrian Business Promotion Agency (SFG) and eFAM4Ind (877409), which is funded by the Austrian funding agency association (FFG) and the federal ministry of climate action, environment, energy, mobility innovation and technology (BMK).

At this point I want to thank all the people, who supported me during my journey. First and foremost, I would like to thank my supervisor Priv.-Doz. Dr. mont. Florian Arbeiter (Materials Science and Testing of Polymers, Montanuniversitaet Leoben) for all the fruitful discussions and advices during my dissertation. I am really grateful to have had such a great supervisor and work group leader.

Furthermore, I would like to thank Univ.-Prof. Dr. mont. Gerald Pinter (Chair of Materials Science and Testing of Polymers, Montanuniversitaet Leoben) for being able to carry out the research work at his institute, where teamwork has a very high priority. I am very grateful to have experienced how social activities with work colleagues have a positive impact on work performance.

Additionally, I want to express my thanks to my mentor Prof. Dr. Ludwig Cardon (Faculty of Engineering and Architecture, Department of Materials, Textiles and Chemical Engineering, Ghent University, Belgium) for his support

during my thesis. Unfortunately, a longer stay at Ghent University and the possibility to forge a closer bond with Ghent University wasn't possible due to COVID-19 pandemic.

Moreover, I would like to thank every member of the team at Materials Science and Testing of Polymers for all their support and always having an open door. I very much enjoyed the exchange during coffee-breaks, even if I don't drink coffee, lunch time and rounds of table soccer. Especially, I would like to thank the members of the minions group led by Florian: Johannes, thank you for always putting up with me and helping me whenever I needed help. Christoph, thank you for all the interesting topics we explored together and the very good cooperation as well as for sharing the same humour. Anja, thank you for all your encouraging words during my thesis, all the happy memories we gathered together and becoming a real friend to me. In addition, I want to thank Jürgen Grosser, Jürgen Föttinger and Franz Grassegger for their experimental and technical support whenever I needed it. Another thank you goes to Rafaela Schwaninger for her coordination work. I would also like to thank Martin Spörk, with whom I had the honour of writing my first publications and learning a lot about scientific writing.

Special thanks go to all my friends who increased the quality of life and are to blame for numerous beautiful memories (Elli, Cathy, Nina, Martin, Jutta, Markus, Johannes, Hubsli, Jessi, Tobi). Particularly, I want to thank my boyfriend Berni, who supports me no matter what and always believes in me when sometimes I don't. Additionally, I would like to thank my brother, who (as a student in a higher semester and now a graduate) made it easier for me to get started in my studies and was always there to help me with advice. Finally, I would like to thank my parents who made this life possible for me and will always stand by me. Thanks also for often being happier about achieved goals than myself and for always telling me that you are proud of me. I consider myself very lucky to have parents like you.

Kurzfassung

Der Einsatz von additiven Fertigungsverfahren für die Entwicklung von Polymerbauteilen nimmt täglich, insbesondere in Bereichen, in denen die Individualisierbarkeit eine wichtige Rolle spielt, wie z. B. in der Medizin, zu. Vor allem der 3D-Druck von Knochenersatzmaterialien wie Schädelimplantaten wird derzeit intensiv erforscht. Unter den verschiedenen Verfahrensvarianten ist die additive Fertigung auf Basis der Materialextrusion von Filamenten für Polymere besonders beliebt. Prozess bedingte Fehlstellen können sich jedoch stark auf die Materialeigenschaften und damit auf die Belastbarkeit der Bauteile auswirken.

Deshalb sollten die in kritischen Anwendungen eingesetzten Materialien und ihr verarbeitungsabhängiges sowie anwendungsbezogenes Materialverhalten vor dem Einsatz systematisch charakterisiert werden. Ziel dieser Arbeit ist es daher, ausgewählte medizinische Polymere skalenübergreifend unter Anwendung einer mechanischen Prüfpyramide, wie ursprünglich von der NASA für Composite Werkstoffe entwickelt, am Beispiel eines Schädelimplantats für den filamentbasierten 3D-Druck zu charakterisieren. Die Pyramide wurde für den additiven Fertigungsprozess adaptiert und startet mit der Materialauswahl/Filament-Ebene und geht über Prüfkörper und Subkomponenten bis hin zur kompletten Bauteilprüfung. Parallel werden Änderungen in der Morphologie und Mikrostruktur berücksichtigt.

Im Zuge der ersten Ebene der Prüfpyramide, wurden sowohl medizinische, als auch verarbeitungstechnische Kriterien für die Materialauswahl herangezogen. Zudem wurde die generelle Temperaturabhängigkeit der mechanischen Eigenschaften der ausgewählten Polymere

(Polyetheretherketon, Polylactid, Polymethylmethacrylat, Glykol-modifiziertes Polyethylenterephthalat, Polyvinylidenfluorid and Polypropylen) an Filamenten analysiert. Es zeigte sich, dass sich die mechanischen Eigenschaften einiger ausgewählter Materialien bereits signifikant zwischen Normtemperatur (23 °C) und Anwendungstemperatur (ca. 37 °C) verändern. Dies verdeutlicht die Bedeutung von Kennwerten, die unter tatsächlichen Anwendungsbedingungen bestimmt wurden.

Auf Prüfkörperebene wurden dehnratenabhängige Zugversuche (zwischen quasi-statisch und Impact) durchgeführt, um situationsabhängige Materialdaten für die simulationsunterstützte Auslegung von Bauteilen zu generieren. Dadurch können nicht nur statische oder monotone Belastungen, wie in der Literatur meist dargestellt, sondern auch schlagartige Belastungen berücksichtigt werden. Zusätzlich wurde der Einfluss von vorgeschalteten Wasch- und Sterilisationsprozessen analysiert. Die Ergebnisse zeigten dabei, dass nach korrekter Auswahl der Prozesse keine signifikanten Einflüsse auf das gedruckte Bauteil zu erwarten sind.

Neben den oben erwähnten medizinischen bzw. anwendungsrelevanten Untersuchungen wurde auch die prozessabhängige Morphologie und deren Einfluss auf thermische und mechanische Kennwerte untersucht. Dies ist vor allem für teilkristalline Polymere von besonderer Bedeutung. Es zeigte sich, dass in Abhängigkeit von Druckgeschwindigkeit, Düsentemperatur, aber auch gewähltem Druckpfad einerseits nahezu homogene und andererseits stark anisotrope Strukturen, inklusive klar ausgeprägter Scher-induzierter Kristallisation und Shish-Kebab Strukturen, erzeugt werden können. Dies bestätigt, dass die von der Slicer-Software vorgeschlagene Druckreihenfolge nicht willkürlich gewählt werden sollte, sondern zur gezielten Adaption der Morphologie verwendet werden kann.

Basierend auf diesen Erkenntnissen wurden Subkomponenten Tests durchgeführt. Ziel war es die optimalen Füllstrukturen für Schädelimplantate unter Stoßbelastung zu finden. Innere 3D-Wabenstrukturen mit 70% Füllung

und geradlinige Strukturen mit 100% Füllung ergaben dabei die beste Kombination aus zulässiger maximaler Deformation, maximaler ertragbarer Kraft und absorbierter Energie bis Bruch. Die Ergebnisse konnten auch nicht durch Steifigkeits-basierende Topologie-Optimierung, oder den Einsatz einer rissstoppenden Zwischenschicht übertroffen werden.

Als letzter Schritt der Prüfpyramide wurden Tests an gedruckten Schädelimplantaten als Bauteilversuch durchgeführt. Durch die Variation von Druckparametern war es möglich, ähnliche mechanische Eigenschaften bei Schlagbelastung wie bei einem handelsüblichen (gefrästen) Implantat, allerdings mit Abstrichen bei der Oberflächenqualität, zu erzielen. Interessanterweise zeigte sich, dass das handelsübliche Implantat bei einem Aufpralltest in mehrere Teile und Splitter zerbrach, wogegen bei gedruckten Implantaten das Bruchverhalten durch den Druckpfad vorgegeben werden kann. Dies würde in der gegenständlichen Anwendung massive Vorteile hinsichtlich Verletzungsrisiko bedeuten.

Durch den gewählten systematischen Ansatz der Testpyramide war es möglich, die wichtigsten Verarbeitungsparameter und Umgebungseinflüsse auf Implantatmaterialien zu identifizieren. Dadurch konnte ein weitreichender Wissenszuwachs im Bereich Struktur-Prozess-Eigenschaftsbeziehungen von mittels filamentbasierten 3D-Druck hergestellten Bauteilen in kritischen Anwendungen erreicht werden.

Abstract

Additive manufacturing processes are becoming increasingly popular for the development of components, especially in areas where customisability plays an important role, such as medicine. In particular, 3D-printing of bone replacement materials such as cranial implants is currently being intensively researched. Among the different process variants, additive manufacturing based on material extrusion is widespread for polymers. However, process-induced defects can strongly affect the material properties and thus the load capacity of printed components. This must be considered during designing, especially for critical applications. Otherwise, a false sense of security could be created. In the field of cranial implants, premature failure could even endanger human lives.

Hence, the materials used in critical applications and their processing-dependent as well as application-related material behaviour should be systematically characterised before use. The aim of this work is therefore to characterise selected medical polymers across scales using a mechanical testing pyramid, as originally developed by NASA for composite materials, based on the example of a cranial implant for material extrusion. The pyramid was adapted for the additive manufacturing process and starts with the material selection/filament level and goes through test specimens and subcomponents to component testing. In parallel, changes in morphology and microstructure are considered.

In the course of the first level of the test pyramid, both medical and processing criteria were used for the material selection. In addition, the general

temperature dependence of the mechanical properties of the selected polymers (polyetheretherketone, polylactide, poly(methyl methacrylate), glycol-modified poly(ethylene terephthalate), poly(vinylidene fluoride) and polypropylene) was analysed on filaments. It was found that the mechanical properties of some selected materials already change significantly between standard temperature (23 °C) and application temperature (approx. 37 °C). This illustrates the importance of characteristic values determined under actual application conditions.

At the specimen level, strain rate-dependent tensile tests (between quasi-static and impact) were carried out to generate situation-dependent material data for the simulation-aided design of components. This means that not only static or monotonic loads, as usually presented in the literature, but also abrupt loads can be taken into account. Furthermore, the influence of preceding cleaning and sterilisation processes was analysed. The results showed that after correct selection of the processes, no significant influences on the printed component are to be expected.

In addition to the above-mentioned medical or application-relevant investigations, the process-dependent morphology and its influence on thermal and mechanical properties was also investigated. This is of particular importance for semi-crystalline polymers. It was shown that, depending on the printing speed, nozzle temperature, but also the selected printing path, on the one hand almost homogeneous and on the other hand strongly anisotropic structures, including clearly pronounced shear-induced crystallisation and shish-kebab structures, can be produced. This confirms that the printing path suggested by the slicer software should not be chosen arbitrarily, but can be used for targeted adaptation of the morphology.

Based on these findings, subcomponent tests were conducted. The aim was to find the optimal filling structures for cranial implants under impact loading. Internal 3D-honeycomb structures with 70% infill and rectilinear structures with

100% infill yielded the best combination of permissible maximum deformation, maximum tolerable force and absorbed energy until fracture. The results could not be surpassed by stiffness-based topology optimisation or the use of a crack-stopping interlayer.

As the final step in the test pyramid, component tests were carried out on printed cranial implants. By varying processing parameters, it was possible to achieve similar mechanical properties under impact loading as a commercial (milled) implant, albeit with compromises in surface quality. Interestingly, it turned out that the commercial implant broke into several pieces and splinters during an impact test, whereas with printed implants the fracture behaviour can be determined by the print path. In this application, this would mean massive advantages with regard to the risk of injury.

Through the chosen systematic approach of the mechanical testing pyramid, it was possible to identify the most important processing parameters and environmental influences on implant materials. This enabled a far-reaching increase in knowledge in the area of structure-process-property relationships of components manufactured using material extrusion-based additive manufacturing in critical applications.

Contents

Outline and summary

1. Motivation and background	3
2. Objectives and structure of the thesis	6
3. Comparison to the state of the art	10
3.1. Cranial implants	10
3.2. Material extrusion-based additive manufacturing.....	13
3.3. Mechanical testing pyramid.....	15
3.3.1. Material selection and filament level	16
3.3.2. Specimen level.....	21
3.3.3. Sub-component level	36
3.3.4. Component level	39
4. Summary and conclusions	44
5. Outlook	49
6. References	52

Appendix

A.1. List of additional article contributions

A.2. Conference contributions

A.3. Supervised theses

Publications of the cumulative thesis

Outline and summary

1. Motivation and background

With the continuous improvement of health care, people's life expectancy has increased rapidly. As a result, the number of medical interventions such as prosthesis implantation is also increasing [1]. With regard to the cranium, approx. 700,000 surgeries are carried out per annum, and in the severest of cases, a part of the cranium has to be reconstructed and a cranial implant is needed [2]. Therefore, finding suitable bone reconstruction materials and improving their processability is of utmost importance. Metals, ceramics and polymers can be used as bone reconstruction materials, whereby the latter stand out due to their adequate heat insulation properties and versatile processability [3].

Manufacturing cranial implants via additive manufacturing (AM) would be a great alternative to traditional manufacturing processes (e.g. milling), but the process has to be sufficiently researched before being used for such critical applications. In 2021, the first cranial PEEK implant was directly additively manufactured in the clinic and implanted in a patient at Skåne University Hospital in Sweden [4]. However, publishable research on the study has not been made available.

Especially in the medical field, the requirements regarding geometric accuracy, durability and safety are very high. Ensuring a safe component is crucial. Poor processing quality can lead to crack- and fracture-prone components. In connection with the targeted application of cranial implants, a human life may be at risk. Therefore, precise understanding of both material and process are vital, before the component can be used in this critical application.

With regards to polymers, material extrusion-based AM (ME-AM) would be a highly interesting candidate. During this process a thermoplastic filament is molten and deposited onto a build platform in a layerwise fashion [5]. Due to the layer-by-layer deposition of the material, several weld lines and cavities are inserted into the material between the individual strands. The amount and geometry of these defects are strongly depending on the used printing parameters. These print errors can subsequently have a strong influence on the resulting properties of the produced component and, in the worst case, endanger the mechanical integrity.

Particularly when dealing with polymers, challenges during printing often depend on the molecular structure, especially for semi-crystalline polymers. Differences in the cooling behaviour during manufacturing change the crystallisation kinetics and thus the morphology, which in turn influences a number of material properties. The crystallisation behaviour also affects shrinkage and warpage and thus geometric accuracy [6].

Besides challenges with printing itself, polymers are also known to show time- and temperature-dependent properties, which makes the characterisation of the materials under application-oriented conditions a prerequisite [7]. For implant materials, these conditions include elevated temperatures, surrounding body fluids and tissue, as well as various loading scenarios. Moreover, all medical devices are cleaned and sterilised prior to application, again applying a combination of temperature, pressure and media on the material, which could also alter the resulting properties.

Considering all aforementioned influences, a wholistic view, considering all length scales from material to the final component is unavoidable. However, systematic characterisations, spanning from the material selection and analyses on filament level over specimens and sub-components to the “real” component, cannot be found for material extrusion-based additive manufacturing in literature yet. The aim of this work is therefore to conduct a systematic investigation of medically approved materials at different length

scales to validate their applicability for cranial implants manufactured using ME-AM.

2. Objectives and structure of the thesis

To overcome the aforementioned issues, a structured testing pyramid has to be implemented. The individual steps and objects are defined as described below, accompanied by analysis of the microstructure and morphology from step 2 onwards:

1) Material selection and filament tests:

The number of implantable and printable materials is limited. With regard to implantability, the material must fulfil several requirements, such as biocompatibility, non-cytotoxicity, inertness, durability, sterilisability and mechanical integrity. In terms of printability, the production of high-quality filaments is required. This is the only way to subsequently produce components with a high quality. A high filament quality usually indicates a controlled production routine with little to no inclusions and low fluctuations in the filament diameter and ovality. An irregular filament diameter or wet filament will result in a loss of quality. During the material selection process, pre-selected materials (e.g. based on the required mechanical properties) are subjected to various additional tests (e.g. cytotoxicity) to limit their number. Many of the analyses to be carried out can already be performed on the filament itself, saving time to prepare test specimens. For example, filaments can be used to check the general temperature or strain-rate dependent material behaviour. However, it must always be considered that the properties of the filament, i.e. material, only reveal the upper limit of the material in question. The printed properties of the chosen materials still have to be validated in detail later on, since they are usually (significantly) lower.

2) Analyses at specimen level:

Classically, analyses on test specimens are carried out to measure how much the processing has changed the properties compared to the values determined on the filaments. Especially with AM, the mechanical properties are often significantly lower compared to the bulk properties. This is particularly significant perpendicular to the direction of strand deposition. However, the explanation for this decrease is often either completely missing or only partly investigated. Analyses of the induced microstructure and morphology often allow conclusions to be drawn about the detailed influence of the processing.

By applying morphological characterisation methods to ME-AM materials, a correlation between process parameters, morphological characteristics and resulting properties can be established. In particular for semi-crystalline polymers, this level of testing is of utmost importance, since the crystallisation behaviour and thus the morphology can strongly be influenced by processing parameters such as the nozzle temperature or printing speed. These morphological changes may further significantly alter several material properties.

Furthermore, analysing the materials at application-oriented conditions is essential for determining proper input parameters for the simulation-based design of the component. For implants, this includes elevated temperature, surrounding body fluids and various possible loading scenarios. Since the material properties of most polymers are significantly dependent on temperature and time during processing, as well as the application, the evaluation of temperature- and time-dependent material properties is required in order to provide reliable data sets. This is also the reason why the influence of cleaning and sterilisation processes needs to be investigated prior to application.

All this has already been sufficiently investigated for polymers produced via conventional methods, such as injection-moulded parts, but there are still gaps in the area of ME-AM.

3) Characterisation of mechanical properties at sub-component level:

Compared to tests on specimen level, sub-component tests are meant to be closer to reality using a simplified geometry of the real component instead of standardised test specimens. Due to the high design freedom of AM, a specific internal architecture can be introduced into the cranial implant, saving material and printing time while improving osseointegration. Osseointegration describes, on the one hand, the absence of a fibrous layer around the implant with an active reaction in the sense of integration into the host bone and, on the other hand, a chemical or physico-chemical connection between implant and bone [8,9]. Curved cranial implants could thus be approximated in the first step by plate-shaped sandwich structures. The internal structure, infill density and topology can be modified to enhance the mechanical properties of cranial implants. Additionally, a multi-material approach can be applied in order to combine the advantages of compliant and stiff materials. Since impact loads are likely to occur in the real application, this level was used to analyse the influence of different internal architectures on the impact behaviour.

4) Final component tests

Finally, tests should be carried out with real components. In the case of this thesis cranial implants were chosen. The knowledge gained through the tests at the other levels of the mechanical testing pyramid should help to find the optimal processing conditions for manufacturing patient-specific cranial implants by means of ME-AM. For the component tests, the real shape of a cranial bone is utilised and application-oriented tests are performed. Since the operating loads of cranial implants tend to be low, application-oriented tests include impact tests to consider scenarios such as falling out of bed. These tests can provide important information about the fracture behaviour of the implants.

By following the pyramid for mechanical testing, these new scientific results should be achieved: Firstly, a better understanding of the relationships between variations in key processing parameters (such as nozzle temperature

and printing speed) and the resulting mechanical properties of polymers produced by ME-AM should be gained. Secondly, new insights into process-induced morphological changes of selected polymers should be given, which is especially important for semi-crystalline polymers. Additionally, the importance of analysing the effects of internal architecture, strain-rate, temperature, cleaning and sterilisation on the mechanical integrity of cranial implants should be addressed and discussed. All the newly gained knowledge should help to narrow down the most important influencing parameters for additive manufacturing by material extrusion.

The aforementioned objectives were examined in the course of this doctoral thesis, with regard to the mechanical integrity of cranial implants produced via material extrusion-based additive manufacturing. The results were published in international peer-reviewed journals. Subsequently, this cumulative thesis consists of a collection of the following publications, which can be found in the annex:

Publication 1: Mechanical properties of polymeric implant materials produced by extrusion-based additive manufacturing

Publication 2: The effects of washing and formaldehyde sterilization on the mechanical performance of poly(methyl methacrylate) (PMMA) parts produced by material extrusion-based additive manufacturing or material jetting

Publication 3: Process-induced morphological features in material extrusion-based additive manufacturing of polypropylene

Publication 4: Impact Optimization of 3D-Printed Poly(methyl methacrylate) for Cranial Implants

Publication 5: Material extrusion-based additive manufacturing of polyetheretherketone cranial implants: Mechanical performance and print quality

In order to summarise the results of all publications, they are presented in reference to the international state of the art in the following chapter.

3. Comparison to the state of the art

3.1. Cranial implants

The ageing world population and the increasing number of traumas are the main reasons for the need to develop suitable cranial implants. However, the selection of materials and processes for the production of adequate cranial bone replacements has posed major challenges for researchers worldwide [3,10]. Synthetic bone substitutes should have a similar structure and similar properties to the adjacent healthy bone. Requirements include biocompatibility, inertness, non-cytotoxicity, sterilisability, long-term stability/durability and mechanical integrity. Biocompatibility refers to the ability of a material to react appropriately when it comes into contact with body tissue or fluids [11]; inertness describes that the material does not interact with the surrounding substances, which is almost impossible in the complex biological system of the human body [12]; cytotoxicity is an in vitro test evaluating whether the medical device causes cell death by diffusing toxic substances or by direct contact [13]; sterilisability means the ability to eliminate any living organisms such as bacteria or viruses via sterilisation before use, otherwise they can become lethal to the host system [14]; durability defines the ability of the material to remain operational during its service life [15]. In terms of mechanical integrity, it is important that the mechanical behaviour of the implant matches the behaviour of the living bone as closely as possible. However, this proves to be difficult as there is hardly any data available in the literature on the mechanical properties of living bone and the properties of dead, dry bone may differ greatly from reality [16,17]. In addition to the

requirements already listed, availability, processability, flexible individualisation and intraoperative workability are to be aimed for [15,18,19].

The reconstruction materials used so far range from human and non-human bones to metals, ceramics and polymers. Among these, polymers stand out in particular due to their preferable heat-insulation properties, their relatively easy processability and thus variety of different processing techniques, as well as their price [3,15]. Polyetheretherketone (PEEK) or poly(methyl methacrylate) (PMMA) are state of the art materials for the reconstruction of cranial defects due to their biocompatibility, rigidity and toughness [20]. Since 1940, PMMA has already been used in cranioplasty, starting with the intraoperative construction of PMMA implants by hand [3,21]. Later, this technique has been replaced by computer-aided prefabrication methods. Implants fabrication was then aided by computed tomography (CT) scans of the bone to be replaced or the resulting hollow space [22]. Afterwards the collected digital imaging and communications in medicine (DICOM) data sets are segmented and reconstructed in order to either generate a computer aided design (CAD) of a mould for casting the implant or the implant itself [23]. With the first variant, the dimensions for the fabrication of moulds via wax elimination techniques [24], additive manufacturing methods [22,25–28], milling [29], or thermoforming [30] for casting PMMA implants were obtained. With the second variant, a model of the implant is created, which can be used to directly manufacture the implant either by subtractive (e.g. milling) or additive manufacturing (AM) techniques. Therefore, the CAD object is converted into a standard triangle language (STL) file and broken down into several layers with assigned process parameters (G-code) [5]. This process chain is schematically shown in Figure 1.

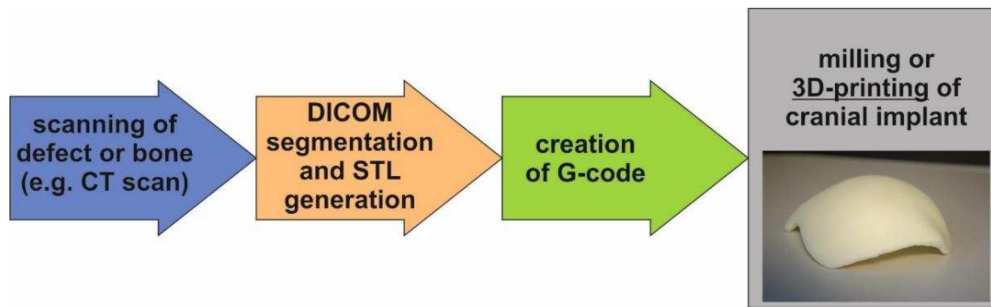


Figure 1: Schematic representation of the process workflow to obtain the 3D model of a cranial implant.

The fabrication of implants by milling is state of the art, but AM has been intensively researched for several years now, as AM offers a higher degree of design freedom and allows the material-saving creation of complex, customised structures. Personalisation plays a major role, especially in the medical field, because no two bodies are alike. In addition, the high degree of design freedom can be used to create internal structures in the implant to tailor the mechanical performance. As cranial bone is a combination of spongy cancellous and compact cortical bone, cranial implants may also have an internal architecture as long as the general requirements are met. With the help of CAD modelling and AM, it is now possible to design and manufacture nature-inspired, biomimetic structures [31]. Cell adhesion, migration, nutrient supply, and biological fixation can be enhanced by using porous structures that increase surface area and thus improve intra- and interconnectivity [32,33]. Highly porous implants with incorporated bioactive substances ensuring the ingrowth of bone can further improve osseointegration [34].

Another advantage of AM methods are their short process times associated with a reduced number of process steps. If the implants are manufactured directly in the clinic, the lead times of the implants will be drastically reduced, which could make interoperative manufacturing possible. Moreover, AM offers the possibility to produce multi-material and multi-colour parts in different sizes [35]. All these benefits of AM are the reasons for the boom in the production and development of 3D-printers and new 3D-printing technologies, especially

since the expiration of the fused deposition modelling patent by Stratasys Inc. in 2009. The result has been falling prices for 3D-printers and greater accessibility for the masses, and thus of course increasing demand in the medical sector.

3.2. Material extrusion-based additive manufacturing

In the last years, the production of prostheses by material extrusion-based additive manufacturing (ME-AM) methods has been given a lot of attention. This AM method is further known as fused filament fabrication or fused deposition modelling. In this process, a thermoplastic filament is transported by two counter-rotating driving wheels to a heating block, where it is melted (Figure 2). In a next step, it is selectively applied to a build platform or previous layer through a moving nozzle, which follows a predefined CAD design. In this way, the desired object is built layer-by-layer [5,35–37]. Once a layer is completed, either the nozzle changes its z-position or the build platform is lowered and printing of the next layer begins.

Depending on the printing parameters used, cavities or weld lines are created by the layerwise deposition of the material. In Table 1, some important process parameters of the ME-AM process are defined according to Ref. [38] for future reference.

Furthermore, the printing parameters of the first layers can be altered individually (e.g. die temperature, build platform temperature, printing speed, layer height). This plays an important role in order to improve the adhesion to the build platform. Adhesives can also be applied to the build platform to further enhance adhesion. Adhesion can also be altered by changing to another build platform material or printing on a raft.

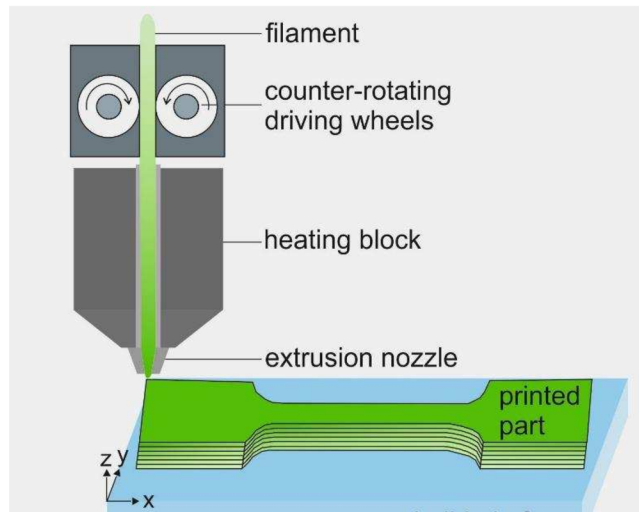


Figure 2: Schematic representation of process workflow for the 3D model of a cranial implant [39].

Table 1: Definition of important process parameters in material extrusion-based additive manufacturing.

Parameter	Definition
<i>Nozzle/die temperature</i>	Temperature of extrusion nozzle
<i>Build platform temperature</i>	Temperature of build platform
<i>Build chamber temperature</i>	Temperature of chamber isolating the printer and providing a controlled environment
<i>Perimeter</i>	Extrusion path that runs around the perimeter of the object; contour lines
<i>Printing speed</i>	Speed of the filament deposition/extruder head along xy-plane
<i>Extrusion multiplier</i>	Determines the amount of material the printer extrudes
<i>Layer height/thickness</i>	Height of a single layer; vertical resolution of z-axis
<i>Line/extrusion/raster width</i>	Width of the extruded strand influenced by gravitation and the contact pressure of the die

<i>Infill/shells</i>	3D-printed parts are generally filled with less material (infill) and wrapped with shells; depending on the position of the shell it is referred to as top layers, bottom layers, walls or infill; infill pattern (rectilinear, gyroid, honeycomb, etc.), infill/raster angle (0-90°) and infill density (0-100%) can be varied
<i>Build orientation</i>	The way in which the part is in contact with the build plate; rotational part orientation
<i>Support</i>	Material which is used to support the structure in the regions of overhangs/bridges and is removed afterwards from the part
<i>Raft</i>	Auxiliary construction in which the actual workpiece is lifted off the print bed; thin layer of filament printed as a "base"
<i>Brim</i>	Auxiliary construction similar to raft but printed around the workpiece and not extending underneath it
<i>Skirt</i>	Test print close to borders of part, which often helps to identify problems before printing

3.3. Mechanical testing pyramid

The mechanical testing pyramid is a bottom-up tool to systematically analyse the applicability of a material for a certain application. It is also known as the building block approach and was originally developed by NASA for their advanced composite technology and high-speed research program [40]. In aerospace, safety is critical and risk is reduced by testing a new laminate design over a variety of length scales prior to application. Thereby, the number of test specimens is decreasing with increasing number of test level. The conventional building block approach generally consists of four levels:

- Level 1: coupon/specimen
- Level 2: element/first geometrical details
- Level 3: sub-component
- Level 4: component/full-structure/system

Safety also plays a major role in the medical field. Here as well, the use of systematic testing paths is recommended. Therefore, the mechanical testing pyramid was adapted for cranial implants produced via ME-AM in this work (Figure 3). The individual levels are described in the following chapters, whereby levels 2-4 are accompanied by the examination of the introduced morphology and microstructure.

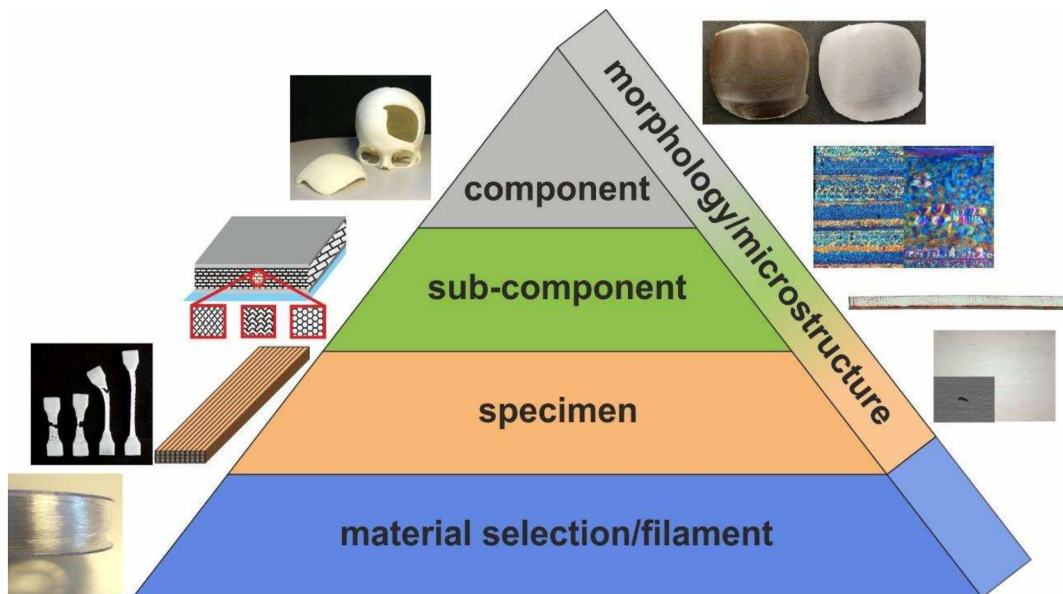


Figure 3: Mechanical testing pyramid adapted for cranial implants produced via material extrusion-based additive manufacturing.

3.3.1. Material selection and filament level

For the fabrication of cranial implants via ME-AM, the material of choice has to be printable as well as implantable. To be printable, the processability of filaments in sufficient quality is a prerequisite. The filament must have a certain stiffness, strength and flexibility so that it can be spooled/unwound and

subsequently pushed into the heating block and out through the nozzle. Additionally, reproducibility is needed with low variations in the filament diameter and ovality. A high filament quality is the key to produce high quality prints. The list of thermoplastic materials that can be processed using ME-AM grows almost daily. However, in terms of food and drug administration (FDA) approval or even certification for implantation, this number is severely limited. For implantation, the material has to meet a large number of demands. First of all, the material must be non-carcinogenic, biocompatible (appropriate response of material when in contact with body tissue or fluids [11]), durable (material remains undamaged/usable during its service life; depends on temperature, media and pH resistance as well as mechanical or electrical stresses [15]) and sterilisable (elimination of all living organisms such as bacteria or viruses without loss in mechanical properties [14]). Another requirement for implant materials is mechanical integrity. The stiffness, strength and flexibility of the material must be suitable for the body part to be replaced [15]. The surface properties of an implant also play an important role. Surface roughness, tension and energy of the implant influence the adsorption of proteins, the wettability by wetting liquids (e.g. blood) and the interaction with cells and tissue [41].

Polymers are often used as implant materials because they have advantageous heat-insulating properties, are easy to process and, unlike metals, do not generate microwaves or electrolytic current, which is advantageous with regard to X-ray scanning [3,41]. Polymer materials that have already been used for implants include PEEK, polylactide (PLA), PMMA, glycol-modified poly(ethylene terephthalate) (PETG), poly(vinylidene fluoride) (PVDF) and polypropylene (PP). On the basis of the available medical approval of these materials, they were examined in more detail in **Publication 1** of this thesis [39]. Among the listed polymers, the use of **PEEK** is most widespread. Several bones of the human body (e.g. spinal, maxillo-facial and cranial implants) are replaced by PEEK implants after an accident or disease [42]. PEEK shows high biocompatibility [43] and durability [44].

However, for the processing of PEEK special printers are needed in order to reach adequate nozzle (~430 °C) and chamber (~160 °C) temperatures [45]. **PLA**, on the other hand, is biodegradable and is therefore used for short-term applications, such as barrier membranes, drug delivery systems, bone scaffolds, stents, sutures and screws [11,46]. The degradation products of PLA are also non-toxic. It is a biopolymer that can be derived from renewable resources such as carbon dioxide, wheat, corn and rice, making it affordable and available. The mechanical properties of PLA are versatile, depending on the molecular weight, degree of crystallinity and stereochemical configuration of the PLA backbone [47]. **PMMA**, on the one hand, is used as intraocular lenses and hard contact lenses due to its excellent light transmission and as bone cement for anchoring hip prostheses, dental applications, orthopaedic and cranial implants due to its sufficient mechanical properties [11,19,48]. PMMA is biocompatible, inert, readily available and affordable and has been used in cranioplasty since 1940 [21]. **PETG** has moderate mechanical properties, making it suitable for parts that do not require high load capacity or elasticity, such as bite guards [39]. Additionally, PETG shows a high biocompatibility. PLA, PMMA and PETG are all easily processible via ME-AM, either because the material crystallises slowly, which is hindered by the high process-related cooling rate (PLA), or because of the amorphous nature of the polymer (PMMA and PETG). However, PLA, PMMA and PETG are all polar materials and their properties could be moisture dependent, which has to be investigated in detail for each type of material prior to application. **PVDF** or **PP** have mainly been used as suture materials or as surgical meshes [11,49]. The main reason for that lies in the high flexibility of those materials. The high ductility of the materials could also be beneficial for bone reconstruction (e.g. cranial implant [50]) in order to prevent splintering if a fracture should occur. The prerequisite for this is a small size of the bone to be replaced, since the materials show too low strength and stiffness values to replace larger parts [39]. Additionally, the deformability of the materials in large implants, e.g. in the skull area, could be too high and in the event of an accident the implant

would be pressed into surrounding sensitive areas, which could have serious consequences. Moreover, PVDF has a high biocompatibility [51], whereas the biocompatibility of PP is controversially discussed in literature [52,53]. In terms of processability, PP and PVDF are more difficult to print due to the crystallisation that occurs during the printing process.

Implant materials have to withstand a large number of different load cases. Firstly, the materials are subjected to temperature and media at all times. Secondly, operating loads as well as incalculable loads (e.g. when you bump into something) should be considered during the design process. As polymers are known to show a temperature and time-dependent material behaviour it is clear that the exact temperature- and time-dependent material properties have to be known as a prerequisite for a meaningful simulation-based design. Therefore, the temperature and strain-rate dependent material properties were evaluated for the aforementioned materials in **Publication 1** of this thesis [39]. It was found that PVDF and PP in particular have strongly temperature-dependent properties in the targeted application area (body temperature range of 37 to 41 °C; Figure 4). For both materials the application temperature is above the glass transition temperature (T_g ; PVDF: - 33 °C; PP: 9 °C) which leads to highly increased chain mobility with rising temperatures. Due to the enhanced mobility of the chains the storage modulus is significantly reduced between 37 and 41 °C (6.5% for PVDF and 10.4% for PP) [39]. The increase in the storage modulus of PLA in the vicinity of 100 °C can be attributed to cold crystallisation (crystallisation during heating), which occurs due to too short a time for complete crystallisation during cooling [54].

Strain-rate dependent tests, discussed in **Publication 1** of this thesis, showed that at lower test speeds there is a tendency towards higher non-linear curve behaviour associated with lower stresses and higher elongations at break for all tested materials (Figure 5). For PMMA, the decrease in strength between crosshead speeds of 10^3 and 10^{-3} mm·s⁻¹ was the highest with approx. 58%.

A change in the type of fracture from brittle to pronounced yielding was evaluated for PLA and PETG.

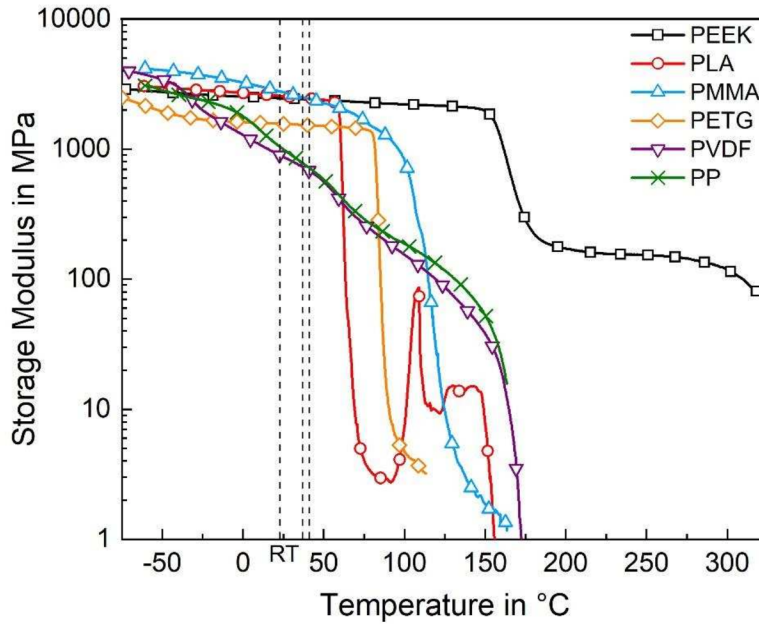


Figure 4: Temperature dependency of several thermoplastic implant materials observed in *Publication 1* of this thesis [39].

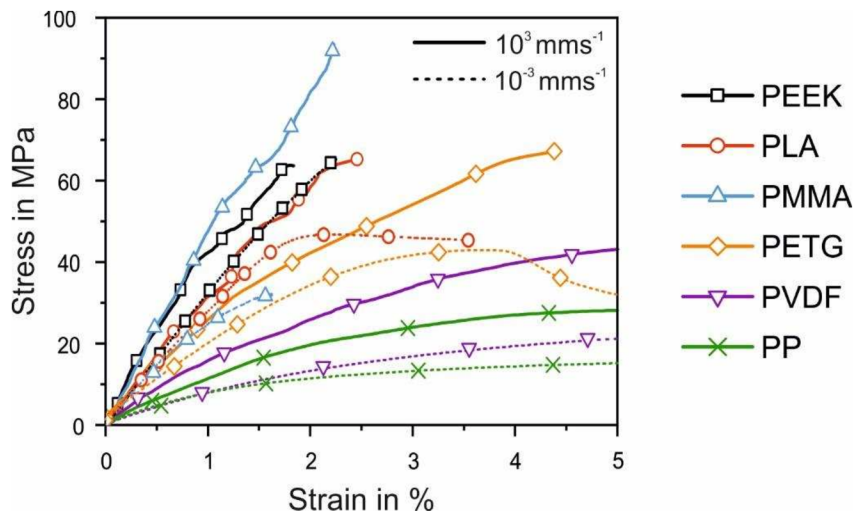


Figure 5: Strain-rate dependency of several thermoplastic implant materials analysed in *Publication 1* of this thesis [39].

3.3.2. Specimen level

The layer-by-layer application of material in additive manufacturing introduces a specific orientation into the component. Depending on the process parameters, heterogeneities such as cavities or entire welding lines are created between the individual strands. Subsequently, it is clear that the material properties are influenced by the processing conditions and the bulk material properties, given in the technical data sheets, are not achievable most of the times. In addition, the resulting **microstructure** often leads to anisotropic material properties. In the direction of the strands near-bulk properties can be achieved, while significantly reduced values can be seen perpendicular to the strands. Furthermore, the layered material deposition results in a waved surface with a topography that is strongly influenced by the chosen process parameters, which affects the interaction with surrounding substances in the case of implants. Depending on the geometry and degree of expression, the waved surface can act similar to notches and weaken the mechanical performance. Hence, tests at specimen level should help to estimate the “real” properties.

Especially for implants, the identification of printing induced defects is of particular importance. Several methods are available to determine the local porosity within a material, such as optical microscopy and scanning electron microscopy (SEM). Both procedures are destructive methods in which the part to be tested is damaged beforehand. When it comes to the global porosity of parts, X-ray micro-computed tomography (μ -CT) is a widely used non-destructive tool to characterise the size, shape and distribution of defects [55]. μ -CT could therefore also be used for quality control prior to implantation; although the relationship between part size, resolution and scan time should be kept in mind. In **Publication 1** of this thesis [39], the local (Figure 6) and global (Figure 7) porosity of tensile test specimens produced via ME-AM using different implant materials were analysed and correlated with the mechanical properties, since printing defects can initiate delaminations and fractures.

Cross-sectional images of a PEEK sample showed a high number of defects in the form of weld lines (Figure 6 a and b). The unsatisfactory printing quality was verified by μ -CT scans of the whole samples, showing a high number of defects (Figure 7 a). High nozzle and chamber temperatures are required for adequate processing of PEEK, which makes printing PEEK challenging. Even if the print quality can still be improved, PEEK has been shown to have a low overall porosity of 1.18%. A small number of defects (Figure 6 c and e) with non-negligible pore sizes (Figure 6 d and f) were found in PLA and PMMA. However, a global observation of the specimens (Figure 7 b and c) revealed satisfying printing qualities with porosity levels between 0.07 and 0.09%. The PETG samples showed more distinct weld lines with increased distance to the build platform (Figure 6 g) and relative small pores (Figure 6 h). For PVDF and PP, small pores (Figure 6 i and k) were observed in small numbers (Figure 6 j and l). All three materials obtained porosity values between 0.11 and 0.20%. In summary, despite large local defects in the parts, the global porosity was low (<2%).

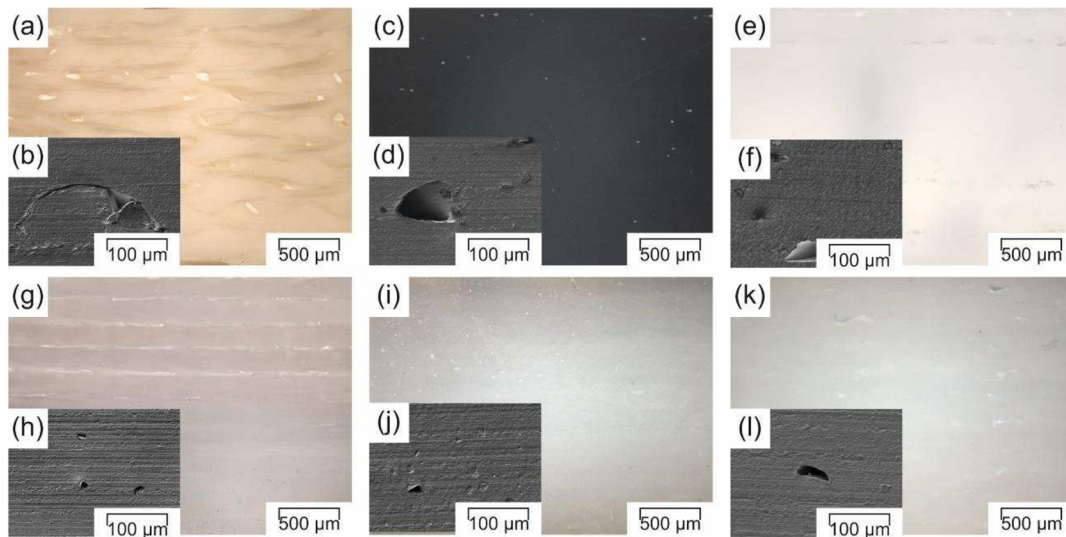


Figure 6: Local representation of defects (optical microscopy and scanning electron microscopy (SEM) images) in tensile bars of PEEK (a and b), PLA (c and d), PMMA (e and f), PETG (g and h), PVDF (i and j) and PP (k and l)

produced via material extrusion-based additive manufacturing, which were evaluated in **Publication 1** of this thesis [39].

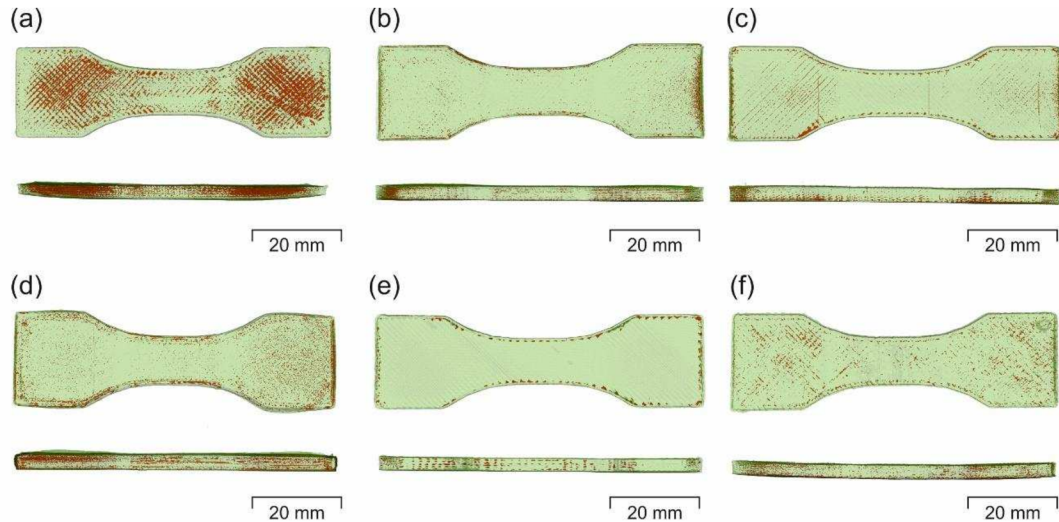


Figure 7: Global representation (2D images of μ -CT measurements) of defects in tensile bars of PEEK (a), PLA (b), PMMA (c), PETG (d), PVDF (e) and PP (f) produced via material extrusion-based additive manufacturing, which were evaluated in **Publication 1** of this thesis [39].

The influence of porosity in ME-AM on the resulting mechanical properties has been studied in numerous research papers. In general, it has been found that as porosity decreases, the mechanical properties of the part produced via ME-AM increase [56–59]. However, as shown in **Publication 2** of this thesis, it was found that if the porosity values of all analysed samples is below 1% (globally – whole sample and locally – predefined local region of highest stresses during testing), no significant influence of differential porosity levels on mechanical properties is observable (Figure 8) [60].

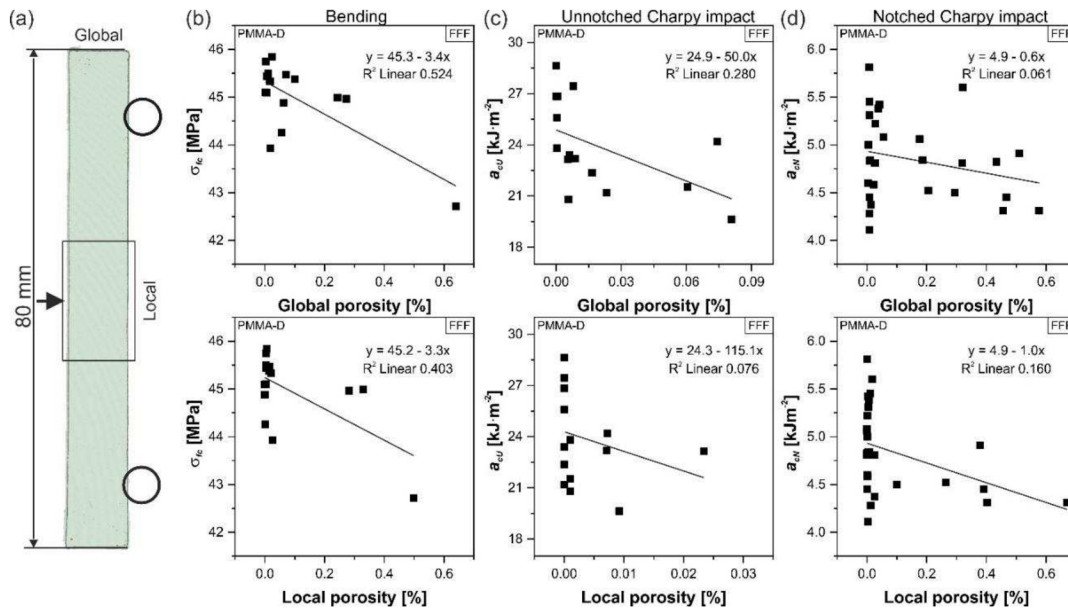


Figure 8: Effect of global and local porosity on mechanical properties of PMMA bars produced via material extrusion-based additive manufacturing according to **Publication 2** of this thesis [60].

Reproducibility and repeatability are important issues when it comes to additive manufacturing. The reliability of the manufacturing process depends on the operator, but also on the printer itself. As mentioned earlier, print quality is largely dependent on the filament quality and the used processing parameters. A slightly different nozzle temperature can change the diffusion between adjacent strands and alter the print quality within the same or a different batch. In the case of AM batch means all samples manufactured during a single print. Within a batch, variations in print quality are most likely due to the uneven temperature distribution on the build platform [61], or uneven levelling of the bed. In addition, the build platform at the bottom is usually set at a specific elevated temperature, resulting in a decrease of temperature in the z-direction. This often leads to larger pore sizes and less diffusion between layers the further the layer is away from the build platform [62]. This has also been shown in **Publication 2** of this thesis, where PMMA was found to show varying porosity within and between different batches (Figure 9) [60].

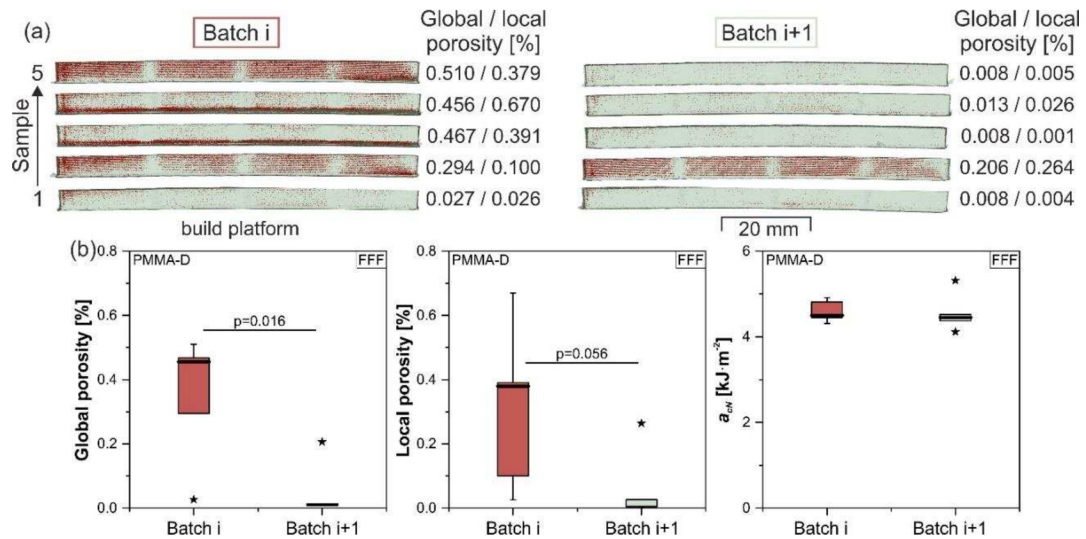


Figure 9: Porosity differences within and between different print batches evaluated for PMMA bars produced via material extrusion-based additive manufacturing in *Publication 2* of this thesis [60].

Varying process conditions do not only alter the introduced microstructure but also the resulting material properties. Exemplarily, higher nozzle **temperatures** result in a lower viscosity of the applied melt, which on the one hand leads to fewer gaps between adjacent strands due to higher liquidity and thus to a larger area of welding and on the other hand to higher diffusion in the contact area between strands due to higher chain mobility. Moreover, increased temperatures (build platform, build chamber and nozzle temperature) generally extend the diffusion time, the weld strength and therefore the mechanical properties. Spoerk et al. [63], for example, investigated that the tensile strength increased from approx. 2 to 54 MPa as the nozzle temperature rose from 190 to 250 °C for 90° oriented PLA samples. Similar results were observed by Refs. [64–66] and explained through the reduced viscosity of the melt at higher temperatures, which increased the interdiffusion depth between adjacent strands. Apart from the influences on the resulting material properties, it should be considered that the actual temperature of the deposited strand usually deviates from the specified

temperature and that the filament cools during extrusion at a rate of about 100 K/s [31].

An opposite relationship is shown by the **printing speed**. A higher speed shortens the diffusion time for adjacent strands as the hot die resides over one spot for a shorter time, and hence, the mechanics of the resulting part are lowered. Furthermore, the print speed has to be correlated with flow rate. As the printing speed increases, the amount of deposited material also increases. This subsequently changes the slippage behaviour in the filament feed system and nozzle head, which alters the material flow. At higher printing speeds, the material flow becomes unstable, which further affects the dimensions of the extruded filament and leads to additional voids [67]. Moreover, a higher printing speed leads to a higher filament feed rate, resulting in a larger diameter of the extruded filament [68,69]. The larger diameter might be associated to die swelling, where the diameter of the extruded polymer increases when exiting the die, which can cause a reduction of voids and thus higher mechanical properties. Additionally, the printing speed has a great influence on the printing time and thus on the lead time of the implant.

Several printing parameters are linked with each other, as is the **extrusion multiplier** with the flow rate, which in turn affects the **line width** [70]. In terms of the extrusion multiplier or line width, Butt et al. [71] found that increasing values of both parameters lead to a greater thickness of the part. The results also show that a better surface quality can be achieved with lower values for the extrusion multiplier. On the contrary, higher multipliers and widths reduced the resulting strain values. Ferretti et al. [72] investigated that the line width plays a key role regarding the printing quality of the final part as it is directly connected to the number and final volume of defects and therefore to the mechanical characteristics of the printed part.

The influence of the **layer height** is controversially discussed in the literature, as different mechanisms overlap here again. Refs. [64,66] stated that a small layer thickness results in low tensile strength since more weld lines also mean

a higher number of printing errors. Refs. [73–76] showed increased tensile strength with decreased layer thickness, explained by an improved cross-flow of the deposited filaments that are more compressed, due to the reduced layer thickness. The improved cross-flow further enhanced the print quality. Therefore, it can be said that it is an interplay between improved cross-flow and a higher number of weld lines. In addition, depending on the geometry of the part to be printed, the passing hot nozzle affects more underlying strands at lower layer heights. That way elevated temperatures are maintained for a longer period of time and thus achieving an annealing effect. However, a lower layer thickness also results in a significantly increased printing time and therefore lead time of an implant [77].

Parts produced via ME-AM mostly display anisotropic tensile behaviour, which is significantly influenced by the orientation of the single strands. Testing in the direction of the strands usually achieves the highest mechanical properties, whereas testing perpendicular to the strands generally tests the welds and therefore shows the lowest performance. Depending on the print quality, the mechanical properties can deteriorate considerably. Zhao et al. [76] showed that the tensile strength and Young's modulus decreased with increasing **infill angle** between 0 to 90° (0° - strands parallel to load direction, 90° - strands perpendicular to load direction). For PLA printed with a layer thickness of 0.3 mm, differences of 26.93 MPa in tensile strength and 0.86 GP in Young's modulus were found. Zimian et al. [78] printed acrylonitrile-butadiene-styrene copolymer (ABS) with different raster orientations. The values for ultimate and yield strength were highest for the 0° (25.15 and 24.18 MPa), followed by ±45 (16.90 and 15.34 MPa) and 90° (9.16 and 8.55 MPa). Considering the tension fatigue life, ABS specimens printed with a raster orientation of ±45 showed the highest value followed by 0°, 45° and 90° rasters.

Similar to the raster orientation, the **build orientation** strongly influences the resulting mechanical properties. Depending on the build orientation, the influence of the heated print bed on the resulting temperature profile and the

deposition of the individual layers on top of each other are differently. Hence, the welding between the adjacent strands is affected. PLA printed with 30% infill obtains the highest tensile strength when printed flat – XY (55.49 MPa) followed by printed on edge – XZ (48.18 MPa) and is weakest when printed upright – Z (35.52 MPa) [79]. Additionally, the Z printed specimens have the longest build time (231 min) compared to XY (29 min) and XZ (59 min) printed samples. For ABS, XZ printed specimens performed best in terms of tensile modulus and strength [80]. Upright printed specimens showed significantly lower ultimate tensile strength and elongation at break. XZ-orientation further resulted in the highest flexural modulus and elongation at break in bending. For torsion, similar moduli and strength values were obtained independently of the build orientation.

As already stated, in additive manufacturing by material-extrusion there is a huge number of influencing factors on the part quality and therefore resulting properties. For this reason, amorphous (e.g. PMMA) or slowly crystallising semi-crystalline polymers (e.g. PLA) are often used, as the number of influencing factors increases further with other semi-crystalline polymers (e.g. PP). Process-induced morphology and crystallography are very complex and print errors such as shrinkage and warpage are often the result. To gain further knowledge about the effects of process-induced morphology in semi-crystalline polymers, PP was printed with different parameter sets and thermal, mechanical and morphological characteristics were examined in **Publication 3** of this thesis [81]. A variation of the printing speed and/or the nozzle temperature affected the size of the spherulites formed and the creation of the oriented crystalline structures (shish-kebab) at the strand boundaries, which spread towards the core of the strand (Figure 10). At a printing speed of $22.5 \text{ mm}\cdot\text{s}^{-1}$ and a low nozzle temperature of $200 \text{ }^\circ\text{C}$ shish-kebab structures were also found within the strands, as a consequence of increased shear in combination with thermal conditions.

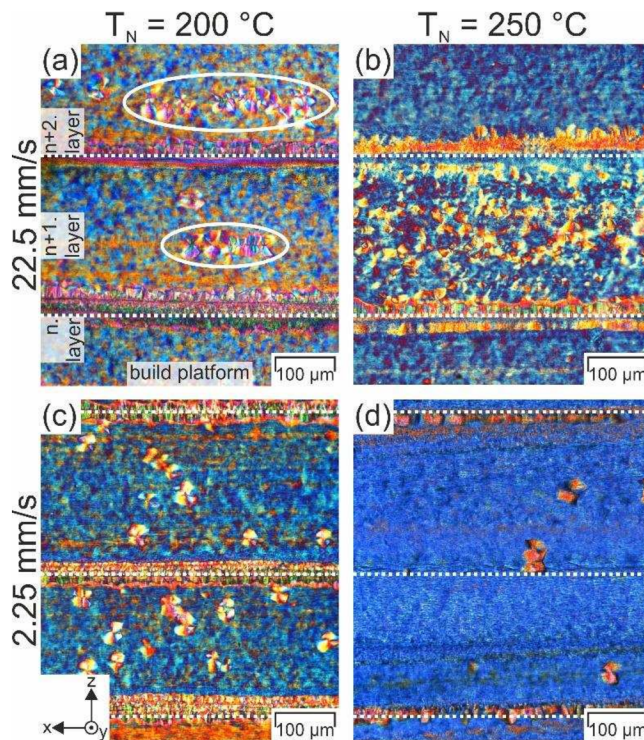


Figure 10: Effect of nozzle temperature and printing speed on the morphology of PP produced by material extrusion-based additive manufacturing, as described in **Publication 3** of this thesis [81].

Moreover, the effect of the printing sequence for two rectangular PP specimens unidirectionally (x-axis) printed at a printing speed of $22.5 \text{ mm} \cdot \text{s}^{-1}$ and a nozzle temperature of $250 \text{ }^\circ\text{C}$ is demonstrated in **Publication 3** of this thesis (Figure 11) [81]. First, the first layer of part 1 is printed than the first layer of part 2 is printed. Afterwards, the second layer of part 2 is printed on a layer which still shows elevated temperatures, whereas the second layer of part 1 is printed on a layer which already had enough time to cool down. This sequence is continued until the parts are finished. Due to this printing sequence, an alternating morphological structure is introduced to the material (layer with big spherulites vs. layer with small spherulites). On the other hand, if the printer would always start with depositing the layer of part 1, and then moving to part 2, a more homogenous structure would be created. This should illustrate how strongly the component properties depend on the print path when using

semi-crystalline polymers. Therefore, tool path generation is a non-neglectable step in AM and can be used to search for paths with a nearly homogenous temperature distributions to provide more homogenous parts and reduce shrinkage and warpage, continuous paths to allow for printing of continuous fibre reinforced thermoplastics, paths to reduce the printing time or save material, to improve precision and surface quality, or to enhance certain mechanical properties such as strength [82–84].

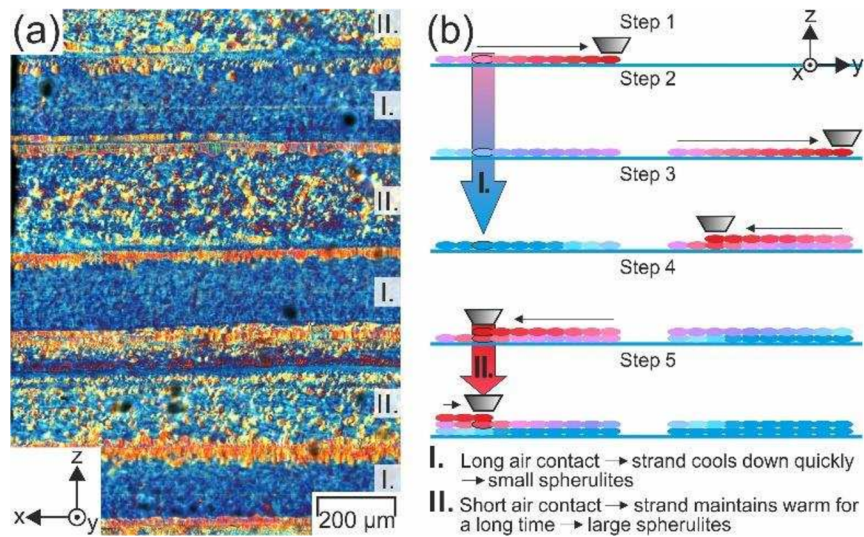


Figure 11: Influence of print path on morphology of PP produced via material extrusion-based additive manufacturing, as shown in **Publication 3** of this thesis [81].

As previously mentioned, higher temperatures enhance the interdiffusion between adjacent strands. In **Publication 3** of this thesis it was verified that this led to less pronounced weld lines and furthermore higher forces were needed to tear the sample apart (Figure 12) [81]. On the other hand, the printing speed does not seem to have a significant influence on the tearing forces for PP produced via ME-AM at very high nozzle temperatures, as the high temperatures led to less pronounced weld lines due to longer weld times.

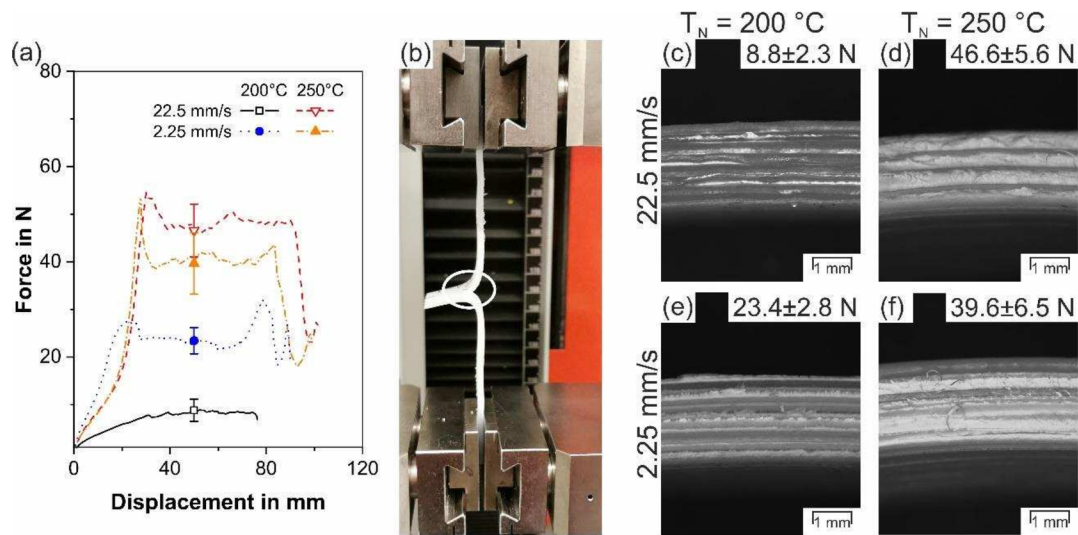


Figure 12: Effect of printing speed and nozzle temperature on weld strength of PP produced by material extrusion using additive manufacturing, as found in **Publication 3** of this thesis [81].

Furthermore, higher oriented structures with oriented crystalline structures in the direction of the strands led to increased thermal conductivity along the strands (axial) but lower values perpendicular to the strands (radial) for unidirectionally printed PP samples analysed in **Publication 3** of this thesis (Figure 13: Impact of printing speed and nozzle temperature on thermal conductivity of PP produced by material extrusion using additive manufacturing, as observed in Publication 3 of this thesis [81].Figure 13) [81].

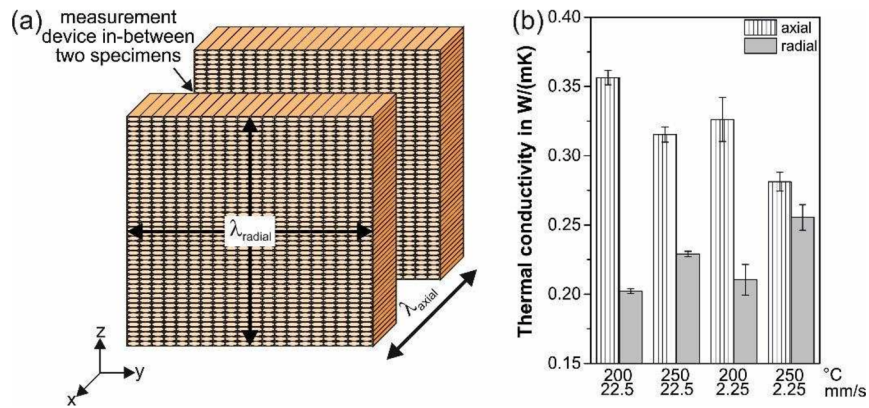


Figure 13: Impact of printing speed and nozzle temperature on thermal conductivity of PP produced by material extrusion using additive manufacturing, as observed in *Publication 3* of this thesis [81].

The process parameters can therefore be used to control the morphology and thus the thermal properties, such as the thermal conductivity, of a component.

Similar to different processing conditions, posttreatment steps can also influence the mechanical properties, morphology and microstructure. One step which all medical devices have to undergo before application is **sterilisation**. Sterilisability is a prerequisite for implant materials, as they must be free of pathogens and contaminants before use [85]. In addition, the sterilisation process must not significantly alter the dimensions or mechanical integrity of the part. The most common sterilisation method is autoclaving, which uses high-pressure steam. This process takes place at temperatures above 120 °C for a prolonged period of time and is therefore only suitable for metals, ceramics and high-performance thermoplastics (e.g. PEEK). However, thermolabile polymers with low melting temperatures (e.g. PLA, PMMA, PETG, PP, PVDF) are deformed at these temperatures, so that other sterilisation processes are required. Chemical sterilisation (ethylene oxide or formaldehyde), radiation sterilisation (gamma, electron or X-rays), plasma sterilisation or microwave sterilisation are possible methods [86,87]. Kumar et al. [88] analysed the repeatability of sterilisation of a PEEK surgical clip in order to investigate its reusability. Therefore, they sterilised the component up to 100

times at 121 °C for 30 min each. After 30 cycles, the compressive force was reduced by ~20%, after 50 cycles lateral dimension decreased by ~6%. The degree of crystallinity and the melting behaviour of PEEK was not significantly affected, whereby the hardness increased by ~49% after 20 cycles. For thermolabile polymers such as PLA, PETG, PVDF and PP, conventional sterilisation methods (heat, gamma irradiation and ethylene oxide) can lead to the release of toxic products, damage the product or change the properties/dimensions due to the thermal and/or hydrolytic sensitivity of these materials. According to Ref. [89], there is no optimal standard sterilisation technique for PLA and the parameters for the chosen sterilisation technique must be evaluated individually for each application. Oth et al. [90] suggested sterilisation with hydrogen peroxide for PLA and PETG surgical genioplasty guides produced by means of ME-AM, as the dimensional deformations are in the submillimetre range and compatible with surgical use. Münker et al. [91] examined the influence of ethylene oxide, hydrogen peroxide gas plasma, autoclaving and γ -irradiation on materials based on PMMA and found that all methods except for autoclave sterilisation seem to be suitable. Chu [92] stated that for PP sterilisation via ethylene oxide gas is suitable, while PVDF can be sterilised using the conventional γ -irradiation method due to the absence of an α -alkyl group. Gahleitner et al. [93] investigated the effects of steam and γ -irradiation on different PP grades and found that the changes in the material are mainly related to degradation (irradiation) and post-crystallisation (steam). The embrittlement of most standard grades can be overcome by using copolymeric systems or special stabilisers.

Another important step for medical devices to consider, especially with polymers, is **cleaning**. This step is performed prior to sterilisation using temperature, pressure and an aqueous cleaning solution [94]. Since polymers are known to have temperature, pressure and moisture dependent properties, the cleaning step could significantly affect the properties of the resulting part. There are several studies in literature on the effects of different sterilisation processes on the material behaviour of different thermoplastic polymers

produced by ME-AM, but not yet in combination with the preceding cleaning process.

Due to the porous structure of additively manufactured samples, they could be more affected by these processes than solid, non-porous, moulded samples, as their absorption-desorption behaviour is expected to be different. For this reason, and because the combination of cleaning and sterilisation has hardly been addressed in literature so far, the combined effect was analysed for a widely used thermolabile implant material, PMMA, in **Publication 2** of this thesis [60]. It was found that the combination of formaldehyde sterilisation and prior cleaning did not significantly affect the flexural properties of two different PMMA materials. One PMMA grade was found to have a significantly lower Charpy impact strength after washing. This change did not correlate with porosity, so it can be attributed to the cleaning process. The effect could not be explained by changes in the chemical structure, the presence of residual media or the analysis of the fracture surfaces. However, the effect was neutralised after sterilisation and no reason was found not to apply this cleaning/sterilisation routine for the PMMA-based materials investigated.

To improve the mechanical properties and surface finish of printed parts, several different post-processes can be applied, such as grinding, polishing, vapor smoothing or annealing. Conventional **grinding and polishing** techniques are mainly suitable for simple parts with straight edges. Since 3D-printing is usually used to produce more complex parts, other processes are favoured here. For parts that are not too complex, the vibratory grinding process can be applied. In this process, the workpieces to be processed are placed in a container together with abrasives and usually an additive in an aqueous solution. An oscillating or rotating movement of the container creates a relative movement between the workpiece and the abrasive, which causes material removal on the workpiece, especially on the edges. Vibratory surface finishing has been successfully performed on 3D-printed Ti-6Al-4V parts, resulting in values for roughness and wettability applicable for medical devices

[95]. In the case of polymers, care should be taken to select an aqueous solution that does not interact physically or chemically with the material. **Vapour smoothing**, on the other hand, is a finishing option that exposes printed parts to an evaporated solvent. Steam smoothing of 3D-printed parts replaces the wavy surfaces caused by the process with smooth, glossy surfaces. Kuo and Mao [96] applied acetone vapours on ME-AM parts, resulting in enhanced surface finish, minimal dimensional changes and increased strength. Garg et al. [97] obtained similar results for other geometries with variable printing orientation. However, the open porosity of ME-AM leads to the penetration of disinfectant solutions, which poses safety problems in the field of medical implants [98].

Among the before listed post-processing techniques, **annealing** is of particular interest when it comes to enhancing mechanical strength [99]. In the ME-AM process, each layer is printed by extruding lines of thermoplastic polymer onto a partially cooled, previously deposited layer (Figure 11). When the next line of polymer is applied to the previous layer, the material interface rises above the material's T_g for some time (depending on the part geometry and processing parameters) allowing some degree of molecular reptation at the interface. In combination with the applied compaction pressures at this interface a more or less firm connection is formed. Generally, the times for sufficient diffusion and re-entanglement are not achieved, resulting in poor interfacial strength, so that the parts cannot be used in many technical applications. By annealing the part at temperatures above the T_g of the material, the time for diffusion can be prolonged, enhancing the mechanical properties. Pazhamannil et al. [100] reached an increase in ultimate tensile strength of ~25% and in compressive strength by ~22% for PLA produced via ME-AM after annealing. Improved physical and mechanical properties were also achieved for ABS manufactured by ME-AM by Singh et al. [101]. However, annealing can also release residual stresses, which can further result in dimensional changes. Therefore, Dunn et al. [102] tried to overcome this by including ABS, a polymer with a low T_g , in a shell of polycarbonate with a high

T_g . After annealing at a temperature between these two T_g values, a structure with high interlaminar strength was obtained while maintaining the geometric dimensions. Single edge notched bending tests showed 1800% higher fracture toughness for annealed samples compared to untreated samples, with the annealed samples fracturing ductile and the untreated specimens showing a brittle fracture behaviour.

3.3.3. Sub-component level

Additive manufacturing offers a high degree of freedom in the design of an object. Nevertheless, not everything is possible. With AM via material extrusion, it must be considered that the printing of an object has to start at the building platform. Due to gravity, not all printing angles or bridges are possible. Therefore, some designs need sacrificial structures, called supports, to connect the object to the build platform. It is important to consider how the supports can be removed later without damaging the printed part. Therefore, designers need to create high-quality digital models of the final product and keeping the printability in mind ("Design for Additive Manufacturing") [103].

Altering the **geometry** and **part size** (AM is scalable) changes the thermal history within the part [104], which further effects the bonding between neighbouring layers and thus the material properties. An optimised print profile evaluated for a specific geometry and size may no longer be the best option when details in the design or the size of the object are changed. This is particularly important in the field of medical implants, as each printing profile for a specific implant has to be certified [105–107]. Therefore, two different printing profiles will probably have to be certified for printing large and small implants with the same material (e.g. one profile for implants below a certain size and one for implants above the threshold).

With AM, nearly all unnecessary materials can be omitted as long as in the resolution of the printer. Not only can solid objects be produced, but also a wide variety of different **internal structures**. As already described in chapter

3.1, internal structures such as porosity can be used to adjust cell adhesion, migration, nutrient supply, and biological fixation [29,30]. In addition to the medical properties, the mechanics also play an important role. Concerning cranial implants, the proper internal structure in terms of mechanical properties – which should absorb a huge amount of energy before failure, should not deform too much and should not splinter when fracturing – was evaluated by printing sandwich-structures with different core patterns. Therefore, in **Publication 4** of this thesis PMMA sandwich structures produced via ME-AM with three different infill patterns (rectilinear, gyroid and 3D-honeycomb) and four different infill densities (30, 50, 70 and 100%) were analysed in terms of their impact properties [48]. The highest impact properties were obtained with 3D-honeycombs compared to rectilinear and gyroid structures with the same infill density (Figure 14). The stresses were distributed radially from the point of impact, but due to the stress concentration at the bottom of the plate (Figure 15), the final failure occurred quite early, resulting in a relatively low total absorbed energy.

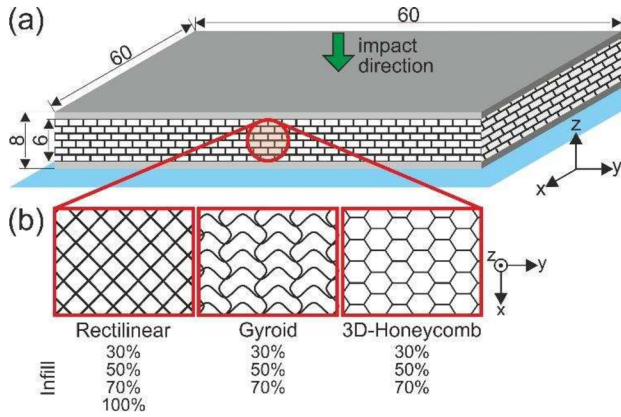


Figure 14: PMMA sandwich structures produced by material extrusion using additive manufacturing with different internal architectures (infill pattern and density) tested in **Publication 4** of this thesis [48].

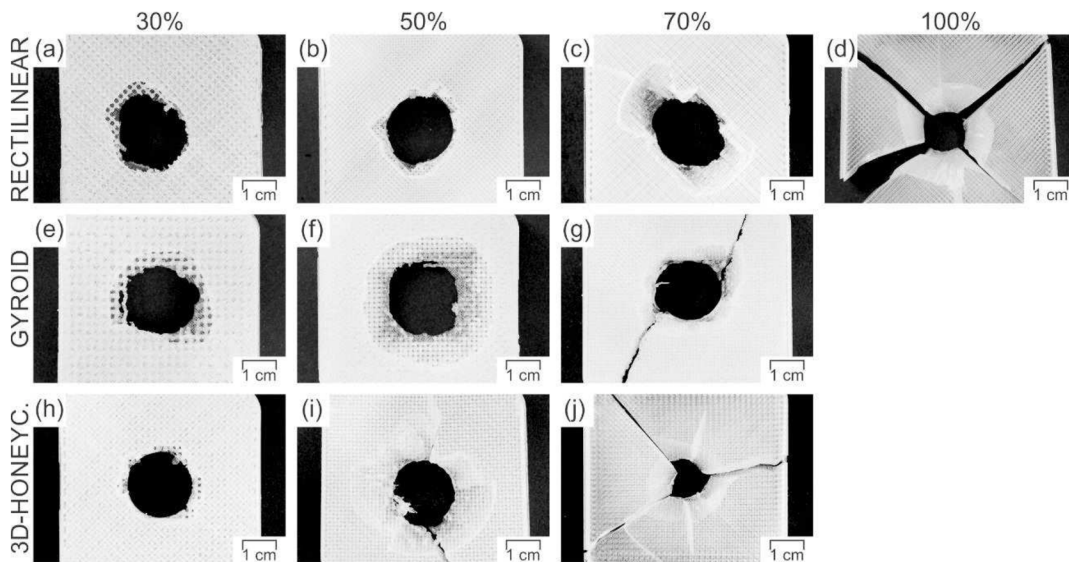


Figure 15: Fracture pattern of PMMA sandwiches produced by material extrusion using additive manufacturing with different internal architectures (infill pattern and density) shown in **Publication 4** of this thesis [48].

At a certain infill density (70% for 3D-honeycombs and 100% for rectilinear structures), there was a transition in transparency and also in the fracture type, from a normal puncture to a more shard-like failure. The individual strands of the structure were no longer separated from each other and rather the material and not the structure was tested.

One method to find the optimal material distribution or load path in a predefined design space for a given load and boundary condition is **topology optimisation** [108]. In **Publication 4** of this thesis a topology optimised PMMA sandwich structure with minimised compliance and a mass-fraction of $\leq 50\%$ (Figure 16 a) resulted in high values for the force at first damage and the corresponding absorbed energy when impact tested [48].

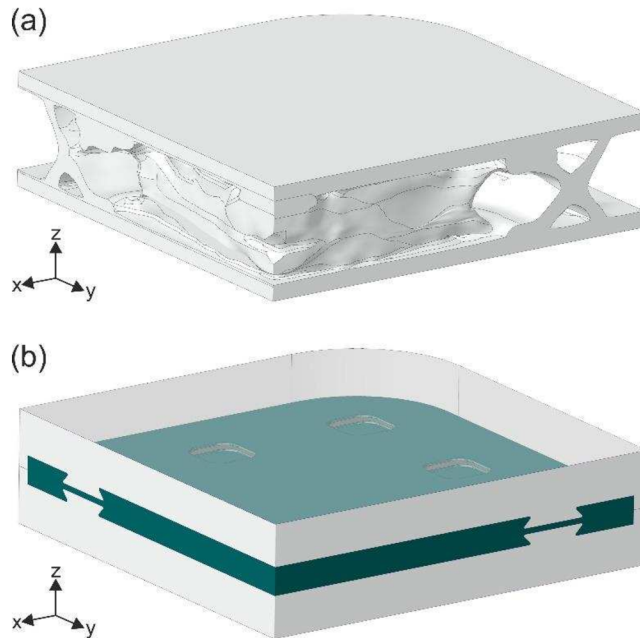


Figure 16: Topology (a) and material optimisation (b) of PMMA sandwich structure investigated in **Publication 4** of this thesis [48].

The mechanical properties and fracture behaviour could also be enhanced by **material optimisation**. By combining a compliant and a stiff material, energy absorption can be improved, if the elastic material acts as a crack stopper [109]. Hence, in **Publication 4** of this thesis, PMMA was tested with a thermoplastic copolyester elastomer interlayer (Figure 16 b). All impact energies were improved due to the ductility of the interlayer, but with a deterioration of stiffness and maximum achieved forces [48]. This means that a lot of work has to be done still in order to achieve optimal mechanical integrity of cranial implants produced by ME-AM.

3.3.4. Component level

Finally, cranial implants were manufactured using the knowledge gained from testing at the other levels of the mechanical testing pyramid to find the optimal processing conditions and application-oriented tests were performed in **Publication 5** of this study [110]. Based on the results of levels 1+2 of the mechanical testing pyramid, PEEK was chosen as the material of choice for

the final component tests due to its adequate mechanical properties with low temperature dependency in the application temperature range. Since PEEK is also a semi-crystalline polymer, the process-structure-property relationships are very complex, but the resulting properties can also be strongly controlled by process changes. Literature research and previous studies have shown that the strand orientation with regard to the load direction and the temperature profile significantly influence the result. For this reason, the last study focused on the influence of the build orientation and the air flow temperature, which indicates the temperature of the air stream flowing upwards through holes in the print bed and is a specific feature of the printer used, as very high ambient temperatures are required to print PEEK, on the mechanical integrity of cranial implants produced via ME-AM. As described in level 3 of the testing pyramid, impact loads are the most critical load case for cranial implants and were therefore applied to the printed components. Additionally, the implants were manufactured with an infill density of 100% and a rectilinear infill pattern, as this turned out to be one of the most promising variants during sub-component testing. The results were compared to a commercial milled PEEK implant.

It was found that, independently of the **build orientation** all PEEK cranial implants manufactured by ME-AM broke into 2 to 4 pieces when impacted, which is a huge advantage over the commercial milled implant that broke into a larger number of pieces (Figure 17). These pieces could injure the surrounding tissue if an accident occurs in the real application. Although the printing process introduces welds that weaken the mechanical behaviour perpendicular to the strands, the direction of crack propagation can be defined by the strand arrangement, preventing splinters when fracturing. Upright printed samples resulted in the lowest mechanical properties, due to the low weld strength in z-direction of the prints. When the samples were tilted by 45°, they still broke between the strands in the z-direction, but the effective cross-section between the layers was increased by the tilting. This led to an improvement in mechanical properties compared to upright printed samples. The mechanical integrity can further be improved by using a horizontal build

orientation, where the loading direction is perpendicular to the strands and the fracture propagates in the direction of the imperfections in the part (e.g. voids).

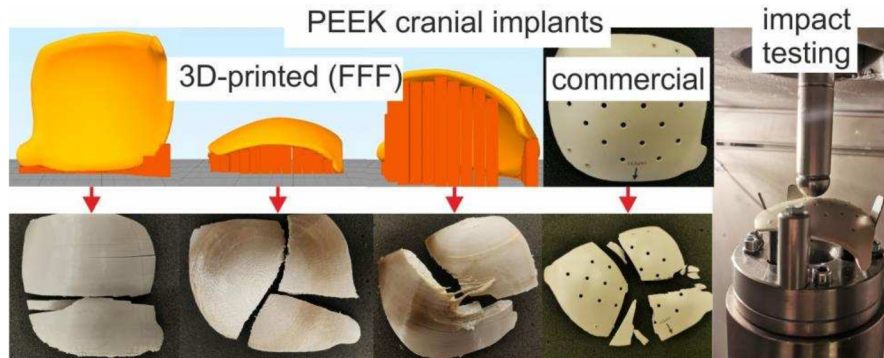


Figure 17: Impact of build orientation on impact behaviour of PEEK cranial implants produced by material extrusion using additive manufacturing, as presented in *Publication 5* of this thesis [110].

As mentioned in chapter 3.3.2, the mechanical properties of parts generated via ME-AM are generally increased by annealing. A similar principle to annealing underlies the application of an increased build chamber or **air flow temperature**, which both increase the surrounding temperature. This results in a reduced cooling speed and prolongs the time for crystallisation. The increased ambient temperature causes an annealing effect during the printing process. In *Publication 5* of this thesis, it was found that with PEEK, insufficient time for crystallisation led to colour inhomogeneity due to remaining amorphous brownish areas [110]. Additionally, low air flow temperatures resulted in lower degrees of crystallinity and bigger amorphous areas (Figure 18). Due to the short crystallisation time and the associated low degree of crystallinity of the parts printed without air flow temperature, crystallisation was observed during the first heat cycle of differential scanning calorimetry analyses, the so-called cold-crystallisation.

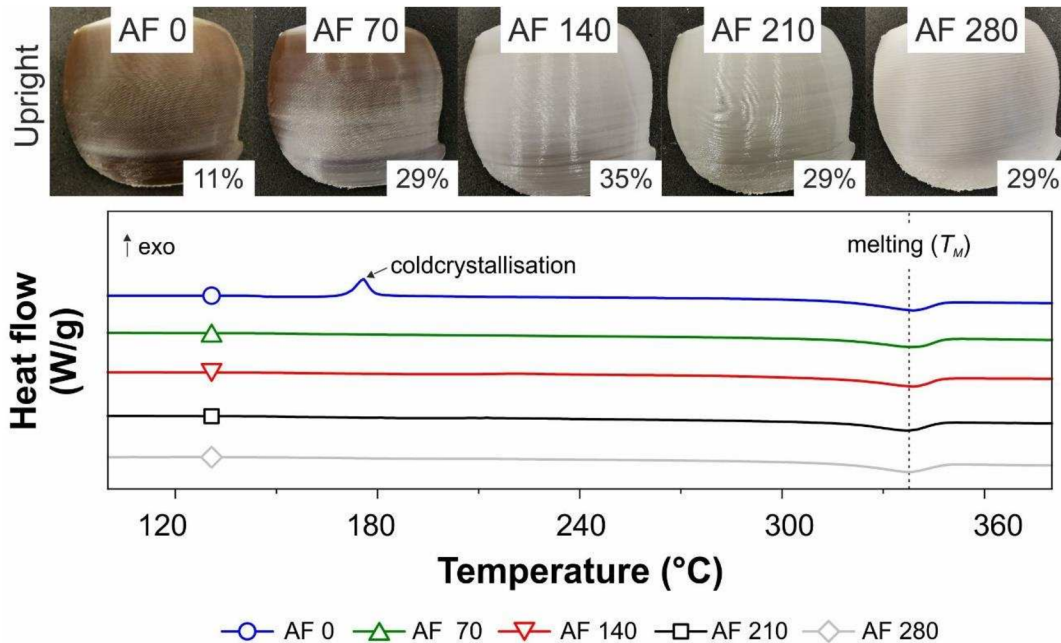


Figure 18: Impact of air flow temperature (AF) on appearance and degree of crystallinity (top) and differential scanning calorimetry curves (bottom) of upright printed PEEK cranial implants analysed in *Publication 5* of this thesis [110].

As the appearance of the implants is crucial for the surgeons, a uniform colour is necessary as they are in charge in the end. Uniformly coloured implants give them a “good feeling” and trust in the implant. Therefore, amorphous areas should be avoided, even though they may show better mechanical behaviour. The amorphous areas are associated with lower degrees of crystallinity and result in moderate maximum impact forces, high deformations up to maximum force - even to final failure - and thus high energy absorption values up to maximum force as well as high values of total absorbed energy. In addition, the amorphous parts have a positive influence on the fracture pattern, as the individual fragments were still partially connected after the impact. The reason for this is plastic deformations of the amorphous areas, which prevent splintering in the event of an accident.

As described in chapter 3.3.2, not only the internal microstructure is influenced by the process, but also the **surface quality**. For implant materials, surface quality plays a crucial role in the interaction between the implant and the surrounding soft tissue or bone. For milled implants, the surface quality can be analysed by its roughness, whereas for components produced via ME-AM, the waviness or rather topology is more important due to the layered structure introduced by the manufacturing process. In **Publication 5** of this thesis, a study investigating the effects of various process parameters on the mechanical performance and implant quality of PEEK cranial implants manufactured by ME-AM, horizontally printed implants were found to have higher waviness compared to 45° tilted and upright printed implants [110]. This was attributed to a greater offset between each printed layer, which is much more pronounced compared to vertical implants where the weld between adjacent layers is tighter as a result of direct pressure through the print nozzle. In addition, the positioning and volume of the support structures contributes to the increased waviness of horizontally printed implants, as residual material is being produced during their removal forming an irregular topology. Therefore, efforts are still being made to optimise the support structures and their removal.

4. Summary and conclusions

Safety plays a key role in the medical field. The use of systematic testing paths, similar to the mechanical testing pyramid developed by NASA for their advanced composite technology and high-speed research program, is recommended during the design process of cranial implants. Therefore, the conventional mechanical testing pyramid was adapted for cranial implant materials produced by material extrusion-based additive manufacturing (ME-AM) in this work, whereby the introduced **morphology and microstructure** play a relevant role once the material has been processed (levels 2-4):

- **Level 1 – material selection/filament:** For each application, the material to be selected has to fulfil a high number of specifications. During material selection, the material in its filaments form can be used to carry out tests without having to produce test specimens beforehand. This benefit was applied in **Publication 1** of this thesis, which analysed the temperature dependent mechanical behaviour of several medical polymers, namely polyetheretherketone (PEEK), polylactide (PLA), poly(methyl methacrylate) (PMMA), glycol-modified poly(ethylene terephthalate) (PETG), poly(vinylidene fluoride) (PVDF) and polypropylene (PP). It was found that for PEEK, PLA, PETG and PMMA the temperature dependence within the application range (37 to 41 °C) is rather small, as the glass transition temperatures (T_g) of these materials are far above the applied temperatures. In contrast, for PVDF and PP, the application temperature range is above the T_g of the two materials, with the storage modulus decreasing by 6.5 and 10.4% between 37 and 41 °C, respectively. It is

therefore crucial to include temperature dependent properties in any design process to obtain correct results for finite element analysis.

- **Level 2 – specimen:** As time and temperature fluctuations may have a considerable influence on the behaviour of polymers, application-related tests should be carried out to gather meaningful input data for simulation-aided design. Therefore, the tensile tests were conducted on PEEK, PLA, PMMA, PETG, PVDF and PP tensile bars manufactured via ME-AM at different crosshead speeds in *Publication 1* of this thesis to determine the strain-rate dependent stiffness, strength and elongation at break of the individual materials. The highest stiffness and strength were evaluated for PEEK and PMMA, which accounts for their use in load-bearing applications such as cranial implants. With decreasing testing speed, higher non-linear curve behaviour was recognised. In the case of PLA and PETG, the overall behaviour changed from a predominantly brittle towards pronounced yielding.

Moreover, medical devices have to undergo a cleaning and sterilisation step prior to application, with either certain temperatures, pressures or various media acting on the material. Hence, the effects of these processes on the resulting properties must be investigated individually for each material-process combination, since several polymers are thermolabile or influenced by media and the manufacturing process introduces a certain structure to the material that could affect the absorption behaviour of the resulting part. For this reason, the influence of a combination of sterilisation (with formaldehyde) and the preceding cleaning process was analysed for PMMA manufactured via ME-AM in *Publication 2* of this thesis. No reason was found not to apply the sterilisation routine used for the PMMA studied. Moreover, it was shown that the porosity of all tested samples was less than 1% and no correlation with mechanical performance was found.

Even if the material is suitable for the application in principle, the mechanical integrity can be lost due to process-related influences. Especially for semi-crystalline polymers the complex relationships between

the processing parameters during material extrusion and the crystallisation behaviour of semi-crystalline polymers are not yet fully understood. Therefore, the influence of process-related orientations on the morphology, and further on the material properties, was analysed for PP in **Publication 3** of this thesis. It was shown that nozzle temperature and printing speed change the thermal profile during printing and therefore the morphology and degree of orientation. Both almost homogeneous structures and strongly anisotropic structures with pronounced weld lines were found. Depending on the combination of temperature and speed, more or less oriented crystalline structures – shish-kebab structures – were formed. One parameter set led to layers with varying spherulite sizes, which could be correlated with the standard printing sequence of the slicer software, where the sample had alternating areas of high heat retention (large spherulites) and areas that cooled quickly (small spherulites). When larger components are printed or many parts are processed at the same time, more pronounced alternating structures could be generated. This confirms that the printing sequence suggested by the slicer software should not be chosen arbitrarily, but can be used to control the morphology. The process-induced morphology further resulted in altered material properties. A more homogenous morphology led to higher weld strength between adjacent strands and nearly isotropic thermal conductivity. In the case of an inhomogenous morphology, strong thermal anisotropy was obtained. In summary, it was found that small changes in the printing parameters impacted the resulting material properties at different length scales.

- **Level 3 – sub-component:** With 3D-printing, the degree of freedom in designing an object is almost limitless. Hence, internal structures can be used to improve cell adhesion, migration, nutrient supply and biological fixation on the one hand and to optimise mechanical performance on the other. For this reason, PMMA sandwich-structures produced via ME-AM including different internal core-architectures and infill densities were analysed in sub-component tests in **Publication 4** of this thesis to evaluate

the structure with the highest mechanical performance on impact. Classical 3D-honeycomb structures outperformed rectilinear and gyroid internal structures at the same infill density in terms of the resulting impact properties. 3D-honeycomb internal structures with 70% infill and rectilinear structures with 100% infill gave the best combination of allowable force level and absorbed energy. A stiffness-based topology optimised structure resulted in high values for the force at first damage and the corresponding absorbed energy, whereas a structure with an incorporated thermoplastic copolyester elastomer interlayer, which should act as a crack stopper, significantly increased impact energies due to the ductility of the compliant interlayer, but at the expense of maximum force and dynamic stiffness. The ductility of the interlayer is associated with a high degree of deformation, which, when used in a cranial implant, could injure the surrounding tissue in the event of an accident. In summary, it was found that the energy to first damage in combination with the deformation to this point and the dynamic stiffness are critical parameters for the design process of cranial implants.

- **Level 4 – component:** At the highest level of the mechanical testing pyramid, tests were carried out on real components - cranial implants. The previous levels of the testing pyramid helped to find the most promising bone reconstruction material, the most influential processing parameters, the optimal infill strategy and the key mechanical properties to be looked at for cranial implants. As a conclusion, the effects of build orientation and air flow temperature on the mechanical performance and implant quality (colour uniformity, surface topography and degree of crystallinity) of PEEK cranial implants produced via ME-AM were investigated in **Publication 5** of this thesis and compared to a commercially available milled PEEK implant. The most similar mechanical properties to the commercial implant were evaluated for horizontally printed implants, where the load is applied perpendicular to the strands, followed by 45° inclined and upright printed parts. In contrast, the surface quality was best for upright printed implants and worst for horizontally printed ones, mainly due to residual support

structures remaining on the surface. In addition, a high air flow temperature was found to improve the crystallisation process by prolonging the time for crystallisation, resulting in a more uniform colour distribution, which is preferred by surgeons. Without air flow temperature, extensive brown amorphous regions formed, resulting in increased ductility, and thus, absorbed energy to fracture due to very high deformation levels. Such high deformations can injure the surrounding soft tissue in the case of an accident. Additionally, the implant must not splinter when fracturing. However, it was observed that the commercially available implant broke into several pieces in an impact test, which could be another advantage of ME-AM, where the fracture path can be predetermined by the printing path.

5. Outlook

Based on the findings so far, several research fields should be addressed in the future. Firstly, in **Publication 1** and **Publication 5** of this thesis, it was shown that the morphology and the resulting material properties of semi-crystalline polymers can significantly be altered by changing the ME-AM process conditions. This can be used to tailor the resulting properties. Furthermore, the introduction of multiple welds into the material due to layer-by-layer deposition weakens the strength of the material, especially perpendicular to strands. However, this could be used to influence the fracture behaviour and set a desired fracture path, which may be advantageous to define the fracture pattern of cranial implants as shown in **Publication 5**. Moreover, the generation of a predefined tool path is a highly underestimated tool to further enhance additive manufacturing processes and needs to be analysed more in future. It could be used to generate a nearly homogenous temperature distribution within parts in order to minimise residual stresses, and thus, warpage and shrinkage. Additionally, the path could be optimised in terms of printing time or material usage, saving energy and costs.

Since thermoplastics among other materials mostly show strain-rate and temperature dependent material properties, the performance of application-oriented tests to evaluate proper material input parameters for finite element analyses is vital (as shown in **Publication 2** of this thesis) and has to be considered for all implant materials in the future. Not only strain-rate and temperature alter the behaviour of most polymers, but also environmental media does. Therefore, a media cell has been developed in order to characterise the properties of implant materials in application-oriented media

in the future to further characterise the medical materials and enhance data sets. The effect of different media and temperature on the behaviour of polymers is also the reason why a proper sterilisation routine for each material-process combination has to be found in a preliminary study, similar to the characterisations performed on PMMA in **Publication 3** of this thesis. However, after cleaning and sterilisation not only the influence on the mechanics and chemical structure should be determined, but also cytotoxicity and biocompatibility should be tested to ensure that no entrapped substances migrate.

To further investigate the applicability of cranial implants produced by material extrusion, tests with loading conditions even closer to the real application compared to the performed component tests are suggested. Sub-component testing on plate-shaped sandwich structures (**Publication 4**) was therefore in a first step advanced by using cranial bone-shaped, curved test specimens for component testing (**Publication 5**). However, in the real application x-y-deformations are restricted by tissue and the scalp, which changes the constraint of the implant significantly. Future tests should therefore include full-structure tests on cranial implants attached to skulls filled with a brain-like substance. This should provide information on whether the implant itself fails when unexpected loads act on the skull, or rather the attachments needed to fix the implant to the bone.

Overall, with additive manufacturing even more than with most other manufacturing processes, it is important to document all changes in processing parameters and environmental conditions to improve repeatability and reproducibility. In order to achieve reliable cranial implants via material extrusion, optimised process parameters have to be found considering changes in microstructure and morphology, load and media dependencies have to be checked before application and robust process chains have to be developed. Thereby, the generation of a predefined tool path and the use of post-processing to further enhance additive manufacturing processes should

not be underestimated and need to be analysed more in future. The biggest challenge, however, will be to connect materials science with the needs of surgeons, making direct collaboration with them indispensable.

6. References

- [1] Nag S, Banerjee R. Fundamentals of Medical Implant Materials. In: Narayan RJ, editor. *Materials for Medical Devices*. ASM International; 2012, p. 6–17.
- [2] Shah AM, Jung H, Skirboll S. Materials used in cranioplasty: a history and analysis. *Neurosurg Focus* 2014;36(4):E19. <https://doi.org/10.3171/2014.2.FOCUS13561>.
- [3] Kriegel RJ. Kalottenplastik für große Schädeldefekte mit PMMA (Polymethylmethacrylat) oder Tutoplast prozessierten autogenen Knochentransplantaten [Dissertation]. Rheinische Friedrich-Wilhelms-Universität Bonn: Bonn; 2006.
- [4] Sher D. World's first surgery with PEEK 3D printed implants made in-hospital, 3D Printing Media Network. [September 27, 2022]; Available from: <https://www.3dprintingmedia.network/worlds-first-surgery-with-peek-3d-printed-implants-made-in-hospital/>.
- [5] Diegel O. Additive Manufacturing. In: *Comprehensive Materials Processing*. Amsterdam, The Netherlands: Elsevier; 2014, p. 3–18.
- [6] Spoerk M, Holzer C, Gonzalez-Gutierrez J. Material extrusion-based additive manufacturing of polypropylene: A review on how to improve dimensional inaccuracy and warpage. *J. Appl. Polym. Sci.* 2020;137(12):48545. <https://doi.org/10.1002/app.48545>.
- [7] Richeton J, Ahzi S, Vecchio KS, Jiang FC, Adharapurapu RR. Influence of temperature and strain rate on the mechanical behavior of three amorphous polymers: Characterization and modeling of the compressive yield stress. *International Journal of Solids and Structures* 2006;43(7-8):2318–35. <https://doi.org/10.1016/j.ijsolstr.2005.06.040>.
- [8] Brånemark PI, Adell R, Albrektsson T, Lekholm U, Lundkvist S, Rockler B. Osseointegrated titanium fixtures in the treatment of edentulousness. *Biomaterials* 1983;4(1):25–8. [https://doi.org/10.1016/0142-9612\(83\)90065-0](https://doi.org/10.1016/0142-9612(83)90065-0).
- [9] Leito E, Barbosa MA, Groot K de. Influence of substrate material and surface finishing on the morphology of the calcium-phosphate coating. *J*

- Biomed Mater Res 1997;36(1):85–90. [https://doi.org/10.1002/\(sici\)1097-4636\(199707\)36:1%3C85:aid-jbm10%3E3.0.co;2-i](https://doi.org/10.1002/(sici)1097-4636(199707)36:1%3C85:aid-jbm10%3E3.0.co;2-i).
- [10] Tesinova P. *Advances in Composite Materials - Analysis of Natural and Man-Made Materials*. London: InTechOpen; 2011.
- [11] Ratner BD. The Biocompatibility of Implant Materials. In: *Host Response to Biomaterials*. Amsterdam, The Netherlands: Elsevier; 2015, p. 37–51.
- [12] Lemons JE. Dental implant biomaterials. *J Am Dent Assoc* 1990;121(6):716–9. <https://doi.org/10.14219/jada.archive.1990.0268>.
- [13] Ramakrishna S, Tian L, Wang C, Liao S, Teo WE. Safety testing of a new medical device. In: *Medical Devices*. Elsevier; 2015, p. 137–153.
- [14] Perez M, Block M, Espalin D, Winker R, Hoppe T, Medina F et al. Sterilization of FDM-Manufactured Parts. *International Solid Freeform Fabrication Symposium 2012*. <https://doi.org/10.26153/tsw/15350>.
- [15] Wintermantel E, Ha S-W. *Medizintechnik*. Berlin, Heidelberg: Springer Berlin Heidelberg; 2009.
- [16] STEVENS J, RAY RD. An experimental comparison of living and dead bone in rats. I. Physical properties. *J Bone Joint Surg Br* 1962;44-B:412–23. <https://doi.org/10.1302/0301-620X.44B2.412>.
- [17] Miles AW, Tanner KE. *Strain Measurement in Biomechanics*. Dordrecht: Springer Netherlands; 1992.
- [18] Abdulai AE, Iddrissu MI, Dakurah TK. Cranioplasty Using Polymethyl Methacrylate Implant Constructed from an Alginate Impression and Wax Elimination Technique. *Ghana Med J* 2006;40(1):18–21.
- [19] Navarro M, Michiardi A, Castaño O, Planell JA. Biomaterials in orthopaedics. *J. Re. Soc. Interface* 2008;5(27):1137–58. <https://doi.org/10.1098/rsif.2008.0151>.
- [20] Siracusa V, Maimone G, Antonelli V. State-of-Art of Standard and Innovative Materials Used in Cranioplasty. *Polymers (Basel)* 2021;13(9). <https://doi.org/10.3390/polym13091452>.
- [21] Ridwan-Pramana A, Marcián P, Borák L, Narra N, Forouzanfar T, Wolff J. Finite element analysis of 6 large PMMA skull reconstructions: A multi-criteria evaluation approach. *PLoS One* 2017;12(6):e0179325. <https://doi.org/10.1371/journal.pone.0179325>.
- [22] Fiaschi P, Pavanello M, Imperato A, Dallolio V, Accogli A, Capra V et al. Surgical results of cranioplasty with a polymethylmethacrylate customized cranial implant in pediatric patients: a single-center experience. *J. Neurosurg. Pediatr.* 2016;17(6):705–10. <https://doi.org/10.3171/2015.10.PEDS15489>.
- [23] Bibb R, Winder J. A review of the issues surrounding three-dimensional computed tomography for medical modelling using rapid prototyping

- techniques. *Radiography* 2010;16(1):78–83.
<https://doi.org/10.1016/j.radi.2009.10.005>.
- [24] Chiarini L, Figurelli S, Pollastri G, Torcia E, Ferrari F, Albanese M et al. Cranioplasty using acrylic material: a new technical procedure. *J Craniomaxillofac Surg* 2004;32(1):5–9.
<https://doi.org/10.1016/j.jcms.2003.08.005>.
- [25] Kim B-J, Hong K-S, Park K-J, Park D-H, Chung Y-G, Kang S-H. Customized cranioplasty implants using three-dimensional printers and polymethyl-methacrylate casting. *J Korean Neurosurg Soc* 2012;52(6):541–6. <https://doi.org/10.3340/jkns.2012.52.6.541>.
- [26] Morales-Gómez JA, Garcia-Estrada E, Leos-Bortoni JE, Delgado-Brito M, Flores-Huerta LE, La Cruz-Arriaga AA de et al. Cranioplasty with a low-cost customized polymethylmethacrylate implant using a desktop 3D printer. *J Neurosurg* 2018:1–7.
<https://doi.org/10.3171/2017.12.JNS172574>.
- [27] Rotaru H, Baciut M, Stan H, Bran S, Chezan H, Iosif A et al. Silicone rubber mould cast polyethylmethacrylate-hydroxyapatite plate used for repairing a large skull defect. *J Craniomaxillofac Surg* 2006;34(4):242–6.
<https://doi.org/10.1016/j.jcms.2006.01.005>.
- [28] La Peña A de, La Peña-Brambila J de, La Pérez-De Torre J, Ochoa M, Gallardo GJ. Low-cost customized cranioplasty using a 3D digital printing model: a case report. *3D Print Med* 2018;4(1):4.
<https://doi.org/10.1186/s41205-018-0026-7>.
- [29] Hieu LC, Bohez E, Vander Sloten J, Oris P, Phien HN, Vatcharaporn E et al. Design and manufacturing of cranioplasty implants by 3-axis cnc milling. *Technol Health Care* 2002;10(5):413–23.
<https://doi.org/10.1046/j.1365-2524.2002.03834.x>.
- [30] Moser M, Schmid R, Schindel R, Hildebrandt G. Patient-specific polymethylmethacrylate prostheses for secondary reconstruction of large calvarial defects: A retrospective feasibility study of a new intraoperative moulding device for cranioplasty. *J Craniomaxillofac Surg* 2017;45(2):295–303. <https://doi.org/10.1016/j.jcms.2016.11.016>.
- [31] Sharma N, Ostas D, Rotar H, Brantner P, Thieringer FM. Design and Additive Manufacturing of a Biomimetic Customized Cranial Implant Based on Voronoi Diagram. *Front Physiol* 2021;12:647923.
<https://doi.org/10.3389/fphys.2021.647923>.
- [32] Heini P, Müller L, Körner C, Singer RF, Müller FA. Cellular Ti-6Al-4V structures with interconnected macro porosity for bone implants fabricated by selective electron beam melting. *Acta Biomater* 2008;4(5):1536–44.
<https://doi.org/10.1016/j.actbio.2008.03.013>.

- [33] Levine B. A New Era in Porous Metals: Applications in Orthopaedics. *Adv Eng Mater* 2008;10(9):788–92. <https://doi.org/10.1002/adem.200800215>.
- [34] Senatov F, Maksimkin A, Chubrik A, Kolesnikov E, Orlova P, Krivozubov M et al. Osseointegration evaluation of UHMWPE and PEEK-based scaffolds with BMP-2 using model of critical-size cranial defect in mice and push-out test. *J Mech Behav Biomed Mater* 2021;119:104477. <https://doi.org/10.1016/j.jmbbm.2021.104477>.
- [35] Gibson, I., Rosen, D.W., Stucker, B., Khorasani, M. *Additive Manufacturing Technologies*. 3rd ed. Cham, Switzerland: Springer International Publishing; 2021.
- [36] Gebhardt A, Kessler J, Thurn L. *3D-Drucken: Grundlagen und Anwendungen des Additive Manufacturing (AM)*. 2nd ed. München: Hanser; 2016.
- [37] Gurr M, Mülhaupt R. 8.04 - Rapid Prototyping. In: *Polymer Science A Comprehensive Reference*. Amsterdam, The Netherlands: Elsevier; 2012, p. 77–99.
- [38] Cojocar V, Frunzaverde D, Miclosina C-O, Marginean G. The Influence of the Process Parameters on the Mechanical Properties of PLA Specimens Produced by Fused Filament Fabrication-A Review. *Polymers (Basel)* 2022;14(5). <https://doi.org/10.3390/polym14050886>.
- [39] Petersmann S, Spoerk M, van de Steene W, Üçal M, Wiener J, Pinter G et al. Mechanical properties of polymeric implant materials produced by extrusion-based additive manufacturing. *J. Mech. Behav. Biomed. Mater.* 2020;104:103611. <https://doi.org/10.1016/j.jmbbm.2019.103611>.
- [40] Rouse M, Jegley D, McGowan D, Bush H, Waters W. Utilization of the Building-Block Approach in Structural Mechanics Research. In: *46th AIAA/ASME/ASCE/AHS/ASC Structures, Structural Dynamics and Materials Conference*. Reston, Virginia: American Institute of Aeronautics and Astronautics; 2005.
- [41] Saini M, Singh Y, Arora P, Arora V, Jain K. Implant biomaterials: A comprehensive review. *World J. Clin. Cases* 2015;3(1):52–7. <https://doi.org/10.12998/wjcc.v3.i1.52>.
- [42] Panayotov IV, Orti V, Cuisinier F, Yachouh J. Polyetheretherketone (PEEK) for medical applications. *J. Mater. Sci. Mater. Med.* 2016;27(7):118. <https://doi.org/10.1007/s10856-016-5731-4>.
- [43] Kurtz SM, Devine JN. PEEK biomaterials in trauma, orthopedic, and spinal implants. *Biomaterials* 2007;28(32):4845–69. <https://doi.org/10.1016/j.biomaterials.2007.07.013>.
- [44] Ferguson SJ, Visser JMA, Polikeit A. The long-term mechanical integrity of non-reinforced PEEK-OPTIMA polymer for demanding spinal

- applications: experimental and finite-element analysis. *Eur. Spine J.* 2006;15(2):149–56. <https://doi.org/10.1007/s00586-005-0915-5>.
- [45] Park SJ, Lee JE, Park J, Lee N-K, Son Y, Park S-H. High-temperature 3D printing of polyetheretherketone products: Perspective on industrial manufacturing applications of super engineering plastics. *Mater. Des.* 2021;211:110163. <https://doi.org/10.1016/j.matdes.2021.110163>.
- [46] Hamad K, Kaseem M, Yang HW, Deri F, Ko YG. Properties and medical applications of polylactic acid: A review. *Express Polym. Lett.* 2015;9(5):435–55. <https://doi.org/10.3144/expresspolymlett.2015.42>.
- [47] DeStefano V, Khan S, Tabada A. Applications of PLA in modern medicine. *ER* 2020;1:76–87. <https://doi.org/10.1016/j.engreg.2020.08.002>.
- [48] Petersmann S, Spoerk M, Huber P, Lang M, Pinter G, Arbeiter F. Impact Optimization of 3D-Printed Poly(methyl methacrylate) for Cranial Implants. *Macromol. Mater. Eng.* 2019;304(11):1900263. <https://doi.org/10.1002/mame.201900263>.
- [49] Maitz MF. Applications of synthetic polymers in clinical medicine. *Biosurf. Biotribol.* 2015;1(3):161–76. <https://doi.org/10.1016/j.bsbt.2015.08.002>.
- [50] Katschnig M, Arbeiter F, Haar B, van Campe G, Holzer C. Cranial Polypropylene Implants by Fused Filament Fabrication. *Adv. Eng. Mater.* 2017;19(4):1600676. <https://doi.org/10.1002/adem.201600676>.
- [51] Laroche G, Marois Y, Guidoin R, King MW, Martin L, How T et al. Polyvinylidene fluoride (PVDF) as a biomaterial: from polymeric raw material to monofilament vascular suture. *J. Biomed. Mater. Res.* 1995;29(12):1525–36. <https://doi.org/10.1002/jbm.820291209>.
- [52] Kelly M, Macdougall K, Olabisi O, McGuire N. In vivo response to polypropylene following implantation in animal models: a review of biocompatibility. *Int. Urogynecol. J.* 2017;28(2):171–80. <https://doi.org/10.1007/s00192-016-3029-1>.
- [53] Lerouge S, Simmons A (eds.). *Sterilisation of biomaterials and medical devices*. Cambridge: Woodhead Publishing; 2012.
- [54] Gonzalez-Garzon M, Shahbikian S, Huneault MA. Properties and phase structure of melt-processed PLA/PMMA blends. *J Polym Res* 2018;25(2). <https://doi.org/10.1007/s10965-018-1438-1>.
- [55] Wang X, Zhao L, Fuh JYH, Lee HP. Effect of Porosity on Mechanical Properties of 3D Printed Polymers: Experiments and Micromechanical Modeling Based on X-ray Computed Tomography Analysis. *Polymers (Basel)* 2019;11(7). <https://doi.org/10.3390/polym11071154>.
- [56] Brackett J, Cauthen D, Condon J, Smith T, Gallego N, Kunc V. Characterizing the Influence of Print Parameters on Porosity and Resulting Density. *Proc. of the 30th Annual International Solid Freeform*

Fabrication Symposium - An Additive Manufacturing Conf., Texas, USA 2019:p. 766.

- [57] Liao Y, Liu C, Coppola B, Barra G, Di Maio L, Incarnato L et al. Effect of Porosity and Crystallinity on 3D Printed PLA Properties. *Polymers (Basel)* 2019;11(9). <https://doi.org/10.3390/polym11091487>.
- [58] Anderson EH. The Effect of Porosity on Mechanical Properties of Fused Deposition Manufactured Polymers and Composites [Master's thesis]. San Jose State University; 2019.
- [59] Fernandez-Vicente M, Calle W, Ferrandiz S, Conejero A. Effect of Infill Parameters on Tensile Mechanical Behavior in Desktop 3D Printing. *3D Print. Addit. Manuf.* 2016;3(3):183–92. <https://doi.org/10.1089/3dp.2015.0036>.
- [60] Petersmann S, Hentschel L, Gonzalez-Gutierrez J, Tödting M, Schäfer U, Arbeiter F et al. The effects of washing and formaldehyde sterilization on the mechanical performance of poly(methyl methacrylate) (PMMA) parts produced by material extrusion-based additive manufacturing or material jetting. *Adv. Eng. Mater.* 2022. <https://doi.org/10.1002/adem.202200225>.
- [61] Sgrulletti M, Bragaglia M, Giarnetti S, Paleari L, Nanni F. Understanding the impact of Fused Filament Fabrication conditions on the microstructure and tensile properties of polyamide 6 by thermal and optical live monitoring. *Mater. Today Commun.* 2021;28:102679. <https://doi.org/10.1016/j.mtcomm.2021.102679>.
- [62] Tao Y, Kong F, Li Z, Zhang J, Zhao X, Yin Q et al. A review on voids of 3D printed parts by fused filament fabrication. *J. Mater. Res. Technol.* 2021;15:4860–79. <https://doi.org/10.1016/j.jmrt.2021.10.108>.
- [63] Spoerk M, Arbeiter F, Cajner H, Sapkota J, Holzer C. Parametric optimization of intra- and inter-layer strengths in parts produced by extrusion-based additive manufacturing of poly(lactic acid). *J. Appl. Polym. Sci.* 2017;134(41):45401. <https://doi.org/10.1002/app.45401>.
- [64] Bayraktar Ö, Uzun G, Çakiroğlu R, Guldas A. Experimental study on the 3D-printed plastic parts and predicting the mechanical properties using artificial neural networks. *Polym. Adv. Technol.* 2017;28(8):1044–51. <https://doi.org/10.1002/pat.3960>.
- [65] Reddy BV, Reddy NV, Ghosh A. Fused deposition modelling using direct extrusion. *Virtual Phys. Prototyp.* 2007;2(1):51–60. <https://doi.org/10.1080/17452750701336486>.
- [66] Torres J, Cole M, Owji A, DeMastry Z, Gordon AP. An approach for mechanical property optimization of fused deposition modeling with polylactic acid via design of experiments. *RPJ* 2016;22(2):387–404. <https://doi.org/10.1108/RPJ-07-2014-0083>.

- [67] Santana L, Ahrens CH, Da Costa Sabino Netto A, Bonin C. Evaluating the deposition quality of parts produced by an open-source 3D printer. *RPJ* 2017;23(4):796–803. <https://doi.org/10.1108/RPJ-05-2016-0078>.
- [68] Geng P, Zhao J, Wu W, Ye W, Wang Y, Wang S et al. Effects of extrusion speed and printing speed on the 3D printing stability of extruded PEEK filament. *JMP* 2019;37:266–73. <https://doi.org/10.1016/j.jmapro.2018.11.023>.
- [69] Mbow MM, Marin PR, Pourroy F. Extruded diameter dependence on temperature and velocity in the fused deposition modeling process. *Prog. Addit. Manuf.* 2020;5(2):139–52. <https://doi.org/10.1007/s40964-019-00107-4>.
- [70] Zeraatkar M, Tullio MD de, Percoco G. Fused Filament Fabrication (FFF) for Manufacturing of Microfluidic Micromixers: An Experimental Study on the Effect of Process Variables in Printed Microfluidic Micromixers. *Micromachines (Basel)* 2021;12(8). <https://doi.org/10.3390/mi12080858>.
- [71] Butt J, Bhaskar R, Mohaghegh V. Investigating the Influence of Material Extrusion Rates and Line Widths on FFF-Printed Graphene-Enhanced PLA. *JMMP* 2022;6(3):57. <https://doi.org/10.3390/jmmp6030057>.
- [72] Ferretti P, Leon-Cardenas C, Ciotti E, Santi GM, Donnici G, Frizziero L. FDM 3D Printing Parameters Optimization: The Key Role of Line Width. *Proceedings of IEOM Conference, Bangalore, India, 2021*.
- [73] Sood AK, Ohdar RK, Mahapatra SS. Parametric appraisal of mechanical property of fused deposition modelling processed parts. *Mater. Des.* 2010;31(1):287–95. <https://doi.org/10.1016/j.matdes.2009.06.016>.
- [74] Rayegani F, Onwubolu GC. Fused deposition modelling (FDM) process parameter prediction and optimization using group method for data handling (GMDH) and differential evolution (DE). *Int. J. Adv. Manuf. Technol.* 2014;73(1-4):509–19. <https://doi.org/10.1007/s00170-014-5835-2>.
- [75] Tymrak BM, Kreiger M, Pearce JM. Mechanical properties of components fabricated with open-source 3-D printers under realistic environmental conditions. *Mater. Des.* 2014;58:242–6. <https://doi.org/10.1016/j.matdes.2014.02.038>.
- [76] Zhao Y, Chen Y, Zhou Y. Novel mechanical models of tensile strength and elastic property of FDM AM PLA materials: Experimental and theoretical analyses. *Mater. Des.* 2019;181:108089. <https://doi.org/10.1016/j.matdes.2019.108089>.
- [77] Szust A, Adamski G. Using thermal annealing and salt remelting to increase tensile properties of 3D FDM prints. *Engineering Failure Analysis* 2022;132:105932. <https://doi.org/10.1016/j.engfailanal.2021.105932>.

- [78] Ziemian S, Okwara M, Ziemian CW. Tensile and fatigue behavior of layered acrylonitrile butadiene styrene. *RPJ* 2015;21(3):270–8. <https://doi.org/10.1108/RPJ-09-2013-0086>.
- [79] ERYILDIZ M. Effect of Build Orientation on Mechanical Behaviour and Build Time of FDM 3D-Printed PLA Parts: An Experimental Investigation. *EMS* 2021;5(3):116–20. <https://doi.org/10.26701/ems.881254>.
- [80] Beattie N, Bock N, Anderson T, Edgeworth T, Kloss T, Swanson J. Effects of Build Orientation on Mechanical Properties of Fused Deposition Modeling Parts. *J. Mater. Eng. Perform.* 2021;30(7):5059–65. <https://doi.org/10.1007/s11665-021-05624-4>.
- [81] Petersmann S, Spoerk-Erdely P, Feuchter M, Wieme T, Arbeiter F, Spoerk M. Process-induced morphological features in material extrusion-based additive manufacturing of polypropylene. *Addit. Manuf.* 2020;35:101384. <https://doi.org/10.1016/j.addma.2020.101384>.
- [82] Xiao X, Roh B-M, Zhu F. Strength Enhancement in Fused Filament Fabrication via the Isotropy Toolpath. *Appl. Sci.* 2021;11(13):6100. <https://doi.org/10.3390/app11136100>.
- [83] Xia L, Lin S, Ma G. Stress-based tool-path planning methodology for fused filament fabrication. *Addit. Manuf.* 2020;32:101020. <https://doi.org/10.1016/j.addma.2019.101020>.
- [84] Krishnanand, Soni S, Nayak A, Taufik M. Generation of Tool Path in Fused Filament Fabrication. In: Agrawal R, Jain JK, Yadav VS, Manupati VK, Varela L, editors. *Recent Advances in Smart Manufacturing and Materials*. Singapore: Springer Singapore; 2021, p. 153–161.
- [85] Seul T, Roth S. *Kunststoffe in der Medizintechnik: Vorschriften und Regularien, Produktrealisierung, Herstellungsprozesse, Qualifizierungs- und Validierungsstrategien*. München: Hanser; 2020.
- [86] Tipnis NP, Burgess DJ. Sterilization of implantable polymer-based medical devices: A review. *Int. J. Pharm.* 2018;544(2):455–60. <https://doi.org/10.1016/j.ijpharm.2017.12.003>.
- [87] Shalaby SW, Nagatomi SD, Powell EF. *Biotextiles as Medical Implants*. 133rd ed. The Textile Institute, Woodhead Publishing: Manchester, UK, Oxford: Elsevier Science; 2013.
- [88] Kumar A, Yap WT, Foo SL, Lee TK. Effects of Sterilization Cycles on PEEK for Medical Device Application. *Bioengineering (Basel)* 2018;5(1). <https://doi.org/10.3390/bioengineering5010018>.
- [89] Pérez Davila S, González Rodríguez L, Chiussi S, Serra J, González P. How to Sterilize Polylactic Acid Based Medical Devices? *Polymers (Basel)* 2021;13(13). <https://doi.org/10.3390/polym13132115>.

- [90] Oth O, Dauchot C, Orellana M, Glineur R. How to Sterilize 3D Printed Objects for Surgical Use? An Evaluation of the Volumetric Deformation of 3D-Printed Genioplasty Guide in PLA and PETG after Sterilization by Low-Temperature Hydrogen Peroxide Gas Plasma. *TODENTJ* 2019;13(1):410–7. <https://doi.org/10.2174/1874210601913010410>.
- [91] Münker TJAG, van de Vijfeijken SECM, Mulder CS, Vespasiano V, Becking AG, Kleverlaan CJ et al. Effects of sterilization on the mechanical properties of poly(methyl methacrylate) based personalized medical devices. *J. Mech. Behav. Biomed. Mater.* 2018;81:168–72. <https://doi.org/10.1016/j.jmbbm.2018.01.033>.
- [92] Chu CC. Materials for absorbable and nonabsorbable surgical sutures. In: *Biotextiles as Medical Implants*. Elsevier; 2013, p. 275–334.
- [93] Gahleitner M, Wolfschwenger J, Fiebig J, Hametner C, Dobianer K. Sterilization effects on polypropylene: Technology and polymer type effects. *Proceedings of European PLACE Conference 2003*.
- [94] Park JH, Olivares-Navarrete R, Baier RE, Meyer AE, Tannenbaum R, Boyan BD et al. Effect of cleaning and sterilization on titanium implant surface properties and cellular response. *Acta Biomater.* 2012;8(5):1966–75. <https://doi.org/10.1016/j.actbio.2011.11.026>.
- [95] Bernhardt A, Schneider J, Schroeder A, Papadopoulous K, Lopez E, Brückner F et al. Surface conditioning of additively manufactured titanium implants and its influence on materials properties and in vitro biocompatibility. *Mater. Sci. Eng. C* 2021;119:111631. <https://doi.org/10.1016/j.msec.2020.111631>.
- [96] Kuo C-C, Mao R-C. Development of a Precision Surface Polishing System for Parts Fabricated by Fused Deposition Modeling. *Mater. Manuf. Process.* 2016;31(8):1113–8. <https://doi.org/10.1080/10426914.2015.1090594>.
- [97] Garg A, Bhattacharya A, Batish A. Chemical vapor treatment of ABS parts built by FDM: Analysis of surface finish and mechanical strength. *Int. J. Adv. Manuf. Technol.* 2017;89(5-8):2175–91. <https://doi.org/10.1007/s00170-016-9257-1>.
- [98] Popescu D, Baciú F, Amza CG, Cotrut CM, Marinescu R. The Effect of Disinfectants Absorption and Medical Decontamination on the Mechanical Performance of 3D-Printed ABS Parts. *Polymers (Basel)* 2021;13(23). <https://doi.org/10.3390/polym13234249>.
- [99] Yang C, Tian X, Li D, Cao Y, Zhao F, Shi C. Influence of thermal processing conditions in 3D printing on the crystallinity and mechanical properties of PEEK material. *J. Mater. Process. Technol.* 2017;248:1–7. <https://doi.org/10.1016/j.jmatprotec.2017.04.027>.

- [100] Pazhamannil RV, Krishnan C N, P G, Edacherian A. Investigations into the effect of thermal annealing on fused filament fabrication process. *Adv. Mater. Process. Technol.* 2021;1–14. <https://doi.org/10.1080/2374068X.2021.1946753>.
- [101] Singh S, Singh M, Prakash C, Gupta MK, Mia M, Singh R. Optimization and reliability analysis to improve surface quality and mechanical characteristics of heat-treated fused filament fabricated parts. *Int. J. Adv. Manuf. Technol.* 2019;102(5-8):1521–36. <https://doi.org/10.1007/s00170-018-03276-8>.
- [102] Dunn RM, Hart KR, Wetzel ED. Improving fracture strength of fused filament fabrication parts via thermal annealing in a printed support shell. *Prog. Addit. Manuf.* 2019;4(3):233–43. <https://doi.org/10.1007/s40964-019-00081-x>.
- [103] Thompson MK, Moroni G, Vaneker T, Fadel G, Campbell RI, Gibson I et al. Design for Additive Manufacturing: Trends, opportunities, considerations, and constraints. *CIRP Annals* 2016;65(2):737–60. <https://doi.org/10.1016/j.cirp.2016.05.004>.
- [104] Vanaei HR, Raissi K, Deligant M, Shirinbayan M, Fitoussi J, Khelladi S et al. Toward the understanding of temperature effect on bonding strength, dimensions and geometry of 3D-printed parts. *J. Mater. Sci.* 2020;55(29):14677–89. <https://doi.org/10.1007/s10853-020-05057-9>.
- [105] Acosta-Vélez G. F., Wu B. M. 3D Pharming: Direct Printing of Personalized Pharmaceutical Tablets. *Polym. Sci.* 2016;2(1). <https://doi.org/10.4172/2471-9935.100011>.
- [106] International Organization for Standardization. Medical devices - Quality management systems — Requirements for regulatory purposes (ISO Standard No. 13485:2016) 2016.
- [107] Honigmann P, Sharma N, Okolo B, Popp U, Msallem B, Thieringer FM. Patient-Specific Surgical Implants Made of 3D Printed PEEK: Material, Technology, and Scope of Surgical Application. *Biomed. Res. Int.* 2018;2018:4520636. <https://doi.org/10.1155/2018/4520636>.
- [108] Peng X. Structural Topology Optimization Method for Morphogenesis of Dendriforms. *OJCE* 2016;06(04):526–36. <https://doi.org/10.4236/ojce.2016.64045>.
- [109] Waly C, Petersmann S, Arbeiter F. Multimaterial Extrusion-Based Additive Manufacturing of Compliant Crack Arrester: Influence of Interlayer Length, Thickness, and Applied Strain Rate. *Adv. Eng. Mater.* 2022:2101703. <https://doi.org/10.1002/adem.202101703>.
- [110] Petersmann S, Smith JA, Schäfer U, Arbeiter F. Material extrusion-based additive manufacturing of polyetheretherketone cranial implants:

Mechanical performance and print quality. under review in J. Mater. Res. Technol. 2022.

Appendix

A.1. List of additional article contributions

Journal Publication, F. J. Arbeiter, S. Petersmann, J. Wiener, F. Oesterreicher, M. Spoerk, G. Pinter. *Using soft interlayers as crack arresters in polymeric 3D-printed structures*, Mater. Perform. Charact. **2020**, 9, 5. <https://doi.org/10.1520/MPC20190201>

Journal Publication, L. Hentschel, Frank Kynast, Sandra Petersmann, Clemens Holzer, Joamin Gonzalez-Gutierrez. *Processing Conditions of a Medical Grade Poly(Methyl Methacrylate) with the Arburg Plastic Freeforming Additive Manufacturing*, Polymers **2020**, 12(11), 2677. <https://doi.org/10.3390/polym12112677>

Journal Publication, F. J. Arbeiter, Lukáš Trávníček, Sandra Petersmann, Pavol Dlhý, Martin Spoerk, Gerald Pinter, Pavel Hutař. *Damage tolerance-based methodology for fatigue lifetime estimation of a structural component produced by material extrusion-based additive manufacturing*, Add. Manuf. **2020**, 36, 101730. <https://doi.org/10.1016/j.addma.2020.101730>

Journal Publication, C. Waly, S. Petersmann, F. Arbeiter. *Multimaterial Extrusion-Based Additive Manufacturing of Compliant Crack Arrester: Influence of Interlayer Length, Thickness, and Applied Strain Rate*, Adv. Eng. Mater. **2022**, 2101703. <https://doi.org/10.1002/adem.202101703>

Journal Publication, L. Hentschel, S. Petersmann, J. Gonzalez-Gutierrez, F. Kynast, U. Schäfer, F. Arbeiter, C. Holzer. *Parameter Optimization of the ARBURG plastic freeforming process by means of a Design of Experiments*

Approach, Adv. Eng. Mater. **2022**, 202200279.

<https://doi.org/10.1002/adem.202200279>

Journal Publication, J. A. Smith, S. Petersmann, F. Arbeiter, U. Schäfer. *A review on the application of PEEK towards the manufacture of 3D-printed (FFF) patient-specific cranial implants*, under review in *Materials & Design*.

A.2. Conference contributions

S. Petersmann, M. Spoerk, P. Huber, M. Lang, G. Pinter, F. Arbeiter (2019). *Mechanical Characterization of PMMA Produced by Fused Filament Fabrication as a Potential Material for Cranial Bone Reconstruction*, Oral presentation, ESIAM19 (First European Conference on Structural Integrity of Additive Manufactured Materials), Trondheim, Norway.

S. Petersmann, P. Spoerk-Erdely, M. Feuchter, T. Wieme, F. Arbeiter, M. Spoerk (2021). *Changing morphological features in a semi-crystalline polymer in material-extrusion based additive manufacturing*, Oral presentation, Polymer Meeting 14, Graz, Austria.

S. Petersmann, A. Primetzhofer, H. Lammer, J. LeBlhumer, G. Pinter, F. Arbeiter (2021). *Morphology and Weld Strength of a Semi-Crystalline Polymer Produced via Material Extrusion-Based Additive Manufacturing*, Virtual presentation, ESIAM21 (Second European Conference on the Structural Integrity of Additively Manufactured Materials), Online.

S. Petersmann, M. Spoerk, W. Van De Steene, M. Üçal, J. Wiener, G. Pinter, F. Arbeiter (2022). *Mechanical properties of additively manufactured polymeric implant materials in dependence of microstructure, temperature and strain-rate*, Oral presentation, EMMC18 (18th European Mechanics of Materials Conference), Oxford, UK.

S. Petersmann, A. Primetzhofer, M. Habicher, J. LeBlhumer, H. Lammer, F. Arbeiter (2022). *Effect of die temperature on the fatigue behaviour of PLA produced by means of fused filament fabrication*, poster presentation,

DYFP2022 (18th International Conference on Deformation, Yield and Fracture of Polymers), Kerkrade, The Netherlands.

S. Petersmann, A. Primetzhofer, M. Habicher, H. Lammer, J. Leßlhuber, F. Arbeiter (2022). *Fatigue behaviour of 3D-printed continuous flax fibre reinforced polylactide*, oral presentation, Verbund 2022 (23. Symposium Verbundwerkstoffe und Werkstoffverbunde), Leoben, Austria.

S. Petersmann, M. Spoerk, P. Huber, M. Lang, G. Pinter, F. Arbeiter (2022). *Material selection and mechanical characterization of 3D-printable polymers for medical applications*, poster presentation, 30th Leoben-Conference in Polymer Engineering and Science, Leoben, Austria.

A.3. Supervised theses

T. Tröscher (2021) *Influence of thermal history on the morphology of semi-crystalline polymers in additive manufacturing*, Bachelor thesis, Montanuniversitaet Leoben.

M. Huemer (2022) *Environmental stress cracking of high impact polystyrene and polycarbonate polyurethane in application oriented media*, Master's thesis, Montanuniversitaet Leoben.

Publications of the cumulative thesis

Publication 1

Bibliographic information

Title: Mechanical properties of polymeric implant materials produced by extrusion-based additive manufacturing

Authors: Sandra Petersmann¹, Martin Spoerk², Willem Van De Steene³, Muammer Üçal⁴, Johannes Wiener¹, Gerald Pinter¹, Florian Arbeiter^{1,*}

Affiliations:

¹Materials Science and Testing of Polymers, Montanuniversitaet Leoben, Otto Gloeckel-Straße 2, 8700, Leoben, Austria

²Polymer Processing, Montanuniversitaet Leoben, Otto Gloeckel-Straße 2, 8700, Leoben, Austria

³Centre for Polymer and Material Technologies, Department of Materials, Textiles and Chemical Engineering, Ghent University, Technologiepark 130, 9052, Zwijnaarde, Belgium

⁴Department of Neurosurgery, Medical University of Graz, Auenbruggerplatz 29, 8036, Graz, Austria

Periodical: Journal of the Mechanical Behavior of Biomedical Materials

DOI: <https://doi.org/10.1016/j.jmbbm.2019.103611>

Relevant contributions to this publication:

Conceptualisation: Martin Spoerk, Florian Arbeiter

Methodology: Sandra Petersmann, Martin Spoerk, Willem Van De Steene, Johannes Wiener, Florian Arbeiter

Investigation: Sandra Petersmann, Willem Van De Steene, Muammer Üçal, Johannes Wiener

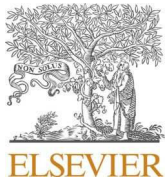
Validation: Sandra Petersmann, Martin Spoerk, Willem Van De Steene, Muammer Üçal, Gerald Pinter, Florian Arbeiter

Writing - Original Draft: Sandra Petersmann, Martin Spoerk

Writing - Review & Editing: Sandra Petersmann, Martin Spoerk, Willem Van De Steene, Muammer Üçal, Gerald Pinter, Florian Arbeiter

Visualisation: Sandra Petersmann, Martin Spoerk, Muammer Üçal

Supervision: Gerald Pinter, Florian Arbeiter



Mechanical properties of polymeric implant materials produced by extrusion-based additive manufacturing

Sandra Petersmann^a, Martin Spoerk^b, Willem Van De Steene^c, Muammer Üçal^d, Johannes Wiener^a, Gerald Pinter^a, Florian Arbeiter^{a,*}

^a Institute of Materials Science and Testing of Polymers, Montanuniversität Leoben, Otto Gloeckel-Straße 2, 8700, Leoben, Austria

^b Institute of Polymer Processing, Montanuniversität Leoben, Otto Gloeckel-Straße 2, 8700, Leoben, Austria

^c Centre for Polymer and Material Technologies, Department of Materials, Textiles and Chemical Engineering, Ghent University, Technologiepark 130, 9052, Zwijnaarde, Belgium

^d Department of Neurosurgery, Medical University of Graz, Auenbruggerplatz 29, 8036, Graz, Austria

ARTICLE INFO

Keywords:

Additive manufacturing
Strain-rate dependent data
Mechanical properties
Implant materials
Polymers

ABSTRACT

The application of material extrusion-based additive manufacturing methods has recently become increasingly popular in the medical sector. Thereby, thermoplastic materials are likely to be used. However, thermoplastics are highly dependent on the temperature and loading rate in comparison to other material classes. Therefore, it is crucial to characterise these influences on the mechanical properties. On this account, dynamic mechanical analyses to investigate the application temperature range, and tensile tests at different crosshead speeds (10^3 , 10^1 , 10^{-1} and 10^{-3} mms^{-1}) were performed on various 3D-printable polymers, namely polyetheretherketone (PEEK), polylactide (PLA), poly(methyl methacrylate) (PMMA), glycol-modified poly(ethylene terephthalate) (PETG), poly(vinylidene fluoride) (PVDF) and polypropylene (PP). It was found that the mechanical properties of PEEK, PLA, PMMA and PETG hardly depend on temperature changes inside the human body. PVDF and PP show a significant decrease in stiffness with increasing body temperatures. Additionally, the dependency of the stiffness on the strain-rate is increasing between PLA, PP, PEEK, PETG, PMMA and PVDF. Besides the mechanical integrity of these materials (strength, stiffness and its strain-rate and temperature dependency inside the body), the materials were further ranked considering their filling density as a measure of their processability. Hence, useful information for the selection of possible medical applications for each material and the design process of 3D-printed implants are provided.

1. Introduction

With the continuously improving health care system, life expectancy of humans has increased rapidly. This leads to an enhancement of the quantity of medical intervention such as the implantation of prostheses. Therefore, finding adequate reconstruction materials and improving their processability are of paramount importance (Soumya and Rajarshi, 2012). Implant materials have to meet a large number of demands such as biocompatibility, durability, sterilisability and processability. Biocompatibility can be defined as the ability of a material to respond appropriately when exposed to body tissue or fluids (Ratner, 2015). Durability means that materials remain undamaged or rather operational during their service life. The durability of polymers is dependent on their resistance against temperature, media, pH-variations and

mechanical or electrical stresses (Wintermantel and Ha, 2009). Furthermore, implants have to be sterile, which means all living organisms such as bacteria or viruses have to be eliminated, otherwise they can become lethal to the host system (Perez et al., 2012). Additionally, the mechanical properties should be adequate for the specific application (Wintermantel and Ha, 2009). Several metals, ceramics and polymers fulfil these requirements (Abdulai et al., 2006). Among them, especially polymeric materials have been gaining popularity due to their preferable heat-insulation properties and huge variety of different processing techniques (Kriegel, 2006).

Strong emphasis has recently been laid on the manufacturing of prostheses by material extrusion-based additive manufacturing (AM) methods, also known as fused filament fabrication (FFF), fused deposition modelling (FDM™) or simply 3D-printing. Thereby, a thermoplastic

* Corresponding author.

E-mail address: florian.arbeiter@unileoben.ac.at (F. Arbeiter).

filament is selectively deposited through a moving nozzle onto a build platform. The nozzle moves according to a computer modelled (CAD) and sliced (STL) design, building the desired object layer-by-layer (Diegel, 2014; Gebhardt et al., 2016; Gibson et al., 2010; Gurr and Mühlaupt, 2012).

AM methods reveal short process times due to reduced numbers of process steps and offer the option of manufacturing parts in multiple materials, colours and scales. In addition, a considerable amount of material is saved in contrast to subtractive manufacturing processes such as CNC milling (Gibson et al., 2010). Furthermore, AM processes are relatively simple and allow the design of complex structures such as personalised implants. A common method to acquire the necessary dimensions of customised medical implants is the use of computed tomography (CT) scans (Fiaschi et al., 2016; Kim et al., 2012; Morales-Gómez et al., 2018; Rotaru et al., 2006). Therefore, the accuracy of printed parts depends strongly on the resolution and overall quality of the CT scans. Additionally, the processing parameters (the temperature of the die and the build platform, the printing speed, the layer thickness, the build chamber temperature, the build platform material, etc.), as well as the viscoelastic and thermal behaviour of the material itself (Spoerk et al., 2017a-c; Spoerk et al., 2018a-c) further influence the implant quality. Moreover, the manufacturing process induces heterogeneities such as air gaps, which have a significant influence on the mechanical properties of the printed parts (Spoerk et al., 2017a). Therefore, identifying printing induced defects in 3D-printed implants is vital for the subsequent discussion of the obtained properties. X-ray micro-computed tomography (μ -CT) has been widely accepted as a non-destructive method for the evolution of sizes, distributions and individual shapes of defects (Wang, X. et al., 2019). This method can be used as a standard quality control process of implants. However, with increasing part size, the distance between the measured object and the X-ray source needs to be increased, which has a significant impact on the obtained resolution. Hence, pores can be missed affecting mechanical properties of the materials (Tóth et al., 2015).

Regarding materials used for FFF, only a limited number of FFF-printable materials, for which the base polymers are approved by the Food and Drug Administration (FDA), exist. Examples are poly-etheretherketone (PEEK), polylactide (PLA), poly(methyl methacrylate) (PMMA), glycol-modified poly(ethylene terephthalate) (PETG), poly(vinylidene fluoride) (PVDF) and polypropylene (PP). PEEK has already been used for load-bearing medical applications such as orthopaedic, spinal, maxillo-facial and cranial implants, fixation plates and screws, dental prosthesis, or intracardiac pumps and heart valves (Panayotov et al., 2016). PLA is degradable and has been applied for barrier membranes, drug delivery systems, bone scaffolds, stents, tissue regeneration and engineering as well as absorbable staples, sutures and screws (Hamad et al., 2015; Ratner et al., 2004). The application fields of PMMA include intraocular and hard contact lenses due to the excellent light transmittance of the material. Additionally, it has been applied as bone cement for orthopaedic and cranial implants, anchoring of hip prostheses, dental applications, vertebroplasties and kyphoplasties (Navarro et al., 2008; Petersmann et al., 2019; Ratner et al., 2004). PETG has been used for orthodontic devices and occlusal splints also known as bite guards (Marcauteanu et al., 2014). On the other hand, PVDF or PP have mainly been used as suture materials or as surgical meshes. PP also serves as hernia, ligament or tendon repair material (Maitz, 2015; Ratner et al., 2004). Moreover, it has recently been suggested as a suitable material for cranial implants (Katschnig et al., 2017) or as an ankle foot orthosis (Banga et al., 2018).

Besides the biocompatibility, the mechanical integrity of medical materials is essential. Tensile, compressive, flexural, buckling, torsional and shear loads are acting inside the human body. For instance, muscle forces result in tension, the body weight in compression and wear occurs in natural knee joints (Van den Bogert, 1994). Moreover, the resulting strains in the associated ligaments change depending on the position of the bone (Crowninshield and Brand, 1981). In general, it can be

distinguished between repetitive or acute, and external or internal loads (Van den Bogert, 1994). Regarding the human thorax, breathing leads to repetitive loads and coughing to acute ones. Both loads are internal loads. On the other hand, accidentally hitting ones head on a wooden beam results in an acute, external load. Here, the impact speed and therefore the emerging stress value are particularly high. To accurately account for all these cases during the design process of implants is not a simple task.

Therefore, finite element analyses (FEA) are commonly conducted in the cycle of component development. By means of FEA, the functional efficiency of different materials and geometries is tested (Hopmann and Klein, 2015). In comparison to practical trial-and-error techniques, FEA save time, material and money (Ridwan-Pramana et al., 2017). However, precise and correct material data are vital for simulating the component behaviour properly in order to accurately design medical 3D-printed parts and avoid failures during their life cycle.

The characterisation of polymers in dependence of the loading type and speed is particularly important as polymers respond to mechanical loads in a nonlinear and time dependent, so called “viscous”, manner. Therefore, their material properties are highly dependent on the loading rate (e.g. (Richeton et al., 2006)). While processing influences have already been thoroughly investigated for 3D-printed acrylonitrile-butadiene-styrene copolymer (ABS) or PLA samples at lower strain rates (Letcher and Waytashek, 2014; Rodríguez et al., 2001; Verius et al., 2011) and mostly at standardised conditions, high-speed tensile test data are still missing in literature. Therefore, at present it is not possible to use correct data for designing components produced by FFF that account for impact loads. Additionally, contrary to other replacement material groups such as metals or ceramics, the properties of polymeric materials might change noticeably in dependence of temperature variations that occur within the target application, ergo the human body. Changes of mechanical properties due to variations of temperature can be especially drastic if a transition temperature such as the glass transition (T_g) is close to the application temperature. Unfortunately, these two rather crucial points, strain-rate and temperature dependency, have not been adequately covered in literature so far although they are imperative for correct component design.

To close this critical gap and offer the possibility to use accurate data in product design, the present work provides tensile test data measured at four different testing speeds in the wide range of 10^{-3} to 10^3 mms^{-1} for six different 3D-printable polymers (PEEK, PLA, PMMA, PETG, PVDF and PP), which could be used for medical applications. Furthermore, the fracture behaviour is analysed after testing to enable a better insight into the materials. To cover the temperature dependent nature, dynamic-mechanical analysis of all tested materials is conducted. This can give insight into the useable temperature range of each polymer. In this way, we offer material data useful for designers and give an understanding into the potential scope of application for each material.

2. Experimental

2.1. Material

The following commercially available filaments (diameter of 1.75 mm) were used in the present study: KetaSpire® PEEK (Solvay S.A., Belgium), black PLA (Prirevo e.U., Austria), clear PMMA (Herz Austria GmbH, Austria), HDglass™ clear PETG (Formfutura BV, The Netherlands) and Fluorinar-C™Kynar® PVDF (Nile Polymers, Inc., USA). As this work serves as a pre-study in order to compare the mechanical properties of the different materials, types of each material, which are not certified as long-term implant materials, were used. Nonetheless, either a detailed analysis of certified types, or a certification of the used materials are required before application.

As most commercially available PP filaments hardly reveal any propylene segments, and therefore their intended molecular structure can strongly be doubted (Spoerk et al., 2019), no commercially available

PP was analysed. Instead, PP heterophasic copolymer pellets (Borealis AG, Austria) were processed to filaments in the single screw extruder FT-E20T-MP-IS (Dr. Collin GmbH, Germany) with a subsequent water bath, haul-off unit and diameter measurement device (Sikora Laser, 2010T and Ecocontrol 600 processor, Sikora AG, Germany). Thereby, the parameters were set as follows: extruder barrel temperatures = 180 °C, 185 °C, and 190 °C; screw speed = 70 rpm, die diameter = 1.9 mm, die length = 25.05 mm, and die temperature = 200 °C. Prior to any 3D-printing step, all materials were stored under standardised conditions (23 °C air temperature, 50% relative humidity) for at least 72 h. PEEK was additionally pre-dried for at least 6 h at 150 °C before each print.

2.2. Processing

The different materials were processed on different FFF printers due to limitations of each machine. For PLA, PMMA, PETG and PVDF a Hage 3DpA2 (Hage3D, Austria) was used. For PEEK, the prints were produced on the SpiderBot 4.0 HT (Qualup, France). For PP, the printing trials were performed on a Duplicator i3 v2 (Wanhao, China). All printers were equipped with a steel nozzle 0.5 mm in diameter. All tensile test specimens were sliced in the software Slic3r Prusa Edition and oriented in a way that the flat surface of the tensile specimens were parallel to the build platform. All specimens were produced in a $\pm 45^\circ$ rectilinear strand orientation. The dimensions of the specimens were according to DIN EN ISO 527-1A apart from the area of parallel length, which was shortened to 10 mm. This is necessary in order to obtain convenient results in high-speed tensile measurements. As no overhangs occurred, support structures were not necessary. All specimens exhibited one outer perimeter and were sliced with a layer thickness of 0.25 mm. The printing temperature and filament flow factor were set for each material individually in a way that each cross section revealed a minimal amount of air gaps, aiming at a real infill of 100%. This was tested as described in section 2.3. The parameters for each material are summarised in Table 1. The PEEK specimens were printed on a build platform at 160 °C in a build chamber heated to 90 °C. In addition, IR-radiants, set at a temperature of 380 °C, were utilised. That way, a part temperature of approx. 200 °C was achieved. Elevated part temperatures during printing were shown to result in a superior inter-layer adhesion (Costa et al., 2017) and reduced warpage effects (Spoerk et al., 2018a) of a complete printed part. Without IR-radiants, the build chamber temperature would have to be at least 60 °C higher to successfully print parts, which is a technical challenge for most 3D-printers currently on the market. The rather high die

temperatures, e.g. for PLA 250 °C, were chosen in order to guarantee best possible inter- and intra-layer cohesion, as has been reported by Refs. (Arbeiter et al., 2018; Spoerk et al., 2017a). For PMMA, PETG and PVDF, the adhering spray Dimafix® (DIMA 3D, Spain) was applied to the glass mirror in order to decrease the risk of warpage and delamination from the build platform. For the same reason, the first layer of PP was deposited onto a plate of a similar, but not identical base polymer (PP random copolymer), as recommended by Refs. (Spoerk et al., 2018a and b). A decent first layer adhesion of PEEK was only achievable by implementing a PEEK raft printed with a speed of 30 mms⁻¹ onto a 1 mm thick polyetherimide (PEI) platform. Within one print, five test specimens were produced. After the completion of one print, the build platform was cooled down to room temperature by natural convection and directly afterwards the parts were removed from the bed with a spatula. The parts were then stored under standardised conditions until subsequent characterisation techniques were conducted.

2.3. Analysis of the print quality

As mentioned before, the printing profile was optimised in terms of minimal amounts of air gaps, resulting in high strength values. In a first step, this was tested by means of cutting out and sanding cross sections of untested tensile test specimens and analysing them by means of optical microscopy (SZH, Olympus Optical Co., Japan). Subsequently, scanning electron microscopy (SEM) was performed on representative untested tensile test specimens using a Tescan Vega II (Tescan Brno, s.r.o., Czech Republic) at 5 kV with secondary electrons. Therefore, parts of the sample's midsection were cut out and the first layers of the cross sections were removed with a microtome, in order to avoid smearing of the pores, especially for "soft" materials such as PP. These prepared parts were fixed on SEM sample holders and were gold-sputtered with the Cressington 108auto Sputter Coater (Cressington Scientific Instruments UK, England) for 160 s at 20 mA.

As the print quality varies throughout the sample, analyses that inspect the whole specimen were applied subsequently. Therefore, the printed samples were scanned by means of the Inveon microCT scanner (Inveon μ -PET/SPECT/CT, Siemens, Germany) using the following scan parameters: 80 kV potential, 500 μ A current, 750 ms exposure time and an effective pixel size of 35.19 μ m. After reconstruction of the raw data using the manufacturer's software (Inveon CT Recon Software v2.04, Siemens AG, Germany), the data was exported and saved in DICOM (Digital Imaging and Communications in Medicine) format. Each specimen was imaged in 2270 sectional images with sagittal and/or horizontal alignment. Segmentation, three-dimensional modelling and volumetric analyses of the printed specimen and the internal pores were done using the open source software 3D Slicer v4.10.2 (Fedorov et al., 2012). A pore in an image slice was defined as an island with a signal intensity below the threshold value without connection to the outer surface through neighbouring image sections. The analyses were conducted with 1135 slices by inclusion of every second DICOM file in order to reduce the required computational power and memory usage to make the analysis compatible with the available resources (1.7 GHz, 32 GB), whilst maintaining a data portion that is fairly representative of the original image data.

2.4. Dynamic mechanical analysis

Dynamic mechanical analyses (DMA) of each filament material were performed with the dynamic mechanical analyser DMA/SDTA861^e (Mettler-Toledo GmbH, Austria). Thereby, a tension load was applied with a frequency of 1 Hz and a dynamic amplitude of 2.5 μ m. The most interesting temperature range for the target application would be around 20 to 40 °C. However, properties were measured in the temperature range from -75/-50 °C to 120/175 °C, depending on the region of the glass transition and melting temperature of the tested thermoplastics, in order to give a more wholesome overview of the temperature

Table 1
Levels of the printing parameters of all printed specimens in this work.

Printing parameters	PEEK	PLA	PMMA	PETG	PVDF	PP
Die temperature (in °C)	427	250	250	230	250	230
Build platform material	PEI sheet + PEEK raft	Glass mirror	Glass mirror + Dimafix	Glass mirror + Dimafix	Glass mirror + Dimafix	PP-plate
Build platform temperature (in °C)	160	70	115	100	110	100
Infrared heater temperature (in °C)	380	-	-	-	-	-
Printing speed of the first layer (in mms-1)	30	30	20	20	8	10
Printing speed of the remaining layers (in mms-1)	20	60	20	20	20	20

dependent material behaviour. For PEEK, an upper temperature limit of 325 °C was used. The heating rate for all tests was 2 Kmin⁻¹.

During the DMA of thermoplastics, mainly four different temperature regions are passed: the energy-elastic, the glass-transition, the entropy-elastic and the melt and/or fluid region (Fig. 1), depending on the type of thermoplastic (semi-crystalline or amorphous) (Grellmann and Altstädt, 2011). For each material, the storage modulus at 23 °C ($E'_{23\text{ °C}}$), at 37 °C ($E'_{37\text{ °C}}$) and at 41 °C ($E'_{41\text{ °C}}$), as well as the glass transition temperature (T_g) were evaluated and compared. The temperatures of 37 and 41 °C represent the average body temperature and a raised body temperature occurring during a fever (Del Bene, 1990). The temperature of 23 °C is the testing temperature in most standards. Therefore, it is used to enable comparability to literature data.

2.5. Tensile tests at different crosshead speeds

As mentioned previously, tensile tests were performed at four different crosshead speeds, namely 10³, 10¹, 10⁻¹ and 10⁻³ mms⁻¹. The measurements were obtained on two different testing machines, depending on the material and the loading rate. All tests at high testing speeds (10³ and 10¹ mms⁻¹) and tests at low testing speeds (10⁻¹ and 10⁻³ mms⁻¹) with materials showing relatively low strain at break values (PEEK, PLA, PMMA) were measured by means of the servo-hydraulic testing machine MTS 831.50 (MTS Systems GmbH, Germany). The tensile tests at low speeds with materials showing relatively high strain at break values (PETG, PVDF and PP) were performed on the universal testing machine Zwick Z250 (Zwick Roell, Germany) equipped with a 10 kN load cell and mechanical clamps. The clamping length was set to 42 mm for all tests.

For high testing speeds, the deformations were measured optically with the high-speed camera Photron FASTCAM SA1 (Photron Europe Limited, Germany). Therefore, a white primer and a graphite sparkle pattern were applied on the front surface of the specimens in order to make deformations trackable. The deformations for tests performed on the MTS 831.50 at low testing rates were recorded by means of a clip-on extensometer. The deformations for measurements performed on the Zwick Z250 were measured with the makroXtens extensometer until yield and afterwards by the crosshead travel.

All stresses and strains are engineering values considering the initial cross section of the sample. For each material, the Young's modulus, the

strain at break, the tensile strength and the yield strength (if available) are evaluated and compared. According to DIN EN ISO 527-1, the Young's modulus is calculated as the slope of the stress-strain curve in the strain interval between 0.05 and 0.25%, the tensile strength as the global stress maximum and the yield strength as the stress at the yield point. The yield point is characterised by a global stress maximum followed by a stress reduction due to a narrowing of the cross section (Grellmann and Altstädt, 2011).

2.6. Fracture analysis

After tensile testing, photographs of representative tensile test specimens per material and testing speed were taken for comparison.

In order to analyse the occurring fracture mechanisms in detail, SEM was performed for each material after testing at 10³ and 10⁻³ mms⁻¹ using a Tescan Vega II (Tescan Brno, s.r.o., Czech Republic) at 5 kV with secondary electrons. Therefore, the specimens were cut to a measurable size, fixed on SEM sample holders and gold-sputtered with the Cressington 108auto Sputter Coater (Cressington Scientific Instruments UK, England) for 160 s at 20 mA.

3. Results

In this chapter the dynamic mechanical, tensile and fracture properties of the six different materials, namely PEEK, PLA, PMMA, PETG, PVDF and PP, are shown. A closer comparison of these results and their meaning towards the use as implant materials will follow in section 4.

3.1. Dynamic mechanical analysis

The storage modulus-temperature-curves (representing the stiffness of the material as a function of temperature) obtained from the DMA measurements are compared in Fig. 2. The respective results of the predefined parameters are summarised in Table 2. All results are in good agreement with data from literature (Amash and Zugenmaier, 2000; Slapnik et al., 2016; Elshereksi et al., 2014; Paszkiewicz et al., 2017; Zhu et al., 2017) and give a rough overview of the application temperature range for each material.

In the most interesting temperature range from 37 to 41 °C, the variations in the storage modulus of PEEK, PLA and PETG are negligible, since the materials are still well below their T_g (compare with Table 2).

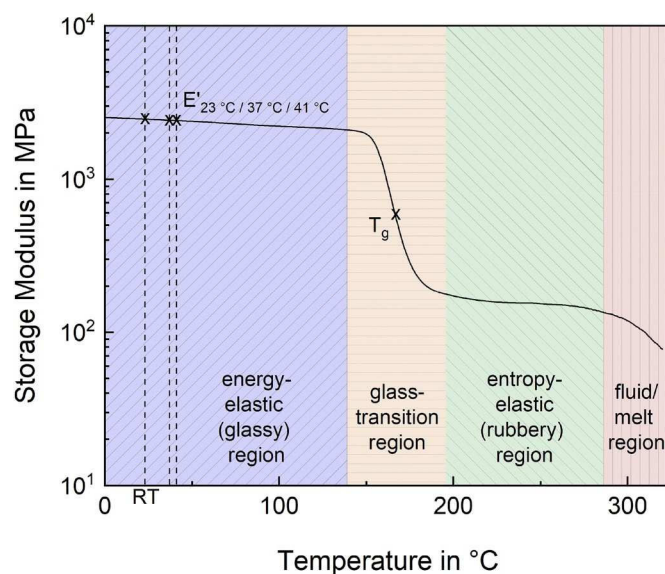


Fig. 1. Main temperature regions passed during dynamic mechanical analyses (DMA) of thermoplastics along with the values that are discussed in the present work, exemplarily shown for polyetheretherketone (PEEK).

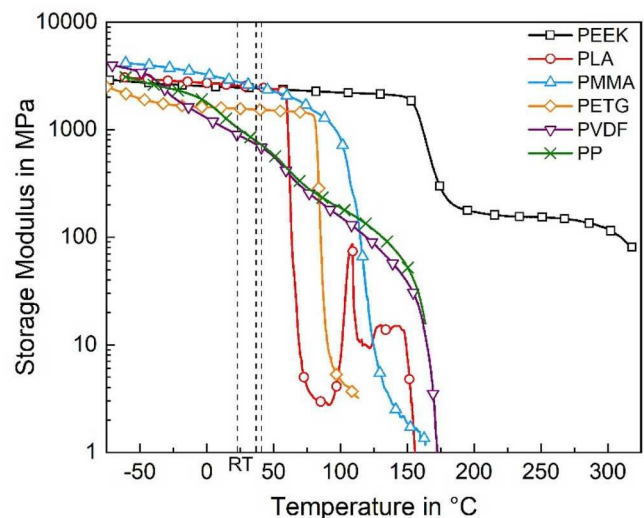


Fig. 2. The storage modulus as a function of the sample temperature for six different polymer filaments. Vertical chain dotted lines are illustrated at room temperature (23 °C, RT), at the average body temperature (37 °C) and an increased body temperature reached during a fever (41 °C).

Table 2

Averaged measurement values for the storage modulus at 23 °C ($E'_{23^\circ\text{C}}$), at 37 °C ($E'_{37^\circ\text{C}}$) and at 41 °C ($E'_{41^\circ\text{C}}$), as well as the glass transition temperature (T_g) obtained from dynamic mechanical analysis (DMA) of six different polymer filaments.

Material	$E'_{23^\circ\text{C}}$ [MPa]	$E'_{37^\circ\text{C}}$ [MPa]	$E'_{41^\circ\text{C}}$ [MPa]	T_g [°C]
PEEK	2413	2375	2367	167
PLA	2365	2296	2276	68
PMMA	2741	2476	2401	118
PETG	1540	1513	1505	86
PVDF	883	712	666	-33
PP	944	713	639	9

For PMMA, small changes are detected (approx. 3%). This high temperature-independency in the application temperature range is beneficial as it facilitates the designing of implants. In the case of the PLA filaments, the increasing storage modulus in the vicinity of 100 °C can be attributed to cold crystallisation, which is typical for PLA (Gonzalez-Garzon et al., 2018; Mofokeng et al., 2012). For PETG, a second relaxation process is investigated at -54 °C. According to Refs. (Paszkievicz et al., 2017; Scheirs and Long, 2004), this second relaxation process is known as β -relaxation, which is related to motions of hydroxyl and carboxyl groups, and ranges from -80 to -30 °C. However, since these are well outside of application temperatures, they will not be further discussed within this work.

In contrast to aforementioned materials, PVDF and PP are both above T_g and their storage modulus decreases nearly continuously until the onset of the melting region at approx. 175 °C. In the temperature range of 37 to 41 °C, the storage modulus decreases by 6.5% and 10.4%, respectively. This indicates a necessity to include temperature dependent properties in any design process to ensure proper results obtained via FEA.

3.2. Analysis of the print quality

The cross-sectional analysis of the 3D-printed samples is important for describing the subsequent tensile test results. Air gaps and other processing induced defects are known to have a significant influence on the mechanical properties of the printed parts (Spoerk et al., 2017a). Air gaps can act as defects and initiations for delamination (Spoerk et al., 2017c) and fractures (Webbe Kerekes et al., 2019). The importance of avoiding air gaps is shown, e.g. in Ref. (Spoerk et al., 2018c). Occurring number and sizes of defects in the cross sections of one representative

3D-printed dumbbell specimen per material are compared in Fig. 3.

For the 3D-printed PEEK sample, defects in the form of weld lines between the single filaments are detected (Fig. 3a and b). The unsatisfactory printing quality is reasonable due to the relatively challenging printing process in the case of PEEK (Wu et al., 2015). However, this also indicates that the results could still be improved by an optimisation of the printing profile, process parameters or printing strategy. The cross sections of the PLA and PMMA samples reveal a few air gaps (Fig. 3c and e) with pore sizes, which may not be negligible (Fig. 3d and f). For PETG, the visibility of the layer contours increases, and therefore the printing quality decreases, from the build platform to the top (Fig. 3g). However, the higher magnification image indicates very small pore sizes (Fig. 3h). PVDF and PP specimens are nearly homogeneously filled, indicating a good printing quality (Fig. 3i and k). Only small amounts of air gaps with small pore sizes are visible (Fig. 3j and l), which should not have a drastic influence on the mechanical behaviour (Spoerk et al., 2017a). Nonetheless, it should be mentioned that the cross-sectional images show the size and shape of pores only very locally. Thus, meaningful statements regarding the corresponding porosity of the whole sample cannot be made.

Therefore, the printing quality is further analysed by means of the overall porosity resulting from μ -CT measurements of representative 3D-printed tensile test specimens (Table 3 and Fig. 4). The highest porosity is evaluated for PEEK with 1.18%, which is in accordance with the results of the cross-sectional analysis (Fig. 3a and b) and the frontal and side view of the μ -CT models (Fig. 4a). The porosity of all other tested materials is in the range of 0.07 to 0.20%. These values are satisfactory if comparing to data found in literature (Wang, X. et al., 2019; Liao, Y. et al., 2019). The μ -CT images of PLA (Fig. 4b), PMMA (Fig. 4c) and PP

Table 3

Porosity values of polyetheretherketone (PEEK), polylactide (PLA), poly(methyl methacrylate) (PMMA), glycol-modified poly(ethylene terephthalate) (PETG), poly(vinylidene fluoride) (PVDF) and polypropylene (PP) resulting from μ -CT measurements of 3D-printed specimens.

Material	Total volume [mm ³]	Volume of voids [mm ³]	Porosity [%]
PEEK	3193.70	37.68	1.18
PLA	3441.95	2.45	0.07
PMMA	3343.06	2.99	0.09
PETG	3801.84	7.58	0.20
PVDF	2961.51	3.41	0.12
PP	3243.34	3.61	0.11

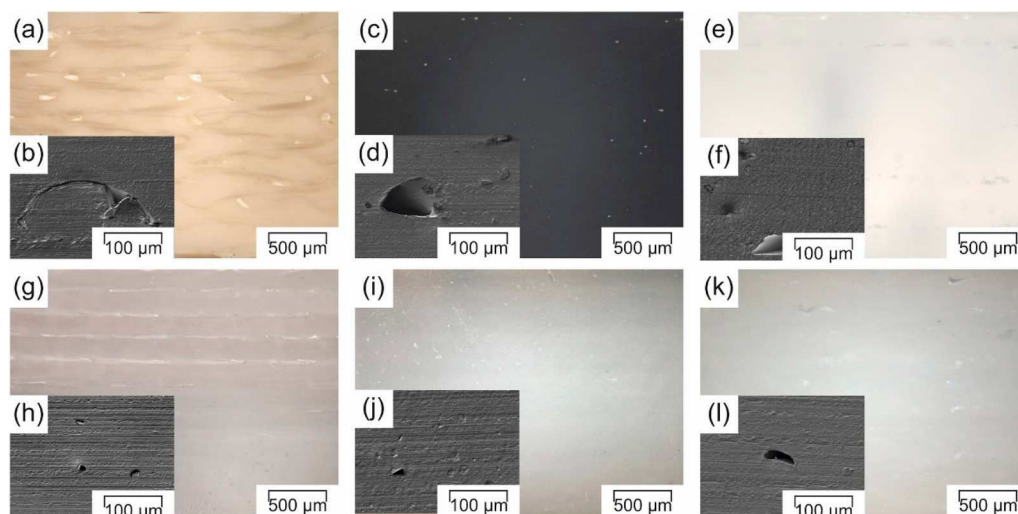


Fig. 3. Optical microscopy (overview) and scanning electron microscopy (SEM) (higher magnification) images of occurring defects in the cross sections of representative 3D-printed tensile test specimens made of PEEK (a and b), PLA (c and d), PMMA (e and f), PETG (g and h), PVDF (i and j) and PP (k and l). The build platform is located on the bottom of each image.

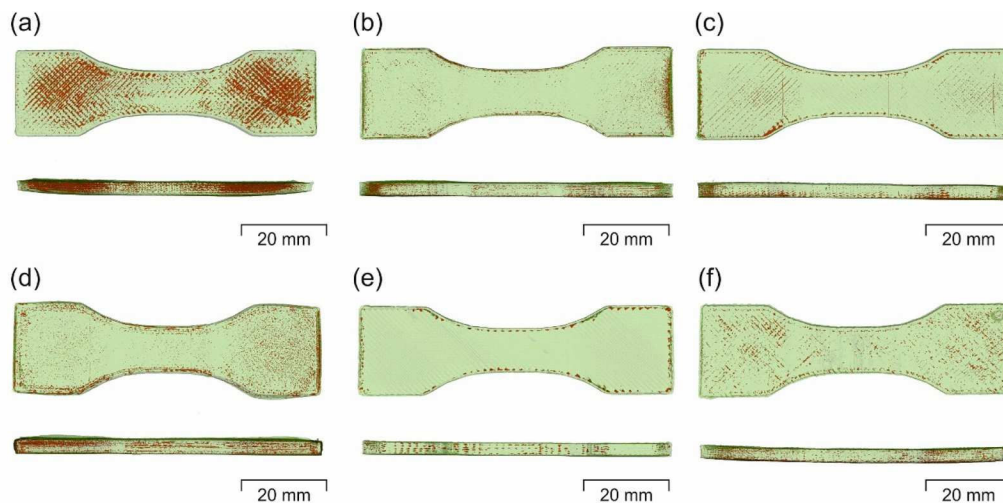


Fig. 4. Two dimensional images (top: frontal view; bottom: side view) of the 3D models of PEEK (a), PLA (b), PMMA (c), PETG (d), PVDF (e) and PP (f) after differential segmentation in micro-CT image data. Green shows the material and red shows the voids inside the printed specimen. The opacity of the material model colour was reduced to 35% so that the voids are visible in the super-positioned 3D models. In the frontal view, the side of the specimen, which was in contact with the build platform, is presented. In the side view, the build platform is located at the bottom.

(Fig. 4f) show similar and relatively low amounts of air gaps, resulting in similar porosity values (Table 3). However, the rather large pore sizes evaluated for PLA (Fig. 3d) and PMMA (Fig. 3f) do not correlate with the low porosity values evaluated for both materials. This indicates a low number of pores with rather big sizes. The μ -CT images of PETG (Fig. 4d) show higher amounts of pores than for PVDF (Fig. 4e), but similar pore sizes (Fig. 3h and j) accounting for its higher porosity value of 0.20% compared to the 0.12% measured for PVDF.

3.3. Tensile tests at different crosshead speeds

While this chapter mainly focuses on the mechanical properties themselves, a more detailed discussion of their impact regarding application will be given in chapter 4. The tensile test results of all materials

as a function of the crosshead speed are summarised in Table 4. For all curves showing a yield point, the yield stress was found to be equal to the tensile strength, since no material showed excessive strain hardening after yielding. The measured tensile properties are compared to tensile properties received from technical data sheets of each material (Ref. 1–5). If data was missing in the data sheets, the results were checked against values obtained for the same material type (Ref. a-c). All reference values were measured according to DIN EN ISO 527 with a testing speed of $1.67 \cdot 10^{-2} \text{ mms}^{-1}$ (1 mmmin^{-1}) for the evaluation of the Young's modulus and $8.3 \cdot 10^{-1} \text{ mms}^{-1}$ (50 mmmin^{-1}) afterwards. It was found that the measured values for the strain at break are generally lower compared to the reference values, but the values for the Young's modulus and strength are in a similar range, except for PEEK. Here, the reference value for the strength is significantly higher. This can be

Table 4

Material properties of polyetheretherketone (PEEK), polylactide (PLA), poly(methyl methacrylate) (PMMA), glycol-modified poly(ethylene terephthalate) (PETG), poly(vinylidene fluoride) (PVDF) and polypropylene (PP) obtained from tensile tests performed at four different crosshead speeds, namely 10^3 , 10^1 , 10^{-1} and 10^{-3} mms^{-1} .

Material	Crosshead speed [mms^{-1}]	Young's modulus [GPa]		Strain at break [%]		Stress at break [MPa]	Tensile strength [MPa]	Ref.
		Measured	Ref.	Measured	Ref.	Measured		
PEEK	10^3	4.8 ± 1.3	3.1 (1)	1.9 ± 0.2	26 (1)	66 ± 4		85/48 (1)
	10^1	3.6 ± 0.6		2.2 ± 0.4		66 ± 11		
	10^{-1}	3.5 ± 0.2		2.3 ± 0.3		60 ± 6		
	10^{-3}	3.2 ± 0.2		2.7 ± 0.3		66 ± 3		
PLA	10^3	4.6 ± 0.5	3.1^a (2)	2.3 ± 0.2	2.3 (a)	64 ± 3		-/65 (a)
	10^1	3.1 ± 0.1		2.3 ± 0.2		55 ± 2		
	10^{-1}	3.4 ± 0.3		4.0 ± 1.0		50 ± 2	53 ± 1	
	10^{-3}	3.3 ± 0.2		3.6 ± 0.5		43 ± 2	46 ± 2	
PMMA	10^3	5.2 ± 0.5	3.1^a (b)	1.9 ± 0.2	15 (3)	77 ± 13		65 at Yield (3)
	10^1	3.6 ± 0.1		1.7 ± 0.1		50 ± 2		
	10^{-1}	3.0 ± 0.3		1.8 ± 0.2		44 ± 4		
	10^{-3}	3.3 ± 0.2		1.5 ± 0.1		32 ± 3		
PETG	10^3	2.9 ± 0.8	1.9 (4)	6.3 ± 3.3	120 (4)	64 ± 2		50/- (4)
	10^1	2.0 ± 0.3		15.7 ± 12.2		32 ± 18	52 ± 4	
	10^{-1}	1.8 ± 0.0		85.7 ± 23.7		17 ± 0	48 ± 0	
	10^{-3}	1.9 ± 0.1		39.4 ± 7.5		23 ± 2	42 ± 1	
PVDF	10^3	2.1 ± 0.3	1.5–2.2 (5)	33.3 ± 3.3	30–200 (5)	39 ± 2		45–60/ 40–70 (5)
	10^1	1.0 ± 0.1		59.5 ± 11.4		28 ± 1	38 ± 0	
	10^{-1}	0.9 ± 0.0		141.4 ± 27.0		26 ± 1	30 ± 0	
	10^{-3}	0.8 ± 0.1		153.0 ± 61.8		24 ± 2	26 ± 0	
PP	10^3	1.4 ± 0.4	0.9^a (c)	14.4 ± 5.8	6.4^a (c)	28 ± 1		18.6^a at Yield (c)
	10^1	1.0 ± 0.3		20.7 ± 5.0		21 ± 0	23 ± 0	
	10^{-1}	1.0 ± 0.1		22.8 ± 4.6		16 ± 0	20 ± 0	
	10^{-3}	1.0 ± 0.0		151.4 ± 34.9		12 ± 1	16 ± 0	

(a) Reference value from Spoerk et al. (2017a)..

(b) Reference value from Gonzalez-Garzon et al. (2018)..

(c) Reference value from Spoerk et al. (2018a)..

^a Reference value not available online for the used material; Ref. from same material type.

explained by the relative high porosity measured for the 3D-printed PEEK samples (Fig. 4a). As processing induced defects have a significant influence on the strain at break, the lower values for the 3D-printed samples in contrast to the reference values, which are generally measured for injection-moulded samples with a more homogenous material distribution, are reasonable. Additionally, the Young's modulus found for 3D-printed PP is below the measured values since the reference samples were printed in a 90° strand orientation, which generally results in lower tensile properties. In the following sections, the stress-strain curves are analysed individually for each material and compared with pictures of the fractured samples as well as SEM images of the fracture surfaces for the highest and lowest testing speed.

3.3.1. Polyetheretherketone (PEEK)

The stress-strain curves measured for 3D-printed PEEK are characteristic for a brittle material behaviour (Fig. 5a) (Grellmann and Altstädt, 2011). The tensile strength is equal to the stress at break and appears to be independent of the testing speed. A trend towards decreased stress levels at lower testing speeds is recognised. The strain at break increases slightly with decreasing testing speed. In contrast to injection-moulded samples, no yield point is identified, even at very low testing speeds (Vaezi and Yang, 2015). Consequently, the evaluated strength values are lower than literature values. This can be explained by the unsatisfactory printing quality of the PEEK specimens as was shown in Figs. 3a and 4a. The occurrence of a brittle fracture mechanism is confirmed by the picture of the fractured samples (Fig. 5b) and the SEM fracture surfaces (Fig. 5c–f), which show no large-scale plastic deformation before failure. Weld lines, already shown in Fig. 3a, are detected, especially in Fig. 5c.

3.3.2. Polylactide (PLA)

The stress-strain curves for 3D-printed PLA are similar for all four testing speeds up to strain values of approx. 1% (Fig. 6a). At higher levels of strain, an increased tensile strength with increasing testing speed is detected. At 10^{-1} and 10^{-3} mms^{-1} , the material shows a pronounced yielding before failure. This results in higher values for the strain at break. Even though the overall behaviour changes, the picture of the fractured samples (Fig. 6b) as well as the SEM images (Fig. 6c–f) do not show significant differences in the fracture behaviour between the investigated testing speeds. Both SEM fracture surfaces indicate a predominantly brittle failure. There are no weld lines and air gaps visible, indicating an excellent inter- and intra-layer bonding (Arbeiter et al., 2018; Spoerk et al., 2017a). This also explains the high repeatability of the measurement results for each loading condition.

3.3.3. Poly(methyl methacrylate) (PMMA)

The stress-strain curves evaluated for 3D-printed PMMA specimens show a strain-rate dependent material behaviour, with a pronounced increase in stiffness and stress level at higher loading rates (Fig. 7a). The shape of all curves indicates a brittle fracture behaviour. Plastic deformations are neither identifiable on a big-scale (Fig. 7b), nor on a small-scale (Fig. 7c–f). SEM fracture surfaces show some air gaps, which account for deviations in the stress-strain curves. The wavy shape of the curves at high strain rates (Fig. 7a) can primarily be attributed to testing related influences, which often occur during impact testing of stiff and brittle materials (Cherif et al., 2010; Hopmann et al., 2017).

3.3.4. Glycol-modified poly(ethylene terephthalate) (PETG)

While the 3D-printed PETG samples appear rather brittle at the highest testing speed, they show pronounced yielding and high strains at break at lower testing speeds (Fig. 8a). At low strains, the curves are similar for all testing speeds. At higher strains, corresponding stresses decrease with decreasing crosshead speed, resulting in lower tensile strength values. Overall properties scale, with testing speed, with the exception of the strain at break for the lowest testing speed. This may be explained by printing induced defects, which can lead to significant scatter, especially for strain at break values. Differences in the fracture behaviour are visible in the picture of the fractured samples (Fig. 8b). SEM fracture surfaces strengthen the assumption about the material behaviour stated above. For the highest testing speed, the fracture surface is smooth and brittle (Fig. 8c–d), while it shows clear indications of plastic deformation before fracture for lower testing speeds (Fig. 8e–f). Regarding the printing quality, it can be stated that weld lines near the top of the sample and some signs of voids are recognisable (Fig. 8c).

3.3.5. Poly(vinylidene fluoride) (PVDF)

The stress-strain curves measured for 3D-printed PVDF specimens are similar at low strain values. For increasing levels of strain, the curves show pronounced differences (Fig. 9a). Strength and strain at break values significantly scale with the testing speed. Contrary to all materials above, PVDF shows a clear yield point at all testing speeds, indicating a more ductile behaviour. Especially at the two lower testing speeds, high strain at break values are reached. The increased deformation values and the necking of the specimens with decreasing testing speed can be identified in the picture of the fractured samples as well (Fig. 9b). The occurrence of a ductile fracture behaviour at high and low testing speeds is confirmed by the SEM fracture surfaces (Fig. 9c–f). Due to the high plastic deformations on the fracture surfaces, an identification of weld lines, air gaps or voids is not possible.

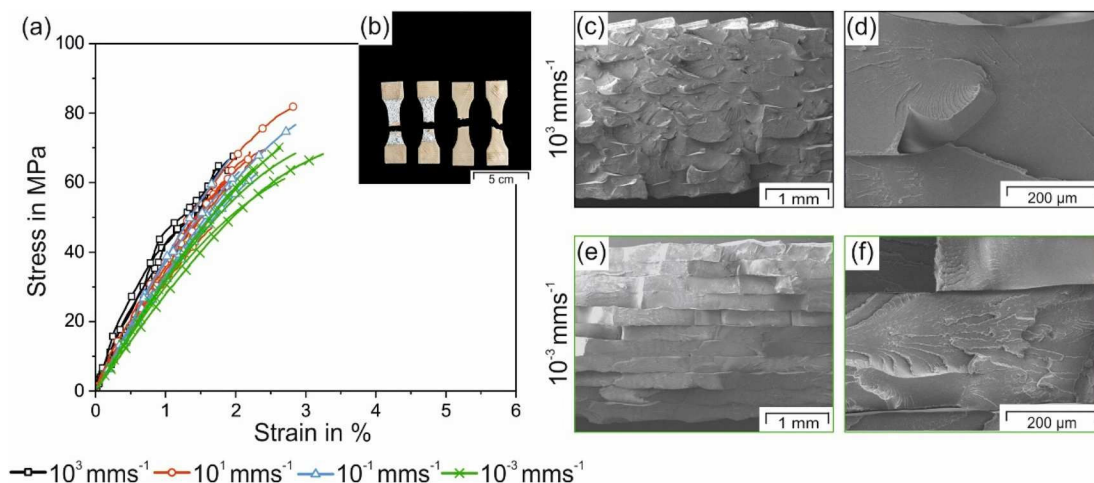


Fig. 5. Stress-strain curves obtained from tensile tests performed on 3D-printed polyetheretherketone (PEEK) specimens at four different crosshead speeds (a), fractured samples after tensile testing (b) and scanning electron microscopy (SEM) fracture surfaces for high (c, d) and low testing speeds (e, f). The test speed in (b) decreases from left to right: 10^3 , 10^1 , 10^{-1} and 10^{-3} mms^{-1} .

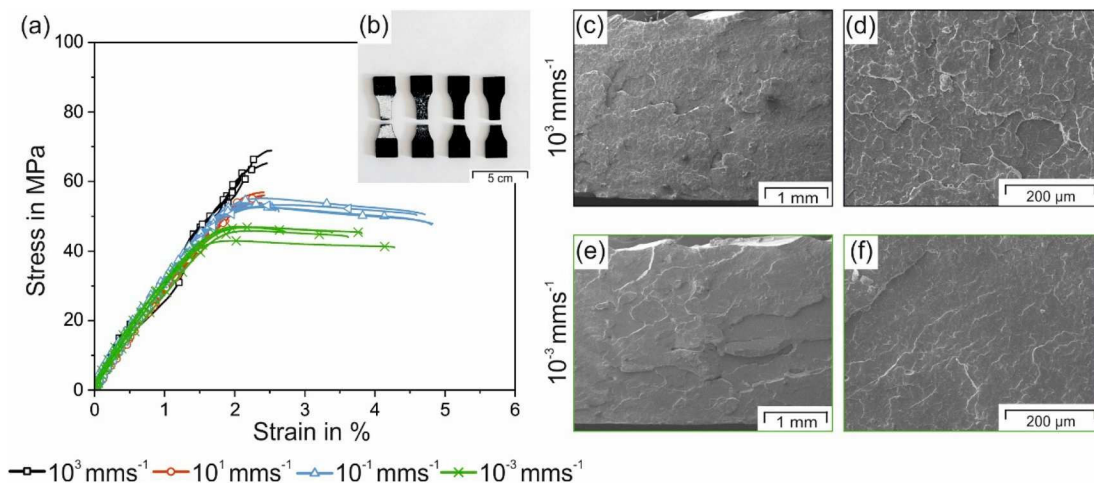


Fig. 6. Stress-strain curves obtained from tensile tests performed on 3D-printed polylactide (PLA) specimens at four different crosshead speeds (a), fractured samples after tensile testing (b) and scanning electron microscopy (SEM) fracture surfaces for high (c, d) and low testing speeds (e, f). The test speed in (b) decreases from left to right: 10^3 , 10^1 , 10^{-1} and 10^{-3} mms^{-1} .

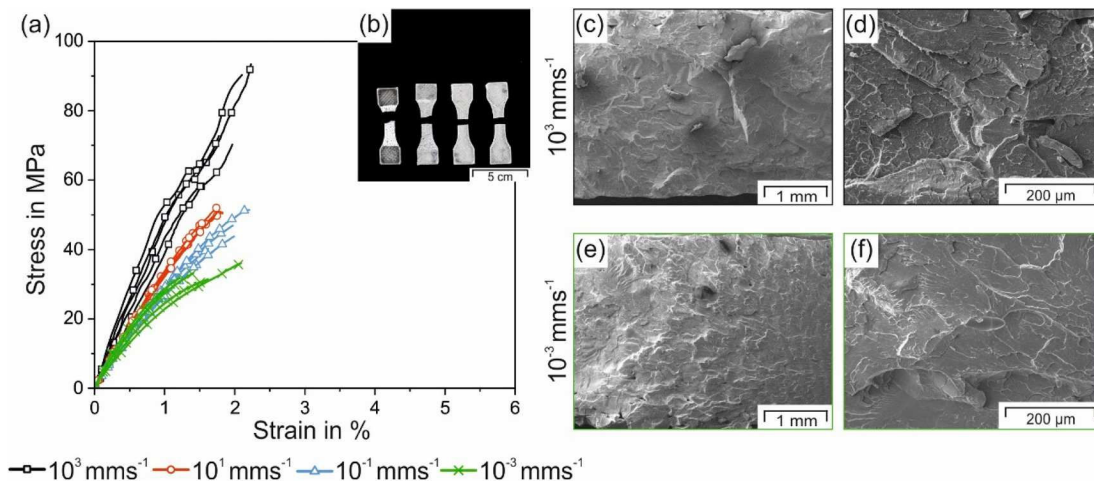


Fig. 7. Stress-strain curves obtained from tensile tests performed on 3D-printed poly(methyl methacrylate) (PMMA) specimens at four different crosshead speeds (a), fractured samples after tensile testing (b) and scanning electron microscopy (SEM) fracture surfaces for high (c, d) and low testing speeds (e, f). The test speed in (b) decreases from left to right: 10^3 , 10^1 , 10^{-1} and 10^{-3} mms^{-1} .

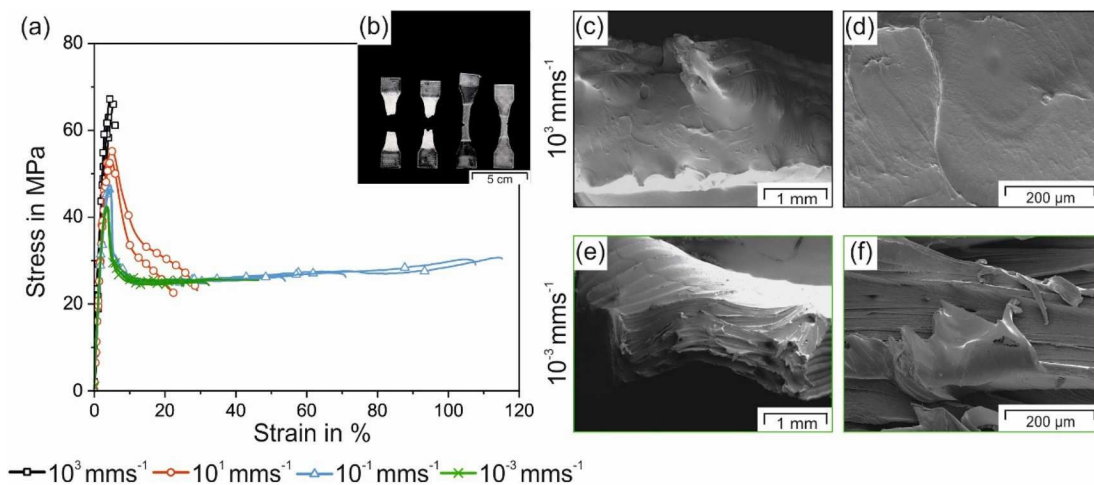


Fig. 8. Stress-strain curves obtained from tensile tests performed on 3D-printed glycol-modified poly(ethylene terephthalate) (PETG) specimens at four different crosshead speeds (a), fractured samples after tensile testing (b) and scanning electron microscopy (SEM) fracture surfaces for high (c, d) and low testing speeds (e, f). The test speed in (b) decreases from left to right: 10^3 , 10^1 , 10^{-1} and 10^{-3} mms^{-1} .

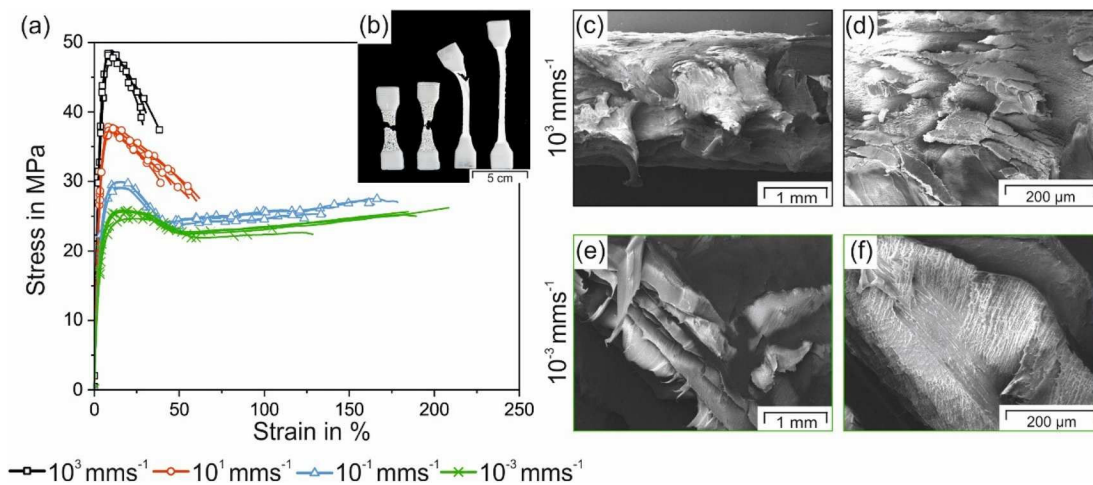


Fig. 9. Stress-strain curves obtained from tensile tests performed on 3D-printed poly(vinylidene fluoride) (PVDF) specimens at four different crosshead speeds (a), fractured samples after tensile testing (b) and scanning electron microscopy (SEM) fracture surfaces for high (c, d) and low testing speeds (e, f). The test speed in (b) decreases from left to right: 10^3 , 10^1 , 10^{-1} and 10^{-3} mms^{-1} .

3.3.6. Polypropylene (PP)

The trend of the stress-strain curves obtained for 3D-printed PP samples is similar to that of the PVDF specimens, but at nearly half the stress level (Fig. 10a). High levels of strain are reached for all testing speeds and necking accompanied with a significant change in cross section is detected (Fig. 10b and e). The SEM images reveal a predominantly ductile fracture surface at testing speeds below 10^3 mms^{-1} (Fig. 10e–f). At the highest testing speed, the fracture surface changes to a somewhat more brittle appearance (Fig. 10c–d). Weld lines are recognisable, especially in Fig. 10c.

4. Comparison and discussion

This chapter is used to ease the comparison of the materials and presented data of this work. While the interpretation of the cross sections and the DMA results is rather straightforward, it is more challenging to compare the stress-strain curves for several materials and testing speeds. Therefore, representative stress-strain curves for each material at the highest and the lowest crosshead speed are shown in Fig. 11. A small strain range is chosen as deformations acting on implant materials are considered relatively small at operating conditions. For individual results of materials and strain rates, the reader is referred to

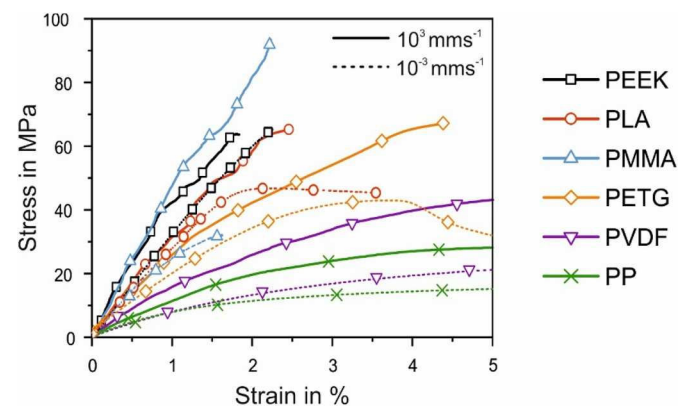


Fig. 11. Comparison of representative stress-strain curves measured for poly-etheretherketone (PEEK), polylactide (PLA), poly(methyl methacrylate) (PMMA), glycol-modified poly(ethylene terephthalate) (PETG), poly(vinylidene fluoride) (PVDF) and polypropylene (PP) dumbbell specimens. The curves were obtained from tensile tests performed at crosshead speeds of 10^3 (solid lines) and 10^{-3} mms^{-1} (dotted lines).

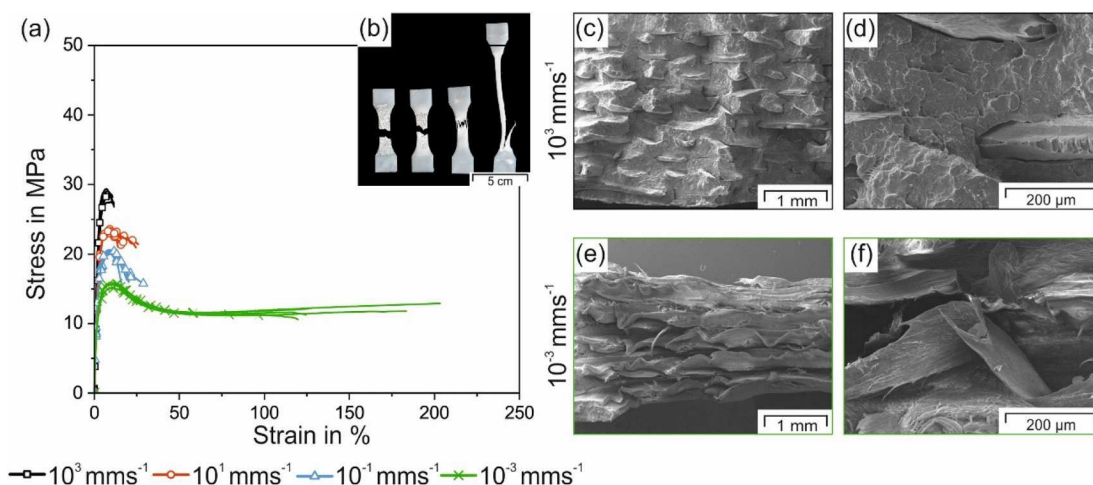


Fig. 10. Stress-strain curves obtained from tensile tests performed on 3D-printed polypropylene (PP) specimens at four different crosshead speeds (a), fractured samples after tensile testing (b) and scanning electron microscopy (SEM) fracture surfaces for high (c, d) and low testing speeds (e, f). The test speed in the picture of the fractured samples decreases from left to right: 10^3 , 10^1 , 10^{-1} and 10^{-3} mms^{-1} .

Table 4.

At the highest testing speed of 10^3 mms^{-1} , PEEK, PLA and PMMA show a characteristic brittle fracture behaviour with high tensile strengths and low strains at break. Moreover, PMMA shows the highest tensile strength, followed by PEEK and PLA. Nevertheless, the strain at break values and moduli are almost identical for these three materials. The fracture behaviour of PETG at such high testing speeds is predominantly brittle, with minor signs of ductility. Due to the higher non-linear behaviour of PETG compared to PEEK or PMMA, the material reaches higher levels of strain at similar levels of stress. Nonetheless, the Young's modulus (evaluated from 0.05 to 0.25%) of PETG is only slightly smaller and the tensile strength values are comparable. On the other hand, PVDF and PP react in a highly non-linear fashion even at the highest investigated testing speed. In comparison to the first group, the stiffness and strength of these two materials are significantly lower and the strain at break values are several times higher. Additionally, the tensile strength and the strain at break measured for PVDF specimens are twice as high as the values evaluated for PP specimens.

At the lowest testing speed of 10^{-3} mms^{-1} , the strength of all materials is significantly lower except for PEEK. For PMMA, this decrease is the most pronounced followed by PVDF. As expected, a trend towards higher non-linear curve behaviour, accompanied with lower levels of stress and higher levels of strain at break can be recognised. In the case of PLA and PETG, the overall behaviour and fracture patterns change towards pronounced yielding and indications of plastic deformations on the fracture surface before final failure. This information should be kept in mind, when selecting a material for component design.

To sum up, all tested materials are compared in terms of properties, which could be highly important for implant design (Fig. 12). This graph is intended as an aid for material selection based on few but crucial properties for polymeric materials, which could be used for 3D-printed implants. As mentioned before, the most interesting strain range for implant materials at standard operating conditions is expected to be relatively small. Therefore, the dependency of the stress-strain behaviour on the strain-rate is ranked in a very small strain range using the Young's modulus (E) measured at a very high (10^3 mms^{-1}) and low (10^{-3} mms^{-1}) testing speed. At such low strains, the mechanical properties of PLA and PP are nearly strain-rate independent and the dependency is increasing from PEEK, PETG, PMMA to PVDF. Regarding unexpected loads occurring during accidents, the stiffness and strength of the

materials (Table 4) are most important. Here, the averaged mean values for all testing speeds are used for the comparison. Material properties, which show only little dependency on temperature in the application range of 37 to 41 °C are beneficial. This parameter is defined as the temperature dependent storage modulus (E') and is ranked by means of the DMA results (Fig. 2, Table 2). Next to the mechanical integrity of the materials, the filling density of the printed specimens, which is a measure for the processability, is compared. The filling density is evaluated with: filling density [%] = $100 - \text{porosity} [\%]$. Additionally, the biocompatibility and durability of each material are discussed since these are highly important parameters regarding implant materials. However, both parameters were not included into Fig. 12 as no quantitative values are available.

PEEK obtains excellent mechanical properties with low temperature dependence as well as high biocompatibility (Kurtz and Devine, 2007) and durability (Ferguson et al., 2006). However, the dependency of the stiffness on the strain-rate is not negligible. Besides that, the processing of PEEK is very difficult resulting in a low filling density. Special printers for the required processing temperatures of approx. 425 °C are needed. PLA and PMMA show satisfying levels of strength and stiffness with satisfactory temperature dependency. Additionally, both materials are easily processible. High filling densities were achieved. For PLA, the stiffness is less dependent on the strain-rate than in the case of PMMA. As PLA is biodegradable (Hamad et al., 2015), its durability can be seen as very low. In general, PLA shows high biocompatibility, but it has been reported that PLA can be changed chemically or through drug incorporation, which may result in inflammatory reactions (Ramot et al., 2016). PMMA suffers from its reputation of being inflammatory (Navarro et al., 2008). Additionally, radiation-induced degradation has been investigated (Thominette and Verdu, 1996). However, it has a reasonable resistance to chemicals, except for chlorinated and aromatic hydrocarbons, esters, or ketones (Ali et al., 2015). PETG shows moderate strength, stiffness and strain-rate dependence. The storage modulus is hardly depending on temperature variations inside the human body. The processing of PETG is relatively easy and high filling densities can be obtained. PETG is biocompatible (Sastri, 2010), but it should be mentioned that the mechanical properties of polar materials such as PLA (Cuiffo et al., 2017), PMMA (N'Diaye et al., 2012) and PETG (Ryokawa et al., 2006) could be affected by moisture. Therefore, especially the water absorption of those materials is a topic of interest and has to be investigated in detail. The stiffness and strength measured for PVDF and PP are low compared to the other materials, whereby PVDF performs better than PP. However, the strain-rate dependency of the stiffness is significantly higher for PP than for PVDF. Nonetheless, both materials reveal a high temperature dependency for the storage modulus. The mechanical properties are graded as low, since this work focuses mostly on materials for structurally loaded components rather than applications within the body, where a high degree of flexibility is needed (e.g. meshes (Maitz, 2015; Ratner et al., 2004)). Furthermore, high filling densities were obtained with both materials. PVDF has proven to show excellent biocompatibility (Laroche et al., 1995a). The biocompatibility of PP has been discussed controversially in literature (Kelly et al., 2017; Lerouge and Simmons, 2012). Supplementary, PVDF outperforms PP in terms of the durability. Exemplarily, the tensile strength was measured with 92.5% for PVDF and 53.4% for PP after 7 years under hydrolytic conditions (Laroche et al., 1995b) leading to a better long-term stability in the case of PVDF. This has also been shown by Schumpelick and Nyhus as they compared PVDF to PET or PP (Schumpelick and Nyhus, 2004). In addition, it has been found that PP may undergo degradation while in vivo, especially due to oxidation (Costello et al., 2007).

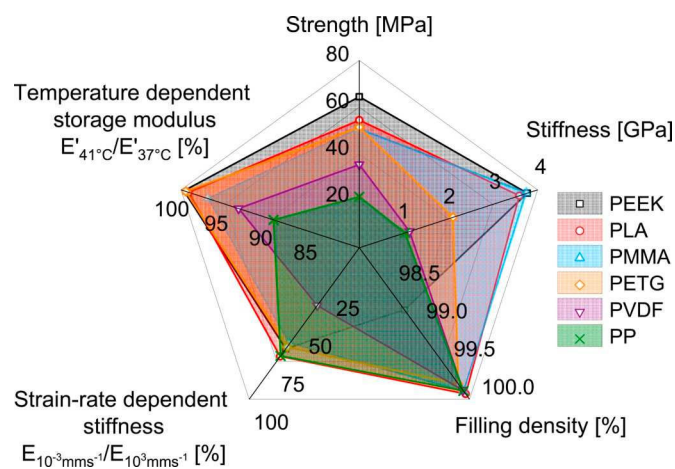


Fig. 12. Comparison of polyetheretherketone (PEEK), polylactide (PLA), poly (methyl methacrylate) (PMMA), glycol-modified poly(ethylene terephthalate) (PETG), poly(vinylidene fluoride) (PVDF) and polypropylene (PP) in terms of their strength, stiffness, filling density, strain-rate dependent stiffness (Young's modulus measured at 10^{-3} mms^{-1} in relation to 10^3 mms^{-1}) and temperature dependent storage modulus (in the application temperature range of 37 to 41 °C). All parameters are represented increasing from inside out (higher values are preferable).

5. Conclusion

The dynamic mechanical and tensile properties evaluated for the 3D-printing materials PEEK, PLA, PMMA, PETG, PVDF and PP provide useful information regarding the range of possible medical applications

for those materials. Due to significant deviations in the material properties evaluated for all materials, the performance of strain-rate dependent tests is vital in the course of the implant designing process. Depending on the level of stiffness, strength and strain at break, the materials are suitable for different types of medical applications. Regarding medical implants, the high stiffness and strength values evaluated for PEEK and PMMA account for their suitability for load-bearing parts such as cranial implants (Navarro et al., 2008; Petersmann et al., 2019; Panayotov et al., 2016). Despite the significantly lower price for PMMA compared to PEEK, PEEK is more likely to be used as an implant material. One reason for this represents the more pronounced temperature and loading rate dependency of the mechanical properties in the case of PMMA. One downside of PEEK and PMMA might be their rather brittle nature of fracture. The occurrence of a plastic region before failure might be preferable for implant applications in order to prevent a sudden, brittle failure. Due to its mechanical properties, PLA is also suitable for load-bearing applications such as short-term screws, but due to its degradability, it is likely used as suture material (Hamad et al., 2015).

On the other hand, the high flexibility of PP and PVDF accounts for their application as suture material or mesh (Maitz, 2015; Ratner et al., 2004). However, their applicability as cranial bone reconstruction material cannot be ruled out (Katschnig et al., 2017), especially for smaller defects where high stiffness is not as crucial. Moreover, the high ductility of PP or PVDF prevents a brittle implant failure into several pieces in the case of an accident. PETG seems to be a satisfying compromise between these two described materials groups. The evaluated material properties account for its applicability for parts, which do not require a high load capacity or elasticity such as bite guards (Marcauteanu et al., 2014).

In conclusion, this paper gives an overview of temperature and loading-rate dependent material properties of thermoplastic 3D-printable implant materials. For polymers, the characterisation of these dependencies is particularly important. The results should serve as guidelines for designers of medical devices or for medical professionals in order to get an impression of the material behaviour of different 3D-printing polymers. However, it has to be kept in mind that the properties of a component are not only depending on the material itself. The mechanical behaviour of components is further influenced by geometrical and processing parameters.

Declaration of competing interest

The authors declare that they have no known competing financial interests or personal relationships that could have appeared to influence the work reported in this paper.

CRediT authorship contribution statement

Sandra Petersmann: Methodology, Investigation, Validation, Writing - original draft, Writing - review & editing, Visualization. **Martin Spoerk:** Conceptualization, Methodology, Validation, Resources, Writing - original draft, Writing - review & editing, Visualization. **Willem Van De Steene:** Methodology, Investigation, Validation, Resources, Writing - review & editing. **Muammer Üçal:** Investigation, Validation, Writing - review & editing, Visualization. **Johannes Wiener:** Methodology, Software, Investigation, Writing - review & editing. **Gerald Pinter:** Validation, Writing - review & editing, Funding acquisition, Supervision. **Florian Arbeiter:** Conceptualization, Methodology, Validation, Visualization, Writing - review & editing, Supervision.

Acknowledgement

This work was partially supported by the project CAMEd (COMET K-Project 871132) which is funded by the Austrian Federal Ministry of Transport, Innovation and Technology (BMVIT) and the Austrian

Federal Ministry for Digital and Economic Affairs (BMDW) and the Styrian Business Promotion Agency (SFG). The authors would like to thank Philipp Huber for his support during the manufacturing of certain samples.

References

- Abdulai, A.E., Iddrissu, M.I., Dakurah, T.K., 2006. Cranioplasty using polymethyl methacrylate implant constructed from an alginate impression and wax elimination technique. *Ghana Med. J.* 40 (1), 18–21. PMID: 17299559.
- Ali, U., Karim, K.J.A., Buang, N.A., 2015. A review of the properties and applications of poly (methyl methacrylate) (PMMA). *Polym. Rev.* 55 (4), 678–705. <https://doi.org/10.1080/15583724.2015.1031377>.
- Amash, A., Zugenmaier, P., 2000. Morphology and properties of isotropic and oriented samples of cellulose fibre-polypropylene composites. *Polymer* 41 (4), 1589–1596. [https://doi.org/10.1016/S0032-3861\(99\)00273-6](https://doi.org/10.1016/S0032-3861(99)00273-6).
- Arbeiter, F., Spoerk, M., Wiener, J., Gosch, A., Pinter, G., 2018. Fracture mechanical characterization and lifetime estimation of near-homogeneous components produced by fused filament fabrication. *Polym. Test.* 66, 105–113. <https://doi.org/10.1016/j.polymertesting.2018.01.002>.
- Banga, H.K., Belokar, R.M., Kalra, P., Kumar, R., 2018. Fabrication and stress analysis of ankle foot orthosis with additive manufacturing. *Rapid Prototyp. J.* 24 (2), 301–312. <https://doi.org/10.1108/RPJ-08-2016-0125>.
- Cherif, C., Seidel, A., Younes, A., Hausding, J., 2010. Evaluation of a tensile test for the determination of the material behaviour of filament yarns under high strain rates. *Autex Res. J.* 10 (4), 88–94.
- Costa, S.F., Duarte, F.M., Covas, J.A., 2017. Estimation of filament temperature and adhesion development in fused deposition techniques. *J. Mater. Process. Technol.* 245, 167–179. <https://doi.org/10.1016/j.jmatprotec.2017.02.026>.
- Costello, C.R., Bachman, S.L., Ramshaw, B.J., Grant, S.A., 2007. Materials characterization of explanted polypropylene hernia meshes. *J. Biomed. Mater. Res. B Appl. Biomater.* 53B (1), 44–49. <https://doi.org/10.1002/jbm.b.30764>.
- Crowninshield, R.D., Brand, R.A., 1981. A physiologically based criterion of muscle force prediction in locomotion. *J. Biomech.* 14 (11), 793–801. [https://doi.org/10.1016/0021-9290\(81\)90035-X](https://doi.org/10.1016/0021-9290(81)90035-X).
- Cuiffo, M.A., Snyder, J., Elliott, A.M., Romero, N., Kannan, S., Halada, G.P., 2017. Impact of the fused deposition (FDM) printing process on polylactic acid (PLA) chemistry and structure. *Appl. Sci.* 7 (6), 579–593. <https://doi.org/10.3390/app7060579>.
- Del Bene, V.E., 1990. Temperature. In: Walker, H.K., Hall, W.D., Hurst, J.W. (Eds.), *Clinical Methods: the History, Physical, and Laboratory Examinations*. Butterworth Publishers, Boston, USA, pp. 990–993.
- Diegel, O., 2014. Additive manufacturing. In: Hashmi, S., Van Tyne, C.J., Batalha, G.F., Yilbas, B. (Eds.), *Comprehensive Materials Processing*. Elsevier, Amsterdam, The Netherlands, pp. 3–18. <https://doi.org/10.1016/B978-0-08-096532-1.01000-1>.
- Elshereksi, N.W., Mohamed, S.H., Arifin, A., Ishak, Z.A.M., 2014. Thermal characterisation of poly(methyl methacrylate) filled with barium titanate as denture base material. *J. Phys. Sci.* 25 (2), 15–27.
- Fedorov, A., Beichel, R., Kalpathy-Cramer, J., Finet, J., Fillion-Robin, J.C., Pujol, S., Bauer, C., Jennings, D., Fennessy, F., Sonka, M., Buatti, J., Aylward, S., Miller, J.V., Pieper, S., Kikinis, R., 2012. 3D slicer as an image computing platform for the quantitative imaging network. *Magn. Reson. Imaging* 30 (9), 1323–1341. <https://doi.org/10.1016/j.mri.2012.05.001>.
- Ferguson, S.J., Visser, J.M.A., Polikeit, A., 2006. The long-term mechanical integrity of non-reinforced PEEK-OPTIMA polymer for demanding spinal applications: experimental and finite-element analysis. *Eur. Spine J.* 15 (2), 149–156. <https://doi.org/10.1007/s00586-005-0915-5>.
- Fiaschi, P., Pavanello, M., Imperato, A., Dallolio, V., Accogli, A., Capra, V., Consales, A., Cama, A., Piatelli, G., 2016. Surgical results of cranioplasty with a polymethylmethacrylate customized cranial implant in pediatric patients: a single-center experience. *J. Neurosurg. Pediatr.* 17 (6), 705–710. <https://doi.org/10.3171/2015.10.PEDS15489>.
- Gebhardt, A., Kessler, J., Thurn, L., 2016. *3D-Drucken: Grundlagen und Anwendungen des Additive Manufacturing (AM)*, second ed. Hanser, München, Germany.
- Gibson, I., Rosen, D.W., Stucker, B., 2010. *Additive Manufacturing Technologies*. Springer US, Boston, USA.
- Gonzalez-Garzon, M., Shahbikian, S., Huneault, M.A., 2018. Properties and phase structure of melt-processed PLA/PMMA blends. *J. Polym. Res.* 25 (2), 58. <https://doi.org/10.1007/s10965-018-1438-1>.
- Grellmann, W., Altstädt, V., 2011. *Kunststoffprüfung*, second ed. Hanser, München, Germany.
- Gurr, M., Mühlaupt, R., 2012. Rapid prototyping. In: Moeller, M., Matyjaszewski, K. (Eds.), *Polymer Science: A Comprehensive Reference*. Elsevier, Amsterdam, The Netherlands, pp. 77–99.
- Hamad, K., Kaseem, M., Yang, H.W., Deri, F., Ko, Y.G., 2015. Properties and medical applications of polylactic acid: a review. *Express Polym. Lett.* 9 (5), 435–455. <https://doi.org/10.3144/expresspolymlett.2015.42>.
- Hopmann, C., Klein, J., 2015. Determination of strain rate dependent material data for FEA crash simulation of polymers using digital image correlation. *Comput. Mater. Sci.* 100, 181–190. <https://doi.org/10.1016/j.commatsci.2015.01.021>.
- Hopmann, C., Klein, J., Schöngart, M., 2017. Tensile impact testing on polymer materials considering the force-oscillation phenomenon. *AIP Conf. Proc.* 1914 (1), 090004. <https://doi.org/10.1063/1.5016750>, 1–090004-6.

- Katschnig, M., Arbeiter, F., Haar, B., van Campe, G., Holzer, C., 2017. Cranial polypropylene implants by fused filament fabrication. *Adv. Eng. Mater.* 19 (4), 1600676. <https://doi.org/10.1002/adem.201600676>.
- Kelly, M., Macdougall, K., Olabisi, O., McGuire, N., 2017. In vivo response to polypropylene following implantation in animal models: a review of biocompatibility. *Int. Urogynecol. J.* 28, 171–180. <https://doi.org/10.1007/s00192-016-3029-1>.
- Kim, B.-J., Hong, K.-S., Park, K.-J., Park, D.-H., Chung, Y.-G., Kang, S.-H., 2012. Customized cranioplasty implants using three-dimensional printers and polymethylmethacrylate casting. *Korean Neurosurg. Soc.* 52 (6), 541–546. <https://doi.org/10.3340/jkns.2012.52.6.541>.
- Kriegel, R.J., 2006. *Kalottenplastik für große Schädeldefekte mit PMMA (Polymethylmethacrylat) oder Tutoplast-prozessierten autogenen Knochentransplantaten. Inaugural-Dissertation. Rheinischen Friedrich-Wilhelms-Universität Bonn.*
- Kurtz, S.M., Devine, J.N., 2007. PEEK biomaterials in trauma, orthopedic, and spinal implants. *Biomaterials* 28 (32), 4845–4869. <https://doi.org/10.1016/j.biomaterials.2007.07.013>.
- Laroche, G., Marois, Y., Guidoin, R., King, M.W., Martin, L., How, T., Douville, Y., 1995a. Polyvinylidene fluoride (PVDF) as a biomaterial: from polymeric raw material to monofilament vascular suture. *J. Biomed. Mater. Res.* 29 (12), 1525–1536. <http://doi.org/10.1002/jbm.b.820291209>.
- Laroche, G., Marois, Y., Schwarz, E., Guidoin, R., King, M.W., Pâris, E., Douville, Y., 1995b. Polyvinylidene fluoride monofilament sutures: can they be used safely for long-term anastomoses in the thoracic aorta? *Artif. Organs* 19 (11), 1190–1199. <https://doi.org/10.1111/j.1525-1594.1995.tb02282.x>.
- Lerouge, S., Simmons, A., 2012. *Sterilisation of Biomaterials and Medical Devices*, first ed. Elsevier, Amsterdam, The Netherlands.
- Letcher, T., Waytashek, M., 2014. Material property testing of 3D-printed specimen in PLA on an entry-level 3D printer, presented at ASME IMECE 2014. Canada, Montreal. <https://doi.org/10.1115/IMECE2014-39379>.
- Liao, Y., Liu, C., Coppola, B., Barra, G., Di Maio, L., Incarnato, L., Lafdi, K., 2019. Effect of porosity and crystallinity on 3D printed PLA properties. *Polymers* 11, 1487. <http://doi.org/10.3390/polym11091487>.
- Maitz, M.F., 2015. Applications of synthetic polymers in clinical medicine. *Biosurf. Biotribol.* 1 (3), 161–176. <https://doi.org/10.1016/j.bsbt.2015.08.002>.
- Marcautuanu, C., Stoica, E.T., Bortun, C., Negrutiu, M.-L., Sinescu, C., Turdor, A., 2014. Advantages of a PETG coated with TPU as an occlusal appliance material. *Rev. Chim. (Bucharest)* 65 (6), 734–736.
- Mofokeng, J.P., Luyt, A.S., Tábi, T., Kovács, J., 2012. Comparison of injection moulded, natural fibre-reinforced composites with PP and PLA as matrices. *J. Thermoplast. Compos. Res.* 25 (8), 927–948. <https://doi.org/10.1177/0892705711423291>.
- Morales-Gómez, J.A., García-Estrada, E., Leos-Bortoni, J.E., Delgado-Brito, M., Flores-Huerta, L.E., de la Cruz-Arriaga, A.A., Torres-Díaz, L.J., de León, Á.R.M.-P., 2018. Cranioplasty with a low-cost customized poly(methylmethacrylate) implant using a desktop 3D printer. *J. Neurosurg.* 130 (5), 1–7. <https://doi.org/10.3171/2017.12.JNS172574>.
- N'Diaye, M., Pascaretti-Grizon, F., Massin, P., Baslé, M.F., Chappard, D., 2012. Water absorption of poly(methyl methacrylate) measured by vertical interference microscopy. *J. Am. Chem. Soc. Langmuir* 28 (31), 11609–11614. <https://doi.org/10.1021/ja302260a>.
- Navarro, M., Michiardi, A., Castaño, O., Planell, J.A., 2008. Biomaterials in orthopaedics. *J. R. Soc. Interface* 5 (27), 1137–1158. <https://doi.org/10.1098/rsif.2008.0151>.
- Panayotov, I.V., Orti, V., Cuisinier, F., Yachouh, J., 2016. Polyetheretherketone (PEEK) for medical applications. *J. Mater. Sci. Mater. Med.* 27 (7), 118. <https://doi.org/10.1007/s10856-016-5731-4>.
- Paszkievicz, S., Szymczyk, A., Pawlikowska, D., Irska, I., Taraghi, I., Pilawka, R., Gu, J., Li, X., Tu, Y., Piesowicz, E., 2017. Synthesis and characterization of poly(ethylene terephthalate-co-1,4-cyclohexanedimethylene terephthalate)-block-poly(tetramethylene oxide) copolymers. *RSC Adv.* 7 (66), 41745–41754. <https://doi.org/10.1039/C7RA07172H>.
- Perez, M., Block, M., Espalin, D., Winker, R., Hoppe, T., Medina, F., Wicker, R., 2012. *Sterilization of FDM-Manufactured Parts*, Presented at. SFF 2012, Austin, Texas.
- Petersmann, S., Spoerk, M., Huber, P., Lang, M., Pinter, G., Arbeiter, F., 2019. Impact optimization of 3D-printed poly(methyl methacrylate) for cranial implants. *Macromol. Mater. Eng.* 304, 1900263. <https://doi.org/10.1002/mame.201900263>.
- Ramot, Y., Haim-Zada, M., Domb, A.J., Nyska, A., 2016. Biocompatibility and safety of PLA and its copolymers. *Adv. Drug Deliv. Rev.* 107, 153–162. <https://doi.org/10.1016/j.addr.2016.03.012>.
- Ratner, B.D., 2015. The biocompatibility of implant materials. In: Badyal, S. (Ed.), *Host Response to Biomaterials*. Elsevier, Amsterdam, The Netherlands, pp. 37–51. <https://doi.org/10.1016/b978-0-12-800196-7.00003-7>.
- Ratner, B.D., Hoffman, A.S., Schoen, F.J., Lemons, J.E., 2004. *Biomaterials Science: an Introduction to Materials in Medicine*, second ed. Elsevier, Amsterdam, The Netherlands.
- Richeton, J., Ahzi, S., Vecchio, K.S., Jiang, F.C., Adharapurapu, R.R., 2006. Influence of temperature and strain rate on the mechanical behavior of three amorphous polymers: characterization and modeling of the compressive yield stress. *Int. J. Solids Struct.* 43 (7–8), 2318–2335. <https://doi.org/10.1016/j.ijsolstr.2005.06.040>.
- Ridwan-Pramana, A., Marcián, P., Borák, L., Narra, N., Forouzanfar, T., Wolff, J., 2017. Finite element analysis of 6 large PMMA skull reconstructions: a multi-criteria evaluation approach. *PLoS One* 12 (6), e0179325. <https://doi.org/10.1371/journal.pone.0179325>.
- Rodríguez, J.F., Thomas, J.P., Renaud, J.E., 2001. Mechanical behavior of acrylonitrile butadiene styrene (ABS) fused deposition materials. *Experimental investigation. Rapid Prototyp. J.* 7 (3), 148–158. <https://doi.org/10.1108/13552540110395547>.
- Rotaru, H., Baciut, M., Stan, H., Bran, S., Chezan, H., Iosif, A., Tomescu, M., Kim, S.-G., Rotaru, A., Baciut, G., 2006. Silicone rubber mould cast polyethylmethacrylate-hydroxyapatite plate used for repairing a large skull defect. *J. Cranio Maxill. Surg.* 34 (4), 242–246. <https://doi.org/10.1016/j.jcms.2006.01.005>.
- Ryokawa, H., Miyazaki, Y., Fujishima, A., Miyazaki, T., Maki, K., 2006. The mechanical properties of dental thermoplastic materials in a simulated intraoral environment. *Orthod. Waves* 65 (2), 64–72. <https://doi.org/10.1016/j.odw.2006.03.003>.
- Sastri, V.R., 2010. Chapter 7 engineering thermoplastics acrylics, polycarbonates, polyurethanes, polyacetals, polyesters, and polyamides. In: *Plastics in Medical Devices*. Elsevier, Amsterdam, The Netherlands, pp. 121–173. <https://doi.org/10.1016/B978-0-8155-2027-6.10007-8>.
- Scheirs, J., Long, T.E., 2004. *Modern Polyesters: Chemistry and Technology of Polyesters and Copolyesters*. John Wiley & Sons, Chichester, UK. <https://doi.org/10.1002/0470090685>.
- Schumpelick, V., Nyhus, L.M., 2004. *Meshes: Benefits and Risks*. Springer, Berlin, Germany. <https://doi.org/10.1007/978-3-642-18720-9>.
- Slapnik, J., Bobovnik, R., Mešl, M., Bolka, S., 2016. Modified polylactide filaments for 3D printing with improved mechanical properties. *Contemp. Mater.* 2 (7), 142–150. <https://doi.org/10.7251/COMEN1602142S>.
- Soumya, N., Rajarshi, B., 2012. Fundamentals of medical implant materials. In: Narayan, R. (Ed.), *Materials for Medical Devices*, vol. 23. ASM International, Ohio, USA, pp. 6–17. <https://doi.org/10.31399/asm.hb.v23.a0005682>.
- Spoerk, M., Arbeiter, F., Cajner, H., Sapkota, J., Holzer, C., 2017a. Parametric optimization of intra- and inter-layer strengths in parts produced by extrusion-based additive manufacturing of poly(lactic acid). *J. Appl. Polym. Sci.* 134 (41), 45401. <https://doi.org/10.1002/app.45401>.
- Spoerk, M., Sapkota, J., Weingrill, G., Fischinger, T., Arbeiter, F., Holzer, C., 2017b. Shrinkage and warpage optimization of expanded-perlite-filled polypropylene composites in extrusion-based Additive Manufacturing. *Macromol. Mater. Eng.* 302 (10), 1700143. <https://doi.org/10.1002/mame.201700143>.
- Spoerk, M., Savandaiah, C., Arbeiter, F., Sapkota, J., Holzer, C., 2017c. Optimization of mechanical properties of glass-spheres-filled polypropylene composites for extrusion-based additive manufacturing. *Polym. Compos.* 38, 768. <https://doi.org/10.1002/pc.24701>.
- Spoerk, M., Arbeiter, F., Raguž, I., Weingrill, G., Fischinger, T., Traxler, G., Schuschnigg, S., Cardon, L., Holzer, C., 2018a. Polypropylene filled with glass spheres in extrusion-based Additive Manufacturing: effect of filler size and printing chamber temperature. *Macromol. Mater. Eng.* 303 (7), 1800179. <https://doi.org/10.1002/mame.201800179>.
- Spoerk, M., Gonzalez-Gutierrez, J., Lichal, C., Cajner, H., Berger, G., Schuschnigg, S., Cardon, L., Holzer, C., 2018b. Optimisation of the adhesion of polypropylene-based materials during extrusion-based additive manufacturing. *Polymers* 10 (5), 490. <https://doi.org/10.3390/polym10050490>.
- Spoerk, M., Savandaiah, C., Arbeiter, F., Traxler, G., Cardon, L., Holzer, C., Sapkota, J., 2018c. Anisotropic properties of oriented short carbon fibre filled polypropylene parts fabricated by extrusion-based additive manufacturing. *Compos. Part A-App. S.* 113, 95–104. <https://doi.org/10.1016/j.compositesa.2018.06.018>.
- Spoerk, M., Holzer, C., Gonzalez-Gutierrez, J., 2019. Material extrusion-based additive manufacturing of polypropylene: a review on how to improve dimensional inaccuracy and warpage. *J. Appl. Polym. Sci.* 48545. <https://doi.org/10.1002/APP.48545>.
- Thominette, F., Verdu, J., 1996. Radiation-induced rejuvenation of poly(methyl methacrylate). *J. Polym. Sci., Polym. Chem.* 34 (15), 3221–3223. [https://doi.org/10.1002/\(SICI\)1099-0518\(19961115\)34:15<3221::AID-POLA12>3.0.CO;2-E](https://doi.org/10.1002/(SICI)1099-0518(19961115)34:15<3221::AID-POLA12>3.0.CO;2-E).
- Tóth, T., Hudák, R., Živčák, J., 2015. Dimensional verification and quality control of implants produced by additive manufacturing. *Qual. Innov. Prosper.* 19 (1), 9–21. <https://doi.org/10.12776/qip.v19i1.393>.
- Vaezi, M., Yang, S., 2015. Extrusion-based additive manufacturing of PEEK for biomedical applications. *Virtual Phys. Prototyp.* 10 (3), 123–135. <https://doi.org/10.1080/17452759.2015.1097053>.
- Van den Bogert, A.J., 1994. Analysis and simulation of mechanical loads on the human musculoskeletal system: a methodological overview. *Exerc. Sport Sci. Rev.* 22 (1), 23–51.
- Verius, M., Marreiros, F., Heuze, Y., Unterhofer, C., Recheis, W., 2011. A Novel Approach for Implant Design of Large Cranial Defects Using PMMA and Rapid Prototyping Techniques. ECR, Vienna, Austria. <https://doi.org/10.1594/ECR2011/C-0950> presented at.
- Wang, X., Zhao, L., Ying, J., Fuh, H., Lee, H.-P., 2019. Effect of porosity on mechanical properties of 3d printed polymers: experiments and micromechanical modeling based on x-ray computed tomography analysis. *Polymers* 11, 1154. <https://doi.org/10.3390/polym11071154>.
- Webb Kerekes, T., Lim, H., Joe, W.Y., Yun, G.J., 2019. Characterization of process-deformation/damage property relationship of fused deposition modeling (FDM) 3D-printed specimens. *Addit. Manuf.* 25, 532–544. <https://doi.org/10.1016/j.addma.2018.11.008>.
- Wintermantel, E., Ha, S.-W., 2009. *Medizintechnik*, fifth ed. Springer, Berlin, Germany. <https://doi.org/10.1007/978-3-540-93936-8>.
- Wu, W., Geng, P., Li, G., Zhao, D., Zhang, H., Zhao, J., 2015. Influence of layer thickness and raster angle on the mechanical properties of 3D-printed PEEK and a comparative mechanical study between PEEK and ABS. *Materials* 8 (9), 5834–5846. <https://doi.org/10.3390/ma8095271>.
- Zhu, W., Ma, J., Nan, X., Liu, J., Qin, W., Yang, Y., 2017. Dielectric and Thermal-Properties of Polyvinylidene Fluoride Composites Filled with Surface-Functionalized Reduced Graphene Oxide presented at: ICCM-21, Xi'an, China.

Web references

- [1] <http://www.solvayamshop.com>. (Accessed 14 November 2019).
- [2] <http://www.redline-filament.com>. (Accessed 14 November 2019).
- [3] <http://shop.filamentonline.de>. (Accessed 14 November 2019).
- [4] <http://www.3djake.at>. (Accessed 14 November 2019).
- [5] <http://www.nilepolymers.com>. (Accessed 14 November 2019).

Publication 2

Bibliographic information

Title: The effects of washing and formaldehyde sterilization on the mechanical performance of poly(methyl methacrylate) (PMMA) parts produced by material extrusion-based additive manufacturing or material jetting

Authors: Sandra Petersmann¹, Lukas Hentschel², Joamin Gonzalez-Gutierrez^{2,+}, Martin Tödting³, Ute Schäfer^{3,4}, Florian Arbeiter¹, Muammer Üçal^{3,4,*}

Affiliations:

¹Materials Science and Testing of Polymers, Montanuniversitaet Leoben, Otto Gloeckel-Straße 2, 8700, Leoben, Austria

²Polymer Processing, Montanuniversitaet Leoben, Otto Gloeckel-Straße 2, 8700, Leoben, Austria

³Research Unit Experimental Neurotraumatology, Department of Neurosurgery, Medical University of Graz, Auenbruggerplatz 22, 8036 Graz, Austria

⁴BioTechMed-Graz, 8036 Graz, Austria

⁺Luxembourg Institute of Science and Technology (LIST), 5 rue Bommel, 4940 Hautcharage, Luxembourg

Periodical: Advanced Engineering Materials - Additive Manufacturing at MU Leoben

DOI: <https://doi.org/10.1002/adem.202200225>

Relevant contributions to this publication:

Conceptualisation: Joamin Gonzalez-Gutierrez, Ute Schäfer, Florian Arbeiter, Muammer Üçal,

Methodology: Sandra Petersmann, Lukas Hentschel, Martin Tödting, Florian Arbeiter

Investigation: Sandra Petersmann, Muammer Üçal

Validation: Sandra Petersmann, Florian Arbeiter, Muammer Üçal

Writing - Original Draft: Sandra Petersmann, Muammer Üçal

Writing - Review & Editing: Sandra Petersmann, Joamin Gonzalez-Gutierrez, Ute Schäfer, Florian Arbeiter, Muammer Üçal,

Visualisation: Sandra Petersmann, Muammer Üçal

The Effects of Washing and Formaldehyde Sterilization on the Mechanical Performance of Poly(methyl Methacrylate) (PMMA) Parts Produced by Material Extrusion-Based Additive Manufacturing or Material Jetting

Sandra Petersmann, Lukas Hentschel, Joamin Gonzalez-Gutierrez, Martin Tödting, Ute Schäfer, Florian Arbeiter, and Muammer Üçal*

Nowadays, personalized medical implants are frequently produced through additive manufacturing. As all medical devices have to undergo specific washing and sterilization before application, the effects of a predefined cleaning routine that is available to the clinical institutes, washing with chemical agent and formaldehyde fumigation, on the mechanical behavior of printed parts are examined. Mechanical properties of parts manufactured by fused filament fabrication (FFF) and ARBURG plastic freeforming (APF) using two poly(methyl methacrylate) (PMMA)-based materials, 3Diakon and CYROLITE MD H12, respectively, are analyzed using flexural and impact tests. An influence of cleaning treatments on the mechanical properties of APF samples is not detected. FFF samples, however, show lower impact strength after washing, but not after sterilization. The fracture surfaces, porosity values, or chemical structure assessed by Fourier-transform infrared (FTIR) spectroscopy could not explain this decrease. Influence of the cleaning treatments on the material itself is assessed using thin compression-molded specimens. The influence on the stress–strain curves is negligible, apart from a slight but significant reduction in the yield stress. FTIR spectroscopy and scanning electron microscopy analyses of the fracture surfaces do not show detectable differences among differentially treated samples.


1. Introduction

Additive manufacturing (AM) is of particular interest in the production of medical implants as it allows faster design and manufacturing of personalized prostheses. For polymers, especially the material extrusion based, AM technology known as fused filament fabrication (FFF) has already been well established.^[1–3] Nonetheless, all AM methods are continuously improving and new technologies are developed. The ARBURG plastic freeforming (APF) process is a relatively new AM method, where granules, instead of filaments, are molten and deposited as droplets. Therefore, a plasticization unit similar to that of an injection-molding machine provides the molten material and pressure for the deposition process. After plasticization, the polymeric material enters the discharge unit, consisting of a nozzle and a piezoelectric valve, which opens the nozzle up to 200 times per second.^[4] As the nozzle opens and closes at such high frequencies, the extruded melt

forms droplets in the freeforming method instead of the continuous string obtained in the FFF process. Hence, it is classified as a material jetting technology according to ISO/ASTM 52 900.

S. Petersmann, F. Arbeiter
Materials Science and Testing of Polymers
Montanuniversitaet Leoben
Otto Gloeckel-Straße 2, 8700 Leoben, Austria

L. Hentschel, J. Gonzalez-Gutierrez
Polymer Processing
Montanuniversitaet Leoben
Otto Gloeckel-Straße 2, 8700 Leoben, Austria

 The ORCID identification number(s) for the author(s) of this article can be found under <https://doi.org/10.1002/adem.202200225>.

© 2022 The Authors. Advanced Engineering Materials published by Wiley-VCH GmbH. This is an open access article under the terms of the Creative Commons Attribution License, which permits use, distribution and reproduction in any medium, provided the original work is properly cited.

DOI: 10.1002/adem.202200225

J. Gonzalez-Gutierrez
Functional Polymers Unit
Materials Research and Technology Department
Luxembourg Institute of Science and Technology (LIST)
5 rue Bommel, 4940 Hautcharage, Luxembourg

M. Tödting, U. Schäfer, M. Üçal
Research Unit Experimental Neurotraumatology
Department of Neurosurgery
Medical University of Graz
Auenbruggerplatz 2.2, 8036 Graz, Austria
E-mail: muammer.uecal@medunigraz.at

U. Schäfer, M. Üçal
BioTechMed-Graz
8010 Graz, Austria

Several materials are suitable for processing with both manufacturing methods. Among these, poly(methyl methacrylate) (PMMA) stands out with its promising properties. It has already been used for many years for various medical applications such as optical lenses, bone cement for orthopedic and cranial implants, or prostheses in dentistry.^[4,5] Therefore, it offers a good starting point for further investigations regarding the use of AM and the impact of nonthermal sterilization methods on its biocompatibility and biomechanical properties.

To enable the implantation of prosthetic devices produced by FFF and APF in humans, the material and manufacturing processes have to comply with the clinical safety measures. In addition to durability and biocompatibility, implant materials have to be sterilizable. The medical products must be free of any pathogens and contaminants, while reliably maintaining their mechanical properties and dimensional accuracy.^[6] Although autoclaving is a suitable sterilization method for implants made of metals, ceramics, and high-performance thermoplastics, polymers with low melting temperatures (e.g., PMMA) are deformed at the high temperatures of the autoclaving process. Sterilization methods that could be utilized for specimens manufactured from polymers with low melting temperatures include chemical sterilization (ethylene oxide or formaldehyde), radiation sterilization (gamma, electron beam, or X-ray), plasma sterilization, and microwave sterilization.^[7,8] In this work, sterilization by formaldehyde fumigation was studied, as it is a sterilization procedure commonly available in most clinical institutes.

Several studies analyzing the effects of different sterilization methods on the resulting properties of PMMA have already been conducted.^[9–14] However, medical devices usually undergo a cleaning step preceding sterilization,^[15] which could influence the material, as this process usually involves temperature, pressure, and an aqueous solution of washing agent.^[16] It is known that polymers in general, and thus also PMMA, exhibit temperature,^[17] pressure,^[18] and moisture-dependent^[19,20] properties. Avila et al.,^[21] for instance, showed that heat treatment of 3D-printed PMMA at 97 °C for 60 min led to an increase in strength of about 20 MPa. Given their porous structure, additive-manufactured specimens could be influenced by these procedures to an extent larger than the molded specimens, as their absorption–desorption behavior might differ from the solid, nonporous, molded specimen with a rather smooth surface.

Furthermore, the AM process introduces a certain level of porosity, which could potentially influence the mechanical performance depending on its extent. Hence, the porosity of FFF and APF samples was analyzed before testing and after the different treatment steps, to rule out the effect of different porosity levels while analyzing the treatment influence on the mechanical performance. This has been done by means of X-ray microcomputed tomography (μ CT), as it is well established as a nondestructive method to evaluate defect sizes, distributions, and individual shapes.^[22]

Consequently, this study investigates the effects of washing and formaldehyde sterilization on the porosity and mechanical properties of PMMA-based materials manufactured with FFF and APF. Bending and impact tests showed that the washing and sterilization procedures did not exert a significant change in mechanical performance of the FFF- and APF-manufactured specimens. μ CT analyses ruled out any confounding influence of porosity on the results.

2. Experimental Section

2.1. Materials

FFF-manufactured samples were produced using the commercially available PMMA filament (diameter of 1.75 mm) 3Diakon (Mitsubishi Chemical Advanced Materials Inc., USA), due to its excellent impact performance, which is preferable for several implant materials, such as cranial reconstruction materials. APF-manufactured samples were produced using pellets of CYROLITE MD H12 (kindly provided by Roehm GmbH, Germany), an amorphous thermoplastic compound based on PMMA (methyl methacrylate/styrene/ethyl acrylate terpolymer with an added impact modifier^[23]). CYROLITE MD H12 meets the requirements of the USA Pharmacopeia Class VI and is ISO 10993-1 certified and approved by the USA Food and Drug Administration (FDA) for clinical use.^[24] Throughout the article, 3Diakon and CYROLITE MD H12, are referred to as PMMA-D and PMMA-C, respectively.

2.2. Experimental Setup

Both PMMA types were divided into three different experimental groups ($n = 25$ samples in each): untreated controls, washing, and washing + sterilization. The “washing” specimens were washed at 60 °C following a specific hygiene protocol. The “washing + sterilization” group was additionally sterilized with formaldehyde fumigation. The mechanical properties of each group were assessed by three different testing methods: three-point bending, Charpy impact test, and Charpy-notched impact test. A flow diagram of the experimental setup is shown in **Figure 1**.

2.3. Processing

Test specimens were manufactured in the shape of a rectangular prism in 80 mm \times 4 mm \times 10 mm dimensions with a single contour line, a 100% infill, and a $\pm 45^\circ$ rectilinear infill strategy. Five samples were fabricated per print batch via so-called sequential printing for FFF and in a layer-by-layer manner for APF (**Figure 2**). A detailed summary of the used processing parameters for both technologies is given in **Table 1**.

FFF samples were manufactured at MedMEX (HAGE3D GmbH, Austria), which works with a dual direct extrusion head. The slicing was done with the software Simplify3D v3.0 (Simplify3D, USA). The printing speed of the first layer was decreased to 15 mm s⁻¹ to get the best adhesion on the glass surface. The samples were removed from the printer after bed temperature cooled down to a temperature of 60-to-80 °C and then stored in vacuumed Allpax GOF 2030 bags (Allpax Products LLC, USA) at ambient temperature.

In APF, an already proven material profile was used for processing PMMA-C with the freeformer 200-3X (ARBURG GmbH + Co KG, Germany).^[4] The print job was prepared in the ARBURG freeformer software v2.30 (ARBURG GmbH + Co KG, Germany). Prior to manufacturing, the material was dried at 70 °C for 5 h in the integrated circulating air dryer (Helios GmbH, Germany). After the drying procedure, the hopper was kept at 50 °C with reduced moisture to keep

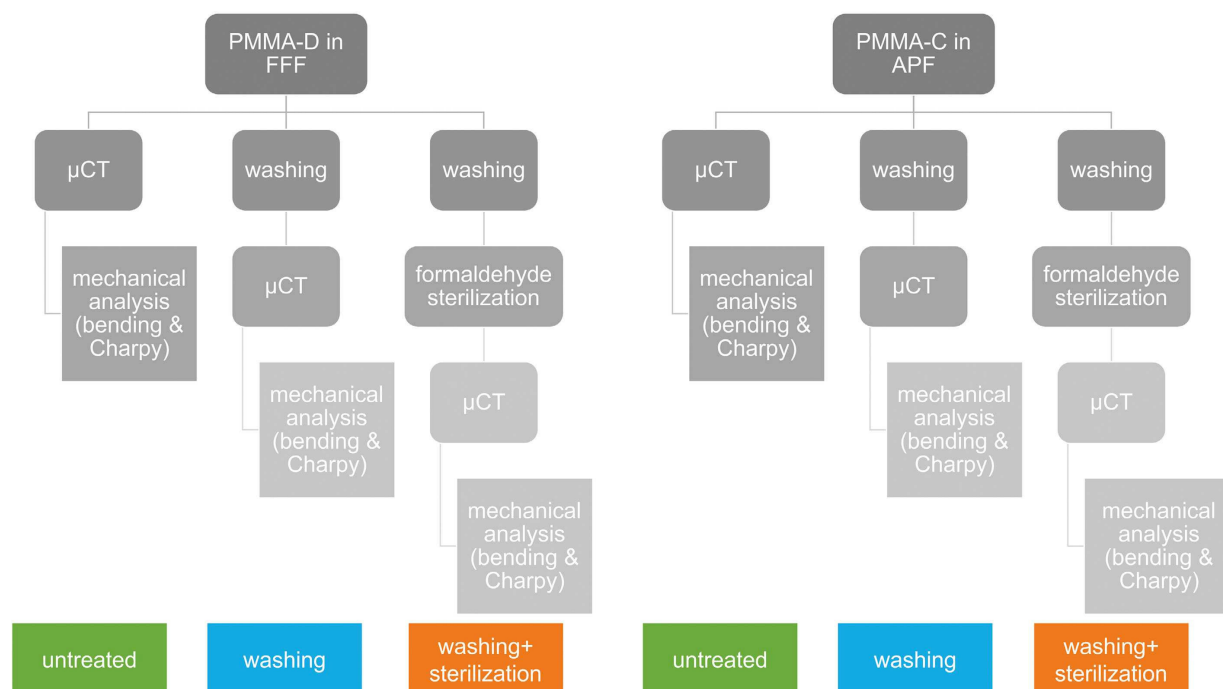


Figure 1. Flow diagram including specimen manufacturing via FFF or APF, treatments (washing and formaldehyde sterilization), performance of μ CT, and mechanical analysis (three-point bending, unnotched and notched Charpy impact tests).

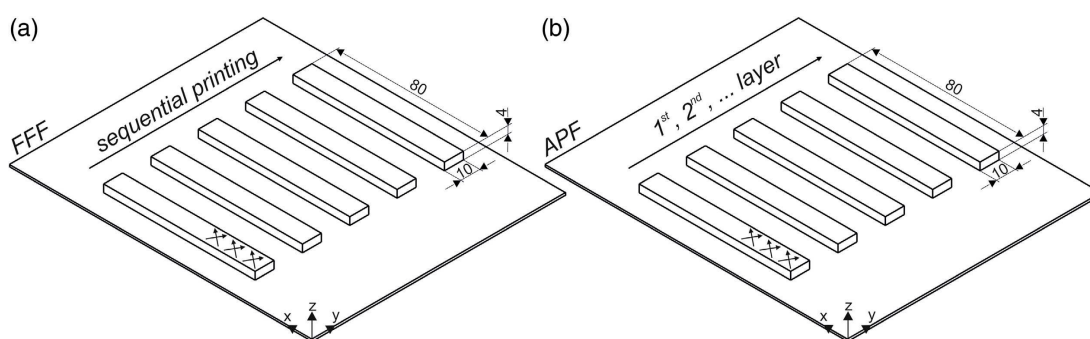


Figure 2. Sample arrangement on the build platform for a) FFF and b) APF. Five samples were manufactured per print batch. Sample dimensions are given in mm.

the material dry. The drop height was 0.22 mm with the set discharge value of 67%, resulting in a layer height of 0.2 mm. The droplet overlap was set to 25%.

Dimensions within the mechanical testing standards could be obtained using APF, but not using FFF. Here, width values in the range of 9.49–9.82 mm were obtained, which were below the tolerance of 10 ± 0.2 mm.

2.4. Washing and Formaldehyde Sterilization

The sample washing and sterilization were performed at the AEMP III (Processing Unit for Medical Devices) at the University Hospital Graz in accordance with ÖNORM EN ISO 25424. Washing was performed using a Miele cleaning–disinfection device (Miele & Cie. KG, Germany) at

60 °C with a disinfectant program suitable for thermolabile materials. Neodisher Septo DN (Chemische Fabrik Dr. Weigert GmbH & Co KG, Germany) was used as the washing agent, which contained 10.5% (w/w) glutaraldehyde and showed bactericidal, fungicidal, mycobactericidal, and viricidal activity. Sterilization was performed with 2% formaldehyde using a Webeco FA95 temperature steam sterilizer (Webeco NV, Belgium). A summary of washing and sterilization procedures is given in Table 2.

2.5. Analysis of Porosity

Samples were scanned in an Inveon μ CT scanner (Inveon μ -PET/SPECT/CT, Siemens, Germany) with scanning parameters of 80 kV potential, 500 μ A current, 750 ms exposure time, and an

Table 1. List of printing parameters for FFF and APF.

Processing parameter	FFF	APF
Nozzle diameter [mm]	0.4	0.2
Nozzle temperature [°C]	260	245
Printing speed for infill [mm s ⁻¹]	50	60
Printing speed for contour lines [mm s ⁻¹]	40	25
Build platform/Chamber temperature [°C]	140	105
Build platform material	borosilicate glass	poly(acrylonitrile-butadiene)/poly(amide) blend
Extrusion multiplier/Drop aspect ratio [–]	1.00	1.29
Layer thickness [mm]	0.1	0.2

Table 2. Brief summary of steps during the washing and sterilization process.

Washing protocol (thermolabile, disinfection)	Sterilization protocol (thermolabile, formaldehyde fumigation)
1. Washing (3 min, water)	1. Air out
2. Washing at 55 °C (3 min, water)	2. Conditioning at 60 °C with 17× alternating pressure (200–220 mbar, 15 s) and vacuum (60–80 mbar, 15 s)
3. Chemical treatment at 55 °C (10 min)	3. Treatment 10 min at 60 °C (3× with intermittent vacuum)
4. 2× washing (3 min, water)	4. Desorption phase at 60 °C with 30× alternating pressure (210 mbar, 30 s) and vacuum (60–80 mbar, 15 s)
5. 1× washing at 60 °C (3 min, water)	5. Drying at 60 °C, 10 min, under vacuum (65 mbar)
6. Drying (15 min, 80 °C)	6. Wash phase at 50–60 °C with 5× alternating pressure (740–750 mbar) and vacuum (65–75 mbar)
7. Drying (15 min, 60 °C)	7. Air in

effective pixel size of 35.19 μm. The raw data was reconstructed using the Inveon CT Recon Software v2.04 software (Siemens, Germany). Image sections were exported from the reconstructed scan data and saved as bitmap digital image files using ImageJ. Each specimen was imaged in 2699 sectional images with sagittal and/or horizontal alignment. Segmentation, 3D modeling, and volumetric analyses of the printed specimens and the internal gaps/holes were done using an open-source software 3D Slicer v4.10.2.^[25] A gap/hole in an image slice was defined as an island that had a signal intensity below the threshold value without connection to the outer surface through neighboring image sections. Porosity was calculated as the percentage of gap volumes with respect to the specimen volume. Local porosity at the midsection was calculated the same way using the image slices that cover one-third of the whole specimen centered at the midlength in the axial orientation.

2.6. Mechanical Tests

2.6.1. Flexural Tests

The flexural tests were performed in three-point bending mode on the universal testing machine Zwick Z10 (Zwick Roell, Germany) equipped with a 10 kN load cell. The tests were carried out according to EN ISO 178 at 23 °C and 50% r.h. The testing speed was 2 mm min⁻¹. The deformations were measured with the makroXtens extensometer. The test ended, if no fracture occurred, at a deflection of 10 mm. The support distance was 64 mm. Supports and loading edges were 5 mm in radius. Prior to testing, the samples were stored at standardized climate (23 °C, 50% r.h.) for at least 48 h. The following flexural material properties were evaluated according to EN ISO 178: the flexural modulus (E_f), the maximum flexural stress (σ_{fM}), the flexural stress at break (σ_{fB}), and the flexural stress at the conventional deflection (σ_{fC}), wherein the conventional deflection (s_C) was equal to 1.5 times the thickness (h) of the test specimen. E_f is defined as the slope of the flexural stress–flexural strain curve in the flexural strain interval between 0.05 and 0.25%. All stresses and strains are engineering values, which take the initial cross section of the specimen into account. Microscopic images of the fracture surface of representative specimens were taken under a light microscope (SZH, Olympus Optical Co., Japan).

2.6.2. Charpy Impact Tests

Instrumented Charpy impact tests were performed on the pendulum impact tester HIT25/50P (Zwick Roell, Germany) equipped with a 2 J pendulum at 23 °C and 50% r.h. The tests were carried out according to EN ISO 179-2 on unnotched and notched specimens via edge-wise blows. The notch was introduced in the geometry of shape A according to ISO 179-1, resulting in a characteristic V-shape with 2 mm depth and 0.25 mm tip radius. The impact speed was 2.9 m s⁻¹ according to the standard. Prior to testing, the samples were stored at standardized climate (23 °C, 50% r.h.) for at least 48 h. The following parameters were evaluated according to standard (EN ISO 179-2): the Charpy unnotched (a_{cU}) and notched (a_{cN}) impact strength. Microscopic images of the fracture surface of representative specimens were taken under a light microscope (SZH, Olympus Optical Co., Japan).

2.7. Analyzing the Influence of the Treatments on the PMMA Material Used in FFF

2.7.1. Preparation of Compression-Molded (CM) Samples

PMMA-D in form of granules was molded at 240 °C and 6.5 bar to 1 mm-thick plates by means of a laboratory platen press COLLIN P 300 E+ (COLLIN Lab & Pilot Solutions GmbH, Germany). Before compression molding (CM), the material was dried at 80 °C for 10 h. Subsequently, the CM plates were used to manufacture tensile test specimens according to DIN EN ISO 527-2 Type 1BA via computer numerical control machining (Deckel FP3, Friedrich Deckel AG, Germany). CM plates

were randomly assigned for differential cleaning treatment (untreated, washing, washing+sterilization, $n = 5$ per group).

2.7.2. Tensile Tests on CM Samples

The tensile tests were performed on a universal testing machine Zwick Z10 (Zwick Roell, Germany) equipped with a 10 kN load cell and mechanical clamps, in accordance with DIN EN ISO 527-1 with a testing speed of 1 mm min^{-1} for the evaluation of the Young's modulus (E) and 50 mm min^{-1} for the recording of the remaining curve. The clamping length was set to 50 mm. The deformations were measured with the makroXtens extensometer until yield and by the crosshead travel afterward. All stresses and strains are engineering values, which consider the initial cross section of the specimen. The Young's modulus and tensile strength (σ_M) or yield stress (σ_y) are calculated and compared. E is defined as the slope of the stress–strain curve in the strain interval between 0.05 and 0.25% according to DIN EN ISO 527-1. Furthermore, the tensile strength is the global stress maximum and the yield stress gives the stress value at the yield point, which is characterized by a global stress maximum followed by stress reduction due to narrowing of the cross section.^[26]

2.7.3. Fourier Transform Infrared Spectroscopy

Fourier transform infrared (FTIR) spectroscopy by attenuated total reflection was performed with a Bruker IFS 66 vs⁻¹ FTIR spectrometer (Bruker Corporation, USA) in the range of $600\text{--}4000 \text{ cm}^{-1}$. The penetration depth into the sample is up to $\approx 10 \mu\text{m}$, depending on the wavelength of light.^[27] Spectra were acquired and examined with 16 scans and 4 cm^{-1} resolution after spectral correction with ambient atmosphere. A spectrum of the washing agent was also recorded for comparison. The spectra were examined for alterations in the chemical structure or the presence of residual media after cleaning treatments.

2.7.4. Scanning Electron Microscopy

Scanning electron microscopy (SEM) was performed for selected unnotched Charpy samples using a TESCAN Vega II (TESCAN Brno, s.r.o., Czech Republic) at 5 kV using secondary electrons. The parts of the specimens to be analyzed were fixed on SEM sample holders and were gold-sputtered with the SCD 005 Cool Sputter Coater (BAL-TEC AG, Liechtenstein) for 160 s at 20 mA.

2.8. Statistical Analyses

Statistical analyses were conducted using SPSS (IBM Corp. Released 2019. IBM SPSS Statistics for Windows, Version 26.0. Armonk, NY: IBM Corp). Normality of data distribution was assessed with visual inspection of Q–Q plots and Shapiro–Wilk test. Variance homogeneity was assessed with Levene's test. When the compared groups had normal distribution, statistical significance of the observed differences was tested either with one-way ANOVA followed by a Tukey's honestly significant

difference (HSD), or Welch's variance-weighted ANOVA followed by Games–Howell posthoc tests, depending on the variance homogeneity across the compared groups. When the compared groups had non-normal distribution, Kruskal–Wallis H test followed by a pairwise comparison with Bonferroni correction was used. Correlation of observed porosity to the flexural stress at the conventional deflection (three-point bending test group) or to the impact strength absorbed in breaking the specimen (Charpy tests) was assessed with Spearman's rank correlation coefficient.

A difference with a p -value ≤ 0.05 in any case was deemed statistically significant.

3. Results

No significant differences between the different types of treatments were observed in the flexural stress–flexural strain curves for both PMMA types as well as manufacturing methods (Figure 3). Furthermore, FFF specimens neither showed a maximum nor failure before the conventional deflection s_C ($1.5 \text{ h} \approx 6 \text{ mm}$, test ended at 10 mm) is reached (Figure 3a). As the test is limited by s_C , the flexural strength (σ_{FM}) and the flexural stress at break (σ_{FB}) were not evaluated and only the flexural modulus (E_f) and the flexural stress at s_C (σ_{fC}) were analyzed. APF specimens fractured before reaching the deflection limit (Figure 3b). Therefore, the maximum flexural stress (σ_{FM}) and the flexural stress at break (σ_{FB}), which were equal were evaluated in addition to the flexural modulus (E_f). Specimens from all treatment groups had comparable flexural moduli in the bending tests with both FFF-printed PMMA-D samples ($F(2) = 0.127$, $p = 0.882$) and APF-printed PMMA-C samples ($F(2) = 1.256$, $p = 0.320$) (Figure 3c). Similarly, the flexural stress (at the conventional deflection or at break) did not show statistically significant differences among the treatment groups either in FFF samples ($F(2) = 1.393$, $p = 0.286$) (Figure 3d) or in APF samples (Welch's $F(2, 6.020) = 1.208$, $p = 0.362$) (Figure 3e). It is important to note that the different flexural behavior was a result of the intrinsic mechanical properties of the different types of PMMA. PMMA-D is more compliant than PMMA-C, as suggested by the manufacturer's specifications.^[24,28] Moreover, the fracture surfaces of the APF samples showed a characteristic brittle fracture and no significant differences between the different treatments were visible (Figure 3f).

In the FFF-manufactured PMMA-D group, statistically significant differences were observed in Charpy impact strength among differentially treated samples for both unnotched ($\chi^2(2) = 11.180$; $p = 0.004$) and notched specimens ($F(2) = 4.165$; $p = 0.027$) (Figure 4a). Pairwise comparisons showed that the impact strength was significantly lower in the washed group in comparison with the untreated controls ($p = 0.003$). Interestingly washed + sterilized specimens were comparable to the controls ($p = 0.143$). In the notched specimens, however, the impact strength values of the washed samples were comparable to the controls ($p = 0.120$), while washed+sterilized samples showed slightly but significantly higher impact strength in comparison with the control group ($p = 0.027$).

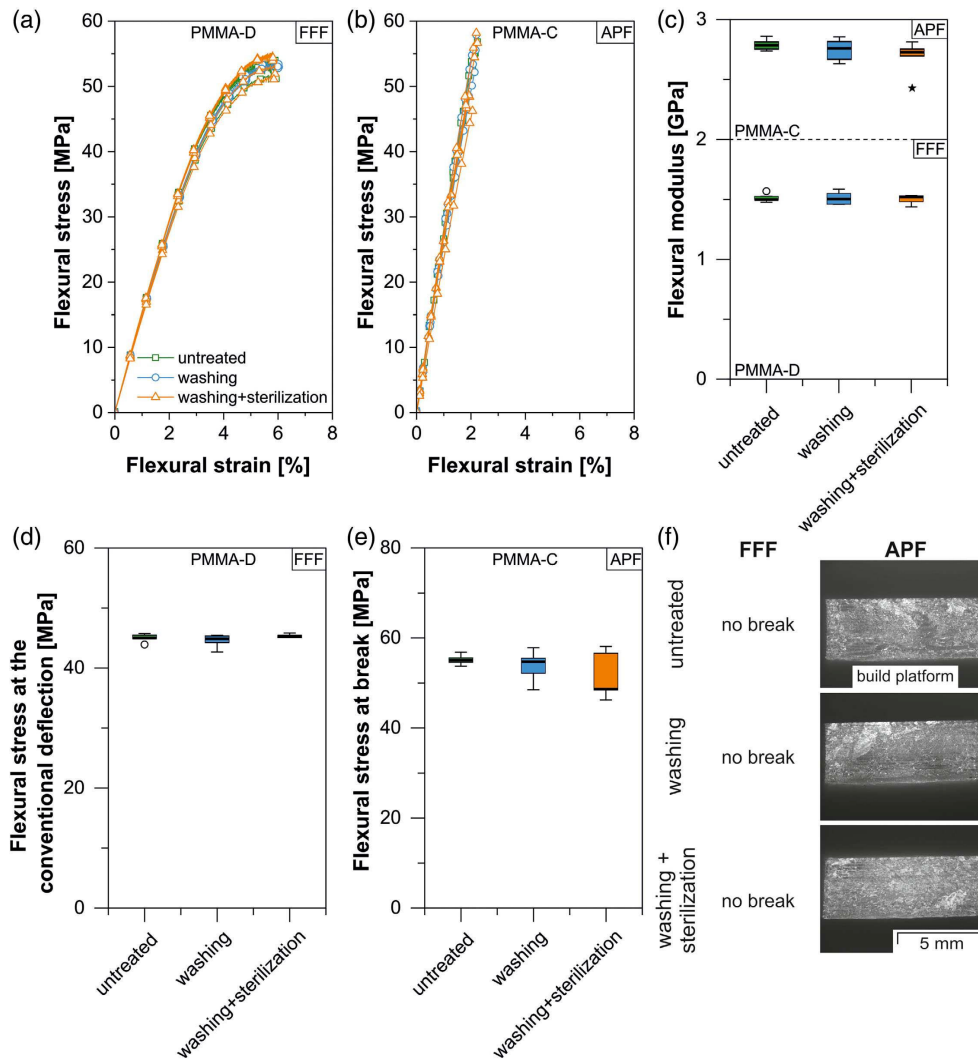


Figure 3. Flexural stress–flexural strain curves obtained for PMMA-D in a) FFF and PMMA-C in b) APF in their untreated state, after washing and after washing + sterilization. c) Flexural moduli (E_f) in APF and FFF samples were shown in and were comparable among the treatment groups. Flexural stress at the conventional deflection (σ_c) in d) FFF samples and maximum flexural stress (σ_{fM}) in e) APF samples were not influenced by cleaning treatments. $n = 5$ samples per treatment in each material group. f) Microscopic images of the representative fracture surfaces for each group are displayed.

In the APF-manufactured PMMA-C group, an influence of cleaning treatment on the impact strength was not observed in the Charpy impact tests with unnotched specimens ($\chi^2(2) = 1.257$; $p = 0.533$). Note that higher impact strength values were observed in the washing + sterilization group with notched specimens, but the differences were statistically not significant ($\chi^2(2) = 5.886$; $p = 0.053$) (Figure 4b).

The fracture surfaces did not show any major differences between the treatment groups for either type of material (Figure 4c). All samples showed characteristic brittle fracture surfaces. In FFF samples, the layer next to the build platform was wider and denser most properly due to the heated print bed. This could also be attributable to the calibration of the nozzle distance to the surface of the platform. Calibration done at ambient temperature does not take the heat-induced expansion in the print bed, which causes the first layer to be deposited by the nozzle from a smaller distance resulting in a wider first layer.^[29] The

individual layers, in addition, could easily be distinguished in FFF, but not in APF samples.

The lower Charpy impact strength observed in unnotched, FFF-printed PMMA-D samples after washing (Figure 4a) could not be explained by a difference in the fracture surface assessed with light microscopy (Figure 4c). Therefore, it was checked whether the observed differences could be associated with variabilities in the porosity level of the specimens. A Spearman's rank correlation coefficient test with all groups pooled (with or without a cleaning treatment) revealed that neither flexural stress at the conventional deflection nor Charpy impact strength showed a statistically significant correlation to the global porosity or to the local porosity levels at the midsection (Figure 5). A significant correlation, moreover, was not observed when the treatment groups were separately analyzed (data not shown).

Given that there was a skewed data distribution, the focus was placed on comparison of the FFF-manufactured PMMA-D

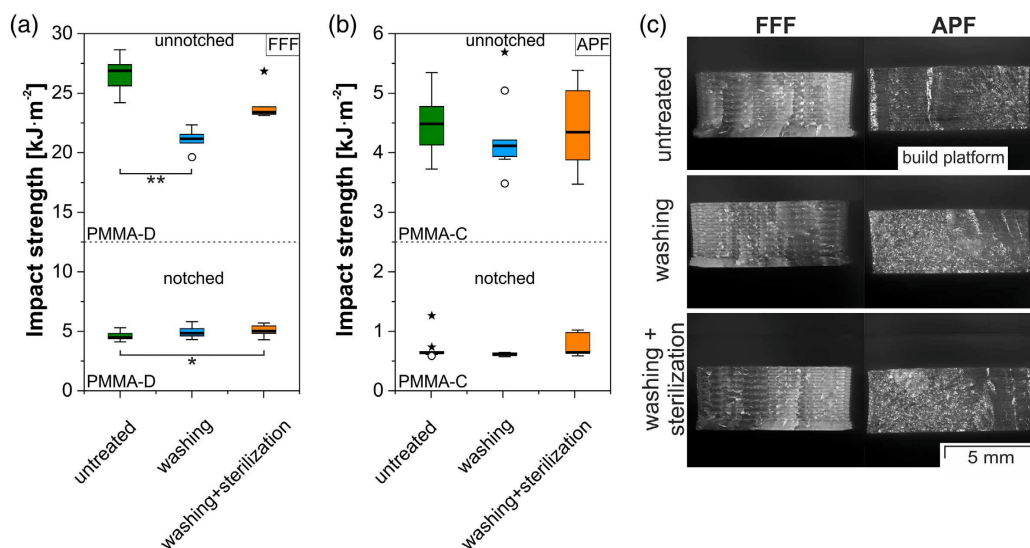


Figure 4. The Charpy impact strength for unnotched and notched (a_{cU} and a_{cN}) PMMA-D in a) FFF and PMMA-C in b) APF in their untreated state, after washing and after washing + sterilization. Representative microscopic images of the fracture surfaces of each group after Charpy impact testing c). The statistical significance of the differences was assessed using Kruskal–Wallis H test followed by a pairwise analysis with Bonferroni correction or using one-way ANOVA followed by a Tukey’s HSD test for posthoc comparison. Circles show outliers. Stars show extreme outliers. $*p \leq 0.05$, $**p \leq 0.01$. $n = 5$ per treatment in FFF unnotched, $n = 10$ per treatment in all other comparisons.

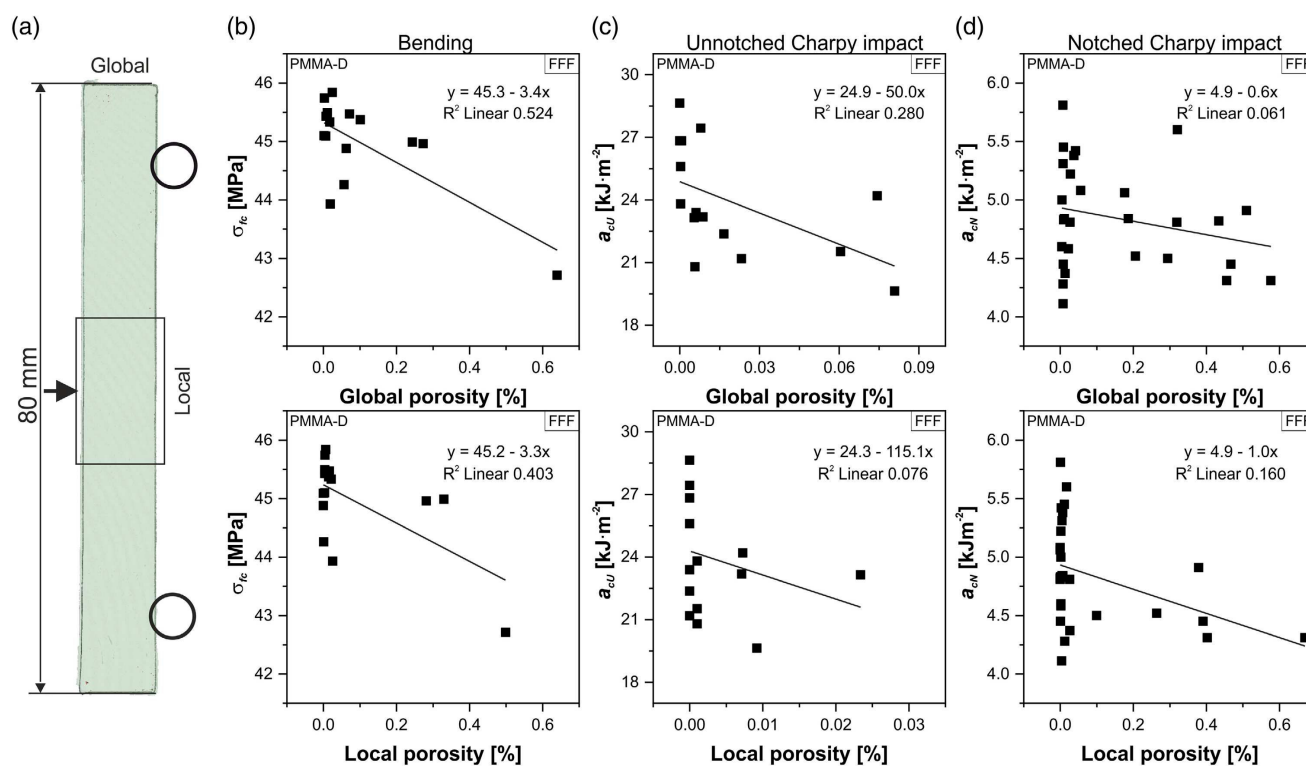


Figure 5. a) Definition of global and local porosity with an image of the 3D reconstructed model of a representative specimen. Porosity levels of PMMA-D in FFF evaluated for the whole sample (global) or at the midsection of the part (local) in correlation with the results of the mechanical tests: b) the flexural stress at the conventional deflection, σ_{fc} , c) the unnotched Charpy impact strength, a_{cU} , and d) the notched Charpy impact strength a_{cN} . The correlation was assessed with Spearman’s rank correlation coefficient independently of the test group.

samples with the most divergent global and local (midsection) porosity levels (Figure 6a). While there were remarkable

differences between the two groups in global and local porosity levels ($p = 0.016$ and $p = 0.056$, respectively), the impact strength

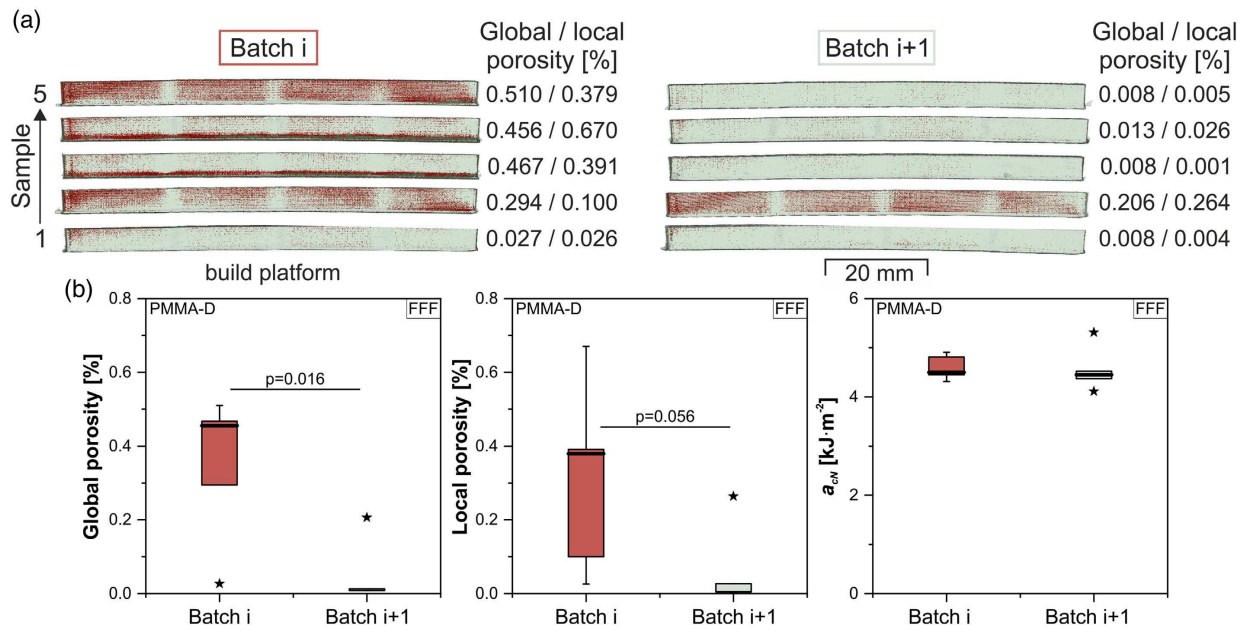


Figure 6. a) 3D models constructed from microcomputed tomography images of two consecutive batches, batch i and batch $i + 1$, printed with PMMA-D in FFF provided along with their global (overall) and local (mid-section) porosity. b) Comparison of their porosity levels (global and local) as well as mechanical performance in notched Charpy impact test. Stars show extreme outliers. The statistical significance of the differences was assessed with Mann–Whitney U Test. $n = 5$ per group.

values evaluated by the Charpy impact test were quite comparable (Figure 6b), suggesting that the observed porosity levels did not have any detectable influence on the mechanical performance.

Next, the porosity levels of the whole samples (global porosity) of randomly selected samples with or without a cleaning procedure were compared (Figure 7). The global porosity in the FFF-printed PMMA-D samples was comparable in all three groups ($\chi^2(2) = 2.880$; $p = 0.237$). In APF-printed samples, however, there was a statistically significant difference in the global porosity levels ($\chi^2(2) = 8.060$; $p = 0.018$). Pairwise comparison showed significantly different values between the washed and washed + sterilized samples ($p = 0.027$). Nevertheless, these differences did not show a detectable effect on the mechanical performance of the specimens (Figure 3 and 4b).

Next, focus was placed on the analyses of PMMA-D to investigate the decreased impact strength observed in FFF-manufactured PMMA-D specimens (Figure 4a), which was explained neither by a difference in porosity nor by a difference in fracture surface. For this purpose, tensile tests on thin compression-molded samples were conducted to check whether the cleaning treatments differentially influence the PMMA-D material itself. No differences in the stress–strain curves among the samples from different treatment groups were observed (Figure 8a). Moreover, the curves show pronounced yielding where the forces decrease after reaching a maximum while the deformation still increases which was accompanied with stress whitening (CM specimens were transparent before testing and opaque along the parallel length afterward). Stress whitening occurs as a color change at macroscale, which is caused by the formation of microvoids between polymer chains during deformation. Further increasing the deformation results

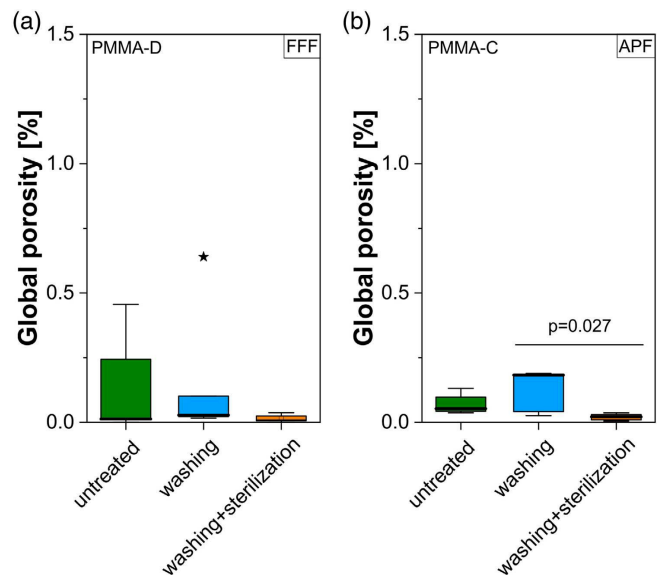


Figure 7. The global porosity of PMMA-D samples in a) FFF and PMMA-C samples in b) APF. The data is presented as the percentage of the internal gap volume of the specimen volume. The statistical significance of the differences was assessed using Kruskal–Wallis H test followed by a pairwise analysis with Bonferroni correction. $n = 5$ per group. Stars show extreme outliers.

in an opening of the voids and therefore microcracks and crazes, causing a dispersion of visible light.^[30] The alignment of the polymer chains in the direction of the load leads to a strengthening of the material and thus to a further increase in the force, which is known as cold drawing (Figure 8a). Statistically significant

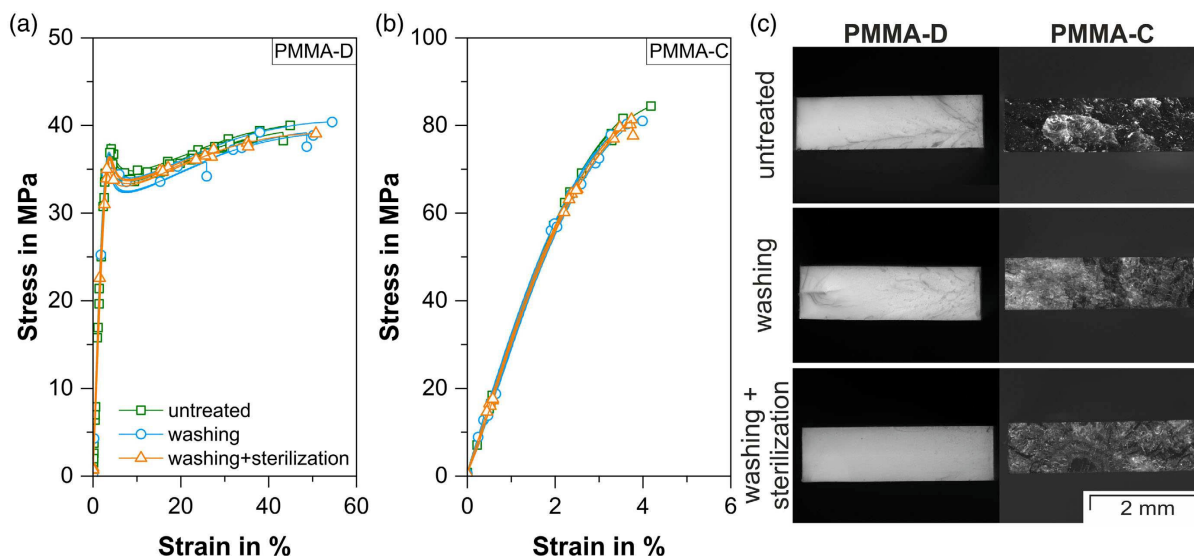


Figure 8. a) Stress–strain curves and b) yield stress (σ_y) obtained for compression-molded PMMA-D in its untreated state, after washing and after washing+sterilization. In c) microscopic images of the representative fracture surfaces for each group after tensile testing are displayed. The statistical significance of the differences was assessed using Kruskal–Wallis H test followed by pairwise analysis with Bonferroni correction. $n = 5$ per group. Stars show extreme outliers.

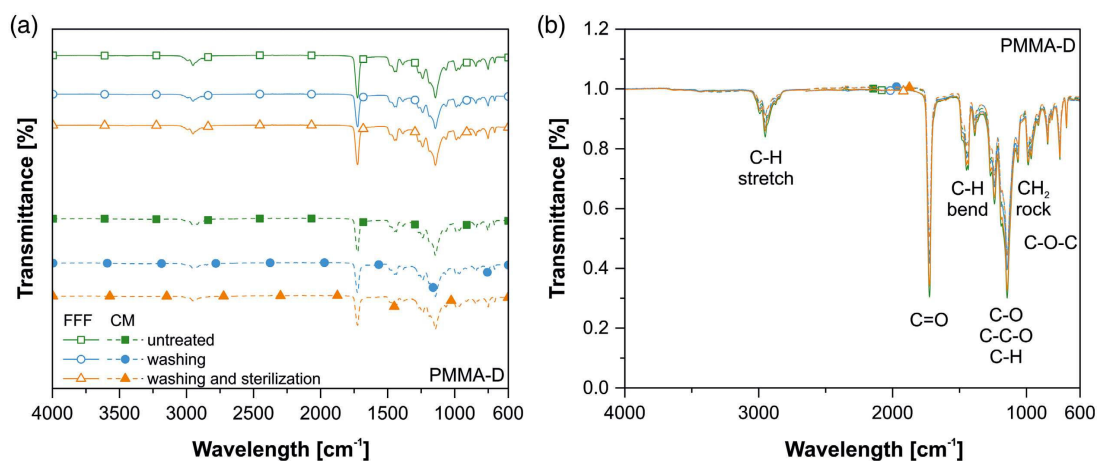


Figure 9. FTIR spectra for PMMA-D manufactured by FFF and CM in its untreated state, after washing, and after washing + sterilization. $n = 3$ per group. In a) the spectra are vertically shifted against each other to better identify the individual spectra. In b) the spectra are shown as measured with the characteristic bands.

decreases in the yield stress (σ_y) were observed among different groups ($\chi^2(2) = 7.340$; $p = 0.025$) (Figure 8b). Pairwise comparisons revealed significantly lower yield stress in washed + sterilized samples ($p = 0.04$) compared with the untreated controls. The differences between the washed and untreated controls, however, were not significant ($p = 0.085$). The fracture surfaces after tensile testing, on the other hand, were indifferent under a light microscope (Figure 8c).

FTIR spectra for FFF as well as CM samples after the different treatments are shown in Figure 9. No major change in the chemical structure of the material or media uptake was observed, as the bands seem to be unaffected. The evaluated spectra are in accordance to literature showing all characteristic bands^[31]: 1) the α -methyl, ester-methyl, and methylene C–H stretching

(3100–2800 cm^{-1}) and bending (1500–1350 cm^{-1}) modes; 2) the C=O stretching mode (1728 cm^{-1}); 3) the ester group stretching vibrations or coupled C–O and antisymmetric C–C–O stretch as well as skeletal vibrations coupled to C–H deformations in the range of 1350–1100 cm^{-1} ; 4) the methylene rocking mode at 843 cm^{-1} ; and 5) the vibrations of the ester group, possibly the C–O–C symmetric stretching mode at 827 and 809 cm^{-1} .

Seeing that attenuated total reflection measurements only characterize the first few micrometers of a material, and no traces of any different media were found in the spectra, it appears unlikely that the used agents penetrate the material at all.

In a final step, SEM images of representative fracture surfaces of unnotched PMMA-D FFF Charpy samples were compared for

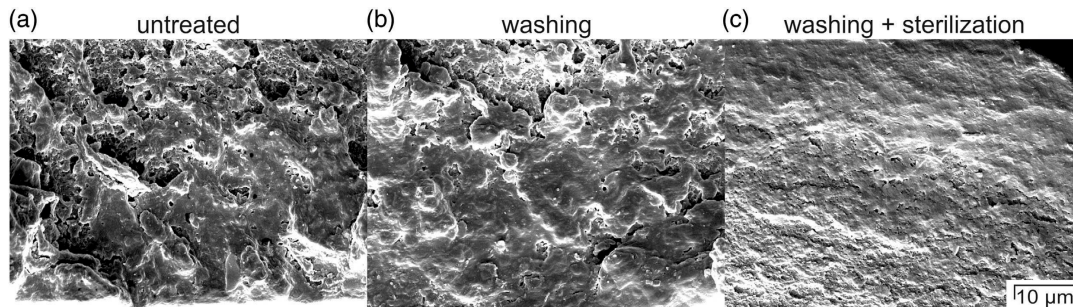


Figure 10. SEM images of PMMA-D in FFF in its a) untreated state, b) after washing, and c) after washing + sterilization. A predefined border region at the side of the build platform was analyzed.

each treatment step (Figure 10). The images were taken at a predefined border region of the sample, as mainly the outer regions should be affected by the treatments. It is observed that the fracture surfaces of the untreated and washed samples look alike (Figure 10a,b), while the fracture surface appears smoother after sterilization (Figure 10c). This finding does not match the Charpy impact strength results in Figure 4a, where only washed samples have significantly lower values compared with the other treatment steps. Nevertheless, the slightly different fracture surfaces should not be overestimated, as during the SEM procedure the sample is only recorded very locally. Similar brittle fracture surfaces were found for FFF PMMA in previous works.^[5,32] Moreover, it is not yet clear whether the differences found are related to the treatment or the print quality. Therefore, the future implementation of a study on the reproducibility of the printing process is recommended.

4. Discussion

Although PMMA-based materials have long been used for medical products such as implants, it seems that no study has yet been conducted analyzing the effects of a combination of washing and formaldehyde sterilization on the mechanical properties. Munker et al.^[10] analyzed the effect of different sterilization methods (ethylene oxide, hydrogen peroxide gas plasma treatments, autoclave sterilization, and γ -irradiation) on the mechanical properties of PMMA-based materials. Whilst autoclave sterilization is not a choice for thermolabile materials like PMMA, the other three methods seem to be suitable candidates, with γ -irradiation resulting in increased flexural strength. Yavuz et al.^[9] investigated the influence of sterilization via supercritical carbon dioxide, ultraviolet, heat, ethylene oxide, and hydrogen peroxide on the chemical structure and surface morphology of PMMA microchips. The chemical techniques slightly affected the surface roughness and channel profile. This effect was even more dominant for ultraviolet sterilization. On the other hand, opaque structures were observed after heat sterilization. Sharifi et al.^[12] showed that electron beam sterilization of PMMA with the right energy dose only slightly affects the chemical, mechanical, and optical properties as well as biocompatibility. As stated by McKeen,^[23] the mechanical properties, such as elongation at break and notched Izod impact, of CYROLITE compounds do not

significantly decrease after gamma radiation at exposures of up to 7.5 Mrad or electron beam exposures up to 7.5 kGy. Moreover, by ethylene oxide sterilization, no significant change in key properties or yellowing takes place. Steam sterilization and dry heat sterilization, on the other hand, are not recommended.

None of the previous studies included the preceding hygiene process, which works with elevated temperatures, pressures, and the addition of a washing agent. Given that PMMA has hygroscopic characteristics,^[19,20] both treatment steps could influence the material itself, but also the structure created by the AM process. Therefore, this study deals with the characterization of the effects of a predefined washing and sterilization routine on the porosity and mechanical properties of additively manufactured parts. Two different PMMA-based materials (PMMA-D: 3Diakon and PMMA-C: CYROLITE MD H12), each optimized for a different AM method (FFF and APF), were analyzed. Washing and formaldehyde sterilization did not influence the flexural modulus at the bending tests in FFF- or APF-printed specimens. In the Charpy impact tests with unnotched specimens, however, remarkably lower impact strengths were observed in the washed group, although the differences were significant only in the FFF-printed PMMA-D samples. As a confounding influence of differential porosity levels was strictly ruled out, the effect was attributable to the cleaning procedure. Samples that were sterilized after washing, however, did not show such a difference, suggesting that the sterilization procedure neutralized the effect introduced by washing. Although, material aging was shown to be induced by prolonged (12–24 months) immersion in water,^[20] it may well be accelerated by water exposure at higher temperatures (60 °C in washing process) followed by water desorption at 80 °C and 60 °C. However, whether this absorption/desorption stress is responsible for reduced impact strength in washed samples is questionable on the grounds that such an effect was not observed when the washing protocol was followed by a sterilization procedure. One major difference between the washing and sterilization procedure is that drying phases after sterilization were conducted under vacuum (alternating between 90 and 210 mbar compared with ≈ 1 bar after washing), which presumably results in a better desorption, particularly considering the porous structure of the printed samples. The fact that such an effect was not detected in impact tests with notched samples indicated that the influence, if any, should rather be effective at a limited depth. Nevertheless,

given that the impact tests were conducted after >48 h of storage at standardized climate (23 °C, 50% r.h.), associating the reduction in impact strength to the residual moisture at the time of testing would be highly unlikely. Comparability of flexural moduli among the groups and identical peak profiles of FTIR spectra further supported this presumption.

Regardless of the evaluation method (global or local), porosity values of less than 1% were measured for all samples. These values are very low in terms of the FFF process, considering that values of up to about 6% have been reported in the literature.^[21,33] In general, the porosity of a printed part is strongly influenced by the material used and the processing parameters, such as the nozzle temperature, build platform temperature, and printing speed.^[34,35] Varying printing qualities were observed in our samples among different batches, but also within one batch. The batch-wise difference could be the result of a minimal lower nozzle temperature, which leads to worsened diffusion between adjacent layers, larger voids, and therefore lower mechanical properties.^[35] Differences within the batch are mostly attributable to the uneven temperature distribution on the print bed.^[36] In addition, the interdiffusion depth decreases and thus the pore size increases the further away the layer is from the print bed.^[34] Several researchers analyzed the effect of different pore sizes and porosity values on the mechanical properties of printed parts. In general, they found increasing mechanical properties with decreasing porosity values.^[37–40] However, the analyzed porosity values in these studies deviated from each other by more than 5%, whereas the porosity values of all samples in this study are less than 1% (on average ≈0.18% for PMMA-D in FFF and 0.07% for PMMA-C in APF). In a previous study, conducted with another type of PMMA, a porosity value of 0.09% could be obtained for FFF-printed samples.^[32] The porosity values from this and the previous study are both very low and the results indicated that the observed porosity levels were below the critical point and did not influence the mechanical properties.

Tensile tests on thin compression-molded samples, where the material is distributed more homogeneously and the thickness of the specimens allows for better identification of surface influences through the treatments, indicated that the influence of cleaning treatments on the obtained stress–strain curves was negligible, apart from a slight but significant reduction in the yield stress. FTIR spectroscopy ruled out any detectable change in the chemical structure as well as presence of residual media in both printed and compression-molded material after washing and formaldehyde sterilization procedures. These results complement previous studies, in which sterilization by ethylene oxide, UV, heat, CO₂, or hydrogen peroxide treatments also did not result in any major change in the chemical structure.^[9]

Comparison of the fracture surfaces in predefined border areas of the samples allows the detection of the presence of diffused media, as media-induced changes in fracture behavior are often accompanied by changes in the fracture surface.^[41] However, scanning electron microscope analyses in our study did not show detectable differences among differentially treated samples, which can explain differences observed in mechanical tests. Nonetheless, variances in interlayer strength or diffusion depth, which can be caused by slight temperature fluctuations,^[35] cannot be evaluated with the applied methods. To maintain a proper environmental temperature and thus maximize the

temperature homogeneity in the printed parts, printers with closed chambers are to be preferred. At this point, it remains unclear whether the reason for changes in the Charpy impact strength lies in the treatment step or varying printing quality. Therefore, it is recommended to perform a reproducibility study of the printing process in the future.

5. Conclusion

Each sterilization method has advantages and disadvantages. As there is no method specified for a certain combination of material and process, the influence of washing and sterilization must be thoroughly analyzed for each new material–process combination before use.

In this study, the influence of formaldehyde sterilization and the preceding washing procedure did not show a significant influence on the bending properties of two different PMMA-based materials, each optimized for a different AM method (FFF and APF). However, significantly lower Charpy impact strengths were observed after washing in the FFF-printed samples. Any confounding influence of variabilities in specimen porosity was excluded. Observed porosity levels (less than 1%) were not found to have any correlation to the mechanical performance. Therefore, the effect was attributable to the cleaning procedure, but was neutralized after sterilization.

No reason was found not to use the applied sterilization routine for the analyzed PMMA-based materials. However, further tests should be conducted, such as the performance of cytotoxicity tests and repeatability/reproducibility tests of the printing process, before using this routine prior to real application.

Acknowledgements

This work was supported by the project CAMEd (COMET K-Project 871132) funded by the Austrian Federal Ministry of Transport, Innovation and Technology (BMVIT) and the Austrian Federal Ministry for Digital and Economic Affairs (BMDW) and the Styrian Business Promotion Agency (SFG). The authors would like to thank project partners HAGE3D GmbH, ARBURG GmbH + Co KG, and Mitsubishi Chemical Advanced Materials Inc. for providing either their AM devices or material. The authors would like to thank the company Roehm GmbH for their material supply, Philipp Huber for his support during the manufacturing of certain samples, and Markus Schwaiger for performing the infrared spectroscopy.

Conflict of Interest

HAGE3D GmbH and ARBURG GmbH + Co KG are project partners in COMET K-Project 871 132 and provided devices for additive manufacturing. Mitsubishi Chemical Advanced Materials Inc. is also a project partner in the COMET K-Project 871 132 and provided the 3Diakon material.

Data Availability Statement

The data that support the findings of this study are available from the corresponding author upon reasonable request.

Keywords

ARBURG plastic freeforming, fused filament fabrication, mechanical properties, PMMA, washing and formaldehyde sterilization

Received: February 14, 2022

Revised: April 14, 2022

Published online:

- [1] M. Katschnig, F. Arbeiter, B. Haar, G. van Campe, C. Holzer, *Adv. Eng. Mater.* **2017**, *19*, 1600676.
- [2] C. Basgul, T. Yu, D. W. MacDonald, R. Siskey, M. Marcolongo, S. M. Kurtz, *J. Mater. Res.* **2018**, *33*, 2040.
- [3] X. Han, N. Sharma, Z. Xu, L. Scheideler, J. Geis-Gerstorfer, F. Rupp, F. M. Thieringer, S. Spintzyk, *J. Clin. Med.* **2019**, *8*, 771.
- [4] L. Hentschel, F. Kynast, S. Petersmann, C. Holzer, J. Gonzalez-Gutierrez, *Polymers* **2020**, *12*, 2677.
- [5] S. Petersmann, M. Spoerk, P. Huber, M. Lang, G. Pinter, F. Arbeiter, *Macromol. Mater. Eng.* **2019**, *304*, 1900263.
- [6] T. Seul, S. Roth, *Kunststoffe in der Medizintechnik: Vorschriften und Regularien, Produktrealisierung, Herstellungsprozesse, Qualifizierungs- und Validierungsstrategien*, Hanser, München **2020**.
- [7] S. W. Shalaby, S. D. Nagatomi, E. F. Powell, in *Biotextiles As Medical Implants*; (Eds: M. W. King, B. S. Gupta, R. Guidoin), The Textile Institute; Woodhead Publishing: Manchester, UK; Oxford, **2013**; no. 133, pp 157–168.
- [8] N. P. Tipnis, D. J. Burgess, *Int. J. Pharm.* **2018**, *544*, 455.
- [9] C. Yavuz, S. N. B. Oliaei, B. Cetin, O. Yesil-Celiktas, *J. Supercrit. Fluids* **2016**, *107*, 114.
- [10] T. J. A. G. Münker, S. E. C. M. van de Vijfeijken, C. S. Mulder, V. Vespasiano, A. G. Becking, C. J. Kleverlaan, L. Dubois, L. H. E. Karssemakers, D. M. J. Milstein, P. R. A. M. Depauw, F. W. A. Hoefnagels, W. P. Vandertop, T. J. J. Maal, E. Nout, M. Riool, S. A. J. Zaat, *J. Mech. Behav. Biomed. Mater.* **2018**, *81*, 168.
- [11] J. Shaw, J. Gary, A. Baker, H. Kaplan, Y. Kim, M. Milhoan, A. Burgess, C. Ambrose, *J. Orthop. Trauma* **2020**, *34*, e109.
- [12] S. Sharifi, M. M. Islam, H. Sharifi, R. Islam, T. N. Huq, P. H. Nilsson, T. E. Mollnes, K. D. Tran, C. Patzer, C. H. Dohlman, H. K. Patra, E. I. Paschalis, M. Gonzalez-Andrades, J. Chodosh, *Macromol. Biosci.* **2021**, e2000379.
- [13] P. Trencart, Y. A. Elce, E. Rodriguez Batista, G. Michaud, *Vet. Comp. Orthop. Traumatol.* **2014**, *27*, 97.
- [14] S. J. Barton, P. J. S. Foot, P. C. M. Tate, M. Kishi, B. Ghatora, *Polym. Polym. Compos.* **2013**, *21*, 1.
- [15] J. H. Park, R. Olivares-Navarrete, R. E. Baier, A. E. Meyer, R. Tannenbaum, B. D. Boyan, Z. Schwartz, *Acta Biomater.* **2012**, *8*, 1966.
- [16] PAHO, <https://www.paho.org/hq/dmdocuments/2017/who-Decontaminationandprocessingofmedicaldevicesforhealthcare-facilities>; <https://www.paho.org> (accessed: April 2021).
- [17] A. A. Abdel-Wahab, S. Ataya, V. V. Silberschmidt, *Polym. Test.* **2017**, *58*, 86.
- [18] A. Aulova, A. Oseli, M. Bek, T. Prodan, I. Emri, in *Encyclopedia of Continuum Mechanics* (Eds: H. Altenbach, A. Öchsner), Springer Berlin Heidelberg; Imprint: Springer, Berlin, Heidelberg **2020**, pp. 1–14.
- [19] *Kunststoff-Lexikon* (Ed: W. Woebcken), Hanser, München, Wien **1998**.
- [20] M. N'Diaye, F. Pascaretti-Grizon, P. Massin, M. F. Baslé, D. Chappard, *Langmuir* **2012**, *28*, 11609.
- [21] E. D. Avila, J. Eo, J. Kim, N. P. Kim, *MATEC Web Conf.* **2019**, *264*, 2001.
- [22] X. Wang, L. Zhao, J. Y. H. Fuh, H. P. Lee, *Polymers* **2019**, *11*, 1154.
- [23] L. McKeen, *The Effects of Sterilization Methods on Plastics and Elastomers*, William Andrew Pub, Norwich, NY **2012**.
- [24] Roehm GmbH., Cyrolite Data Sheet, <https://www.cyrolite.com/> (accessed: October 2021).
- [25] A. Fedorov, R. Beichel, J. Kalpathy-Cramer, J. Finet, J.-C. Fillion-Robin, S. Pujol, C. Bauer, D. Jennings, F. Fennessy, M. Sonka, J. Buatti, S. Aylward, J. V. Miller, S. Pieper, R. Kikinis, *Magn. Reson. Imaging* **2012**, *30*, 1323.
- [26] *Kunststoffprüfung* (Ed: W. Grellmann), Hanser, München **2011**.
- [27] J. J. Schmidt, J. A. Gardella, L. Salvati, *Macromolecules* **1989**, *22*, 4489.
- [28] MCPN Netherlands BV., Datasheet 3Diakon, <https://mcpn-3dp.com/3diakon/> (accessed: October 2021).
- [29] G. Hsiang Loh, E. Pei, J. Gonzalez-Gutierrez, M. Monzón, *Appl. Sci.* **2020**, *10*, 4776.
- [30] W. Grellmann, S. Seidler, *Deformation and Fracture Behaviour of Polymers*, Springer Berlin Heidelberg, Berlin, Heidelberg **2001**.
- [31] S. Sain, D. Ray, A. Mukhopadhyay, S. Sengupta, T. Kar, C. J. Ennis, P. K. S. M. Rahman, *J. Appl. Polym. Sci.* **2012**, *126*, E127.
- [32] S. Petersmann, M. Spoerk, W. van de Steene, M. Üçal, J. Wiener, G. Pinter, F. Arbeiter, *J. Mech. Behav. Biomed. Mater.* **2020**, *104*, 103611.
- [33] H. Nouri, S. Guessasma, S. Belhabib, *J. Mater. Process. Technol.* **2016**, *234*, 113.
- [34] Y. Tao, F. Kong, Z. Li, J. Zhang, X. Zhao, Q. Yin, D. Xing, P. Li, *J. Mater. Res. Technol.* **2021**, *15*, 4860.
- [35] M. Spoerk, F. Arbeiter, H. Cajner, J. Sapkota, C. Holzer, *J. Appl. Polym. Sci.* **2017**, *134*, 45401.
- [36] M. Sgrulletti, M. Bragaglia, S. Giarnetti, L. Paleari, F. Nanni, *Mater. Today Commun.* **2021**, *28*, 102679.
- [37] J. Brackett, D. Cauthen, J. Condon, T. Smith, N. Gallego, V. Kunc, C. Duty, *Proc. of the 30th Annual International Solid Freeform Fabrication Symposium—An Additive Manufacturing Conf.*, TX, USA **2019**.
- [38] Y. Liao, C. Liu, B. Coppola, G. Barra, L. Di Maio, L. Incarnato, K. Lafdi, *Polymers* **2019**, *11*.
- [39] E. H. Anderson, Master Thesis, San José State University **2019**.
- [40] M. Fernandez-Vicente, W. Calle, S. Ferrandiz, A. Conejero, *3D Print. Addit. Manuf.* **2016**, *3*, 183.
- [41] J. C. Arnold, *J. Mater. Sci.* **1998**, *33*, 5193.

Publication 3

Bibliographic information

Title: Process-induced morphological features in material extrusion-based additive manufacturing of polypropylene

Authors: Sandra Petersmann¹, Petra Spoerk-Erdely², Michael Feuchter¹, Tom Wieme³, Florian Arbeiter^{1,*}, Martin Spoerk^{4,+}

Affiliations:

¹Materials Science and Testing of Polymers, Montanuniversitaet Leoben, Otto Gloeckel-Straße 2, 8700, Leoben, Austria

²Department Materials Science, Montanuniversitaet Leoben, Franz Josef-Straße 18, 8700, Leoben, Austria

³Centre for Polymer and Material Technologies, Department of Materials, Textiles and Chemical Engineering, Ghent University, Technologiepark 130, 9052, Zwijnaarde, Belgium

⁴Polymer Processing, Montanuniversitaet Leoben, Otto Gloeckel-Straße 2, 8700, Leoben, Austria

+Present address: Research Center Pharmaceutical Engineering, Inffeldgasse 13, 8010, Graz, Austria.

Periodical: Additive Manufacturing

DOI: <https://doi.org/10.1016/j.addma.2020.101384>

Relevant contributions to this publication:

Conceptualisation: Sandra Petersmann, Petra Spoerk-Erdely, Martin Spoerk

Methodology: Sandra Petersmann, Petra Spoerk-Erdely, Martin Spoerk

Validation: Sandra Petersmann, Petra Spoerk-Erdely, Tom Wieme, Martin Spoerk

Formal analysis: Sandra Petersmann

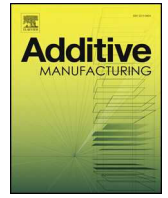
Data Curation: Sandra Petersmann, Petra Spoerk-Erdely, Michael Feuchter, Tom Wieme

Writing - Original Draft: Sandra Petersmann, Petra Spoerk-Erdely, Michael Feuchter, Tom Wieme, Florian Arbeiter, Martin Spoerk

Writing - Review & Editing: Sandra Petersmann, Petra Spoerk-Erdely, Michael Feuchter, Tom Wieme, Florian Arbeiter, Martin Spoerk

Visualisation: Sandra Petersmann, Martin Spoerk

Project administration: Funding acquisition: Michael Feuchter



Research Paper

Process-induced morphological features in material extrusion-based additive manufacturing of polypropylene

Sandra Petersmann^a, Petra Spoerk-Erdely^b, Michael Feuchter^a, Tom Wieme^c, Florian Arbeiter^{a,*}, Martin Spoerk^{d,1}^a Materials Science and Testing of Polymers, Montanuniversitaet Leoben, Otto Gloeckel-Straße 2, 8700, Leoben, Austria^b Department Materials Science, Montanuniversitaet Leoben, Franz Josef-Straße 18, 8700, Leoben, Austria^c Centre for Polymer and Material Technologies, Department of Materials, Textiles and Chemical Engineering, Ghent University, Technologiepark 130, 9052, Zwijnaarde, Belgium^d Polymer Processing, Montanuniversitaet Leoben, Otto Gloeckel-Straße 2, 8700, Leoben, Austria

ARTICLE INFO

Keywords:

Polypropylene
Fused filament fabrication
Morphology
Crystallography
Mechanical property

ABSTRACT

Fused filament fabrication is a material extrusion-based additive manufacturing technique that has been strongly growing in popularity, for it is accessible, versatile, and affordable. The 3D-printing of semi-crystalline polymers still faces major challenges, though. Apart from common issues such as shrinkage and warpage phenomena, a variety of process-related morphological and crystallographic changes can occur. Since these changes strongly influence the resulting material properties, it is crucial to understand the complex relationships between the material, its processing and final properties on a fundamental level. In this context, the present work examines the impact of different nozzle temperatures and printing speeds on 3D-printed polypropylene (PP) samples. One extreme parameter set (high nozzle temperature, low printing speed) reveals a homogeneous morphology, weak flow-induced orientations, isotropic thermal conductivities and a strong inter-layer diffusion. In contrast, the other extreme parameter set (low nozzle temperature, high printing speed) forms an inhomogeneous morphology with a complex growth of shish-kebab structures, a pronounced weld line morphology and a highly anisotropic behaviour. By in-depth analyses of four parameter sets, this paper offers novel insights into the complex formation of crystalline structures in 3D-printed semi-crystalline polymers and suggests how to purposefully design the property portfolio of these materials.

1. Introduction

Semi-crystalline polymers are processed by numerous methods including injection moulding, film blowing and, since recently, also additive manufacturing (AM). Regarding these manufacturing methods, the importance of AM techniques has been continuously increasing, since they offer a variety of advantages, such as high freedom of design, reduced numbers of process steps and simplified supply chains [1]. Especially material extrusion-based AM methods are gaining popularity as a result of their relatively easy handling and affordability. Among these methods, the filament-based process fused filament fabrication (FFF) is widely spread. During the FFF process, a thermoplastic filament is selectively transported through a heated nozzle onto a build platform. Thereby, the nozzle follows a pre-defined computer-generated path, and the object is fabricated in a layer-by-layer manner [1–5]. Manifold

materials have been commercialised for the use in FFF, and an even larger number has been under investigation recently [6]. In particular, amorphous thermoplastics or semi-crystalline materials that crystallise slowly, e.g. poly(lactic acid) (PLA), have been used extensively to investigate material properties in connection with FFF [7–10]. However, for 3D-printed semi-crystalline polymers, which reveal more complex crystallisation kinetics, such as polypropylene (PP) or poly(oxymethylene), many fundamental phenomena known from traditional manufacturing techniques (e.g. the formation of flow-induced oriented spherulites [11–13], the nucleation and growth conditions for the metastable β crystal modification [14] or the morphology of weld lines [15,16]) have hardly been understood. As a result, such semi-crystalline polymers still remain difficult to 3D-print [9].

Apart from shrinkage and warpage issues caused by the high degree of crystallinity of the material [6], the morphology and crystallography

* Corresponding author.

E-mail address: florian.arbeiter@unileoben.ac.at (F. Arbeiter).¹ Present address: Research Center Pharmaceutical Engineering, Inffeldgasse 13, 8010, Graz, Austria.

of 3D-printed semi-crystalline polymers were shown to be highly complex. In particular, X-ray scattering techniques used to monitor crystallographic changes during processing [17], recently opened the door to fundamentally understand these complex phenomena. For example, it was shown that the degree of crystallinity can vary within a single 3D-printed part: For print patterns with high heat retentions [18] or at regions such as corners, where the printing speed is lower [19], crystallisation can occur during elongated periods, resulting in an elevated degree of crystallinity. In addition, the crystalline morphology of 3D-printed PP was found to vary greatly within a single deposited strand. Two individual studies recently revealed that the bulk of the 3D-printed PP strand shows a significantly higher degree of crystallinity than the vicinity of the interfaces [19,20], which in turn can positively affect the diffusion length of adjacent layers due to partial melting of the strand interface.

Additionally, the morphology of additively manufactured semi-crystalline polymers is critically influenced by even small changes in process parameters [6], which can complicate the processability of these promising materials. For example, the temperature of the 3D-printed strands, which is strongly influenced by the complex temperature distribution within the 3D-printer, determines the nucleation and growth of the spherulites, but also the type of crystal modification that is formed [21]. PP specimens prepared with a nozzle temperature of 200 °C, for instance, showed a mixture of α (monoclinic [22]) and β (hexagonal [22]) crystals, whereas an increase of the nozzle temperature of 50 °C resulted in only the α modification [21,23]. This led to significantly different mechanical properties due to the different morphologies of the α and β modifications. Similar alterations in the crystal modification as well as significant changes in the spherulite size of 3D-printed PP were further observed for an increase in the chamber temperature of only 30 °C [21].

Depending on the process settings, also the weld lines of additively manufactured semi-crystalline polymers can vary greatly. For prints undertaken at room temperature, both PLA and PP [19–21,24] exhibit a variety of different degrees of crystallinity, spherulite sizes, orientations and growth directions. These differences are a result of the large temperature differences between the freshly deposited and the previously deposited adjacent strand, and the fast cooling rates of freshly deposited strands [15]. For such process settings, Cole et al. [25] found that the chemical composition of the strand interface of printed acrylonitrile butadiene styrene (ABS) can vary by up to 40 % compared to the bulk strand material. As soon as the temperature differences are reduced, e.g. by increasing the build platform temperature or the chamber temperature, a rather homogeneous strand morphology with hardly detectable weld lines can be formed [24].

For semi-crystalline polymers, the naturally occurring rapid movements of the printer head and the desired fast printing speeds can additionally result in complex elongation and/or shear flow fields acting on the polymer melt already in the nozzle [27], which in turn introduces different degrees of anisotropy and elongated crystals [12,26]. Such flow-induced orientations were observed in strands as shish-kebab structures [20,21,28], that are composed of fibrillar crystalline structures (shish) with lamellae radially growing outwards (kebabs) [13]. By using in-situ X-ray scattering on 3D-printed PP, these shish-kebab structures were recently identified to nucleate at the surface of the freshly deposited strand and propagate inward towards the core of the strand [20]. In the case of unfilled 3D-printed PP such flow-induced orientations augment the alignment of anisotropic PP spherulites, leading to anisotropic thermal conductivities [23]. Such studies enable a basic understanding of the formation of flow-induced oriented spherulites during FFF. However, the consequences of changes in standard printing parameters, such as the printing speed or the nozzle temperature, on the degree of orientation of the spherulites in the strand or in the strand interface and on the occurring crystal modifications have not been investigated yet.

The present manuscript aims at closing this gap by providing

qualitative and quantitative information on the impact of different technologically relevant process parameters on the crystallisation morphology of 3D-printed PP. The drastic differences in the degree of orientation, the prevalence of different crystal modifications, spherulite sizes and strand interfaces found for minor changes in the printing speed and the nozzle temperature, and their effect on macroscopic properties of 3D-printed components, illustrate the significance of a fundamental understanding of the material in correlation with the complex process.

2. Material and methods

2.1. Materials

PP heterophasic copolymer pellets (Borealis AG, Austria) with a melting temperature (T_m) of 166 °C and a melt flow rate (230 °C/2.16 kg) of 5 g/10 min were used throughout the present manuscript. Basic mechanical properties of this material include a flexural modulus of 950 MPa, a tensile strain at break of 700 %, a tensile strength of 50 MPa and a tensile modulus of 590 MPa.

2.2. Processing of the 3D-printed specimens

The PP pellets were processed to filaments with a diameter of 1.75 ± 0.05 mm (Sikora Laser 2010 T diameter measurement device, Sikora AG, Germany) in the single screw extruder FT-E20T-MP-IS (Dr. Collin GmbH, Germany) by employing the following settings: temperature of the extruder barrels = 175–185 °C, screw speed = 30 rpm, die diameter = 1.9 mm. The extrudate was cooled by a water bath, pulled/spooled by a self-developed winding unit and stored on a spool under standardised conditions (23 °C air temperature, 50 % relative humidity) for at least 72 h prior to the 3D-printing trials.

Two specimen geometries, namely bar-shaped specimens according to the standard EN ISO 20753:2018–11 Type B and square-shaped samples with suitable dimensions for thermal conductivity measurements according to the standard ISO 22007–2 (Fig. 1), were sliced in the software Simplify3D Version 3.0 (Simplify3D, USA) and processed in a Duplicator i3 v2 (Wanhao, China) with the printing parameters summarised in Table 1. As displayed in Fig. 1, the standard alternating printing sequence of the slicer software was used. For the bar-shaped geometry (Fig. 1a), two specimens were processed per printing cycle, whereas for the thermal conductivity specimens (Fig. 1b) one specimen was fabricated per print. In total, 10 specimens were fabricated per specimen geometry. In order to obtain different degrees of orientation, the most influential process parameters, namely printing speed and nozzle temperature, were varied. Both test geometries were printed at the two extreme nozzle temperatures of 200 °C and 250 °C, since usually PP is reported to be 3D-printed around 230 °C [6]. As the melt strength was significantly lower at 200 °C [29], the fast printing speed (22.5 mm/s) was selected at this printing temperature as the highest possible printing speed at which no melt fractures occurred in the nozzle. The slow printing speed (2.25 mm/s) was set at a tenth of the fast one to enable a study of distinct differences in the morphology and the mechanical properties between differently printed specimens. The four different print settings and their designations used throughout this manuscript are summarised in Table 2.

To minimise warpage and maximise the first layer adhesion during printing [6], a self-made PP build platform was employed and the printing speed of the first layer was reduced by 50 %, whilst welding to the PP-plate was avoided by keeping the first layer height to 0.1 mm [30,31]. After finalising each print, the specimens were detached from the build platform with a spatula and were stored under standardised conditions for at least 72 h. The subsequent characterisations were performed either directly on the completed 3D-printed specimens (XRD, trouser tear tests on the bar-shaped specimens (Fig. 1a), thermal conductivity on the thermal conductivity specimens (Fig. 1b)) or on

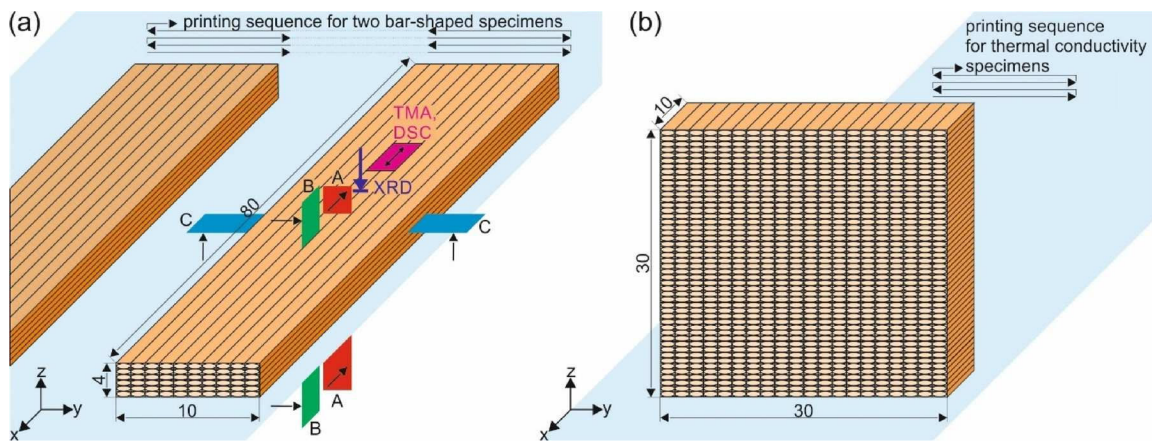


Fig. 1. Schematic representation of the 3D-printing orientation and sequence of the bar-shaped specimens (a) and the thermal conductivity specimens (b) (dimensions in mm). In (a), the approximate location of the cut samples for the thermo-mechanical analysis (TMA) and differential scanning calorimetry (DSC) are indicated in pink, and the direction of the X-ray beam (XRD) in dark blue. The location and orientation of the microtome cuts for the polarised optical microscopy analyses are specified by A (cross-sectional cut), B (inter-layer cut), and C (intra-layer cut).

Table 1

Summary of the printing parameters of all specimens.

Printing parameters	Levels
Nozzle temperature T_N (°C)	200, 250
Printing speed (mm/s)	22.5, 2.25
Printing speed of the first layer (% of the printing speed of subsequent layers)	50
Nozzle material	Steel
Nozzle diameter (mm)	0.6
Build platform material	PP-plate
Build platform temperature (°C)	110
Surrounding temperature (°C)	23
Layer thickness (mm)	0.25
First layer thickness (mm)	0.1
Infill pattern	Rectilinear
Infill density (%)	100
Infill angle (°)	0
Number of perimeters	0

Table 2

The four different print settings and sample designations.

Designation	Nozzle temperature in °C	Printing speed in mm/s
PP/200/22.5	200	22.5
PP/250/22.5	250	22.5
PP/200/2.25	200	2.25
PP/250/2.25	250	2.25

segments cut from the bar-shaped specimens (DSC, TMA, polarised optical microscopy (A, B, C)) according to Fig. 1a.

2.3. Polarised optical microscopy

Microtome sections were prepared by means of the Leica RM 2255 (Leica Microsystems GmbH, Germany) microtome. Thereby, cross-sectional, inter- and intra-layer samples were cut as shown in Fig. 1a. These microtome sections were subsequently put onto a glass slide and covered with a coverslip. In between the glass slide and the coverslip a drop of paraffinum liquidum with known refractive index was added. Polarised optical microscopy was performed on the Olympus BX51 (Olympus Life Science Europe GmbH, Germany) under transmitted light.

2.4. Wide-angle X-ray scattering (WAXS) measurements

Wide-angle X-ray scattering (WAXS) measurements were performed using a Bruker NanoStar (Bruker AXS, Germany). This system was equipped with a two-dimensional X-ray detector, an X-ray sensitive image plate ($50 \times 50 \mu\text{m}^2$) and the image analyser Typhoon FLA 7000 (Certified Genetool, Inc., US). Two SCATEX pinholes of $300 \mu\text{m}$ in diameter were utilised. The samples were measured in transmission mode with a wavelength of 0.154 nm ($\text{CuK}\alpha$) under vacuum. The exposure time was set to 900 s. The distance between the sample and the detector was 48.5 mm. For this configuration, the accessible diffraction angle (2θ) ranged from 5 to 50° . All specimens were aligned with their

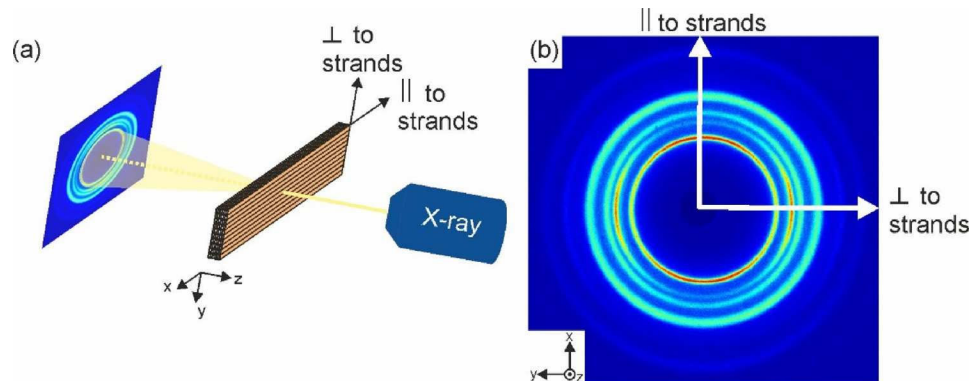


Fig. 2. The specimens were measured in transmission geometry (a). For further analysis, the obtained X-ray patterns were rotated by 90° in order to align the ordinate points in the direction of the strands (b).

strands oriented perpendicular to the impinging X-ray beam (Fig. 2). The obtained 2D WAXS patterns were corrected for transmission.

The 2D WAXS patterns were integrated with the aid of the software package Fit2D [32] using 1000 radial and 360 azimuthal bins. In each of the generated spread-sheets, each line hence corresponded to an intensity vs. Bragg angle (2θ) diffraction pattern for an azimuthal angle range of 1° . For the further analysis, several PP unit-cell reflections (α -110, β -300, α -040, α -130, etc.) in these patterns were fit using Gaussian peaks, simultaneously considering the background and amorphous scattering intensity. A custom-made Python script based on the lmfitt package was used for this purpose [33]. In this way, azimuthal intensity traces of these reflections could be generated to further quantify the orientation of the crystal planes [34].

For the evaluation of Hermans's orientation function, the direction parallel to the strands (azimuth angle of 90°) was selected as reference axis ($\chi = 0$). As proposed in [35,36], the intensity distributions $I_{hkl}(\chi)$ along the individual azimuthal traces were fit using Lorentzian functions. This allowed the calculation of Hermans's orientation factor f_H as

$$f_H = \frac{3\cos^2\chi - 1}{2},$$

in which χ represents the angle between the polymer chain segment and the reference axis. The orientation parameter $\cos^2\chi$ is given by

$$\cos^2\chi = \frac{\int_0^{\pi/2} (I_{hkl}(\chi) \cdot \cos^2\chi \cdot \sin\chi) d\chi}{\int_0^{\pi/2} (I_{hkl}(\chi) \cdot \sin\chi) d\chi}.$$

The Lorentzian fitting procedure thus enabled the analytical integration of these latter terms. The calculated values of Hermans's orientation function f_H were then used for the interpretation of the degree of orientation of the crystalline phases α and β , since $f_H = 0$ corresponds to random orientation, $f_H = 1$ to perfect alignment along the reference axis, and $f_H = -0.5$ to perfect alignment perpendicular to the reference axis.

The degree of crystallinity $X_{c,WAXS}$ in the specimens was estimated as the ratio between the summed intensities (integrated peak areas) I of the reflections of the crystalline phases α and β , and the total scatter intensity pertaining to both crystalline and amorphous fractions [37]:

$$X_{c,WAXS} = \frac{\sum I_{crystal}}{\sum I_{crystal} + \sum I_{amorphous}} \cdot 100\%.$$

Similarly, the relative amount of the β -phase K_β in the crystalline fraction was determined according to

$$K_\beta = \frac{I_{\beta-300}}{I_{\alpha-110} + I_{\alpha-040} + I_{\alpha-130} + I_{\beta-300}} \cdot 100\%,$$

as described in Ref. [38]. The influence of the orientation was attempted to be averaged out by summing over all azimuthal angle bins, and the results were critically compared with those obtained by means of differential scanning calorimetry (DSC).

2.5. Thermal analyses

DSC was carried out on the DSC 214 Polyma by NETZSCH (NETZSCH Group, Germany). Specimens of a mass of 14 ± 0.5 mg were cut out of the centre of the thermal conductivity samples. Each sample was placed in an aluminium Concavus® pan with pierced lid. The heat-cool-heat runs were conducted at a heating/cooling rate of 10 K/min in the temperature range of 20–210 °C under nitrogen atmosphere (20 mL/min nitrogen flow). The degree of crystallinity $X_{c,DSC}$ was calculated as

$$X_{c,DSC} = \frac{\Delta H}{\Delta H_0} \cdot 100\%,$$

in which ΔH is defined as the specific enthalpy of fusion of the semi-crystalline PP specimen determined from the peak area and ΔH_0 as the

heat of fusion of a fully crystalline PP [39], which was approximated as 176 J/g according to Li et al. [40].

Additionally, thermo-mechanical analyses (TMA) were performed on a TMA/SDTA841^e (Mettler-Toledo, USA) according to the standard ISO 11359-1:2014. The TMA specimens were cut from the standard bar-shaped test specimens according to Fig. 1a. The measurements were performed in the direction of the strands. A temperature region of 25–165 °C was covered with a heating rate of 5 K/min. The specimens were pre-loaded with 0.02 N. The coefficient of linear thermal expansion (CLTE) was evaluated as

$$CLTE = \frac{1}{L_0} \cdot \frac{dL}{dT},$$

in which L_0 is the initial length of the specimen and dL/dT the rate of change of the length per unit change in temperature [41].

2.6. Thermal conductivity

The axial and radial thermal conductivity were measured on 3D-printed PP plates (Fig. 1b) in the anisotropic double-sided mode according to the standard ISO 22007-2. The tests were performed on the thermal conductivity analyser TPS 2500 S with the Kapton sensor 5465 3.189 mm (both Hot Disk AB, Sweden) under standardised conditions. The measurement time was set to 40 s and the output power to 45 mW. The heat capacity tests were performed on the same equipment with the golden sensor 5501. The necessary density values were measured according to the standard ISO/FDIS 1183-1 in ethanol. The thermal conductivity values were evaluated in the software Hot Disk Thermal Constants Analyser 7.3 to a significance level of 5 %.

2.7. Trouser tear test

The trouser tear test specimens were manufactured exactly as the bar-shaped test specimens (as described in Section 2.2 and shown in Fig. 1a) except that the thickness was set to half of the standard value ($80 \times 10 \times 2$ mm³), as shown in Fig. 3a. Prior to testing, the specimens were split parallel to the long side up to the centre of the sample. Additionally, a razor-blade notch was introduced. The trouser tear tests were performed on the universal testing machine Zwick Z001 (Zwick Roell Gruppe, Germany) equipped with a 1 kN load cell. The testing speed was set to 10 mm/min. Pneumatic clamps (6 bar pressure) with serrated grip inserts were utilised. The clamping length was 20 mm. The direction of the loading is shown in Fig. 3b.

After testing, one representative sample of each setting was examined using an Olympus SZX12 (Olympus, Germany) stereo-microscope under reflected light.

3. Results and discussion

3.1. Polarised optical microscopy

In order to understand the consequences of the investigated printing speeds and T_N on the morphology of the 3D-printed PP specimens, polarised optical microscopy images from inter-layer, intra-layer and cross-sectional microtome cuts are discussed in the following paragraphs. Polarised optical microscopy images from inter-layer microtome cuts show spherulites varying in their size as well as oriented crystalline structures, which are formed at the strand interfaces and propagate towards the core of the strand (Fig. 4). For PP/200/22.5, additionally shish-kebab structures within the strands are detected (Fig. 4a). As represented in Fig. 5, these developed shish-kebab structures reveal a distinctly different morphology due to the fast welding process.

For the higher nozzle temperature of 250 °C (Fig. 4b), no shish-kebab structures in the core are found, whereas the weld line appears to be similarly pronounced as in Fig. 4a. Interestingly, alternating

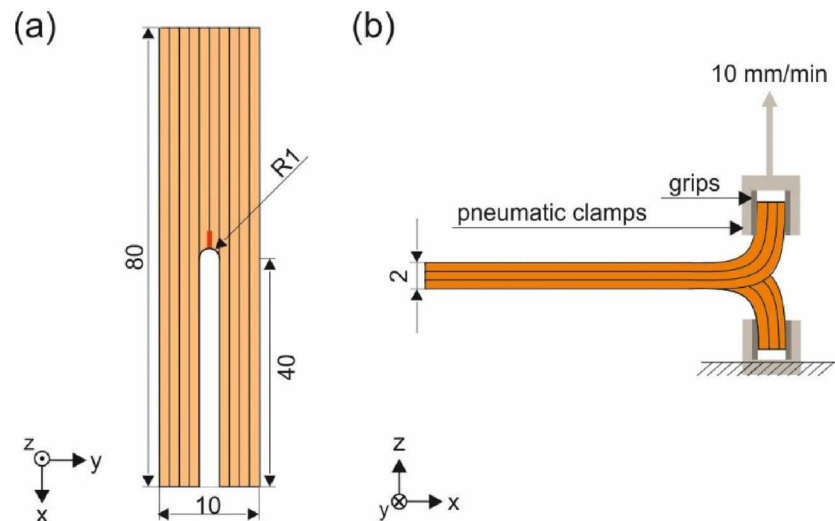


Fig. 3. Dimensions of trouser tear test specimens (a) and schematic representation of load application during testing (b). The introduced razor-blade notch is illustrated as a red line in (a).

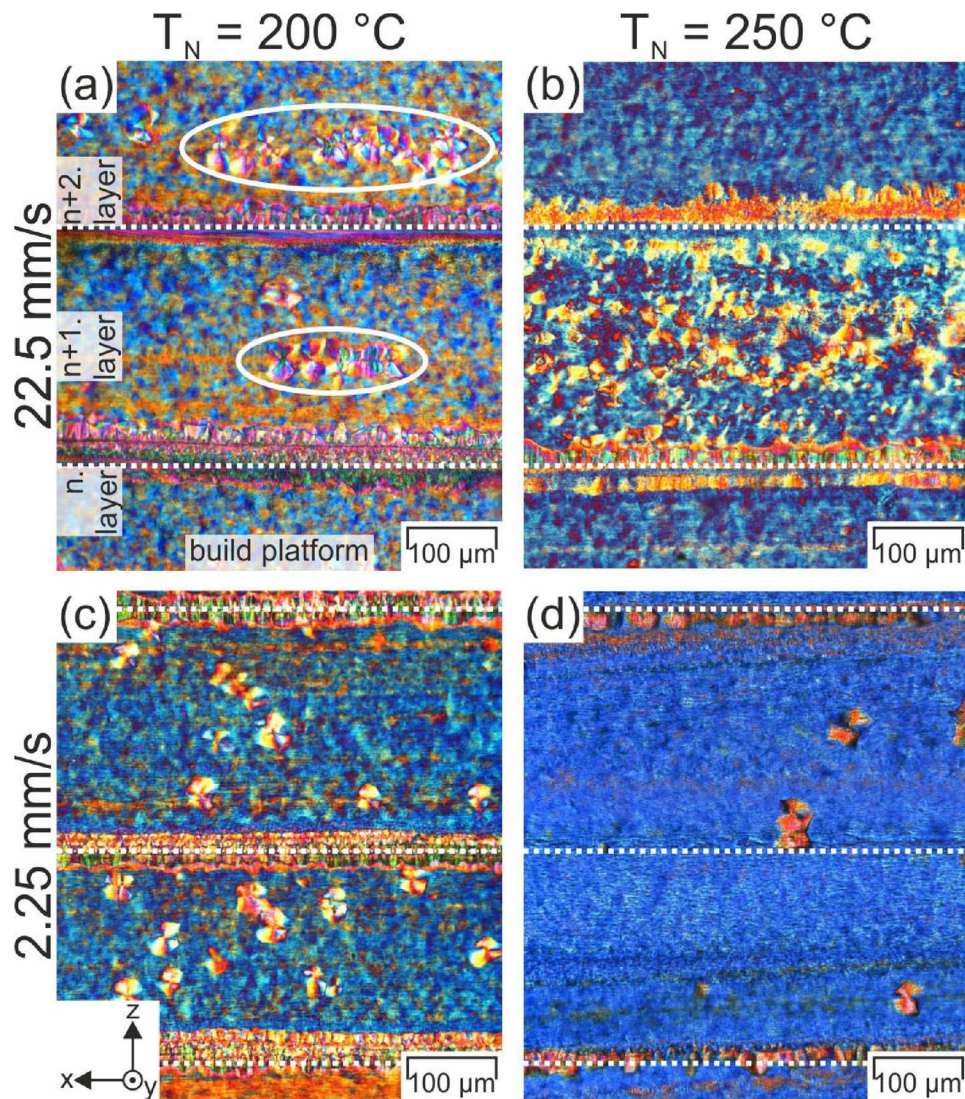


Fig. 4. Polarised optical microscopy images of inter-layer microtome cuts of neat PP shown for the two nozzle temperatures (T_N) and printing speeds. The build platform is located on the bottom of each image, as shown in (a). Dashed white lines mark the interfaces between adjacent layers. Possible oriented spherulites (shish-kebab structures) within the strands are circled. The printing direction is along the x-axis.

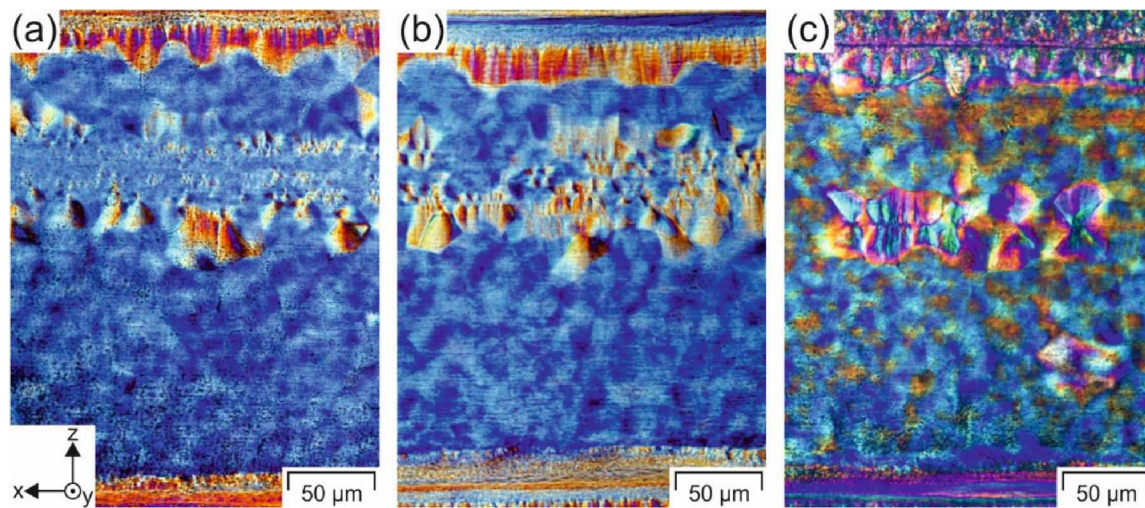


Fig. 5. Polarised optical microscopy images of different stages of shish-kebab structures found in inter-layer microtome cuts of PP/200/22.5 specimens. The printing direction is along the x-axis.

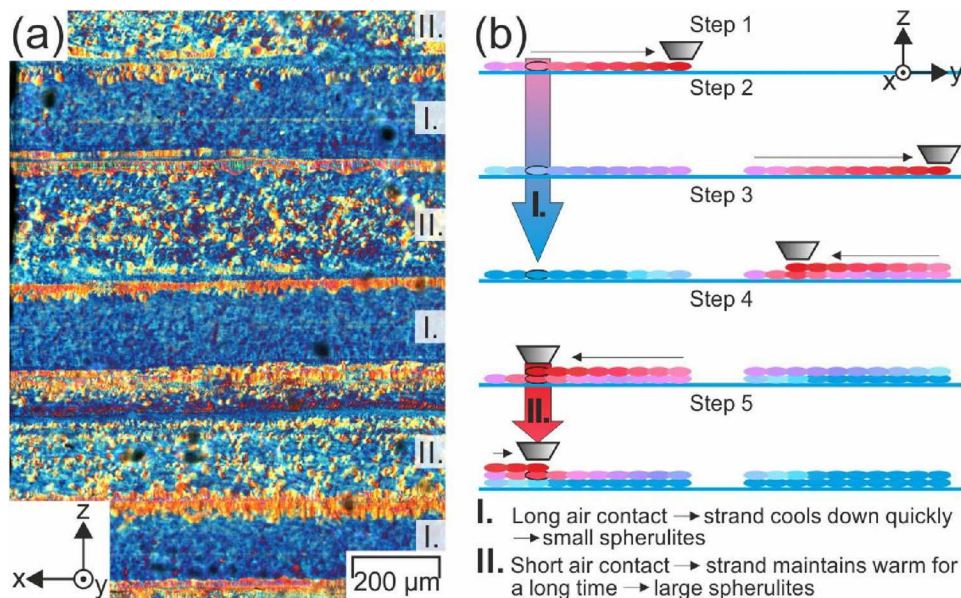


Fig. 6. Polarised optical microscopy image of the alternating spherulite sizes found in the inter-layer microtome cut of PP/250/22.5 (a). In (b), the underlying mechanism based on the printing sequence of two bar-shaped specimens is depicted schematically. In (b), the colour grade of the strands represents the approximate strand temperature (red = hot, blue = cold). The two different cooling mechanisms are highlighted by I. and II., and marked in (a) in the respective layers of the microtome cut. The printing direction along the strands is along the x-axis.

spherulite sizes in adjacent layers are visible due to the printing sequence of the slicer software (Fig. 1a), which is illustrated in detail in Fig. 6. Please note that for all subsequent morphological discussions, the local temperature profile during printing and cooling must be considered. This temperature profile, and the local heat retention in particular, critically depend on several factors, such as the nozzle temperature [42–44], the build platform temperature [44], the surrounding temperature [21,45], the use of a fan [46], the layer thickness [42,45], the printing speed [15,42–45,47–49] and the printing sequence in combination with the component size [51] and number of components printed. In principle, a high local heat retention can be obtained printing at both fast and slow speeds. In the present work, only two small components were printed during one printing job. Therefore, heat retention effects, creating different morphologies, can be observed in all specimens.

The alternating spherulite sizes in adjacent layers in specimen PP/250/22.5 (Fig. 6) are the result of a particular printing sequence involving two alternating cooling mechanisms. One strand effectively cools by the surrounding temperature for a prolonged time under the influence of natural convection (mechanism I. in Fig. 6). Quick cooling results in small spherulites. In contrast to this, the strand of the

subsequent layer remains heated upon deposition for a longer period (mechanism II. in Fig. 6), because of the combined influence of the nozzle passing again while depositing yet another layer [48], and radiative heat transfer [15]. As a consequence of this local heat retention, larger spherulites are formed in this layer. The printing of two specimens with the printing sequence described, thus, promotes the formation of alternating spherulite structures in adjacent layers of the specimens. Considering the findings of Shmueli et al. [18], it is likely that with the printing sequence also the degree of crystallinity changes from layer to layer. Therefore, the choice of printing sequence of the slicer can have tremendous consequences on the morphology and consequently on several properties of 3D-printed semi-crystalline polymers. When more parts are printed simultaneously or larger area parts are printed, this effect will be reinforced, leading to an even stronger variation in inter-layer morphology.

At the low printing speed of 2.25 mm/s, the parts need, in contrast to higher printing speeds, in general more time to locally cool down [47,49], since the hot nozzle resides over one spot for a longer time. Combined with the heat transfer from previously deposited strands [15] this results in a high local heat retention. Therefore, some isolated spherulites have enough time to grow to larger spherulites (Fig. 4c and

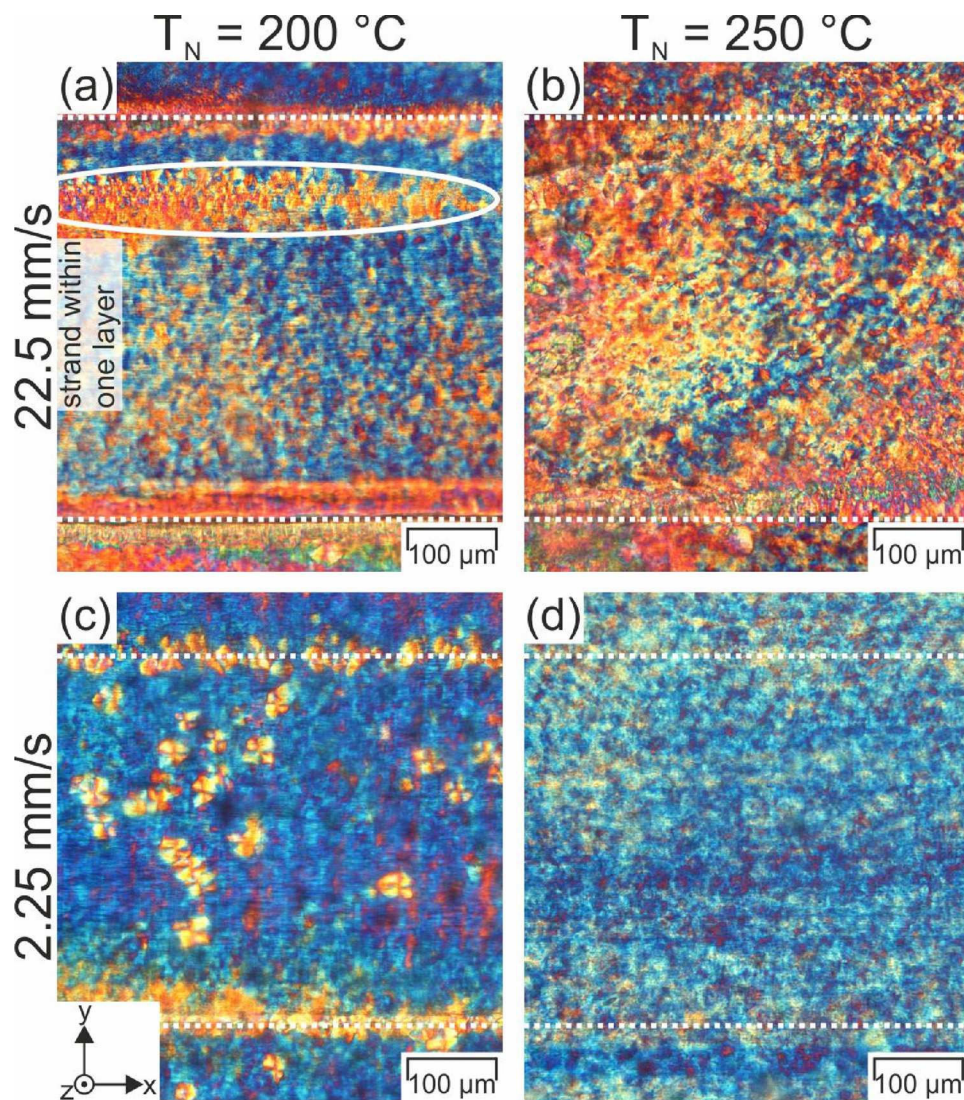


Fig. 7. Polarised optical microscopy images of intra-layer microtome cuts of neat PP shown for the two nozzle temperatures (T_N) and printing speeds. Dashed white lines mark the interfaces between adjacent strands within one layer. Possible oriented spherulites (shish-kebab structures) within the strands are encircled. The printing direction is along the x-axis.

d). Yet, low printing speeds also result in longer periods, in which the deposited strands are exposed to the surrounding room temperature. As the nucleation rate at room temperature is higher than the crystal growth rate, the majority of spherulites remains small [52]. Due to the low printing speed, no elongated spherulites in the form of shish-kebab structures are formed within the strands as opposed to specimen PP/200/22.5.

At 200 °C, distinct weld lines are formed due to a low degree of inter-diffusion resulting from the low nozzle temperature (Fig. 4c) [18]. At a nozzle temperature of 250 °C, the degree of inter-diffusion is considerably higher and weld lines are less pronounced (Fig. 4d). Partly, the weld lines are not observed at all. This is the result of a high degree of inter-diffusion due to a long exposure to high temperatures [18] and the low viscosity of the melt [9]. Similar weakly pronounced weld lines have been observed for PP 3D-printed at high build platform temperatures of 105 °C [24]. Another reason could be gaps between the strands generated through the deposition of a second filament, which enhances chain relaxation across the interface due to the high chain mobility of the just deposited strand [18].

The polarised microscopy images of intra-layer microtome cuts (Fig. 7) reveal a similar trend as observed for the inter-layer cuts. Again, oriented spherulites in the form of shish-kebab structures are found for

PP/200/22.5 within the strands (Fig. 7a). For the specimen with alternating spherulite sizes (Fig. 7b), the cut was apparently taken from a layer exposed to high heat retention, as the spherulites appear relatively large. For such printing geometries, it was shown that the intra-layer diffusion depth is considerably larger than the inter-layer one, as the time between the deposition of adjacent strands within one layer is much lower than that of adjacent layers [9,18]. Additionally, an increase in temperature results in a larger cross-flow of the low viscosity material [18], which in turn further improves the intra-layer cohesion [9]. Consequently, the intra-layer weld lines, particularly for Fig. 7b and d, are significantly less pronounced than the inter-layer weld lines shown in Fig. 4.

For the polarised microscopy images of cross-sectional cuts (Fig. 8), the printing sequence (coming from the left or right side) is clearly observable by rounded edges. For PP/200/22.5, distinct weld lines and homogeneous spherulite sizes are detected (Fig. 8a). Furthermore, due to the high viscosity at such low nozzle temperatures, a weak inter-layer weld line is formed [9]. A higher printing temperature results in alternating regions with different spherulite sizes (Fig. 8b), as explained in Fig. 6. In region I, vertical intra-layer weld lines and evenly small spherulites are found, whereas in region II, the weld lines are less pronounced. They appear to be diagonal due to bulk-flow of the

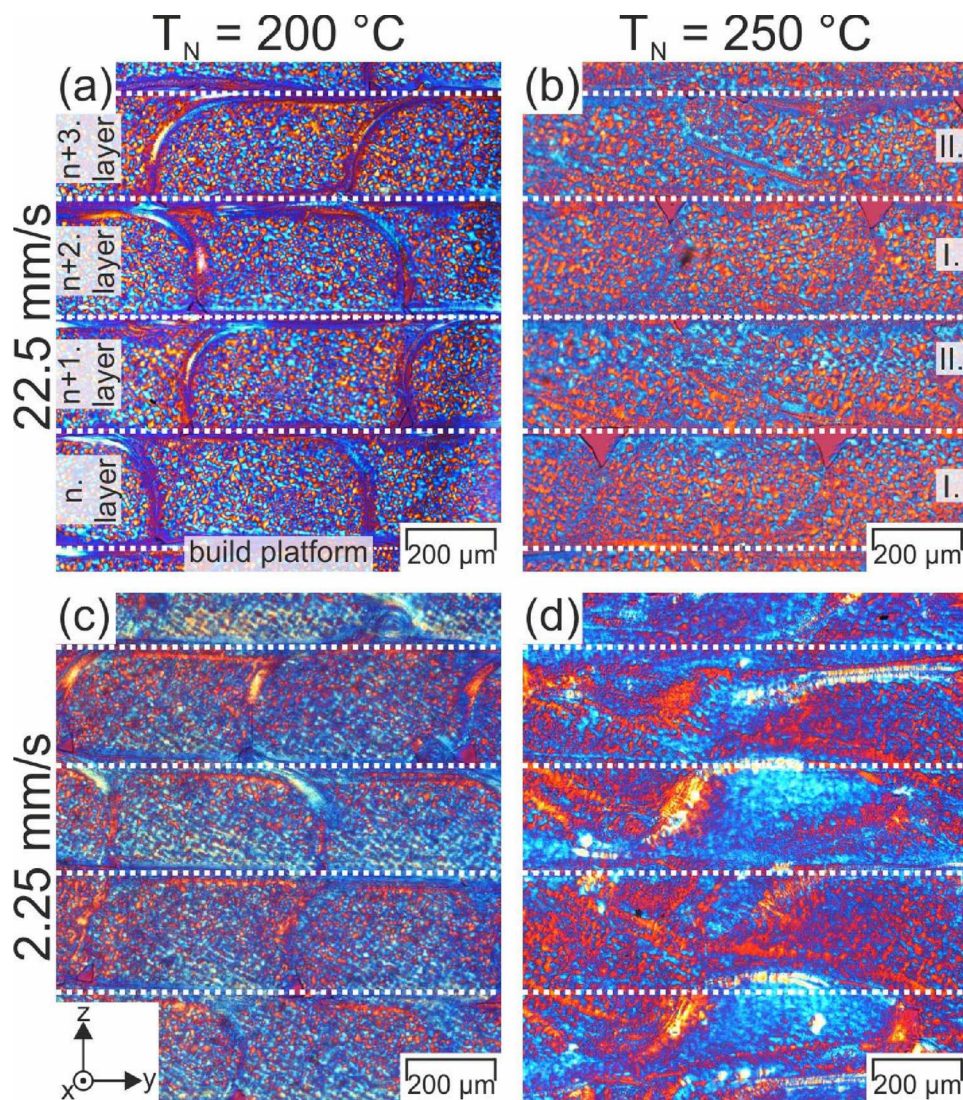


Fig. 8. Polarised optical microscopy images of cross-sectional microtome cuts of neat PP shown for the two nozzle temperatures (T_N) and printing speeds. The build platform is located on the bottom of each image. Dashed white lines mark the interfaces between adjacent strands within one layer. The printing direction is along the x-axis.

deposited strands resulting from the low viscosity at the highest temperature and a prolonged heat retention. PP/200/2.25 (Fig. 8c) shows a behaviour similar to PP/200/22.5 (Fig. 8a). Due to the lower printing speed and a longer local heat exposure, a higher degree of intra- and inter-layer diffusion is observable, though. Similar to the previous thin cuts, the cross-section of PP/250/2.25 does not reveal any distinct weld lines anymore (Fig. 8d).

3.2. WAXS measurements

The morphological studies discussed in Section 3.1. indicate the presence of oriented chains, especially in specimens printed at lower T_N and higher printing speeds. As a result of sufficiently high shear strains during FFF [20], shish-kebab structures were identified e.g. in PP/200/22.5 even near the core of the strands. In all samples, further crystalline structures were observed, i.e. spherulites of varying size in the bulk of the strands as well as crystalline structures along the weld lines. These latter structures appeared predominantly in specimens PP/200/22.5, PP/250/22.5 and PP/200/2.25, in which the inter-diffusion between the strands during printing might not have been as developed as in PP/250/2.25. To study the nature of the crystalline structures in the PP samples in greater detail, WAXS experiments on the bulk specimens

were conducted.

In the 2D WAXS patterns (Fig. 9), diffuse scattering from the amorphous polymer fraction forms a broad and relatively weak backdrop, which is superimposed with distinct Debye-Scherrer rings. These rings can be ascribed to selected lattice planes of the α and β unit cells. A qualitative comparison reveals that all samples have crystallised in the α polymorph of iPP, since the main reflections α -110, α -040, α -130, and α -111/041 are present in all WAXS patterns [53]. By contrast, additional β crystals can be detected only in specimens PP/200/22.5, PP/250/22.5 and PP/200/2.25 by the presence of the β -300 reflection (Fig. 9a–c), while PP/250/2.25 appears to contain no β phase (Fig. 9d). By plotting the azimuthally integrated and normalised intensity of the rings as a function of the Bragg angle (Fig. 10), this finding regarding the existence of the β modification can easily be verified (β -300 at 16.2°). As shown indexed, reflections pertaining to the α modification appear at 14.1 , 17.0 , 18.6 , and 21.5° , respectively. These peak positions are in accordance with Refs. [21,54], which also examined 3D-printed PP with Cu- K_α radiation.

Comparing the diffractograms of the four 3D-printed specimens in Fig. 10, it is evident that the peak intensities related to the two crystal morphologies α and β differ relative to each other. Hence, based on such diffractograms, the degree of crystallinity ($X_{c,WAXS}$) as well as the

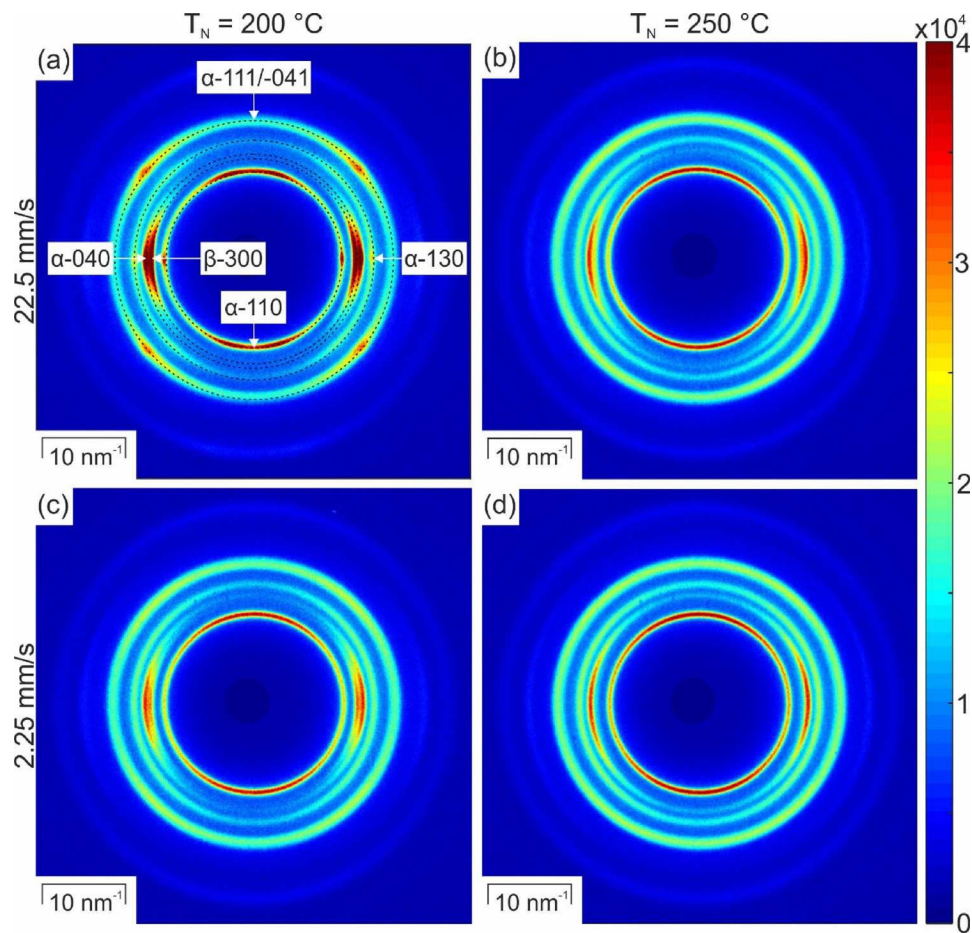


Fig. 9. 2D wide-angle X-ray scattering (WAXS) patterns of 3D-printed PP-samples in dependence of the nozzle temperature (T_N) and the printing speed. The Debye-Scherrer rings of the occurring α and β crystal modifications are shown indexed in (a).

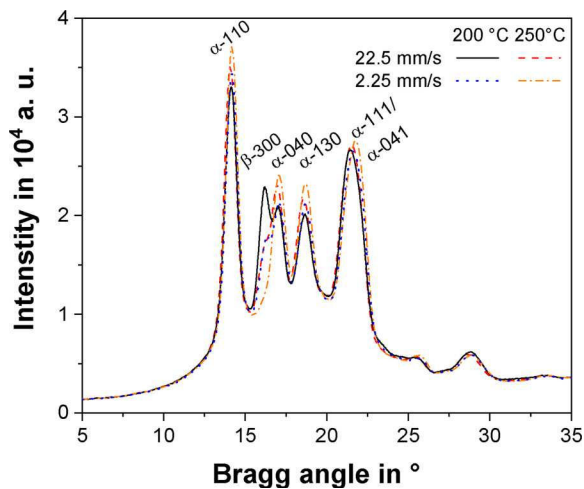


Fig. 10. Azimuthally integrated intensity as a function of the Bragg angle (2θ) measured for 3D-printed PP samples manufactured with two different nozzle temperatures and printing speeds. For the sake of clarity, the diffraction patterns were normalised to the background of PP/200/22.5.

relative amount of β phase (K_β) were quantified (Table 3). Regarding $X_{c,WAXS}$ it was found that, in general, all four samples had developed a similar level of crystallinity in the range of 42–44 %. This is in accordance with the works of Shmueli et al. [18,20], who concluded that – in terms of final degree of crystallisation – iPP is less dependent on the exact thermal profile during 3D-printing than other materials such as

Table 3

Degree of crystallinity ($X_{c,WAXS}$), relative amount of β phase (K_β), and Hermans's orientation factors (f_H) evaluated for the individual reflections α -110 (parents at equator, daughters near meridian), α -040 and β -300.

Designation	$X_{c,WAXS}$ in %	K_β in %	f_H			
			α -110 parent	α -110 daughter	α -040	β -300
PP/200/22.5	42.5	17.6	–0.24	0.44	–0.36	–0.35
PP/250/22.5	43.5	8.2	nan	0.16	–0.27	–0.30
PP/200/2.25	42.8	10.1	nan	0.17	–0.29	–0.33
PP/250/2.25	44.0	0.0	nan	0.09	–0.23	nan

e.g. PLA. Specimens PP/250/2.25 and PP/250/22.5 showed slightly higher values for $X_{c,WAXS}$ compared to the specimens printed at a T_N of 200 °C. This finding can be rationalised by an increased heat retention at higher T_N , which prolongs the time for crystallisation and, therefore, positively affects $X_{c,WAXS}$ [18]. For the same reason, a decrease in printing speed also leads to a slightly higher $X_{c,WAXS}$ [19].

The relative amount of β phase (K_β), in turn, was found to strongly increase with decreasing T_N and increasing printing speed (Table 3). This is in accordance with Ref. [54], in which a similar decrease of 50 °C in nozzle temperature was shown to enhance the growth of β crystals, as well as with Refs. [53,55–57], which link the tendency to form β crystals with the imposition of shear, even at low shear rates. Considering the relatively small deviations in $X_{c,WAXS}$, this means that with decreasing T_N and increasing printing speed, more β crystals are formed, while at high T_N and low printing speeds, such as in PP/250/

2.25, the α modification is clearly preferred. A complementing view on $X_{c,WAXS}$ and K_{β} will be given in Section 3.3, in which the results of the DSC measurements are analysed.

Returning once again to the 2D WAXS patterns in Fig. 9, one further aspect of the Debye-Scherrer rings remains to be explored. In the case of both α and β , the diffracted intensity is not evenly distributed along the rings. This indicates the presence of preferred orientations, i.e. the polymer chains are, to certain degrees, aligned with respect to the vertical flow direction [58]. Basically, all specimens reveal similar orientational components, which evoke diffraction patterns such as analysed e.g. by Dean et al. [34] or Assouline et al. [53]. However, these components strongly vary in their intensity.

Considering the innermost α -110 reflections, an accumulation of intensity around the meridian can be observed in all specimens. PP/200/22.5 (Fig. 9a) shows the most localised distribution of all samples. In contrast to the other samples, though, the intensity is also clearly accumulated along the equator in PP/200/22.5. The strong α -040 and, if present, β -300 rings, which are in close vicinity to each other, generally show increased intensities at the equator positions. From the comparison of the heights and breadths of the intensity distributions of all samples, it can be concluded in analogy to Ref. [56] that, qualitatively, PP/200/22.5 (Fig. 9a) has the highest degree of orientation, and PP/250/2.25 (Fig. 9d) with its more uniform distributions the lowest. This trend is also reflected in the outer α -130 and α -111/041 rings. Especially this latter double reflection may demonstrate the differences between the samples: PP/200/22.5 (Fig. 9a) shows clear intensity maxima at azimuthal angles of 45, 135, 225 and 315°, while PP/250/2.25 (Fig. 9d) is characterised by nearly uniform intensity. The other two samples, PP/250/22.5 and PP/200/2.25, range between these two extreme cases in terms of degree of orientation.

In order to interpret and quantify the differences between the four PP samples, the intensity of the three innermost Debye-Scherrer rings has been plotted as a function of the azimuth angle (Fig. 11). In specimen PP/200/22.5, the azimuthal trace of the α -110 ring (Fig. 11a) proves the presence of two distinct populations of lamellae. In accordance with Refs. [34,53,55,59], these populations can be interpreted in the framework of the parent-daughter model, which links the mixed bimodal orientation corresponding to the α -110 reflections to a crystallographic branching phenomenon unique to the α monoclinic structure in iPP. In this model, intensity accumulations along the equator (0 and 180° in Fig. 11a) are ascribed to the presence of primary

parent lamellae, whose c-axes align in shear direction parallel to the strands, while the b-axes align perpendicularly to the strands. In α -PP, secondary lamellae, the so-called daughters, have been observed to grow epitaxially on the surfaces of the parent lamellae. In doing so, the a-axes of the daughters align parallel to the strands. The orientation of the b- and c-axes are defined as in spherulitic iPP by the relative orientation of the daughter lamellae with respect to the parents [53]. Hence, the b-axes of parents and daughters are parallel [55], and tilted meridional reflections (around 90 and 270° in Fig. 11a) in the α -110 traces are created. The azimuthal trace of specimen PP/200/22.5 does not only show the presence of parent and daughter populations (Fig. 11a), but also proves the parallelism of the b-axes of these populations, as well as their orientation perpendicular to the strands, via the α -040 rings (Fig. 11c).

While cross-hatched parent-daughter morphologies have often been linked to transcrystalline layers in the presence of added fibres [34,53], the parent-daughter model has recently also been applied to model shish-kebab structures in iPP [13,60]. In this context, the daughter lamellae are thought to epitaxially grow on the kebab surfaces. Thus, in accordance with the morphological findings of Section 3.1, the texture of specimen PP/200/22.5 can be attributed to the observed shish-kebab structures as well as the oriented crystalline layer along the weld lines.

Comparing the azimuthal traces of all printed PP-specimens, good agreement is found regarding the β -300 (Fig. 11b) and α -040 (Fig. 11c) reflections. Here, the same orientational components can be observed, which just vary in their texture sharpness. The azimuthal traces of α -110, however, appear to differ from each other, since a sharply oriented parent population is only visible in specimen PP/200/22.5. Specimens PP/200/2.25, PP/250/22.5, and PP/250/2.25 also show meridional reflections linked to daughter populations, but these reflections are much broadened and overlapping. Furthermore, the overall intensity level differs between specimen PP/200/22.5 and the other samples.

Yet, these apparent contradictions can be explained based again on the morphological findings of Section 3.1. In the present study, WAXS patterns average across samples that are spatially inhomogeneous. In specimen PP/200/22.5, the majority of the crystalline fraction is made up of shish-kebabs in the core of the strands as well as oriented structures along the weld lines. Consequently, the characteristics of these structures appear relatively sharp and distinct in the WAXS patterns. Specimens PP/250/22.5 and PP/200/2.25 also show an oriented crystalline phase along the weld lines, but the core of the strands mainly

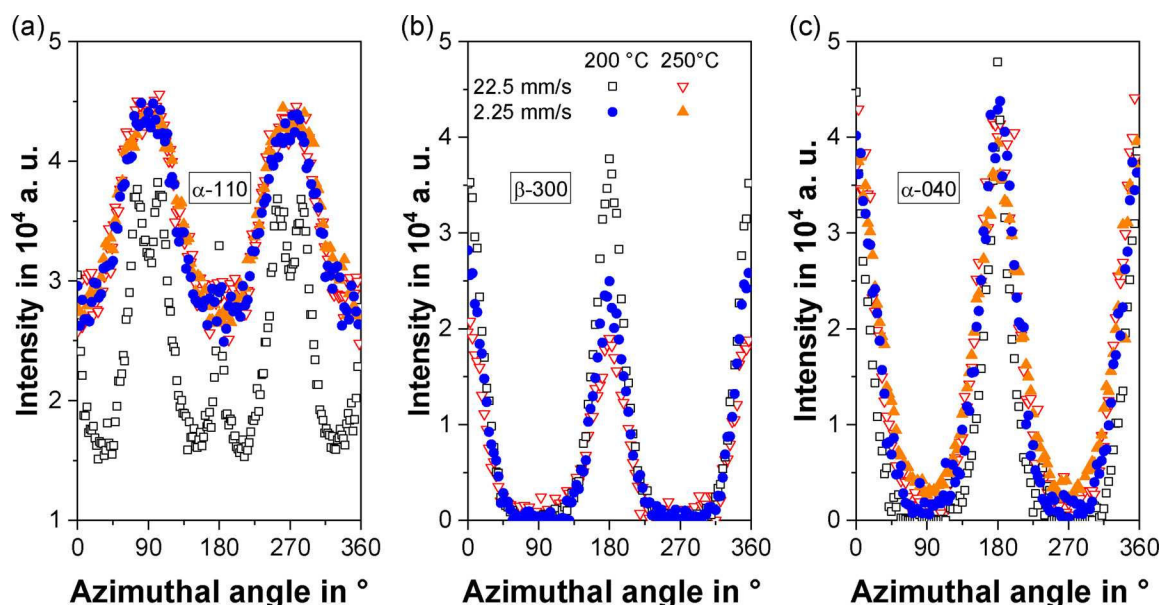


Fig. 11. Intensity distribution of α -110 (a), β -300 (b) and α -040 (c) as a function of the azimuth angle for 3D-printed PP samples manufactured with two different nozzle temperatures and printing speeds.

consists of spherulites. As the cross-section of the X-ray beam was much larger than single spherulites, the measurement averaged over a large number of spherulites, which, based on their radial growth pattern, revealed no preferred orientation. Spherulitic regions, thus, contributed to the overall WAXS patterns in the shape of isotropic, full, uniform intensity rings [53]. Therefore, the final WAXS patterns (Fig. 9) and azimuthal traces (Fig. 10) have to be interpreted as an average of apparently unoriented crystalline parts as well as a smaller fraction of oriented crystalline structure along the weld lines. As a consequence, the baseline of the azimuthal traces in specimens PP/250/22.5 and PP/200/2.25 must be higher, and the overall degree of orientation smaller. As observed in Fig. 11a, the daughter populations (around 90 and 270° in Fig. 11a) appear smeared, and the contribution of the small fraction of parent lamellae (around 0 and 180° in Fig. 11a) may even disappear in the higher background noise. Specimen PP/250/2.25 possesses the smallest fraction of crystalline structures along the weld lines. Consequently, its WAXS pattern appears most uniform.

For a concluding quantitative comparison of the four PP samples in terms of their overall degree of orientation, Hermans's orientation factors (f_H) were calculated based on the α -110, α -040, and β -300 traces (Table 3). For the evaluation of the α -110 reflections in PP/200/22.5, parent and daughter populations were separated as in Refs. [13,34,53,60], because the normal vectors of the (110) lattice planes of the parent population are preferentially oriented perpendicularly to the strands (negative f_H , -0.5 for maximum alignment, 0 for random orientation), while the respective normal vectors of the daughter populations are – allowing for a certain tilt – rather aligned parallel to the strands (positive f_H , 1 for maximum alignment, 0 for random orientation). In the case of the other samples, only the meridional intensity accumulations of α -110 could be evaluated.

Independent of the phase and lattice plane, the degree of orientation shows the following trend: PP/200/22.5 > PP/200/2.25 > PP/250/22.5 > PP/250/2.25, whereby PP/200/2.25 and PP/250/22.5 maintain a similar level. The degree of orientation, expressed by $|f_H|$, thus quantitatively increases with decreasing T_N and increasing printing speed. This trend appears to be in accordance with Refs. [56,61], in which the degree of crystal orientation (f_H) as well as the fraction of oriented crystals was found to increase with the stretching ratio, shear rate or shear duration until a plateau was reached. Yet, as the previous discussion in connection with the morphological observations may have illustrated, the crystallography of 3D-printed, multi-layered structures can easily become complex and should, therefore, not without great care be reduced to single factors.

3.3. Thermal analyses

In accordance with the 1D WAXS pattern (Fig. 10), all specimens apart from PP/250/2.25 exhibit a shoulder in the vicinity of 150 °C in the DSC thermograms, corresponding to the β -modification (Fig. 12a). The β -peak intensities, ranging from a weak shoulder for PP/250/22.5 to a distinct double peak at 150 °C (β -modification) and 158 °C (β' crystals due to recrystallisation [62]) for both specimens processed at 200 °C, are in qualitative agreement with the calculated β phase fractions from the WAXS measurements (Table 3). A similar trend has also been reported in Refs. [54,63]. Furthermore, for prints fabricated with lower T_N , the T_m is shifted to higher temperatures (Table 4) as larger crystalline structures are formed (Fig. 4) [64,65].

The degrees of crystallinity ($X_{c,DSC}$) of all samples are in close vicinity of each other and are in accordance with values available for commercial PP filaments [6]. Furthermore, the $X_{c,DSC}$ are in agreement with the values measured by WAXS ($X_{c,WAXS}$, Table 3). Deviations mainly occur due to the definition of the onset-point and the choice of the heat of fusion of a fully crystalline PP in the course of the DSC evaluation [61,66]. In detail, the specimen that revealed the highest degree of orientation (PP/200/22.5) exhibits not only the highest β phase content (Table 3), but also the lowest overall degree of

crystallinity (42.4 %, Table 4). This can be explained by the considerably lower heat retentions of the strands for high printing speeds due to the fast movements of the hot nozzle, which in turn alleviates the crystallisation [18,19]. This has also been shown by Gomes et al. for poly(vinylidene fluoride) [67].

The TMA curves for PP/200/22.5 also show a curve discontinuity at approx. 150 °C (Fig. 12b and c), relating to the β crystal modification. Another change in the slope can be detected around 115 °C, especially for PP/250/2.25, which corresponds to the secondary relaxation of PP in the vicinity of 110 °C shown in the DSC curve and already reported in Ref. [68]. Due to relaxations, the specimens with higher degrees of orientation shrink more at elevated temperatures than those with lower degrees leading to a lower total length change ($\Delta L/L_0$) [69]. The $\Delta L/L_0$ is highest for PP/250/2.25 (0.030 ± 0.001) and lowest for PP/200/22.5 (0.022 ± 0.002). However, a significant difference for $\Delta L/L_0$ is only observed for the two extreme process settings (Fig. 12b), other to 3D-printed PLA, which revealed a significantly lower total dimension change at higher T_N [70] or at lower printing speeds [52]. The CLTE shortly before melting (Fig. 12c) revealed the same trend as the $\Delta L/L_0$. Initial effects result in an upturn around 30 °C followed by a plateau region. In contrast to injection-moulded PP [52], curve discontinuities appear before the CLTE increases steeply in the vicinity of the T_m . As mentioned before, these irregularities are connected with the β -modification [62]. If comparing the CLTE values in the plateau region (approx. 40–90 °C), all curves show the same value of $1.22 \cdot 10^{-4}/K$, whereas the plateau value in Ref. [52] for injection-moulded PP gives approx. $0.85 \cdot 10^{-4}/K$. This finding confirms anisotropic CLTE values with varying values in and perpendicular to the direction of the strands, which were found for 3D-printed materials [71].

3.4. Thermal conductivity

The printing pattern of the thermal conductivity specimens was chosen in a way so that the axial thermal conductivity (λ_{axial}) determines the conductivity along the strands, whereas the radial thermal conductivity (λ_{radial}) is measured perpendicular to the strands (Fig. 13a). With such a set-up, thermal conductivity measurements give an insight into both the degree of orientation and the formation of weld lines. In Fig. 13b, a clear trend towards increased λ_{axial} for specimens with higher orientations (Table 3) is observed, as the aligned anisotropic crystallites augment the thermal conductivities [23,72]. λ_{axial} is significantly highest for PP/200/22.5 (0.356 ± 0.005 W/(mK)), and lowest for PP/250/2.25 (0.281 ± 0.007 W/(mK)). For the other two parameter sets, the λ_{axial} lie between these two extremes and are insignificantly different from each other (0.315 ± 0.005 W/(mK) and 0.326 ± 0.016 W/(mK), respectively). Yet, the higher values for PP/200/2.25 even correspond to the slightly higher degree of orientation determined by means of WAXS (Table 3). In general, these results correspond well to values for PP 3D-printed with standard processing settings (0.300 ± 0.001 W/(mK) [23]).

A strong difference between the λ_{axial} and λ_{radial} is observed for those specimens that exhibit the highest degree of orientation. Additionally, the specimens with the highest degree of orientation reveal the most pronounced interface between adjacent strands (Fig. 7a and c) and adjacent layers (Fig. 4a and c) [73]. Therefore, the λ_{radial} of PP/200/22.5 (0.202 ± 0.002 W/(mK)) and PP/200/2.25 (0.210 ± 0.011 W/(mK)) are significantly lower than those of PP/250/22.5 (0.229 ± 0.002 W/(mK)) and PP/250/2.25 (0.256 ± 0.009 W/(mK)). For lower nozzle temperatures, voids and air gaps between strands and layers (Fig. 8a) are likely to form due to a lower cross-flow [74]. This, in turn, extensively reduces the thermal conductivity [47]. For PP/250/22.5, considerably less pronounced interfaces between adjacent strands of one layer (Fig. 7b) and less voids are detected. However, the radial thermal conductivity is limited by the alternating crystalline structure (Fig. 6a), which stops the propagation of phonons and therefore decreases λ_{radial} . PP/250/2.25 exhibits the highest λ_{radial} .

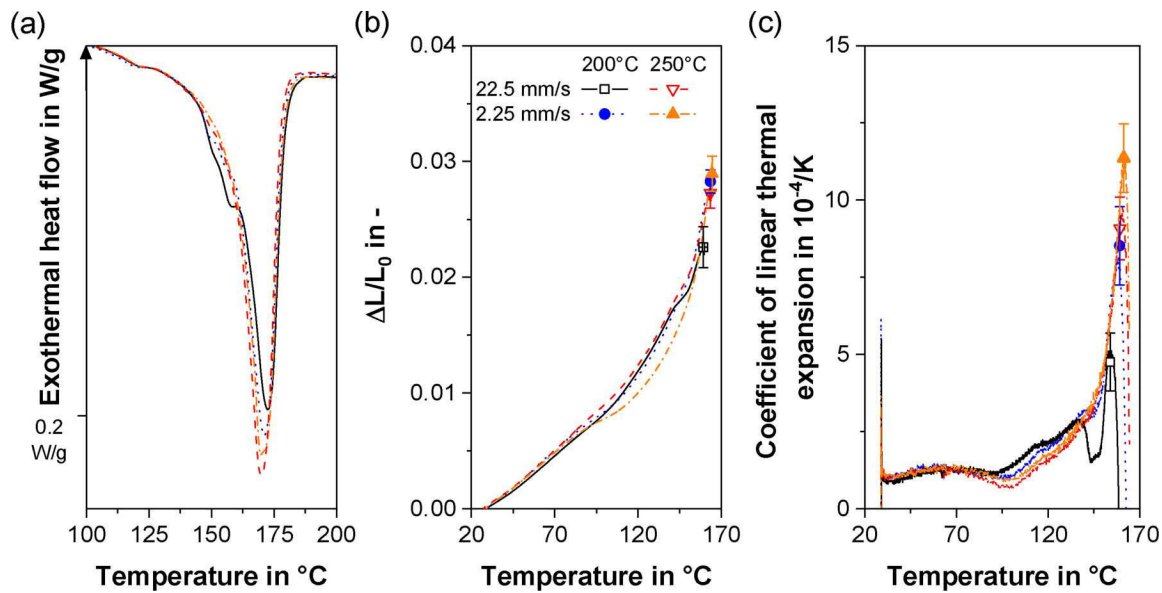


Fig. 12. Differential scanning calorimetry (DSC) thermograms (a) and thermal mechanical analyses (TMA) curves (b and c) evaluated for PP specimens printed with two different nozzle temperatures and printing speeds.

Table 4

The melting temperature (T_m), the specific enthalpy of fusion (ΔH) and the degree of crystallinity obtained through DSC ($X_{c,DSC}$) for the four different print settings.

Designation	T_m in °C	ΔH in J/g	$X_{c,DSC}$ in %
PP/200/22.5	173.0	74.7	42.4
PP/250/22.5	169.9	77.0	43.8
PP/200/2.25	171.2	75.6	43.0
PP/250/2.25	170.0	79.9	45.4

In fact, the λ_{radial} is nearly identical to its λ_{axial} , since nearly no interfaces or air gaps are developed and the degree of orientation is decreased (Fig. 4d). To sum up, the λ_{radial} is strongly influenced by the degree of the formation of weld lines, as they can be seen as a type of defect [75].

3.5. Trouser tear test

As the observed changes in the processing settings resulted not only in strong differences in the degree of orientation, but also in the

morphology of the weld line, the mechanical behaviour of 3D-printed components is strongly influenced by such morphological changes. Therefore, trouser tear tests are discussed in the following. The obtained force-displacement curves show a nearly steady force increase until reaching the force maximum needed for crack-initiation from the razor-blade notch (Fig. 14a) [18]. Deviations from a constant initial slope are mainly due to aligning and stretching of the samples until the two halves are properly positioned. After the crack initiation and its corresponding force peak, the force decreases until it reaches a plateau indicating steady-state crack propagation. The averaged force of this plateau gives the tearing force, which is required to propagate a crack through the specimen and can be used to compare the intra-layer strength of the weld lines. In Fig. 14b, a specimen is shown during the time of testing in the region of this plateau.

Lower nozzle temperatures led to very pronounced and therefore weak interlayers. As a result, lower tearing forces are required for crack propagation (Fig. 14a). At 200 °C, the lower printing speed results in less pronounced weld lines (Fig. 7c) due to longer heat retentions and an improved inter-diffusion, which is confirmed by significantly higher tearing forces (23.4 ± 2.8 N) compared to the specimen processed at 22.5 mm/s (8.8 ± 2.3 N). This difference is also discernible in the

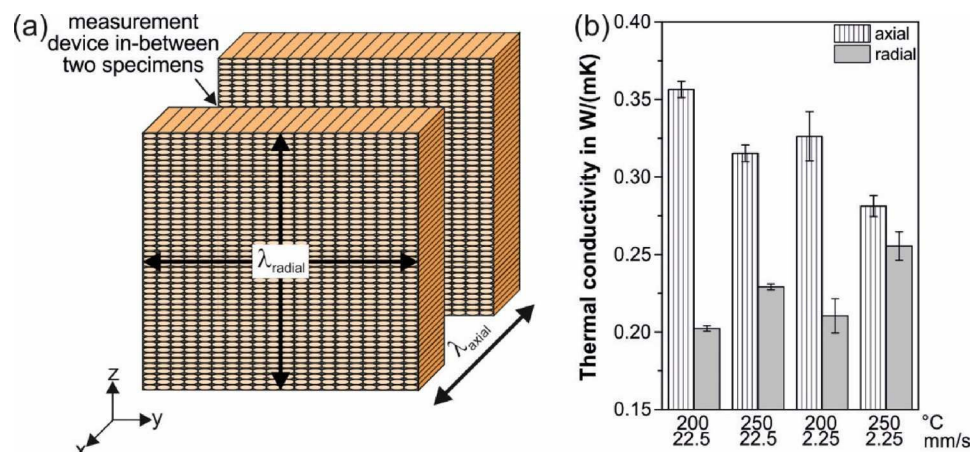


Fig. 13. Specimen orientation during the measurement (a) and thermal conductivity as a function of the nozzle temperature and printing speed (b). The thermal conductivity in axial direction (λ_{axial}) is measured in x-direction, whereas that in radial direction (λ_{radial}) is measured in the yz-plane.

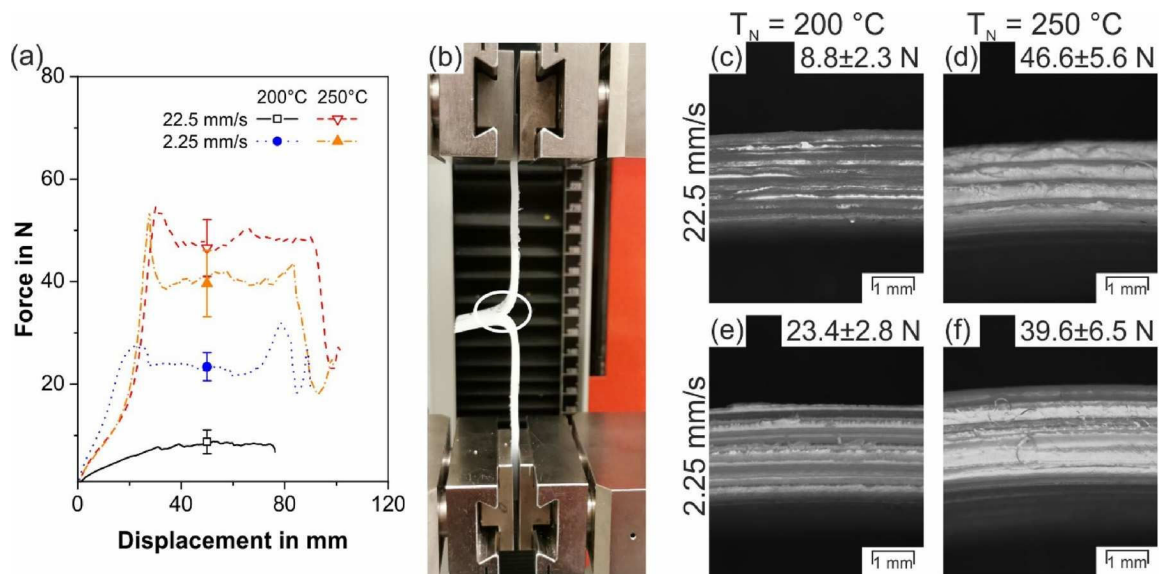


Fig. 14. Force-displacement curves (a), specimen during testing (b) and fracture surfaces (c-f) obtained from trouser tear tests performed on 3D-printed PP specimens manufactured with two different nozzle temperatures (T_N) and printing speeds. In (b), the region of the fracture surface images is encircled in white. In (c-f), the averaged force plateau values of 10 samples and their standard deviations are given.

fracture surfaces: The sample processed at the lower printing speed (Fig. 14c) reveals minor plastic deformations on the fracture surface, whereas the one at the higher printing speed (Fig. 14d) appears very smooth without clearly visible plastic deformations, indicating a low inter-diffusion depth. A similar behaviour has been investigated for double cantilever beam tests [9,76] and tensile as well as bending experiments performed on 3D-printed PLA [77,78]. Similarly to Ref. [43], the specimens processed at higher nozzle temperature revealed less pronounced weld lines and a higher diffusion depth due to longer weld times and, thus, significantly elevated tearing forces (46.6 ± 5.6 N and 39.6 ± 6.5 N, respectively) compared to specimens processed at 200°C . Additionally, the higher degree of inter-diffusion at higher printing temperatures shown in the optical microscopy images (e.g. Fig. 7b and d) is confirmed by the fracture surfaces in Fig. 14e and f. Both surfaces appear rougher, indicating a higher degree of plastic deformation before fracture, similarly to Ref. [10]. Moreover, all fracture surfaces indicate a crack propagation along the weld lines. For the higher temperature prints, the printing speed does not have a significant influence on the forces needed to propagate the crack. This confirms that the alternating morphology does not have negative consequences on the inter-layer weld line behaviour.

3.6. Final discussion

Finally, the question should be addressed, why oriented crystalline layers are formed in some 3D-printed parts along the weld lines, and how the printing conditions influence the crystallographic homogeneity of the samples. In general, the discussion of such questions is very complex, since crystallisation in polymers depends on a wide variety of aspects: material properties such as chain molecular weight [56,58], temperature profiles and processing conditions in general [58,59] as well as dimensional boundaries [59] or complex geometries and thermal cycles connected with 3D-printing [20]. Nevertheless, we may venture to interpret the underlying mechanisms in the four PP-specimens considered in this work.

In samples printed at high T_N and low printing speeds, such as PP/250/2.25, almost no distinct weld lines are observed, and the microstructure appears largely homogenous (Fig. 4d). This is further reflected in similar values for the radial and axial thermal conductivity (Fig. 13b) as well as relatively high forces needed to tear samples apart (Fig. 14a). Thus, full interfacial merging at the weld lines can be expected, very

much in accordance with the observations by Shmueli et al. [20] on carefully 3D-printed PP. In contrast to this, specimens PP/200/22.5, PP/250/22.5, and PP/200/2.25 must have cooled faster, considering in particular that the printing length of the present samples was four times larger than in Ref. [20], meaning that even during the deposition of the second filament layer, the bulk temperature was already much lower. Under these conditions, it can be expected that the shorter cooling times have hindered the chain migration across the interfaces, and that the inter-diffusion and interfacial merging at the weld lines might not have been complete [54]. Consequently, the thermal conductivity is strongly anisotropic and apparent weld lines result in low tearing forces especially for specimens printed at a low T_N .

During printing, the large shear from the nozzle near the weld lines provokes the stretching and orientation of coiled polymer chains [56]. Thus, the nucleation of oriented structures along the weld lines is enhanced [20,55]. In faster cooling conditions, the relaxation of these crystallised structures may remain on a lower level, i.e. the structures are relatively stable. These crystalline precursors formed during flow may then template crystal growth even after the cessation of shear [55]. It may be suggested that in iPP, cross-hatched parent-daughter structures are developed in the course of the complex thermal cycles imposed by 3D-printing [57,60], in which shear rates [13,59] and thermal conditions determine the relative amount of parent lamellae compared to daughter structures. Depending on the shear forces, material properties and cooling conditions, oriented structures such as shish-kebabs may spread from the filament surface to the inner core of the strands, such as observed in specimen PP/200/22.5, by a mechanism as described in Ref. [20]. Else, the core may crystallise principally during cooling and reheating, i.e. under comparably conventional processing conditions, forming spherulitic structures of varying size (specimens PP/250/22.5, PP/200/2.25) [57,58]. Although all weld lines in the present study appear to be of good quality (no air gaps, good adhesion etc.), it is shown that the printed structures have to be interpreted – crystallographically – rather as layered skin-core structures similar to Refs. [55,57], unless full interfacial diffusion is achieved (compare PP/250/2.25). As a result, the printing sequence in connection with the specimen dimensions may play a much more vital role than previously expected, particularly when considering the transfer from small to medium sized specimens towards larger components for real applications.

4. Conclusion

The influence of process-induced orientations on the morphology and material properties of 3D-printed polypropylene (PP) was analysed by means of polarised optical microscopy, wide-angle X-ray scattering, differential scanning calorimetry, thermal mechanical analysis, thermal conductivity measurements and trouser tear tests. Low (200 °C and 2.25 mm/s) and high (250 °C and 22.5 mm/s) parameter settings for the nozzle temperature (T_N) and the printing speed were examined. On the basis of these experiments, the following conclusions can be drawn:

- For a given semi-crystalline polymer (PP) and material extrusion-based additive manufacturing process (FFF), four specimens with a completely different property portfolio in terms of morphology were generated by varying the standard process parameters T_N (in °C) and printing speed (in mm/s).
- One parameter set (250 °C, 2.25 mm/s) enabled the formation of a near-homogeneous morphology with low degrees of orientations. Due to enlarged heat retentions, the degree of crystallinity was highest, and only the α -crystal modification was present. As process-induced weld lines were hardly discernible, a strong inter-diffusion between adjacent strands and layers must have evolved, resulting in the highest separation forces between neighbouring layers in trouser-tear tests. In addition, a nearly isotropic behaviour in terms of direction-dependent thermal conductivities was found.
- In contrast to this, if both parameters were set to the other extremes (200 °C, 22.5 mm/s), the weld line inter-diffusion was considerably weaker. As a consequence, low forces were needed to separate layers in the trouser-tear tests. Moreover, an inhomogeneous morphology was developed, whereby a crystalline phase was formed along the weld line. Additionally, it was observed that only this parameter set promoted the formation of shish-kebab structures within the bulk of the strands. Consequently, the strongest crystal and chain orientations as well as highest quantity of the β -crystal modification were determined for this parameter set, which led to a strong thermal anisotropy.
- The other two parameter sets ranged for all investigated properties between the two extreme settings discussed above. In both cases, an inhomogeneous morphology with pronounced weld lines was obtained. In the bulk of the strands, spherulitic structures were formed. Therefore, the measured overall degrees of orientation and anisotropy were lower than in the in the previous case of low nozzle temperature and high printing speed.
- For one parameter set (250 °C, 22.5 mm/s) in particular, layers with alternating spherulite size were found. This finding could be correlated with the default printing sequence of the slicer software, in which the specimen alternately exhibited areas with high heat retention (large spherulites) and areas that cooled down quickly (small spherulites). In case larger components are printed or many parts are processed simultaneously, more pronounced alternating structures will be formed. This confirms that the printing sequence suggested by the slicer software should not be arbitrarily chosen, but can be used to control the morphology and, hence, the mechanical properties of 3D-printed semi-crystalline polymers.

In conclusion, this paper demonstrates that minor changes in the printing parameters exert a major impact on the resulting material properties at different length scales. Hence, when dealing with semi-crystalline polymers such as PP, the characterisation of process-related morphological changes is particularly important and should never be neglected for future product developments. By considering the revealed relationships in load-bearing components, the properties of the 3D-printed parts can be controlled through the purposeful incorporation of isotropic or anisotropic regions.

CRedit authorship contribution statement

Sandra Petersmann: Conceptualization, Investigation, Methodology, Validation, Formal analysis, Data curation, Writing - original draft, Writing - review & editing, Visualization. **Petra Spoerk-Erdely:** Conceptualization, Methodology, Validation, Writing - original draft, Data curation, Writing - review & editing, Investigation, Software, Visualization. **Michael Feuchter:** Data curation, Writing - original draft, Writing - review & editing, Project administration, Funding acquisition. **Tom Wieme:** Data curation, Validation, Writing - original draft, Writing - review & editing. **Florian Arbeiter:** Resources, Funding acquisition, Project administration, Conceptualization, Methodology, Supervision, Writing - original draft, Writing - review & editing. **Martin Spoerk:** Conceptualization, Methodology, Investigation, Supervision, Validation, Writing - original draft, Writing - review & editing, Visualization.

Declaration of Competing Interest

The authors declare that they have no known competing financial interests or personal relationships that could have appeared to influence the work reported in this paper.

Acknowledgement

This work was partly supported by the European Union's Horizon 2020 research and innovation program as part of the INEX-ADAM project (grant agreement 810708), as well as by CAMED (COMET K-Project 871132) which is funded by the Austrian Federal Ministry of Transport, Innovation and Technology (BMVIT) and the Austrian Federal Ministry for Digital and Economic Affairs (BMDW) and the Styrian Business Promotion Agency (SFG), and the Austrian Research Promotion Agency (FFG) as part of the NextGen3D project (Next Generation 3D, grant agreement 848624). Special thanks go to Dr. Joamin Gonzalez-Gutierrez for the assistance in filament extrusion and printing trials and to Dr. Gerald Pilz for the assistance in the thermal mechanical analyses.

References

- [1] Wohlers Associates, Wohlers Report 2016: 3D Printing and Additive Manufacturing State of the Industry Annual Worldwide Progress Report, Wohlers Associates, Inc., Fort Collins, USA, 2016.
- [2] I. Gibson, D.W. Rosen, B. Stucker, Additive Manufacturing Technologies, Springer US, Boston, MA, 2010.
- [3] M. Gurr, R. Mülhaupt, Rapid prototyping, in: K. Matyjaszewski, M. Möller (Eds.), Polymer Science: A Comprehensive Reference, 1st Ed., Elsevier, Amsterdam, The Netherlands, 2012, pp. 77–99.
- [4] A. Gebhardt, J. Kessler, L. Thurn, 3D-Drucken: Grundlagen Und Anwendungen Des Additive Manufacturing (AM), 2nd Ed., Hanser, Munich, Germany, 2016.
- [5] O. Diegel, Additive manufacturing: an overview, in: S. Hashmi, C.J. Van Tyne, G.F. Batalha, B. Yilbas (Eds.), Comprehensive Materials Processing, 1st Ed., Elsevier, Amsterdam, The Netherlands, 2014, pp. 3–18.
- [6] M. Spoerk, C. Holzer, J. Gonzalez-Gutierrez, Material extrusion-based additive manufacturing of polypropylene: a review on how to improve dimensional inaccuracy and warpage, J. Appl. Polym. Sci. 10 (2019) 48545, <https://doi.org/10.1002/app.48545>.
- [7] M.A. Cuiffo, J. Snyder, A.M. Elliott, N. Romero, S. Kannan, G.P. Halada, Impact of the fused deposition (FDM) printing process on polylactic acid (PLA) chemistry and structure, Appl. Sci. 7 (2017) 579, <https://doi.org/10.3390/app7060579>.
- [8] Y. Liao, C. Liu, B. Coppola, G. Barra, L. Di Maio, L. Incarnato, K. Lafdi, Effect of porosity and crystallinity on 3D printed PLA properties, Polymers 11 (2019) 1487, <https://doi.org/10.3390/polym11091487>.
- [9] M. Spoerk, F. Arbeiter, H. Cajner, J. Sapkota, C. Holzer, Parametric optimization of intra- and inter-layer strengths in parts produced by extrusion-based additive manufacturing of poly(lactic acid), J. Appl. Polym. Sci. 134 (2017) 45401, <https://doi.org/10.1002/app.45401>.
- [10] F. Arbeiter, M. Spoerk, J. Wiener, A. Gosch, G. Pinter, Fracture mechanical characterization and lifetime estimation of near-homogeneous components produced by fused filament fabrication, Polym. Test. 66 (2018) 105–113, <https://doi.org/10.1016/j.polymertesting.2018.01.002>.
- [11] F.J. Padden, H.D. Keith, Spherulitic crystallization in polypropylene, J. Appl. Phys. 30 (1959) 1479–1484, <https://doi.org/10.1063/1.1734985>.

- [12] Q. Zhou, F. Liu, C. Guo, Q. Fu, K. Shen, J. Zhang, Shish-kebab-like cylindrite structures resulted from periodical shear-induced crystallization of isotactic polypropylene, *Polymer* 52 (2011) 2970–2978, <https://doi.org/10.1016/j.polymer.2011.05.002>.
- [13] P.C. Roozmond, Z. Ma, K. Cui, L. Li, G.W.M. Peters, Multimorphological crystallization of shish-kebab structures in isotactic polypropylene: quantitative modeling of parent–daughter crystallization kinetics, *Macromolecules* 47 (2014) 5152–5162, <https://doi.org/10.1021/ma501108c>.
- [14] J. Varga, β -modification of isotactic polypropylene: preparation, structure, processing, properties, and application, *J. Macromol. Sci. Part B- Phys.* 41 (2002) 1121–1171, <https://doi.org/10.1081/MB-120013089>.
- [15] J.E. Seppala, K.D. Migler, Infrared thermography of welding zones produced by polymer extrusion additive manufacturing, *Addit. Manuf.* 12 (2016) 71–76, <https://doi.org/10.1016/j.addma.2016.06.007>.
- [16] J.-Y. Nieh, L.J. Lee, Hot plate welding of polypropylene. Part I: crystallization kinetics, *Polym. Eng. Sci.* 38 (1998) 1121–1132, <https://doi.org/10.1002/pen.10279>.
- [17] L. Wiegart, G.S. Doerk, M. Fukuto, S. Lee, R. Li, G. Marom, M.M. Noack, C.O. Osuji, M.H. Rafailovich, J.A. Sethian, Y. Shmueli, M. Torres Arango, K. Toth, K.G. Yager, R. Pindak, Instrumentation for in situ/operando X-ray scattering studies of polymer additive manufacturing processes, *Synchrotron Radiat. News* 32 (2019) 20–27, <https://doi.org/10.1080/08940886.2019.1582285>.
- [18] Y. Shmueli, J. Jiang, Y. Zhou, Y. Xue, C.-C. Chang, G. Yuan, S.K. Satija, S. Lee, C.-Y. Nam, T. Kim, G. Marom, D. Gersappe, M.H. Rafailovich, Simultaneous in situ X-ray scattering and infrared imaging of polymer extrusion in additive manufacturing, *ACS Appl. Polym. Mater.* 1 (2019) 1559–1567, <https://doi.org/10.1021/acsapm.9b00328>.
- [19] A. Nogales, E. Gutiérrez-Fernández, M.-C. García-Gutiérrez, T.A. Ezquerra, E. Rebolgar, I. Šics, M. Malfois, S. Gaidukovs, E. Ge'cis, K. Celms, G. Bakradze, Structure development in polymers during fused filament fabrication (FFF): an in situ small- and wide-angle X-ray scattering study using synchrotron radiation, *Macromolecules* 52 (2019) 9715–9723, <https://doi.org/10.1021/acs.macromol.9b01620>.
- [20] Y. Shmueli, Y.-C. Lin, S. Lee, M. Zhernenkov, R. Tannenbaum, G. Marom, M.H. Rafailovich, In situ time-resolved X-ray scattering study of isotactic polypropylene in additive manufacturing, *ACS Appl. Mater. Interfaces* 11 (2019) 37112–37120, <https://doi.org/10.1021/acsami.9b12908>.
- [21] M. Spoerk, F. Arbeiter, I. Raguz, G. Weingrill, T. Fischinger, G. Traxler, S. Schuschnigg, L. Cardon, C. Holzer, Polypropylene filled with glass spheres in extrusion-based additive manufacturing: effect of filler size and printing chamber temperature, *Macromol. Mater. Eng.* 303 (2018) 1800179, <https://doi.org/10.1002/mame.201800179>.
- [22] S. Brückner, S.V. Meille, V. Petraccone, B. Pirozzi, Polymorphism in isotactic polypropylene, *Prog. Polym. Sci.* 16 (1991) 361–404, [https://doi.org/10.1016/0079-6700\(91\)90023-E](https://doi.org/10.1016/0079-6700(91)90023-E).
- [23] M. Spoerk, C. Savandaiha, F. Arbeiter, G. Traxler, L. Cardon, C. Holzer, J. Sapkota, Anisotropic properties of oriented short carbon fibre filled polypropylene parts fabricated by extrusion-based additive manufacturing, *Compos. Part A Appl. Sci. Manuf.* 113 (2018) 95–104, <https://doi.org/10.1016/j.compositesa.2018.06.018>.
- [24] S. Hertle, M. Drexler, D. Drummer, Additive manufacturing of poly(propylene) by means of melt extrusion, *Macromol. Mater. Eng.* 301 (2016) 1482–1493, <https://doi.org/10.1002/mame.201600259>.
- [25] D.P. Cole, J.C. Riddick, H.M. Iftekhhar Jaim, K.E. Strawhecker, N.E. Zander, Interfacial mechanical behavior of 3D printed ABS, *J. Appl. Polym. Sci.* 133 (2016) 913, <https://doi.org/10.1002/app.43671>.
- [26] F. Jay, J.M. Haudin, B. Monasse, Shear-induced crystallization of polypropylenes: effect of molecular weight, *J. Mater. Sci.* 34 (1999) 2089–2102, <https://doi.org/10.1023/A:1004563827491>.
- [27] F. Liu, C. Vyas, G. Pooologasundarampillai, I. Pape, S. Hinduja, W. Mirihanage, P. Bartolo, Structural evolution of PCL during melt extrusion 3D printing, *Macromol. Mater. Eng.* 303 (2018) 1700494, <https://doi.org/10.1002/mame.201700494>.
- [28] M. Spoerk, F. Arbeiter, I. Raguz, G. Traxler, S. Schuschnigg, L. Cardon, C. Holzer, The consequences of different printing chamber temperatures in extrusion-based additive manufacturing, *International conference on polymers and moulds innovations*, 2018 Minho, Portugal.
- [29] H.C. Lau, S.N. Bhattacharya, G.J. Field, Melt strength of polypropylene: its relevance to thermoforming, *Polym. Eng. Sci.* 38 (1998) 1915–1923, <https://doi.org/10.1002/pen.10362>.
- [30] M. Spoerk, J. Gonzalez-Gutierrez, C. Lichal, H. Cajner, G.R. Berger, S. Schuschnigg, L. Cardon, C. Holzer, Optimisation of the adhesion of polypropylene-based materials during extrusion-based additive manufacturing, *Polymers* 10 (2018) 490, <https://doi.org/10.3390/polym10050490>.
- [31] M. Spoerk, J. Gonzalez-Gutierrez, J. Sapkota, S. Schuschnigg, C. Holzer, Effect of the printing bed temperature on the adhesion of parts produced by fused filament fabrication, *Plast., Rubber Compos.* 47 (2018) 17–24, <https://doi.org/10.1080/14658011.2017.1399531>.
- [32] A.P. Hammersley, S.O. Svensson, M. Hanfland, A.N. Fitch, D. Hausermann, Two-dimensional detector software: from real detector to idealised image or two-theta scan, *High Pressure Res.* 14 (1996) 235–248, <https://doi.org/10.1080/08957959608201408>.
- [33] M. Newville, T. Stensitzki, D.B. Allen, A. Ingargiola, LMFIT: Non-Linear Least-Square Minimization and Curve-Fitting for Python, Version 0.8.0, (2014), <https://doi.org/10.5281/zenodo.11813> Zenodo.
- [34] D.M. Dean, L. Rebenfeld, R.A. Register, B.S. Hsiao, Matrix molecular orientation in fiber-reinforced polypropylene composites, *J. Mater. Sci.* 33 (1998) 4797–4812, <https://doi.org/10.1023/A:1004474128452>.
- [35] J. Ščudla, M. Raab, K.-J. Eichhorn, A. Strachota, Formation and transformation of hierarchical structure of β -nucleated polypropylene characterized by X-ray diffraction, differential scanning calorimetry and scanning electron microscopy, *Polymer* 44 (2003) 4655–4664, [https://doi.org/10.1016/S0032-3861\(03\)00287-8](https://doi.org/10.1016/S0032-3861(03)00287-8).
- [36] S. Ran, D. Fang, X. Zong, B.S. Hsiao, B. Chu, P.M. Cunniff, Structural changes during deformation of Kevlar fibers via on-line synchrotron SAXS/WAXD techniques, *Polymer* 42 (2001) 1601–1612, [https://doi.org/10.1016/S0032-3861\(00\)00460-2](https://doi.org/10.1016/S0032-3861(00)00460-2).
- [37] L. Zhang, Y. Qin, G. Zheng, K. Dai, C. Liu, X. Yan, J. Guo, C. Shen, Z. Guo, Interfacial crystallization and mechanical property of isotactic polypropylene based single-polymer composites, *Polymer* 90 (2016) 18–25, <https://doi.org/10.1016/j.polymer.2016.02.052>.
- [38] A. Turner-Jones, J.M. Aizlewood, D.R. Beckett, Crystalline forms of isotactic polypropylene, *Makromol. Chem.* 75 (1964) 134–158, <https://doi.org/10.1002/macp.1964.020750113>.
- [39] G.M. Swallowe, J.O. Fernandez, S. Hamdan, Crystallinity increases in semi-crystalline polymers during high rate testing, *J. Phys. IV France* 7 (1997) C3–453–C3–458, <https://doi.org/10.1051/jp4:1997378>.
- [40] J.X. Li, W.L. Cheung, D. Jia, A study on the heat of fusion of β -polypropylene, *Polymer* 40 (1999) 1219–1222, [https://doi.org/10.1016/S0032-3861\(98\)00345-0](https://doi.org/10.1016/S0032-3861(98)00345-0).
- [41] W. Grellmann, V. Alstätt, *Kunststoffprüfung*, 2nd Ed., Hanser, Munich, Germany, 2011.
- [42] A.C. Abbott, G.P. Tandon, R.L. Bradford, H. Koerner, J.W. Baur, Process-structure-property effects on ABS bond strength in fused filament fabrication, *Addit. Manuf.* 19 (2018) 29–38, <https://doi.org/10.1016/j.addma.2017.11.002>.
- [43] J.E. Seppala, S. Hoon Han, K.E. Hillgartner, C.S. Davis, K.B. Migler, Weld formation during material extrusion additive manufacturing, *Soft Matter* 13 (2017) 6761–6769, <https://doi.org/10.1039/c7sm00950j>.
- [44] J. Yin, C. Lu, J. Fu, Y. Huang, Y. Zheng, Interfacial bonding during multi-material fused deposition modeling (FDM) process due to inter-molecular diffusion, *Mater. Design* 150 (2018) 104–112, <https://doi.org/10.1016/j.matdes.2018.04.029>.
- [45] J. Zhang, X.Z. Wang, W.W. Yu, Y.H. Deng, Numerical investigation of the influence of process conditions on the temperature variation in fused deposition modeling, *Mater. Design*, Volume 130 (2017) 59–68, <https://doi.org/10.1016/j.matdes.2017.05.040>.
- [46] H. Prajapati, D. Ravoori, A. Jain, Measurement and modeling of filament temperature distribution in the standoff gap between nozzle and bed in polymer-based additive manufacturing, *Addit. Manuf.* 24 (2018) 224–231, <https://doi.org/10.1016/j.addma.2018.09.030>.
- [47] D. Ravoori, H. Prajapati, V. Talluru, A. Adnan, A. Jain, Nozzle-integrated pre-deposition and post-deposition heating of previously deposited layers in polymer extrusion based additive manufacturing, *Addit. Manuf.* 28 (2019) 719–726, <https://doi.org/10.1016/j.addma.2019.06.006>.
- [48] A. D'Amico, A. Peterson, An adaptable FEA simulation of material extrusion additive manufacturing heat transfer in 3D, *Addit. Manuf.* 21 (2018) 422–430, <https://doi.org/10.1016/j.addma.2018.02.021>.
- [49] F. Peng, B. Vogt, M. Cakmak, Complex flow and temperature history during melt extrusion in material extrusion additive manufacturing, *Addit. Manuf.* 22 (2018) 197–206, <https://doi.org/10.1016/j.addma.2018.05.015>.
- [50] A. Paolini, S. Kollmannsberger, E. Rank, Additive manufacturing in construction: a review on processes, applications, and digital planning methods, *Addit. Manuf.* 30 (2019) 100894, <https://doi.org/10.1016/j.addma.2019.100894>.
- [51] G.W. Ehrenstein, *Polymer-Werkstoffe: Struktur - Eigenschaften - Anwendung*, 3rd Ed., Hanser, Munich, Germany, 2011.
- [52] E. Assouline, E. Wachtel, S. Grigull, A. Lustiger, H.D. Wagner, G. Marom, Lamellar twisting in α isotactic polypropylene transcrystallinity investigated by synchrotron microbeam X-ray diffraction, *Polymer* 42 (2001) 6231–6237, [https://doi.org/10.1016/S0032-3861\(01\)00087-8](https://doi.org/10.1016/S0032-3861(01)00087-8).
- [53] L. Wang, D.J. Gardner, Effect of fused layer modeling (FLM) processing parameters on impact strength of cellular polypropylene, *Polymer* 113 (2017) 74–80, <https://doi.org/10.1016/j.polymer.2017.02.055>.
- [54] G. Kumaraswamy, R.K. Verma, A.M. Issaian, P. Wang, J.A. Kornfield, F. Yeh, B.S. Hsiao, R.H. Olley, Shear-enhanced crystallization in isotactic polypropylene Part 2. Analysis of the formation of the oriented “skin”, *Polymer* 41 (2000) 8931–8940, [https://doi.org/10.1016/S0032-3861\(00\)00236-6](https://doi.org/10.1016/S0032-3861(00)00236-6).
- [55] R.H. Somani, L. Yang, B.S. Hsiao, T. Sun, N.V. Pogodina, A. Lustiger, Shear-induced molecular orientation and crystallization in isotactic polypropylene: effects of the deformation rate and strain, *Macromolecules* 38 (2005) 1244–1255, <https://doi.org/10.1021/ma048285d>.
- [56] D. Mi, C. Xia, M. Jin, F. Wang, K. Shen, J. Zhang, Quantification of the effect of shish-kebab structure on the mechanical properties of polypropylene samples by controlling shear layer thickness, *Macromolecules* 49 (2016) 4571–4578, <https://doi.org/10.1021/acs.macromol.6b00822>.
- [57] D. Dikovskiy, G. Marom, C.A. Avila-Orta, R.H. Somani, B.S. Hsiao, Shear-induced crystallization in isotactic polypropylene containing ultra-high molecular weight polyethylene oriented precursor domains, *Polymer* 46 (2005) 3096–3104, <https://doi.org/10.1016/j.polymer.2005.01.086>.
- [58] G.A. Tanami, E. Wachtel, G. Marom, Crystalline structure and thermodynamic analysis of ultra-low diameter VGCF-polypropylene nanocomposite monofilaments, *Polym. Compos.* 37 (2016) 1641–1649, <https://doi.org/10.1002/pc.23336>.
- [59] Y. Shalom, E. Wachtel, G. Marom, Restructuring of confined crystalline morphology in the drawing process of VGCF-iPP nanocomposite filaments, *Polymer* 154 (2018) 218–224, <https://doi.org/10.1016/j.polymer.2018.09.015>.
- [60] D. Milicevic, M. Micic, G. Stamboliev, A. Leskovac, M. Mitric, E. Suljovrujic, Microstructure and crystallinity of polyolefins oriented via solid-state stretching at an elevated temperature, *Fibers Polym.* 13 (2012) 466–470, <https://doi.org/10.1007/s12221-012-0466-4>.

- [62] Y. Fujiwara, Das Doppelschmelzverhalten der β -Phase des isotaktischen Polypropylens, *Colloid & Polymer Sci.* 253 (1975) 273–282, <https://doi.org/10.1007/BF02352075>.
- [63] L. Wang, J.E. Sanders, D.J. Gardner, Y. Han, Effect of fused deposition modeling process parameters on the mechanical properties of a filled polypropylene, *Prog. Addit. Manuf.* 3 (2018) 205–214, <https://doi.org/10.1007/s40964-018-0053-3>.
- [64] S.J.A. Rizvi, Effect of injection molding parameters on crystallinity and mechanical properties of isotactic polypropylene, *Int. J. Plast. Technol.* 21 (2017) 404–426, <https://doi.org/10.1007/s12588-017-9194-3>.
- [65] M. Nie, X. Li, X. Hu, Q. Wang, Effect of die temperature on morphology and performance of polyethylene pipe prepared via mandrel rotation extrusion, *J. Macromol. Sci. Part B- Phys.* 53 (2014) 1442–1452, <https://doi.org/10.1080/00222348.2014.928161>.
- [66] M.F.S. Lima, M.A.Z. Vasconcellos, D. Samios, Crystallinity changes in plastically deformed isotactic polypropylene evaluated by x-ray diffraction and differential scanning calorimetry methods, *J. Polym. Sci. Part B: Polym. Phys.* 40 (2002) 896–903, <https://doi.org/10.1002/polb.10159>.
- [67] J. Gomes, J. Serrado Nunes, V. Sencadas, S. Lanceros-Mendez, Influence of the β -phase content and degree of crystallinity on the piezo- and ferroelectric properties of poly(vinylidene fluoride), *Smart Mater. Struct.* 19 (2010) 65010, <https://doi.org/10.1088/0964-1726/19/6/065010>.
- [68] J.E. Mark, *Physical Properties of Polymers Handbook*, 2nd Ed., Springer, New York, USA, 2007.
- [69] K. Oberbach, E. Baur, S. Brinkmann, E. Schmachtenberg, H. Saechtling, *Saechtling-Kunststoff-Taschenbuch*, 29th Ed., Hanser, Munich, Germany, 2004.
- [70] M. Bodaghi, R. Noroozi, A. Zolfagharian, M. Fotouhi, S. Norouzi, 4D printing self-morphing structures, *Materials* 12 (2019) 1353, <https://doi.org/10.3390/ma12081353>.
- [71] S.N. Economidou, D. Karalekas, Optical sensor-based measurements of thermal expansion coefficient in additive manufacturing, *Polym. Test.* 51 (2016) 117–121, <https://doi.org/10.1016/j.polymertesting.2016.03.001>.
- [72] C.L. Choy, F.C. Chen, W.H. Luk, Thermal conductivity of oriented crystalline polymers - a model, *J. Polym. Sci. Part B: Polym. Phys.* 18 (1980) 1187–1207, <https://doi.org/10.1002/pol.1980.180180603>.
- [73] V. Srinivas, C.S.J. van Hooy-Corstjens, G.B.M. Vaughan, B. van Leeuwen, S. Rastogi, J.A.W. Harings, Interfacial stereocomplexation to strengthen fused deposition modeled poly(lactide) welds, *ACS Appl. Polym. Mater.* 1 (2019) 2131–2139, <https://doi.org/10.1021/acscapm.9b00421>.
- [74] J. Wang, H. Xie, Z. Weng, T. Senthil, L. Wu, A novel approach to improve mechanical properties of parts fabricated by fused deposition modeling, *Mater. Design* 105 (2016) 152–159, <https://doi.org/10.1016/j.matdes.2016.05.078>.
- [75] H.-X. Huang, Self-reinforcement of polypropylene by flow-induced crystallization during continuous extrusion, *J. Appl. Polym. Sci.* 67 (1998) 2111–2118, [https://doi.org/10.1002/\(SICI\)1097-4628\(19980321\)67:12<2111::AID-APP18>3.0.CO;2-3](https://doi.org/10.1002/(SICI)1097-4628(19980321)67:12<2111::AID-APP18>3.0.CO;2-3).
- [76] A. Khudiakova, F. Arbeiter, M. Spoerk, M. Wolfahrt, D. Godec, G. Pinter, Inter-layer bonding characterisation between materials with different degrees of stiffness processed by fused filament fabrication, *Addit. Manuf.* 28 (2019) 184–193, <https://doi.org/10.1016/j.addma.2019.05.006>.
- [77] J.M. Chacón, M.A. Caminero, E. García-Plaza, P.J. Núñez, Additive manufacturing of PLA structures using fused deposition modelling: effect of process parameters on mechanical properties and their optimal selection, *Material. Design* 124 (2017) 143–157, <https://doi.org/10.1016/j.matdes.2017.03.065>.
- [78] M.Á. Caminero, J.M. Chacón, E. García-Plaza, P.J. Núñez, J.M. Reverte, J.P. Becar, Additive manufacturing of PLA-based composites using fused filament fabrication: effect of graphene nanoplatelet reinforcement on mechanical properties, dimensional accuracy and texture, *Polymers* 11 (2019) 799, <https://doi.org/10.3390/polym11050799>.

Publication 4

Bibliographic information

Title: Impact Optimization of 3D-Printed Poly(methyl methacrylate) for Cranial Implants

Authors: Sandra Petersmann¹, Martin Spoerk², Philipp Huber², Margit Lang³, Gerald Pinter¹, Florian Arbeiter^{1,*}

Affiliations:

¹Materials Science and Testing of Polymers, Montanuniversitaet Leoben, Otto Gloeckel-Straße 2, 8700, Leoben, Austria

²Polymer Processing, Montanuniversitaet Leoben, Otto Gloeckel-Straße 2, 8700, Leoben, Austria

³Designing Plastics and Composite Materials, Montanuniversitaet Leoben, Otto Gloeckel-Straße 2, 8700, Leoben, Austria

Periodical: Macromolecular Materials and Engineering

DOI: <https://doi.org/10.1002/mame.201900263>

Relevant contributions to this publication:

Conceptualisation: Martin Spoerk, Gerald Pinter, Florian Arbeiter

Methodology: Sandra Petersmann, Philipp Huber, Margit Lang

Investigation: Sandra Petersmann, Florian Arbeiter

Validation: Sandra Petersmann, Florian Arbeiter

Writing - Original Draft: Sandra Petersmann, Martin Spoerk, Florian Arbeiter

Writing - Review & Editing: Sandra Petersmann, Martin Spoerk, Gerald Pinter, Florian Arbeiter

Visualisation: Sandra Petersmann, Martin Spoerk



Impact Optimization of 3D-Printed Poly(methyl methacrylate) for Cranial Implants

Sandra Petersmann, Martin Spoerk, Philipp Huber, Margit Lang, Gerald Pinter, and Florian Arbeiter*

Material extrusion-based additive manufacturing, also known as fused filament fabrication (FFF) or 3D printing facilitates the fabrication of cranial implants with different materials and complex internal structures. The impact behavior plays a key role in the designing process of cranial implants. Therefore, the performance of impact tests on novel implant materials is of utmost importance. This research focuses on investigating the dependency of the infill density and pattern on the impact properties of 3D-printed poly(methyl methacrylate) (PMMA) sandwich specimens including internal rectilinear, gyroid, and 3D-honeycomb (3D-HC) structures. 3D-HC structures show higher impact forces and dissipated energies as well as dynamic stiffness values compared to rectilinear and gyroid structures at the same infill density. 70% infill 3D-HC and 100% infill rectilinear structures prove to be most promising. In addition, two different optimization techniques to further improve the impact properties of these specimens, namely a material and a topology optimization, are applied. Topology optimization shows promising results until first damage and material optimization regarding dissipated energies. However, both are not able to outperform the 3D-HC pattern.

increasing emergence of traumata are main reasons for the necessity of developing proper cranial implants.^[1–3] The structure and biomechanical properties of synthetic bone substitutes should be as similar to the properties of the adjoining natural bone as possible. Characteristics such as inertness, biocompatibility, sterilizability, long-time stability, good storage capability, adequate strength, and durability, as well as availability, processability, flexible individualization, and intraoperative workability are required.^[4–7]

So far, a variety of different materials has been used for the reconstruction of bone defects ranging from human and non-human bones to metals, ceramics, and polymers. Polymers are of particular interest because they are relatively easy to process and mostly inexpensive.^[7] Cranial implants made of polyetheretherketone (PEEK), high-density polyethylene, polypropylene (PP), PMMA, and poly(tetrafluoroethylene) are already on

1. Introduction

Finding adequate cranial bone substitutes has been challenging researchers worldwide. The world's aging population and the

the market.^[2] PEEK and PMMA represent the most widely used polymeric materials for the reconstruction of cranial defects. Both thermoplastics are inert, biocompatible, and reveal adequate mechanical properties in order to replace bone. PEEK outpaces PMMA in terms of strength, stiffness, and durability. In contrast, PMMA is easily obtainable and affordable.^[8,9]

The use of PMMA in cranioplasty dates back to 1940.^[8] Historically, the intraoperative construction of PMMA implants by hand was the predominant fabrication technique.^[3,10,11] However, hand-forming of PMMA implants has been replaced by computer-aided prefabrication methods. Implants are fabricated with the help of computed tomography scans and subsequent production of molds for casting PMMA implants via wax elimination techniques,^[12] additive manufacturing methods,^[13–20] milling,^[21] or thermoforming.^[22]

Recently, the direct replication of bone defects by various additive manufacturing techniques has been investigated.^[23–25] PMMA has gained particular attention due to its processability using FFF, also known as 3D printing or fused deposition modeling.^[26] In the scope of a typical FFF process, a thermoplastic filament is selectively molten and deposited through a hot nozzle that moves according to a pre-defined computer-aided design contour onto a build platform.^[27] As soon as the first layer is deposited, subsequent layers are added to the first layer

S. Petersmann, Prof. G. Pinter, Dr. F. Arbeiter
Materials Science and Testing of Polymers
Montanuniversitaet Leoben
Otto Gloeckel-Straße 2, 8700 Leoben, Austria
E-mail: florian.arbeiter@unileoben.ac.at

Dr. M. Spoerk, P. Huber
Polymer Processing
Montanuniversitaet Leoben
Otto Gloeckel-Straße 2, 8700 Leoben, Austria

M. Lang
Designing Plastics and Composite Materials
Montanuniversitaet Leoben
Otto Gloeckel-Straße 2, 8700 Leoben, Austria

The ORCID identification number(s) for the author(s) of this article can be found under <https://doi.org/10.1002/mame.201900263>.

© 2019 The Authors. Published by WILEY-VCH Verlag GmbH & Co. KGaA, Weinheim. This is an open access article under the terms of the Creative Commons Attribution-NonCommercial License, which permits use, distribution and reproduction in any medium, provided the original work is properly cited and is not used for commercial purposes.

DOI: 10.1002/mame.201900263

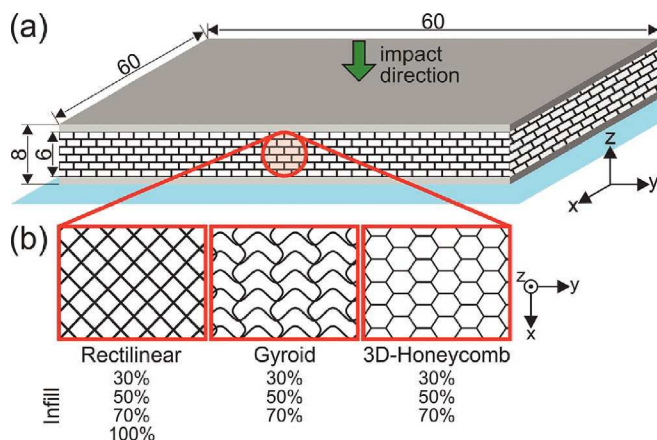


Figure 1. Schematic representation of one 3D-printed impact specimen with the investigated sandwich structure and its dimensions in mm a) and of the three investigated infill patterns of the sandwich core along with the respective infill densities b). In (a), the blue surface depicts the build platform during printing and the green arrow the impact direction during testing. The specimens are oriented in a way that the consecutive layers of printing are in z-direction.

by increasing the distance between the build platform and the die.^[28–30]

3D printing is gaining popularity, especially because it allows the immediate fabrication of complex geometries,^[29,31–33] such as patient-specific implants. As cranial bone is a combination of spongy cancellous and compact cortical bone, cranial bone defects are likely to be reconstructed with ‘sandwich-structured’ implants.^[1] Sandwich structures are generally composed of layers with different orientation or structure.^[34] By embedding a structured core to two stiff and thin outer layers, the mechanical properties of 3D-printed porous structures can be improved. This has already been shown for acrylonitrile butadiene styrene (ABS) or poly(lactic acid) (PLA).^[35–41] However, unlike PMMA, PLA and ABS do not serve as possible long-term implant materials.^[42]

Therefore, the present work aims to compare the impact properties of PMMA sandwich structures that are 3D-printed with three different infill patterns and four infill densities. The fracture properties are analyzed and optimized by two strategies, namely a topology and a material optimization approach.

2. Experimental Section

2.1. Material

A transparent PMMA filament (Herz Austria GmbH, Austria) was chosen as the main material of this study. For soft interlayers, a black thermoplastic copolyester elastomer, namely Arnitel ID 2045 (TPC, Nexeo Solutions 3D-EMEA, Spain), was used. The materials were processed as received (diameter of 1.75 mm). Both material types exist as Food and Drug Administration approved pellets. For the present study, non-approved filaments were used to understand the mechanisms behind the impact fracture behavior.

2.2. Processing

All PMMA specimens were sliced in the software Slic3r Prusa Edition. Bottom and top sandwich panels consisted of 1 mm thick plates with 100% infill density. The inner sandwich core was varied by a parametric study investigating both the infill pattern (rectilinear, gyroid, and 3D-HC) and the infill density (30%, 50%, 70%, and 100% [if applicable]), as shown in **Figure 1**.

The specimens were processed on a Hage 3DpA2 FFF printer (Hage3D, Austria). The printing parameters are summarized in **Table 1**. For best possible inter- and intra-layer weld strengths, the rather high nozzle temperature of 250 °C was used, as recommended by refs. [43,44]. In contrast to semi-crystalline 3D-printed materials, where shrinkage can be a severe issue,^[45–48] no warpage of the 3D-printed specimens was observed, as long as sufficient first layer adhesion was guaranteed.^[27,49] Therefore, the adhesive spray Dimafix (DIMA 3D, Spain) was applied to the glass mirror. Five specimens were produced per print. After completing the print, the build platform was cooled down below 50 °C and the parts were removed from the build platform. The parts were stored under standardized conditions for at least 48 h before testing. The multi-material prints were processed on a Hage3D 140L FFF printer (Hage3D, Austria). The printing parameters were slightly altered in order to obtain an identical infill density (**Table 1**).

Table 1. Values of the FFF parameters of all 3D-printed specimens in this work.

Printing parameters	Full PMMA, Hage 3DpA2	Multi-material specimen, Hage3D 140L	
		PMMA	TPC
Nozzle diameter [mm]	0.5	0.6	0.5
Nozzle temperature [°C]	250	250	250
Build platform material	Glass mirror + Dimafix	Glass mirror + Dimafix	Glass mirror + Dimafix
Build platform temperature [°C]	120	120	120
Layer thickness [mm]	0.25	0.2	0.2
Printing speed [mms ⁻¹]	20	20	10
Extrusion multiplier	1.00	0.98	0.90

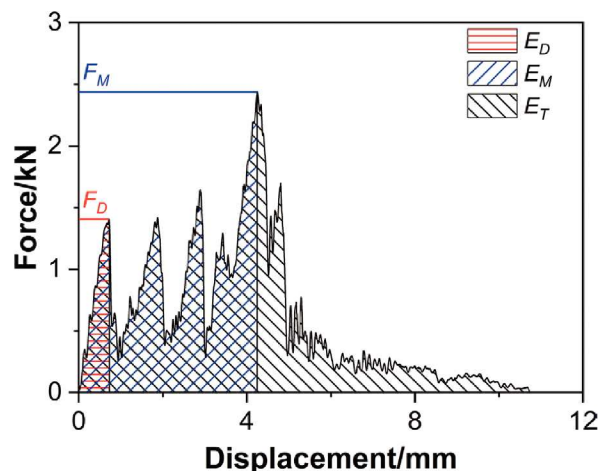


Figure 2. Definition of force (F_D) and energy at first damage (E_D), maximum global force (F_M), and energy at global force maximum (E_M) as well as total absorbed energy (E_T) exemplarily shown for the impact test performed on a PMMA sandwich plate with 50% rectilinear infill.

2.3. Impact Tests

The impact measurements were performed on the CEAST 9350 Drop Tower Impact System (Instron Deutschland GmbH, Germany) according to ISO 6603-2. For data acquisition purposes, the CEAST DAS 64K (Instron Deutschland GmbH, Germany) was used. The testing speed, deviating from the ISO standard, was set to 1 ms^{-1} . The impact setup included a 22 kN piezo striker model M2098, with a 20 mm hemispheric head. In addition to the tup holder mass of 4.3 kg, a mass of 55.18 kg was added to ensure complete puncture with minimal reduction of velocity during the test. During the impact measurements, time and force were measured. Subsequently, the energy, displacement, and velocity were calculated. Representative force-displacement graphs measured for each sample type were compared. The following predefined parameters were evaluated according to ISO 6603-2 to compare the impact behavior of the different specimens (Figure 2):

1. The maximum force reached at first damage (F_D)
2. The global force maximum (F_M)
3. The absorbed energy until first damage (E_D)
4. The absorbed energy up to the global force maximum (E_M)
5. The total absorbed energy (E_T)

Instead of evaluating 50% of F_M (F_p) and the corresponding energy value (E_p), as described in ISO 6603-2, the total amount of absorbed energy (E_T) was chosen for comparison. The reason for this is that the measured curves do not show a standard brittle or ductile behavior, where the force immediately drops to zero or reaches the maximum and gradually decreases afterward.

2.4. Optimization Techniques

In order to enhance the impact behavior of PMMA-plates, two different optimization techniques were applied. Depending on the actual application, high levels of either stiffness and

strength, or high amounts of absorbed energies before fracture can be desirable. Design optimization toward high levels of stiffness and strength have the advantage of remaining components undamaged up to high stresses. However, if stresses are higher than the material strength, this type of optimized structure usually fails in a rather brittle and catastrophic way. On the contrary, optimization toward absorbed energy is more destruction tolerant but starts to damage earlier. Both methods are viable and the choice is usually up to the designer of the component.^[50] The selected methods in this work are a topology and a material optimization approach. The topology optimization aims at finding the best distribution of material within a given design space. In other words, the optimization seeks to find the optimal load path for a particular load and boundary condition.^[51] The topology optimization was performed with the software Altair OptiStruct (Altair, USA). A Hertzian pressure distribution was used to simulate the loading via the hemispheric striker head. The optimization parameters were set as follows:

- Objective function: minimization of compliance
- Design constraint: mass-fraction of $\leq 50\%$

The minimization of the compliance was chosen as the objective function in order to increase F_D and thereby E_D . Additionally, manufacturing constraints (MINDIM = minimum member size control) were imposed to account for the minimum attainable layer thickness and the minimum nozzle diameter. In order to ensure printability, support structures were needed at the border area, as can be seen on the quarter section of the final topology-optimized part (Figure 3a).

The main idea behind improving the impact properties of PMMA-plates by means of the material was to include an elastic component to the brittle PMMA material. The elastic component should lead to an increased absorbed energy value by serving as a biomimetically inspired fracture stopper.^[51] For this purpose, a TPC interlayer was included into the PMMA-plate. To enhance the cohesion between the TPC interlayer and the PMMA outer layers, PMMA hooks were designed and fabricated into the TPC layer (Figure 3b).

2.5. Optical Fracture Analysis

To investigate the effect of different infill densities and structures, the occurrence of deviating failure mechanisms was analyzed. As a first step, photographs of the PMMA-plates after testing were recorded. To achieve a more precise analysis of the fracture behavior, scanning electron microscopy (SEM) was performed for selected impact fracture surfaces using a Tescan Vega II (Tescan Brno, s.r.o., Czech Republic) at 5 kV using secondary electrons. Prior to the measurement, the samples, fixed on SEM sample holders, were gold-sputtered with the SCD 005 Cool Sputter Coater (BAL-TEC AG, Liechtenstein) for 160 s at 20 mA.

3. Results and Discussion

The impact behavior of a material represents an important factor in terms of component design. Exemplarily, a high

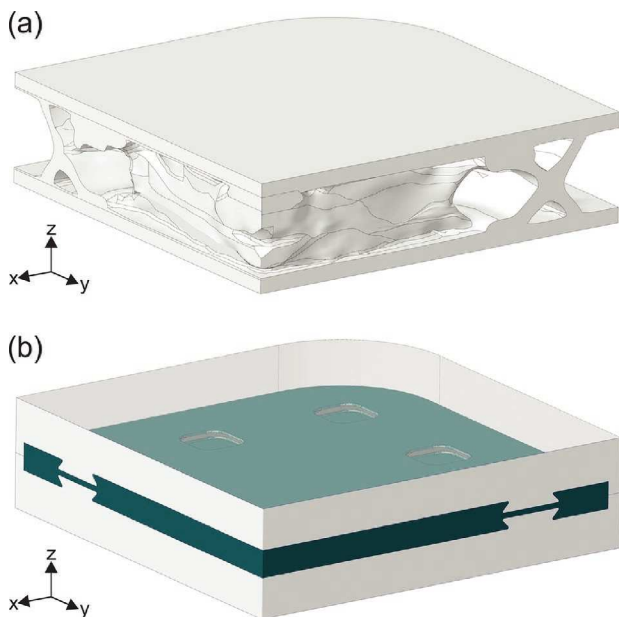


Figure 3. Quarter section of the PMMA impact specimens optimized by a topology a) and material b) optimization technique. The grey material refers to PMMA, whereas the green interlayer represents the soft TPC. The specimens are oriented in a way that the consecutive layers of printing are in z-direction.

amount of energy absorption is necessary in order to avoid implant failure in the case of an accidental trauma. Additionally, the implant should possess a certain stiffness in order to inhibit buckling. Therefore, a combination of stiffness, maximum force before fracture and energy absorption should be considered. In the following, the impact properties of 3D-printed sandwich structures with different internal struc-

tures and infill densities are discussed and compared to the material- and topology-optimized structures.

3.1. Classical Sandwich Structures

As shown in **Figure 4**, the force maximum increases independent of the infill structure with increasing infill density. This trend has also been evaluated for impact tests performed at rectilinear, octagonal, and concentric 3D-printed PLA cylinders.^[41] All tests, regardless of infill density and structure, show a step-wise failure behavior, which can be seen as several peaks in the force–displacement curves. This is a quite common phenomenon in sandwich structures,^[52] since the fracture behavior of the surface layers and the core material is quite different. Furthermore, the dynamic stiffness, which is described by the slope of the first peak, increases for all structures with increasing infill density. Interestingly, the 3D-HC structure shows a much higher stiffness compared to the other two infill patterns.

When comparing the force–displacement plots of rectilinear and gyroid structures, it can be seen that the overall behavior remains rather similar with infill densities of 30–70% (Figure 4a–c). For these six parameters, the force–displacement plots always exhibit a rather small initial peak, followed by a damage onset (sudden load drop). Subsequently, damage or crack propagation through the rest of the sample occurs, which is shown by the peaks at higher deformation. In contrast, the shape of the force–displacement plots measured for the 3D-HC structure changes its appearance already at 50% infill density. At 70% infill density (Figure 4c), the failure behavior transforms from a rather small damage onset force, followed by continuous damage propagation, to a very high initial force peak, followed by a significant load

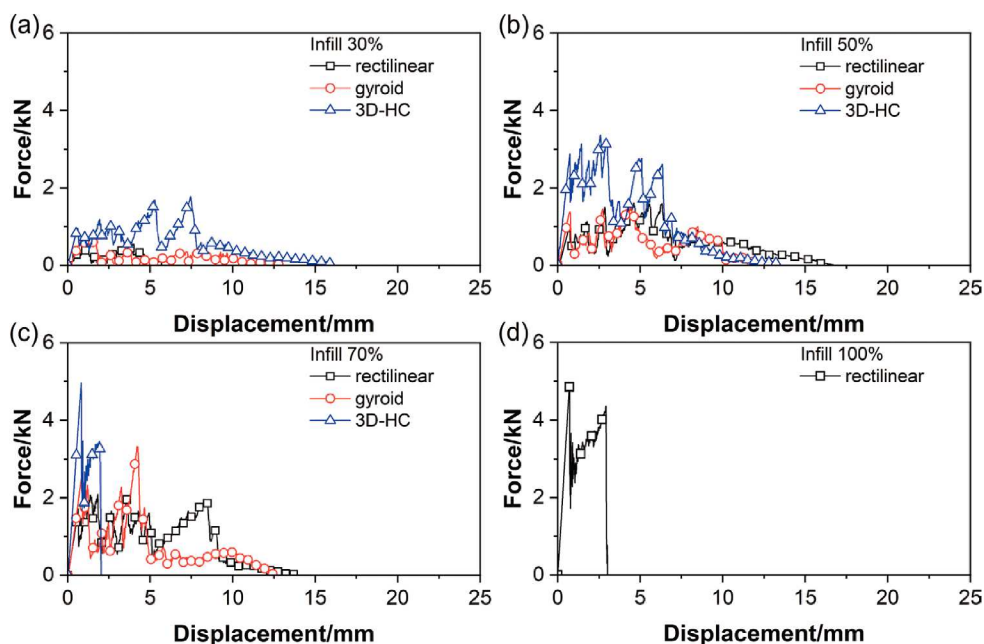


Figure 4. Force–displacement plots obtained from impact tests on 3D-printed PMMA specimens as a function of infill pattern for the infill densities of a) 30, b) 50, c) 70, and d) 100%.

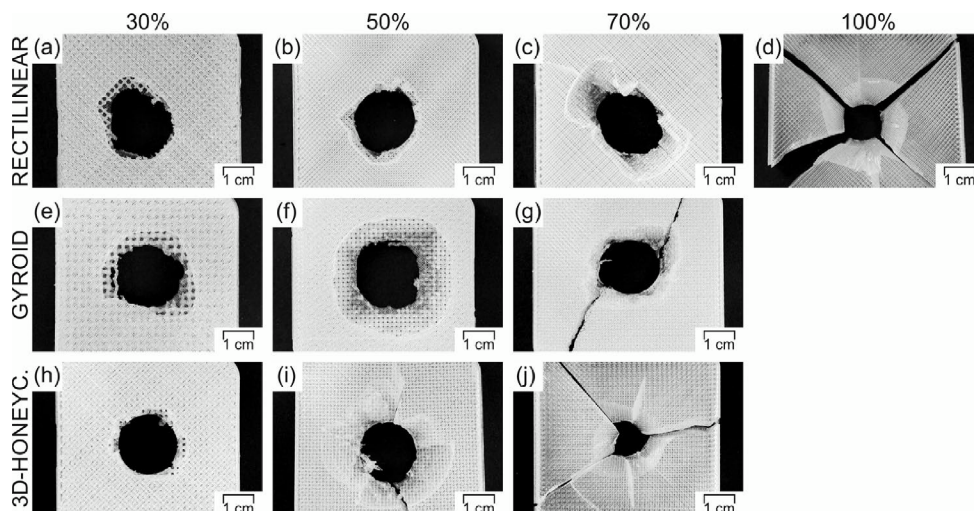


Figure 5. Comparison of the occurring failure mechanisms after impact testing 3D-printed PMMA specimens including a–d) rectilinear, e–g) gyroid, and h–j) 3D honeycomb (3D-HC) core structures with infill densities of 30%, 50%, 70%, and 100%. The side of the specimen toward the impactor is represented.

drop. This indicates the formation of a rather large initial crack. Afterward, the crack is stopped only shortly before the whole specimen ruptures in a complete brittle failure. This can be seen by the second abrupt force-drop down to 0 N^[50] at around 2 mm displacement. The rectilinear infill structure was also realized with 100% infill density. When comparing the resulting force–displacement curve of this setting (Figure 4d) to the other curves, it is noticeable that it shows the same overall behavior as the 70% infill density 3D-HC structure. Additionally, it reveals a rather high dynamic stiffness and maximum force at the first peak, followed by crack initiation and brittle failure within a few millimeters of displacement.

In order to explain the different fracture mechanisms, photos of each sandwich structure were taken after impact testing (Figure 5). The side of the specimen facing the impactor, defined as the front, is represented. Looking at the 30% infill structures in Figure 5a,e,h, the reason for the shape of the force–displacement curves in Figure 4a is obvious. Due to the low infill density, the impactor is penetrating a meshed structure instead of a homogeneous material. This explains the multitude of peaks in the force–displacement diagram. These peaks and load drops are a result of the individual material bridges being broken by the impactor.

At 70% infill density, the fracture appearance is similar for rectilinear and gyroid structures. For 70% 3D-HC (Figure 5i,j) and 100% rectilinear structures (Figure 5c,d), the transparency changes. The inner structures are no longer individually separated by air and the core of the composite begins to form a more homogeneous material. This leads to the transition in type of fracture and explains their similar force–displacement curves, even though the infill patterns are different (Figure 4c,d). The first high initial peak creates a crack, similar to the other infill patterns. Subsequently, the whole specimen, instead of individual material bridges, is destroyed. Therefore, the fracture appearance changes from a normal puncture to a more shard-like fracture (Figure 5d,j).

Furthermore, the big differences in the initial stiffness can be explained with the pictures of the fractured specimens in Figure 5. For low infill densities of gyroid and rectilinear structures, it is mainly determined by the stiffness of the top layer of the composite. In the 3D-HC structure,^[53,54] the core layers provide additional support.

For a better understanding and more direct comparison, the respective forces and energies are compared in Figures 6 and 7 in detail. As mentioned above, independent of the infill structure, F_D and F_M increase with growing infill density (Figure 6). This increase is nearly linear with the exception of infill densities between 70% and 100% in the case of rectilinear internal structures. A significant increase in the tensile strength for such high infill densities was also reported for 3D-printed

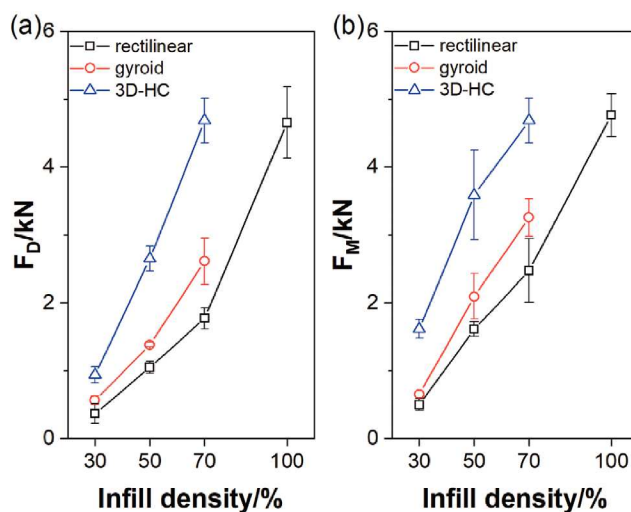


Figure 6. Force at first damage (F_D) a) and global force maximum (F_M) b) of 3D-printed PMMA impact specimens as a function of infill density and infill pattern. Each point is the average of five samples with an error bar to indicate deviation.

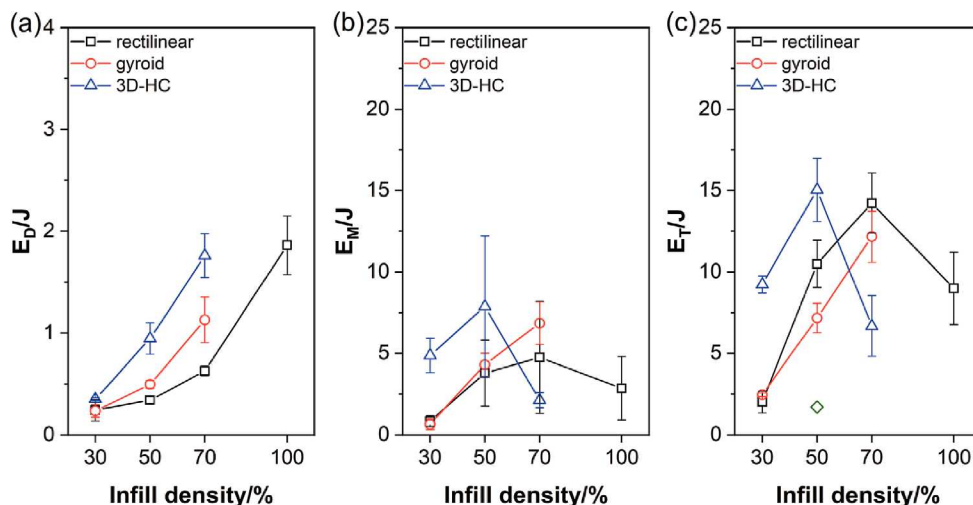


Figure 7. Energy at first damage (E_D) a), energy at maximum force (E_M) b), and total absorbed energy (E_T) c) of 3D-printed PMMA impact specimens as a function of infill density and infill pattern. Each point is the average of five samples with an error bar to indicate deviation.

ABS.^[55] In addition, 3D-HC internal structures result in higher forces at the same degree of infill compared to rectilinear and gyroid structures. The high-impact energy absorption for honeycomb structures is well known,^[56,57] due to the better distribution of loads and strains, compared to other infill structures. The maximum values for F_D and F_M are reached for 70%-filled 3D-HC internal structures and 100%-filled rectilinear core structures.

As shown in Figure 7a, the dissipated energy up to first damage (E_D) follows the same trend as the forces (F_D and F_M). On the other hand, E_M and E_T reveal a completely different trend (Figure 7b,c). Only gyroid structures show a continuous increase in E_M and E_T with rising infill density. For rectilinear and 3D-HC internal structures, E_M and E_T increase with the infill density up to 50% for 3D-HC and 70% for rectilinear. Afterward, the energies decrease drastically. This drop in E_M and E_T can directly be attributed to the change in fracture behavior (Figure 5c,d,i,j). Due to the brittle nature of the fracture, F_D and E_D are equal to F_M and E_M most of the time for those two parameter settings. The brittle fracture behavior of PMMA has already been shown for 4.5 mm thick casted plates. These plates resulted in total absorbed energies of approx. 7 J.^[58] As the impact energy increases with increasing samples thickness, the 14 J evaluated for the 8 mm thick, 3D-printed PMMA plates including a 100%-filled rectilinear structure are reasonable.^[59]

The standard deviation for E_M at 50% 3D-HC is very high, due to the occurrence of F_M at strongly varying deformation levels (depending on whether $F_D = F_M$ or not). It is questionable, whether the application of E_M for the designing of implants is reasonable. The total amount of energy dissipated before failure (E_T) shows a similar trend, compared to E_M . However, due to the high levels of displacement, it might not be a viable design criterion.

To further investigate the difference between the two occurring failure mechanisms (step-wise and more homogeneous brittle), the fracture surface of 30%- and 100%-filled specimens including rectilinear core-structures were analyzed by means of

SEM (Figure 8). Considering the low infill density, the shape of the individual filaments is clearly visible at 30% (Figure 8a). The change in the strand diameter is caused by bridging. The strands themselves reveal a sufficient connection, since they are still attached to each other even in close vicinity of the fracture. In detail, the fracture surface (Figure 8b) shows some signs of minor micro-ductility, but is brittle in its overall appearance.

For the fracture surface of completely filled specimens, neither weld lines nor air gaps between the filaments are recognizable. This indicates excellent inter- and intra-layer bonding (Figure 8c), similarly to refs. [43,44]. Furthermore, it affirms the assumption of an almost homogeneous material, as indicated above. The fracture surface shows a rather homogeneous brittle failure, even on a small-scale level (Figure 8d).

The brittle fracture behavior of PMMA is well known and has also been shown for heat-cured PMMA denture base after impact testing.^[60]

3.2. Optimized Sandwich Structures

To further improve the achievable levels of stiffness and energy absorption during impact, topology and material optimization techniques were applied. The topology-optimized PMMA impact specimens were designed considering a reduction of 50% in weight as a boundary condition. The calculated internal structure was printed with an infill density of 100%. Therefore, a representative force–displacement curve measured for a topology-optimized plate is compared with other 50%-filled specimens (Figure 9b), since they are closest in the used infill volume. Compared to other 50% infill density settings, the topology-optimized structure performs quite well in terms of dynamic stiffness and F_D . Both values are similar to 3D-HC and higher than rectilinear and gyroid internal structures. However, in terms of overall fracture behavior it is close in shape to 70% 3D-HC and 100% rectilinear structures, since it fails rather brittle without a pronounced stepwise crack propagation phase.

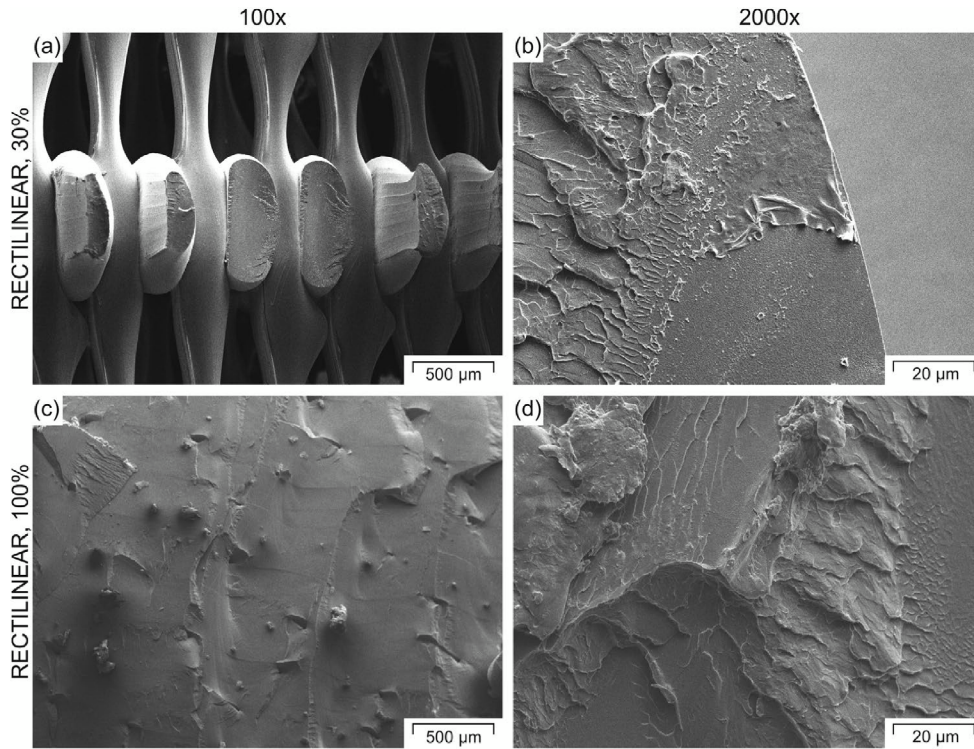


Figure 8. Scanning electron microscopy (SEM) fracture surfaces of 3D-printed PMMA impact specimens, including a rectilinear core structure with infill densities of 30% and 100%.

The material optimization technique was applied for plates including a rectilinear core structure with infill densities of 30 and 100% (Figure 9a,c). Representative force–displacement curves of the optimized structure are shown in comparison with 30% and 100% filled classical sandwich structures. Inde-

pendent of the infill density, the TPC interlayer leads to very high overall displacement values before ultimate failure of the structure. Regarding an infill density of 30%, material-optimized samples reach insignificantly higher forces compared to pure rectilinear and gyroid internal structures, but lower forces

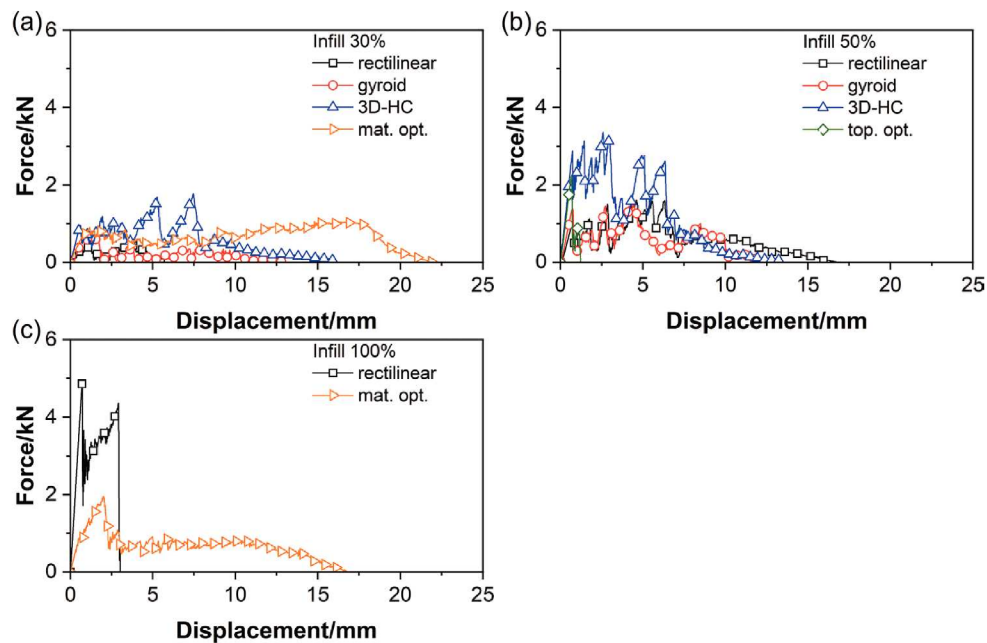


Figure 9. Force–displacement plots of topology- (top. opt.) and material-optimized (mat. opt.) samples. Data of classical sandwich structures at similar infill volume from Figure 4 are included for comparison.

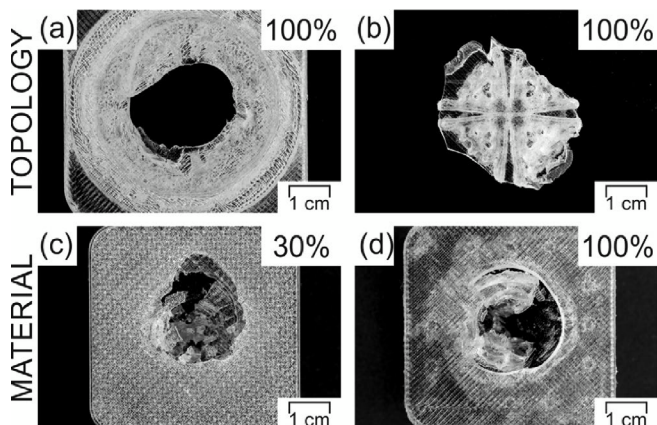


Figure 10. 3D-printed PMMA specimens including the topology-optimized sandwich structure a, punctured plate and b, counterpart) and material-optimized sandwich structures with 30% infill c) and 100% infill d) after impact testing.

in contrast to 3D-HC structures (Figure 9a). Additionally, the maximum force occurs at extremely high deformation values, limiting its use for the targeted application.

Figure 10a,b shows a representative topology-optimized plate after impact testing. In Figure 10b, the removed counterpart is shown. The counterpart was pressed out by the impactor during the impact test. The topology-optimized structure was designed to divert the absorbed energy away from the center, resulting in a nearly centrosymmetric structure. The effectiveness is proven by the fact that the location of the impact site itself is not destroyed during the test but rather fails due to the fracture of the bottom layers.

For the 30%-filled (Figure 10c) and 100%-filled (Figure 10d) material-optimized plates, only the impacted plates are represented. The PMMA material detached almost completely from the TPC layer, indicating a rather insufficient bonding between these two materials. De-bonding of layers is always critical in composite structures, since it severely degrades stiffness and maximum forces.

For both optimized sandwich structures, the PMMA matrix itself fractured in a macroscopically brittle way. Therefore, SEM images of the fracture surface of these specimens were not included, as their appearance should be similar to the fracture surfaces represented in Figure 8.

The respective forces and energies are compared to the standard infill densities and structures in Figures 11 and 12. The values of F_D and F_M obtained for the topology-optimized structure are high but cannot outperform the values reached with 3D-HC structures (Figure 11). Similar is true for the 30% infill material-optimized structure. The F_D and F_M values of the 100% infill material-optimized structure only reach around 50% of the 100% rectilinear structure.

The absorbed energies show a different trend, tough (Figure 12). Since the topology optimization was done for maximum stiffness and not amount of absorbed energy, it is not surprising that the resulting absorbed energies E_M and E_T are rather small for these structures. However, up to the damage onset (E_D) it is on par with the 3D-HC structure with an infill density of 50%.

For the material-optimized specimens, E_D and E_T are highest independently of the infill density (Figure 12a,c). For an infill density of 30%, E_M is highest for material-optimized samples as well. This can mainly be attributed to energy dissipated by the soft interlayer up to very high levels of deformation before failure. On the other side, completely filled plates with a soft interlayer showed no increase of dissipated energy compared to 100% rectilinear infill. Different slopes in Figure 9c indicate that the two PMMA parts of the sandwich structure were not supporting each other, due to insufficient bonding with the TPC interlayer.

The total energy dissipated by the material-optimized structure (E_T) by itself seems very promising (Figure 12c). For infill densities of 30% and 100%, the absorbed energies are the highest of all tested structures. If the main goal is to maximize energy absorption before failure without accounting for deformation limits, material optimization can be used quite well. Since this is not the case for the target application, E_T should not be taken into account.

4. Conclusion

The present study gives an insight into the dependency of impact properties of sandwich structures on the internal core-architecture and the infill density. It was determined that the impact properties of classical 3D-HC structures outperform rectilinear and gyroid internal structures at the same infill density. Furthermore, high values for the force at first damage (F_D) and the corresponding absorbed energy (E_D) were achieved with the stiffness-based topology optimization approach. The fracture pattern indicates that a diversion of stresses radial from the center of impact was successfully established. However, due to the resulting stress concentration at the bottom of the plate, the whole structure failed quite early leading to rather small overall absorbed energies.

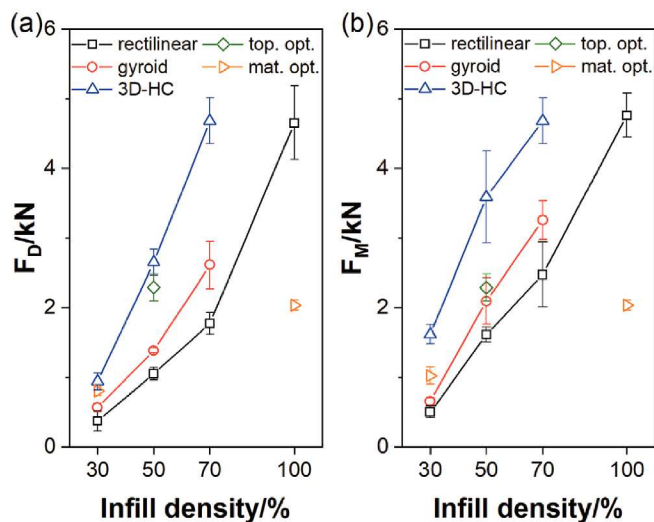


Figure 11. Force at first damage (F_D) a) and global force maximum (F_M) b) of 3D-printed PMMA impact specimens including classical, as well as optimized sandwich structures as a function of infill density and infill pattern. Each point is the average of five samples with an error bar to indicate deviation.

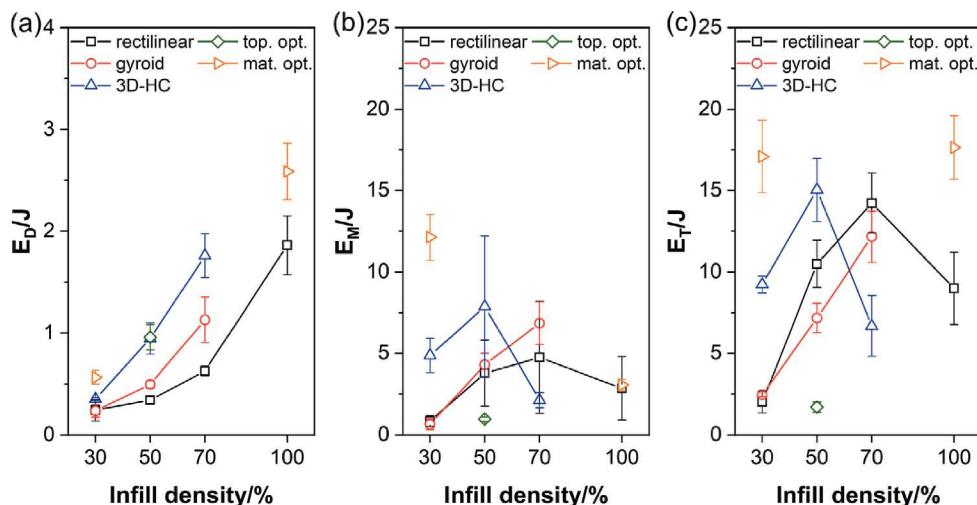


Figure 12. Energy at first damage (E_D) a), energy at maximum force (E_M) b), and total absorbed energy (E_T) c) of 3D-printed PMMA impact specimens, including classical as well as optimized sandwich structures as a function of infill density and infill pattern. Each point is the average of five samples with an error bar to indicate deviation.

By means of material optimization techniques, wherein a soft TPC interlayer is embedded into a PMMA matrix material to act as a crack stopper, all characteristic impact energies (E_D , the absorbed energy at the maximum force – E_M and the total absorbed energy – E_T) were increased. Unfortunately, the maximum force (F_M) and the dynamic stiffness were decreased. Therefore, these values have to be taken with caution, as they are achieved at large deformations, which might be dangerous in real application. One way to improve this method would be to change to a different compliant interlayer, which has a higher affinity toward PMMA to avoid de-cohesion. Thus, it should be possible to reach higher forces before failure.

Furthermore, application-driven tests are suggested for future studies, as cranial bone generally has a curved shape and x - y deformations are restricted by surrounding bone, which changes the constraint of the implant significantly.

Concluding the results, it appears that E_D in combination with the dynamic stiffness or deformation reached up to this point represent a very critical parameter regarding the designing process of implants. If a high tolerated force level in relation to the absorbed energy is desired, 3D-HC internal structures at an infill density of 70% and rectilinear structures with an infill density of 100% are recommended at this time.

Acknowledgements

This work was supported by CAMed (COMET K-Project 871132) which is funded by the Austrian Federal Ministry of Transport, Innovation and Technology (BMVIT), Austrian Federal Ministry of Digital and Economic Affairs (BMDW), and the Styrian Business Promotion Agency (SFG). Furthermore, the authors would like to thank Dr. Joamin Gonzalez-Gutierrez for the fruitful discussions.

Conflict of Interest

The authors declare no conflict of interest.

Keywords

3D printing, additive manufacturing, impact testing, poly(methyl methacrylate), polymer implants

Received: April 30, 2019

Revised: July 30, 2019

Published online: August 30, 2019

- [1] M. Puska, A. J. Aho, P. Vallittu, in *Advances in Composite Materials* (Ed: P. Tesinova), Vol. 1, InTech, Rijeka, Croatia **2011**.
- [2] G.-Y. Park, *Inaugural-Dissertation*, Ruhr-Universität Bochum, Germany **2012**.
- [3] R. J. Kriegel, *Inaugural-Dissertation*, Rheinischen Friedrich-Wilhelms-Universität Bonn, Germany **2006**.
- [4] A. E. Abdulai, M. I. Iddrissu, T. K. Dakurah, *Ghana Med. J.* **2006**, 40, 18.
- [5] C. J. White, *BTEC Higher National Diploma*, Lambeth College, London **1998**.
- [6] M. Navarro, A. Michiardi, O. Castaño, J. A. Planell, *J. R. Soc., Interface* **2008**, 5, 1137.
- [7] E. Wintermantel, S.-W. Ha, *Medizintechnik*, Springer, Berlin **2009**.
- [8] A. Ridwan-Pramana, P. Marcián, L. Borák, N. Narra, T. Forouzanfar, J. Wolff, *PLoS One* **2017**, 12, e0179325.
- [9] E. Caro-Osorio, R. de La Garza-Ramos, S. R. Martínez-Sánchez, F. Olazarán-Salinas, *Surg. Neurol. Int.* **2013**, 4, 136.
- [10] D. Marchac, A. Greensmith, *J. Plast. Reconstr. Aes. Surg.* **2008**, 61, 744.
- [11] A. L. Fernandes da Silva, A. M. Borba, N. R. Simão, F. L. M. Pedro, A. H. Borges, M. Miloro, *Case Rep. Surg.* **2014**, 8.
- [12] L. Chiarini, S. Figurelli, G. Pollastri, E. Torcia, F. Ferrari, M. Albanese, P. F. Nocini, *J. Cranio. Maxill. Surg.* **2004**, 32, 5.
- [13] P. Fiaschi, M. Pavanello, A. Imperato, V. Dallolio, A. Accogli, V. Capra, A. Consales, A. Cama, G. Piatelli, *J. Neurosurg-Pediatr.* **2016**, 17, 705.
- [14] H. Rotaru, H. Stan, R. Schuhmacher, G. Baciut, H. Chezan, S.-G. Kim, presented at 21st Int. DAAAM Symp., Zadar, Croatia, October **2010**.
- [15] B.-J. Kim, K.-S. Hong, K.-J. Park, D.-H. Park, Y.-G. Chung, S.-H. Kang, *J. Korean Neurosurg. Soc.* **2012**, 52, 541.



- [16] J. A. Morales-Gómez, E. Garcia-Estrada, J. E. Leos-Bortoni, M. Delgado-Brito, L. E. Flores-Huerta, A. A. de La Cruz-Arriaga, L. J. Torres-Díaz, Á.R. M.-P. de León, *J. Neurosurg.* **2018**, *5*, 1721.
- [17] H. Rotaru, M. Baciut, H. Stan, S. Bran, H. Chezan, A. Iosif, M. Tomescu, S.-G. Kim, A. Rotaru, G. Baciut, *J. Cranio. Maxill. Surg.* **2006**, *34*, 242.
- [18] E. T. W. Tan, J. M. Ling, S. K. Dinesh, *J. Neurosurg.* **2016**, *124*, 1531.
- [19] M. Verius, F. Marreiros, Y. Heuze, C. Unterhofer, W. Recheis, presented at European Congress of Radiology, Vienna, Austria, March **2011**.
- [20] A. de La Peña, J. de La Peña-Brambila, J. la Pérez-De Torre, M. Ochoa, G. J. Gallardo, *3D Print. Med.* **2018**, *4*, 4.
- [21] L. C. Hieu, E. Bohez, J. Vander Sloten, P. Oris, H. N. Phien, E. Vatcharaporn, P. H. Binh, *Technol. Health Care* **2002**, *10*, 413.
- [22] M. Moser, R. Schmid, R. Schindel, G. Hildebrandt, *J. Cranio. Maxill. Surg.* **2017**, *45*, 295.
- [23] P. S. D'Urso, W. J. Earwaker, T. M. Barker, M. J. Redmond, R. G. Thompson, D. J. Effeney, F. H. Tomlinson, *Br. J. Plast. Surg.* **2000**, *53*, 200.
- [24] U. Gbureck, T. Hölzel, C. J. Doillon, F. A. Müller, J. E. Barralet, *Adv. Mater.* **2007**, *19*, 795.
- [25] J. Parthasarathy, *Ann. Maxillofac. Surg.* **2014**, *4*, 9.
- [26] S. C. Ligon, R. Liska, J. Stampfl, M. Gurr, R. Mülhaupt, *Chem. Rev.* **2017**, *117*, 10212.
- [27] M. Spoerk, J. Gonzalez-Gutierrez, J. Sapkota, S. Schuschnigg, C. Holzer, *Plast., Rubber Compos.* **2018**, *47*, 17.
- [28] Wohlers Associates, *Wohlers Report 2016*, Wohlers Associates, Fort Collins, CO **2016**.
- [29] A. Gebhardt, J. Kessler, L. Thurn, *3D-Drucken*, Hanser, München, Germany **2016**.
- [30] I. Gibson, D. W. Rosen, B. Stucker, *Additive Manufacturing Technologies*, Springer, Boston, MA **2010**.
- [31] M. Gurr, R. Mülhaupt, in *Polymer Science: A Comprehensive Reference* (Eds: M. Moeller, K. Matyjaszewski), Vol. 1, Elsevier, Amsterdam **2012**.
- [32] O. Diegel, in *Comprehensive Materials Processing* (Eds: S. Hashmi, C. J. vanTyne, G. F. Batalha, B. Yilbas), Vol. 1, Elsevier, Amsterdam **2014**.
- [33] S. Bose, S. Vahabzadeh, A. Bandyopadhyay, *Mater. Today* **2013**, *16*, 496.
- [34] L. C. Magalhães, N. Volpato, M. A. Luersen, *J. Braz. Soc. Mech. Sci. Eng.* **2014**, *36*, 449.
- [35] J. Cantrell, S. Rohde, D. Damiani, R. Gurnani, L. DiSandro, J. Anton, A. Young, A. Jerez, D. Steinbach, C. Kroese, P. Ifju, in *Advancement of Optical Methods in Experimental Mechanics* (Eds: S. Yoshida; L. Lamberti, C. Sciammarella), Vol. 3, Springer International Publishing, Cham, Switzerland **2017**.
- [36] D. Farbman, C. McCoy, presented at ASME 2016 Int. Manufacturing Science and Engineering Conf., Blacksburg, VA, June–July **2016**.
- [37] C. Lu, M. Qi, S. Islam, P. Chen, S. Gao, Y. Xu, X. Yang, *Int. J. Precis. Eng. Manuf. Green Technol.* **2018**, *5*, 47.
- [38] H. Yazdani Sarvestani, A. H. Akbarzadeh, A. Mirbolghasemi, K. Hermenean, *Mater. Des.* **2018**, *160*, 179.
- [39] R. Rajpal, K. P. Lijesh, K. V. Gangadharan, *Addit. Manuf.* **2018**, *22*, 583.
- [40] L. Villalpando, H. Eiliat, R. J. Urbanic, *Proc. CIRP* **2014**, *17*, 800.
- [41] A. Tsouknidas, M. Pantazopoulos, I. Katsoulis, D. Fasnakis, S. Maropoulos, N. Michailidis, *Mater. Des.* **2016**, *102*, 41.
- [42] D. H. Rosenzweig, E. Carelli, T. Steffen, P. Jarzem, L. Haglund, *Int. J. Mol. Sci.* **2015**, *16*, 15118.
- [43] M. Spoerk, F. Arbeiter, H. Cajner, J. Sapkota, C. Holzer, *J. Appl. Polym. Sci.* **2017**, *134*, 45401.
- [44] F. Arbeiter, M. Spoerk, J. Wiener, A. Gosch, G. Pinter, *Polym. Test.* **2018**, *66*, 105.
- [45] M. Spoerk, C. Savandaiah, F. Arbeiter, J. Sapkota, C. Holzer, *Polym. Compos.* **2019**, *40*, 638.
- [46] M. Spoerk, C. Savandaiah, F. Arbeiter, G. Traxler, L. Cardon, C. Holzer, J. Sapkota, *Composites, Part A* **2018**, *113*, 95.
- [47] M. Spoerk, J. Sapkota, G. Weingrill, T. Fischinger, F. Arbeiter, C. Holzer, *Macromol. Mater. Eng.* **2017**, *302*, 1700143.
- [48] M. Spoerk, F. Arbeiter, I. Raguž, G. Weingrill, T. Fischinger, G. Traxler, S. Schuschnigg, L. Cardon, C. Holzer, *Macromol. Mater. Eng.* **2018**, *303*, 1800179.
- [49] M. Spoerk, J. Gonzalez-Gutierrez, C. Lichal, H. Cajner, G. Berger, S. Schuschnigg, L. Cardon, C. Holzer, *Polymers* **2018**, *10*, 490.
- [50] J. Kimberley, L. E. Lamberson, S. Mates, in *Dynamic Behavior of Materials* (Eds: V. Chalivendra, B. Song, D. Casem), Vol. 1, Springer International Publishing, Cham, Switzerland **2019**.
- [51] O. Sigmund, K. Maute, *Struct. Multidiscip. Optim.* **2013**, *48*, 1031.
- [52] Grace Xiang Gu, presented at 14th Int. LS-DYNA Conf., Dearborn, MI, June **2016**.
- [53] E. Provaggi, C. Capelli, B. Rahmani, G. Burriesci, D. M. Kalaskar, *Mater. Des.* **2019**, *163*, 107540.
- [54] J. Podroužek, M. Marcon, K. Ninčević, R. Wan-Wendner, *Materials* **2019**, *12*, 499.
- [55] M. Fernandez-Vicente, W. Calle, S. Ferrandiz, A. Conejero, *3D Print. Addit. Manuf.* **2016**, *3*, 183.
- [56] Q. Zhang, X. Yang, P. Li, G. Huang, S. Feng, C. Shen, B. Han, X. Zhang, F. Jin, F. Xu, T. J. Lu, *Prog. Mater. Sci.* **2015**, *74*, 332.
- [57] L. L. Hu, T. X. Yu, *Int. J. Impact Eng.* **2010**, *37*, 467.
- [58] K. C. Jajam, H. V. Tippur, S. A. Bird, M. L. Aud, in *Dynamic Behaviour of Materials* (Eds: V. Chalivendra, B. Song, D. Casem), Vol. 1, Springer International Publishing, Cham, Switzerland **2014**.
- [59] M. W. Money, *Dissertation*, Queen Mary University of London **1988**.
- [60] A. O. Alhaleb, H. M. Akil, Z. A. Ahmad, *Saudi J. Dent. Res.* **2017**, *8*, 26.

Publication 5

Bibliographic information

Title: Material extrusion-based additive manufacturing of polyetheretherketone cranial implants: Mechanical performance and print quality

Authors: Sandra Petersmann¹, James A. Smith², Ute Schäfer^{2,3}, Florian Arbeiter^{1,*}

Affiliations:

¹Materials Science and Testing of Polymers, Montanuniversitaet Leoben, Otto Gloeckel-Straße 2, 8700, Leoben, Austria

²Research Unit Experimental Neurotraumatology, Department of Neurosurgery, Medical University of Graz, Auenbruggerplatz 22, 8036 Graz, Austria

³BioTechMed-Graz, 8036 Graz, Austria

Periodical: Journal of Materials Research and Technology

DOI: under review

Relevant contributions to this publication:

Conceptualisation: Florian Arbeiter

Methodology: Sandra Petersmann, James A. Smith

Investigation: Sandra Petersmann, James A. Smith, Florian Arbeiter

Validation: Sandra Petersmann, Florian Arbeiter

Formal analysis: Sandra Petersmann

Data Curation: Sandra Petersmann

Funding Acquisition: Ute Schäfer

Project Administration: Ute Schäfer

Resources: Ute Schäfer

Supervision: Florian Arbeiter

Writing - Original Draft: Sandra Petersmann, James A. Smith

Writing - Review & Editing: Sandra Petersmann, James A. Smith, Ute Schäfer, Florian Arbeiter

Visualisation: Sandra Petersmann

Material extrusion-based additive manufacturing of polyetheretherketone cranial implants: Mechanical performance and print quality

Sandra Petersmann^a, James A. Smith^b, Ute Schäfer^{b,c}, Florian Arbeiter^{a,*}

^aMaterials Science and Testing of Polymers, Montanuniversitaet Leoben, Otto Gloeckel-Straße 2, 8700 Leoben, Austria

^bResearch Unit Experimental Neurotraumatology, Department of Neurosurgery, Medical University of Graz, Auenbruggerplatz 2², 8036 Graz, Austria

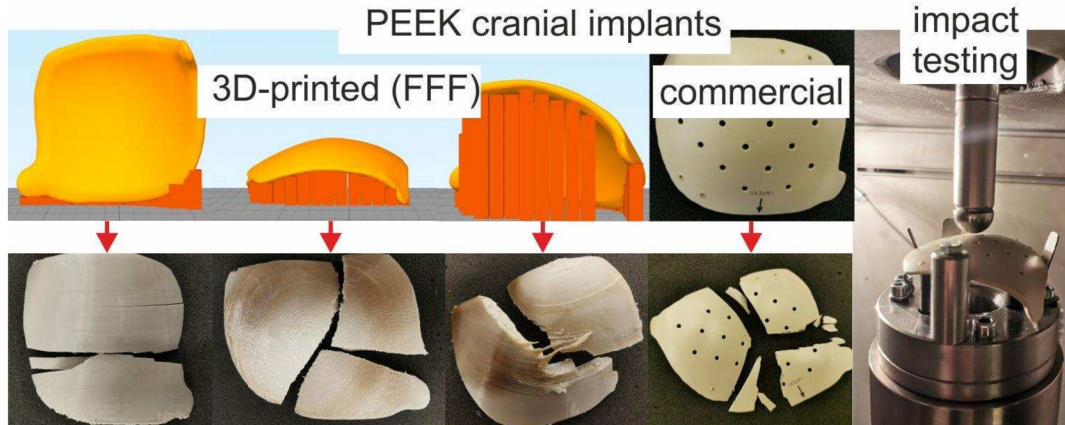
^cBioTechMed-Graz, Graz, Austria

*Corresponding author: mail: florian.arbeiter@unileoben.ac.at, phone: +43 3842 402 2122

Abstract

Polyetheretherketone (PEEK) is considered a 'gold-standard' material choice for cranial bone reconstruction. The introduction of additive manufacturing (AM) into the pipeline for patient specific cranial implant (PSCI) fabrication could accelerate supply chain needs and improve patient outcomes. Fused filament fabrication (FFF), a material extrusion-based technology, is a much-researched process due to its accessibility and ease of use. However, the quality of PEEK processed by FFF is highly affected by the applied printing profile. Therefore, in this study, the effects of printing parameters such as build orientation and air flow temperature on mechanical performance (cyclic and impact tests) and implant quality (characterisation of surface topography, discoloration and crystallinity) were analysed and compared with a commercial milled PEEK implant. It has been found that horizontally printed implants show higher mechanical integrity compared to implants printed upright or tilted by 45°, but obtain lower surface quality. In addition, lower air flow temperatures lead to strong implant discolorations due to high amounts of amorphousness, which further result in high absorbed energies during impact as well as large deformations until complete failure. The best results from a mechanical point of view were achieved with PSCIs printed at a build orientation of 180°, an air flow temperature of 210 °C, a shell number of 3, a layer height of 0.15 mm, a printing speed of 50 mm/min, a rectilinear ±45° infill pattern and an implant thickness of 5 mm. However, the surface quality of implants produced this way is not completely satisfactory, and the arrangement of the support structures must be further improved.

Graphical abstract



Highlights

- Comparison of commercial (milled) and 3D-printed PEEK cranial implants
- Impact of build orientation and air flow temperature on mechanics and print quality
- Crystallinity, discoloration and waviness of FFF PEEK cranial implants
- Correlation between crystallinity and mechanical performance

Keywords

polyetheretherketone; PEEK; fused filament fabrication; cranial implant; mechanical integrity; crystallinity

Introduction

Polyetheretherketone (PEEK) is a high-temperature thermoplastic that has become a default surgical material of choice for cranial reconstruction post-trauma [1,2]. Clinical favour is credited to its mechanical behaviour, which is comparable to cranial bone. Furthermore, PEEK has a high thermal resistance with a glass transition temperature (T_g) of approx. 143 °C and a melting temperature (T_M) of around 345 °C. Together with its high chemical resistance, the polymer is able to withstand autoclave/gamma ray sterilisation processes and degradation from body fluids [3–10]. PEEK is also bio-inert, non-hygroscopic, non-magnetic and translucent under X-ray [11–14]. The latter allows clinical check up by computed tomography (CT) and magnetic resonance imaging, which is a limitation for metallic implants. Moreover, the polymer can be shaped, machined and polished with ease, reinstating patient aesthetic to high levels of surgical satisfaction [2,15].

Presently, the logistics of fabricating patient specific cranial implants (PSCIs) is time consuming, with lead times of several weeks, and expensive [14,16]. Both could be improved by implementing additive manufacturing (AM) into the manufacturing process. AM enables a high freedom of design, a reduction in process steps and a simplified supply chain [17]. Especially material extrusion-based AM methods, which have become increasingly popular, since they are relatively affordable and are easy to handle. Among them, fused filament fabrication (FFF) is a widely accessible technology that traditionally purposes thermoplastic filaments into three-dimensional objects of varying complexity, in a layer-by-layer manner [18,19]. Numerous materials are processible via FFF. However, the application is mainly limited to amorphous or semi-crystalline thermoplastics, which crystallise very slowly (e.g. polylactide). This is due to problems such as shrinkage and warpage that arise from the complex crystallisation behaviour of most semi-crystalline polymers. This crystallisation behaviour is further influenced by the printers processing parameters, which makes finding optimal parameter settings difficult and time-consuming [20]. Besides, special printers are required to process high-temperature thermoplastics such as PEEK, in order to, achieve working temperatures of approx. 425 °C [21].

Over the past decade numerous studies have been performed to optimise FFF PEEK printing of mechanical test specimens. However, few attempts have been made to translate these results into clinically approved PSCIs [22–37]. Some of the earliest PEEK PSCI feasibility studies were performed by Honigmann et al. [38], who adopted traditional implant fabrication strategies – CT scan of patient segmentation, computer-aided design

(CAD) implant generation, tessellation and conversion from standard triangle language (STL) file format to G-code, which is readable by the printer – before substituting conventional fabrication technologies with the FFF process. Qualitative results confirmed that PEEK could be purposed into PSCIs. However, no quantitative data on the print variables used, or their subsequent performance were presented. A recent study by Sharma et al. [16] assessed the impact of layer thickness, infill rate and pattern as well as shell number/perimeter on the geometrical accuracy of FFF PEEK. Through statistical analysis it was confirmed that infill pattern, followed by layer thickness, followed by shell number and finally by infill rate caused the greatest deviation in specimen dimensions. The optimal printing parameters were defined as those which caused the least deviation: 150 µm layer thickness, 80% infill rate, 2 shells and a rectilinear print infill. These parameters were then applied to fabricate PSCIs in a vertical (upright) position. Surface inspection revealed colour variability, which was credited to instable air flow temperatures throughout the chamber, causing non-isotropic crystallisation in the specimens upon cooling. It is understood that fluctuations in % crystallinity has a direct impact on the mechanical performance of the final part, as demonstrated by Yang et al. [35], who showed that higher crystallinity increases stiffness and yield strength of FFF PEEK. The level of crystallinity in FFF parts is mostly determined by the temperature profile resulting from the printing parameters selected and the heat distribution around the part, both of which effect the cooling rate and subsequently the time for crystallisation [29,39,40]. Follow up studies by Sharma et al. [41] focused upon the dimensional accuracy, dimensional repeatability and morphological symmetry, as well as compressive performance of FFF PSCIs. Despite attaining cranial bone-like performance, large standard deviations driven by microcavities pose concern i.e., PSCIs could break into multiple pieces and/or increased displacement may harm surrounding soft tissues. Limitations to the study also included the use of a testing speed (1 mm/min) that was not akin to a specific trauma scenario.

The first clinic to directly print and implant a FFF PEEK PSCI in a patient, on site, was Skåne University hospital in Sweden in 2021 [42]. As this surgery has only recently taken place, there is currently no short- or long-term data on the performance of the PSCI and the health status or recovery of the patient. Nevertheless, the literature clearly supports the geometric, morphological and mechanical feasibility and implantability of in-house FFF PEEK PSCIs. Hence, further studies are needed to truly understand the impact of processing conditions on final performance [16,38,41].

In this study, the impact of both thermal and non-thermal printing variables on the final aesthetic and mechanical behaviour of FFF PEEK-PSCIs was assessed. Key print variables such as air flow temperature and build orientation were used among others to optimise the crystallisation and surface resolution of the PSCIs, in an attempt to promote colour uniformity and smoothness, as haptics and appearance are very important to surgeons. Differential scanning calorimetry (DSC) was performed to assess whether changes in the print variables led to alterations in the degree of crystallinity. Levels of discoloration were analysed via Vis-spectroscopy. The surface quality was examined by measuring the waviness of the implant's surfaces. Cyclic and impact tests were performed to identify the FFF implants that match the mechanical performance of a conventionally milled PEEK PSCI. Findings from this study could be used to establish robust protocols, helping to standardise the fabrication of FFF PEEK PSCIs in clinics world-wide.

1. Material and methods

1.1. Materials

VESTAKEEP® i4 3DF-T (Evonik Industries AG, Germany), a commercially available PEEK filament 1.75 mm in diameter, was used throughout the study. The “T” in the material designation stands for “Testing Grade”. It has the same processing and mechanical product properties as the Implant Grade (VESTAKEEP® i4 3DF) but without the documentation required for approval in medical technology. The printed PSCIs were compared with a customised milled PEEK implant manufactured by Stryker (Michigan, US).

1.2. Processing of the 3D-printed specimens

The PSCIs were sliced in the software Simplify3D Version 3.0 (Simplify3D, USA) and processed in an Apium M220 (Apium Additive Technologies GmbH, Germany) with the printing parameters summarised in Table 1. The nozzle temperature for the first layer was 440 °C before rising to 470 °C for better adhesion. One specimen was fabricated per print. In total, 3 specimens were fabricated per printing profile. Before printing, the filament was stored and dried at 120 °C for at least 12 h in an Apium F300 filament dryer (Apium Additive Technologies GmbH, Germany).

Table 1: Summary of the printing parameters for all specimens (standard values in bold).

Printing parameters	Levels
Nozzle temperature (°C)	470
Printing speed (mm/s)	50 / 10
Printing speed of the first layer (% of the printing speed of subsequent layers)	100
Nozzle material	Steel
Nozzle diameter (mm)	0.4
Build platform material	Stainless steel 316L
Air flow temperature (°C)	0 / 70 / 140 / 210 / 280
Layer thickness (mm)	0.15 / 0.30
First layer thickness (mm)	0.15 / 0.30
Infill pattern	Rectilinear / Grid
Infill density (%)	100
Infill angle (°)	±45 / 0/90
Build orientation (°)	45 / 90 / 180
Number of concentric perimeters (shells)	1 / 3

The printing speed, air flow temperature, layer thickness, build orientation and infill structure (infill pattern, infill angle and number of concentric perimeters) were varied to find the optimal printing profile for PEEK PSCIs. The most promising variant per build orientation was processed with a higher average thickness of 5 mm (standard average thickness = 4 mm), to better approximate the mechanical characteristics of the milled implant. The two print profiles, which showed the most similar mechanical behaviour to the commercial implant overall, were used to produce parts with holes corresponding to the commercial implant. These holes are integrated in cranial implants for fluid exchange, tissue integration, osteosynthesis, re-expansion of the dura and resuspension of the temporalis muscle [43]. The holes were drilled using a rotary tool (Fortiflex 9100-21, Dremel, US) with a drill-bit 7103 attachment. Prior to drilling the holes were marked out to align with those of the conventional milled implant. This results in the matrix of process parameters shown in Table 2.

Table 2: Matrix and designation of all implants analysed in this study (BO...build orientation, AF...air flow temperature in °C, S...number of shells, LH...layer height in mm, V...printing speed in mm/s, IP...infill pattern, T...average implant thickness in mm, H...drilled holes), where only deviations from the **standard** values of **AF 210 – S 3 – LH 0.15 – V 50 – IP Rec±45 – T 4** are indicated.

Printing parameters	BO 90	BO 180	BO 45
standard	x	x	x
AF 0	x	x	x
AF 70	x		
AF 140	x		
AF 280	x	x	
T 5	x	x	x
S 1	x	x	
LH 0.30	x		
IP Rec0/90		x	
IP Gr0/90	x		
V 10		x	
T 5 + H		x	x

The PSCIs in the three different build orientations (BO) are depicted in Fig. 1. In addition, the graphic also includes the support structures used.



Fig. 1: The three different build orientations (BO) of the PSCIs displayed in the slicer software.

1.3. Mechanical testing

Cyclic tests for the determination of the implant compliance were performed on the ElectroPuls™ E3000 Linear-Torsion All-Electric Dynamic Test Instrument (Instron, USA)

equipped with a loadcell calibrated for 3 kN. The tests were carried out at 1 Hz between compression loads of -5 and -50 N for 1000 cycles. The loads were kept low in order not to initiate any damage and not to leave the linear-viscoelastic range of the material. Cycle number, forces and displacements were measured by the machine. Secant (C_{sec}) and dynamic compliance (C_{dyn}) were calculated according to

$$C_{sec} = \frac{v_{max}}{F_{max}}$$

$$C_{dyn} = \frac{v_a}{F_a}$$

where v_{max} and v_a are the maximum and amplitude displacement and F_{max} and F_a are the maximum and amplitude force. For a comparison between the different printed implants and the commercial implant, C_{sec} and C_{dyn} were evaluated after 500 cycles for each printing profile (Fig. 2).

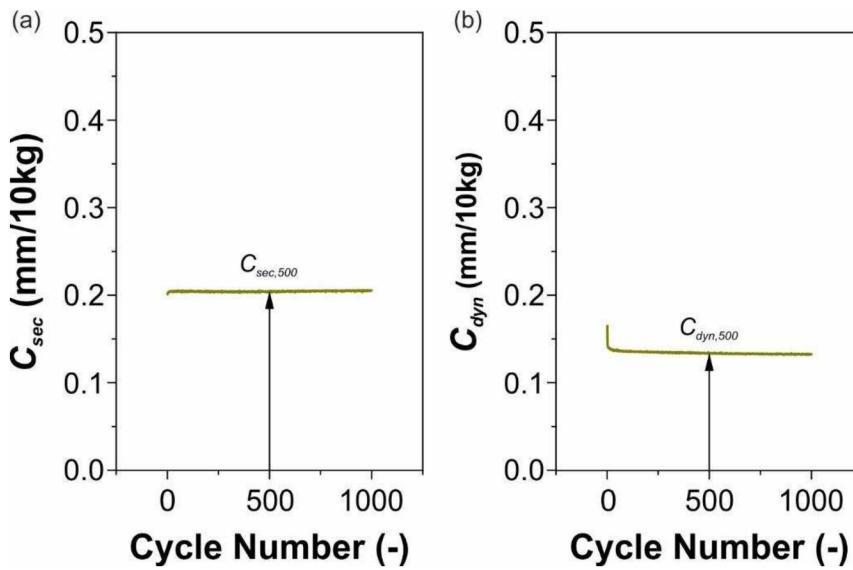


Fig. 2: Secant (C_{sec}) and dynamic compliance (C_{dyn}) over 1000 cycles measured for the commercial implant including the evaluation of the values after 500 cycles.

The impact tests were carried out on the CEAST 9350 Drop Tower Impact System (Instron Deutschland GmbH, Germany), which fulfils the requirements of ISO 6603-2. Data acquisition was done with the CEAST DAS 64K (Instron Deutschland GmbH, Germany). The drop height was 1 m resulting in a testing speed of approximately 4.43 m/s. A 22 kN piezo striker model M2098 with a Ø20 mm hemispheric head was used. A mass of 10 kg was added to the tup holder mass of 4.3 kg in order to minimise the reduction of velocity during testing. A lubricant was applied to the striker before each

test in order to reduce friction between the drop-weight and the implant. Time and force were measured. From these values, energy, displacement and velocity were calculated. Representative force-displacement curves were compared for each printing profile. Furthermore, the maximum force (F_M), the displacement until maximum force (l_M), the absorbed energy until maximum force (E_M) and the total absorbed energy (E_T) were evaluated.

To perform the mechanical tests, a three-point bending device was manufactured that can be attached to both machines (Fig. 3).

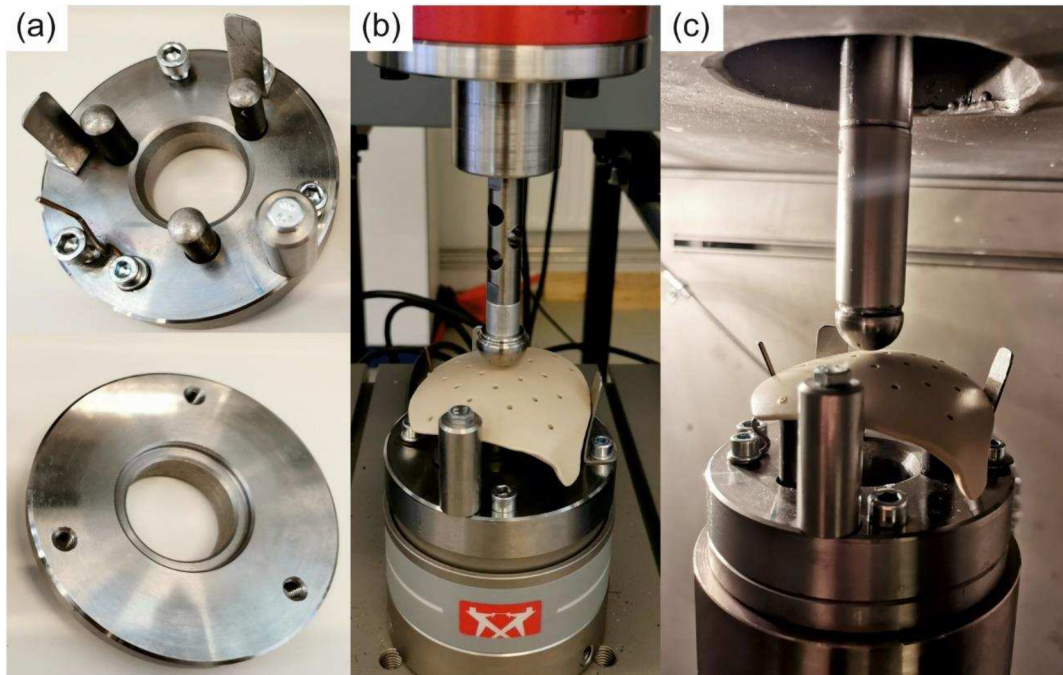


Fig. 3: Special fixture with 3 support points and attachments that can be mounted on two different machines (top – cyclic, top+bottom – impact) (a) for performing cyclic (b) and impact tests (c).

After impact testing, the specimens were examined for the occurrence of various failure mechanisms. Photographs of the tested samples were recorded and the fracture surfaces were analysed by digital microscope VHX-7000 (Keyence Corporation, Japan) equipped with a VHX-7100 (Keyence Corporation, Japan) 4K fully-integrated head under reflected light.

1.4. Thermal analyses

Differential scanning calorimetry was carried out on the DSC 214 Polyma by NETZSCH (NETZSCH Group, Germany). Specimens with a mass of 6 ± 0.5 mg were cut out from

the centre of the implant, in the area where the impact during mechanical testing took place. Each sample was placed in an aluminium Concavus® pan with pierced lid. Single heat runs were conducted at a heating rate of 10 K/min in the temperature range of 50 to 390 °C under nitrogen atmosphere (20 ml/min nitrogen flow) to analyse the thermal history of the implants. The degree of crystallinity X_c was calculated as

$$X_c = \frac{\Delta H}{\Delta H_0} \cdot 100 \%$$

in which ΔH is defined as the specific enthalpy of fusion of the semi-crystalline PEEK specimen determined from the melting peak area and ΔH_0 as the heat of fusion of a fully crystalline PEEK, which was approximated as 112.5 J/g according to Ref. [44]. Furthermore, the melting peak temperature (T_m) was evaluated and compared.

1.5. Characterisation of surface quality

In order to quantify the differences in surface quality of the top (surface where the impactor hits the sample during impact testing) and bottom surface (surface laying on the three-point fixture during cyclic and impact testing) of the implant, deeply focused images of both sides, for all representative implants per printing profile were recorded, including those of the commercial implant. This was done with the digital microscope VHX-7000 (Keyence Corporation, Japan) equipped with a VHX-7100 (Keyence Corporation, Japan) 4K fully-integrated head under reflected light. The recorded 3D images were corrected regarding the curvature of the implants using the integrated software. Afterwards, the waviness profile was evaluated across the strand deposition over a measuring length of 7 mm.

To analyse the degree of discoloration between the different printing profiles, colour measurements were performed on the UV-Vis (Ultraviolet-visible) spectrophotometer LAMBDA™ 950 (PerkinElmer, Inc., US) in reflectance mode. A combination of tungsten-halogen and deuterium lamps generated light between 380 and 780 nm. The wavelength interval was 5 nm and the slit width was 4.0 nm. A Spectralon® white reflectance standard (Edmund Optics Inc., Germany) was used to measure the 100% reflectance baseline. Colour was measured using the L^* , a^* , b^* coordinates of the CIE (Commission International d'Eclairage) 1976 colour space [45]. The lightness of the colour is represented by L^* , whereby a value of 0 means black and a value of 100 diffuse white. The position between red and green is characterised by a^* . Negative values of a^* indicate green and positive values indicate red. The position between yellow and blue is given by b^* . Negative values of b^* indicate blue and positive values indicate yellow. The values for a^* and b^* are between -128 and +127. The CIELab colorimetric coordinates (L^* , a^* ,

b^*) were calculated according to ISO/CIE 11664-4:2019 for a standard observer of 10° and the daylight standard illuminant D65. Total colour differences (ΔE_{ab}^*) is given with the following equation:

$$\Delta E_{ab}^* = \sqrt{(L^* - L_0)^2 + (a^* - a_0)^2 + (b^* - b_0)^2}$$

where (L^*, a^*, b^*) and (L_0, a_0, b_0) are the measured CIELab coordinates for the commercial and printed implants, respectively. Each colour difference reported in this paper is the average of two measurements. For implants with both large light and dark areas, 2 measurements were taken per area and the mean value was calculated from this.

2. Results

2.1. Processing of the 3D-printed specimens

In Fig. 4 representative samples of all printing profiles analysed in this study are displayed. The side of the implant facing the scalp is shown. The influence of build orientation (BO) and air flow temperature (AF) on the colour distribution can be clearly seen. With lower AF, the amount of dark brown regions increased. A lower printing speed (V 10) or increased sample thickness (T 5) had the opposite effect, whereas the speed effect was more pronounced. Variations in the shell number (S 1), layer height (LH 0.30) and infill pattern (IP Gr0/90 and IP Rec0/90) did not show much effect on the appearance of the implants.

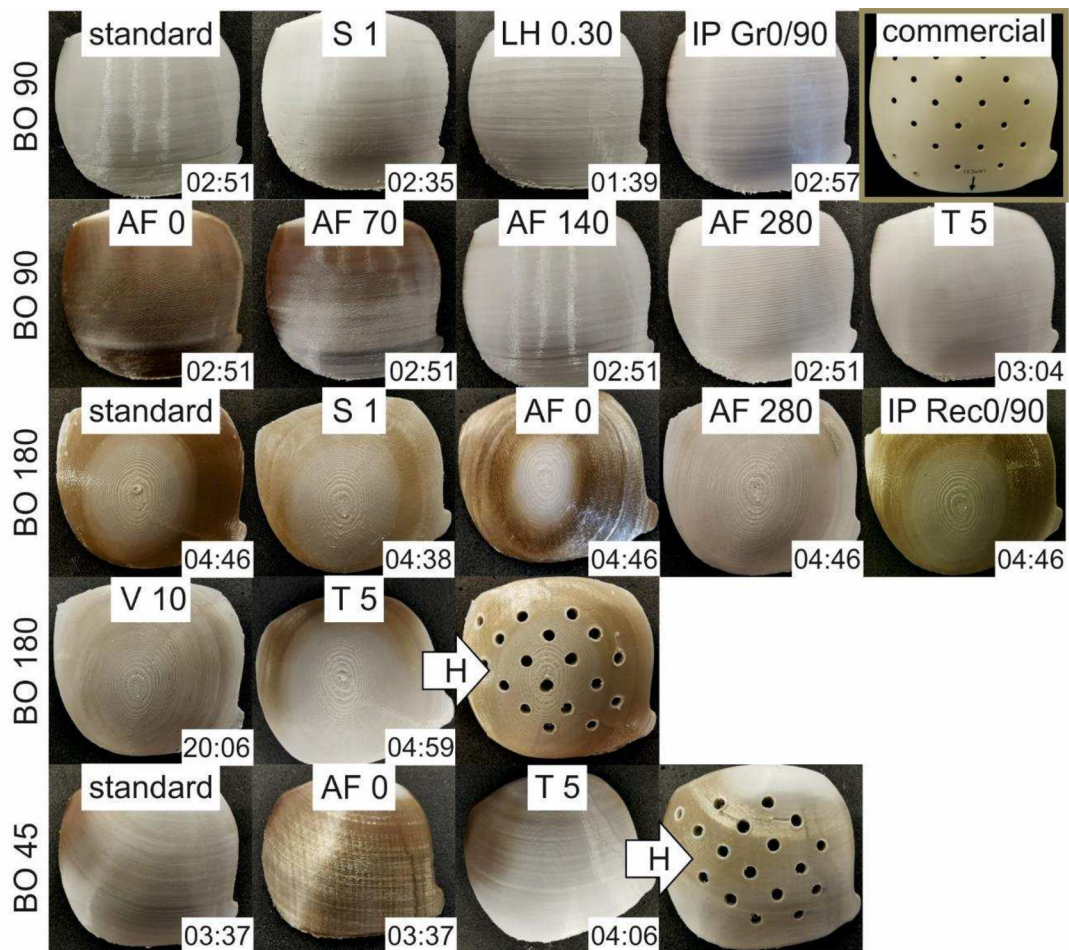


Fig. 4: Examples of PEEK PSCIs for the individual printing profile and their printing times in hh:mm in the lower right corner. The commercial implant is shown in the upper right corner of the figure.

The upright printed PSCIs had the lowest printing time, followed by the 45° tilted and the horizontally printed samples, when fabricated with identical printing parameters. The AF did not influence the print time. A lower shell number (S), slightly decreased print time, while a lower layer height (LH) increased it. The infill pattern (IP) hardly showed any influence, whereas a reduced printing speed (V) significantly lowered the manufacturing time.

2.2. Mechanical testing

The secant (Fig. 5 a) and dynamic (Fig. 5 b) compliance of most implants is in a similar range to one another and the commercial implant. The exact values of both parameters are given in Table A.1. There is a trend towards higher compliance when going from BO 90, to BO 45 and further to BO 180.

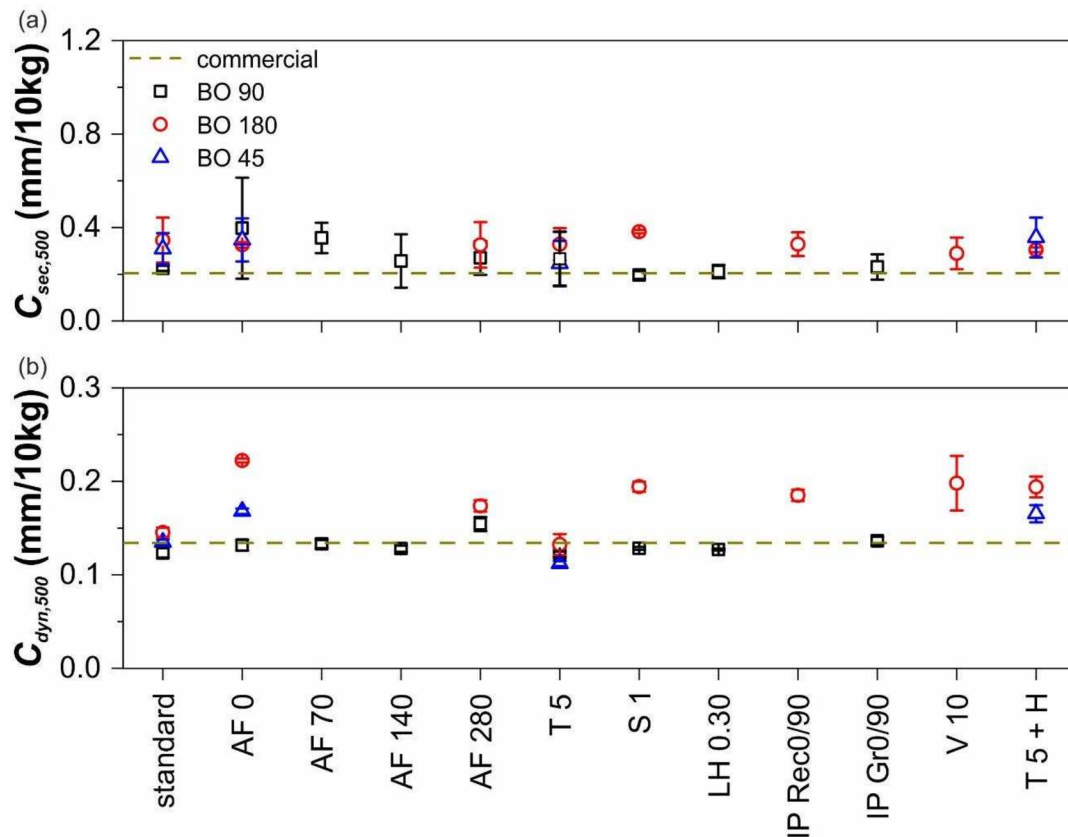


Fig. 5: The secant ($C_{sec,500}$) and dynamic ($C_{dyn,500}$) compliance after 500 cycles obtained through cyclic tests on PEEK PSCIs manufactured using different printing profiles (mean and standard deviation of $n=3$ per group) in comparison to a commercial implant.

On impact, the commercial implant showed a characteristic brittle fracture behaviour, achieving a high impact force and a low displacement until complete failure (Fig. 6).

Overall, the printed implants achieved higher deformations until they failed. A build orientation of 90 yielded lower mechanical integrity compared to BO 45 and BO 180, respectively.

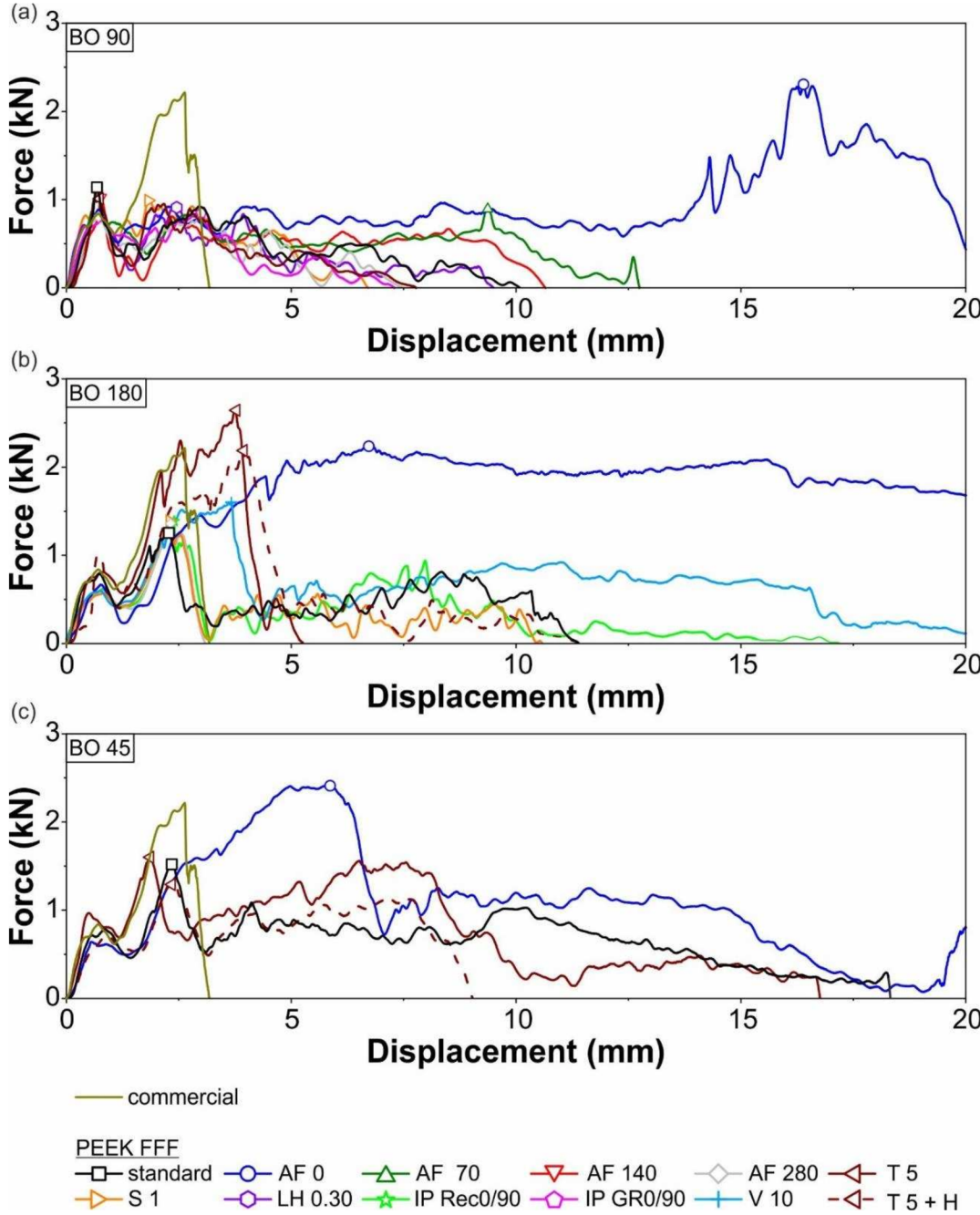


Fig. 6: Representative force-displacement curves from impact tests on PEEK PSCIs manufactured with different printing profiles in comparison to a commercial implant.

Furthermore, a higher AF resulted in higher displacements until maximum force and failure, and therefore, higher absorbed energy values. For BO 90, the different print profiles led to similar force levels in the low displacement region (Fig. 6 a). Even increasing the thickness from 4 to 5 mm did not improve the impact behaviour of the implants. For BO 180 (Fig. 6 b) and BO 45 (Fig. 6 c), the behaviour of the commercial implant could be better reproduced by a thickness increase of 1 mm. As BO 180 and BO 45 T 5 showed the most promising mechanical results, they were also tested after drainage holes had been drilled into the specimens, corresponding to the holes of the commercial implant to allow for better comparison. This shifted both curves to lower force values at similar deformation values. In the case of BO 180, the force values of the commercial implant could still be achieved, but again with a higher degree of deformation.

The samples manufactured at BO 90 (except for AF 0) only reached about half of the maximum force that was obtained for the commercial implant (Fig. 7 a). By using BO 180 or BO 45 instead, the values shifted closer to those of the commercial implant. This was especially the case with AF 0 or T 5, which matched similar levels of maximum force to that of the commercial implant. However, AF 0 experienced much higher levels of deformation up until maximum force, when compared to the commercial implant (Fig. 7 b), whereas all other implants reached values within a comparable range of maximum deformation. As a consequence of the high l_M and similar F_M values for AF 0 implants, E_M values were very high compared to the commercial implant (Fig. 7 c). However, due to the high l_M , which could already lead to serious injury, these values should be considered in a wary manner. Overall, the trend for E_M and F_M is alike. In the case of E_T , the values obtained for the printed implants were equal to or higher than the values evaluated for the commercial implant. This was due to higher levels of deformation up until final failure, which was reached by most printed implants (Fig. 7 d). The exact impact parameters are given in Table A.1.

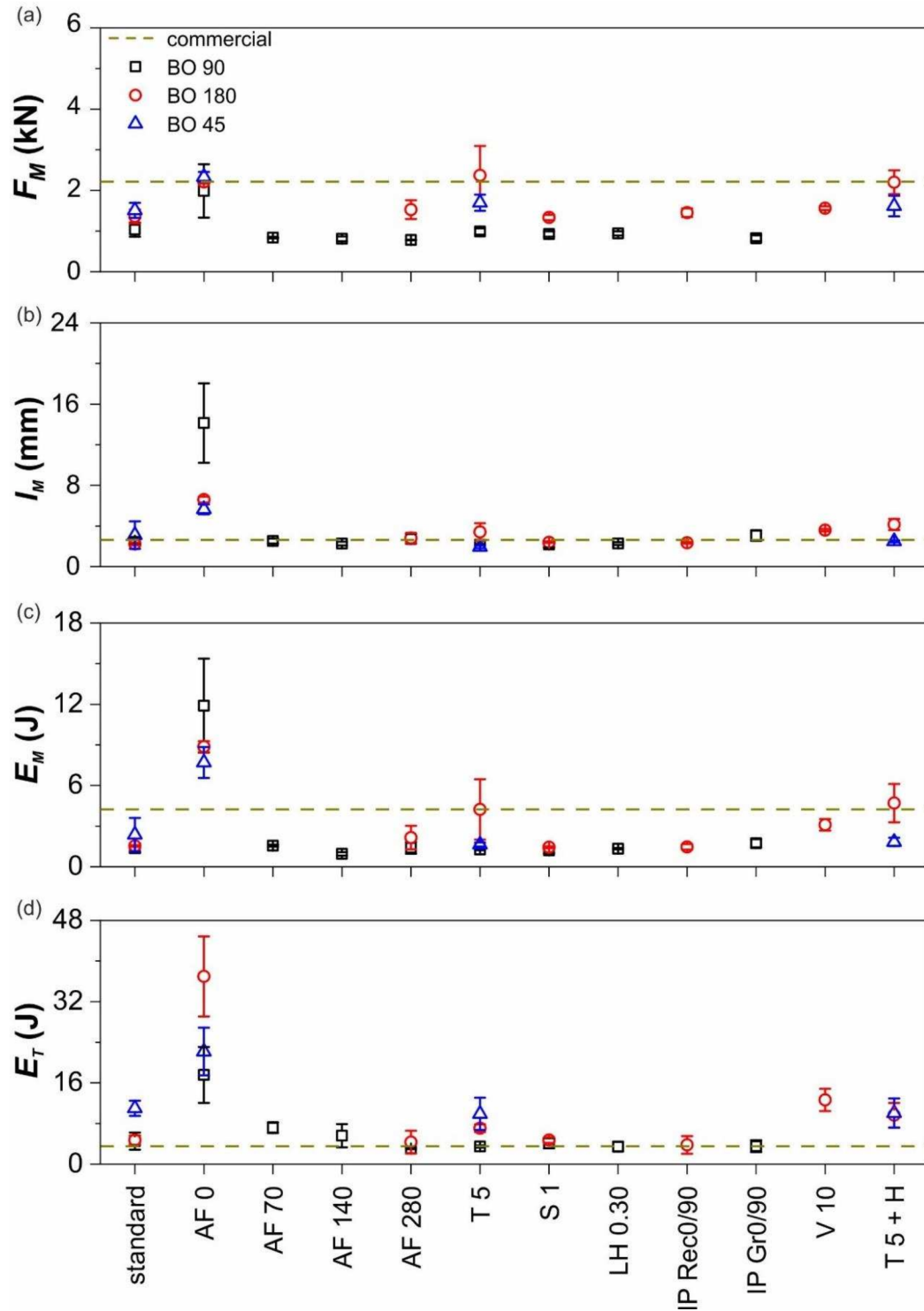


Fig. 7: The maximum impact force (F_M) (a), the displacement until F_M (I_M) (b), the energy uptake until F_M (E_M) (c) and the total absorbed energy (E_T) (d) obtained through impact tests on PEEK PSCIs manufactured using different printing profiles (mean and standard deviation of $n=3$ per group) in comparison to a commercial implant.

All printed PSCIs fractured into 2-4 pieces, whereas the commercial milled implant shattered into a larger number of fragments (Fig. 8). For BO 90 samples, the crack propagated between the individual printing layers. Similar was true for the BO 45 specimens. Horizontally printed PSCIs most likely fractured in the direction of internal defects within the print. Implants printed at lower AF showed highly deformed regions (e.g. BO 45 standard) after impact testing. A very low printing speed of 10 mm/min (V 10), resulted in delamination of the top layers. The insertion of holes in the test specimens had no visible influence on fracture behaviour.

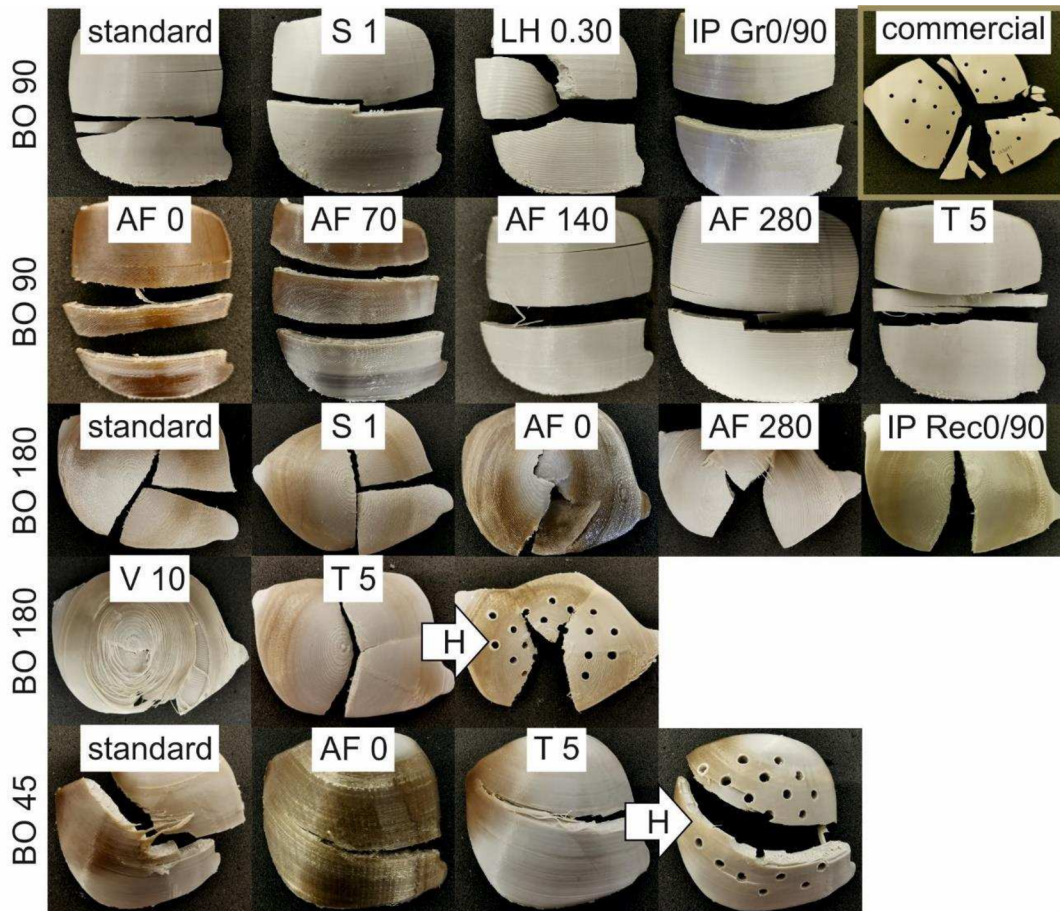


Fig. 8: Fracture patterns of a representative PEEK PSCI per printing profile as well as of the milled implant (top right) after impact testing.

The corresponding fracture surfaces are given in Fig. 9. It can be seen that the brown areas mainly appear on the surface of the samples, with the exception of no AF and BO 90 / BO 45, where the areas penetrate almost completely into the centre. Additionally, the bonding between neighbouring layers is stronger and the porosity lower for PSCIs manufactured at BO 90 and BO 45 compared to BO 180. A large number of

voids, and thus higher porosity, was found in the horizontal prints. Using a grid infill pattern (IP Gr0/90) also led to several cavities in the BO 90 implants. The fracture surface of the commercial implant is rather smooth compared to the fracture surfaces of the printed implants, showing no cavities at magnification.

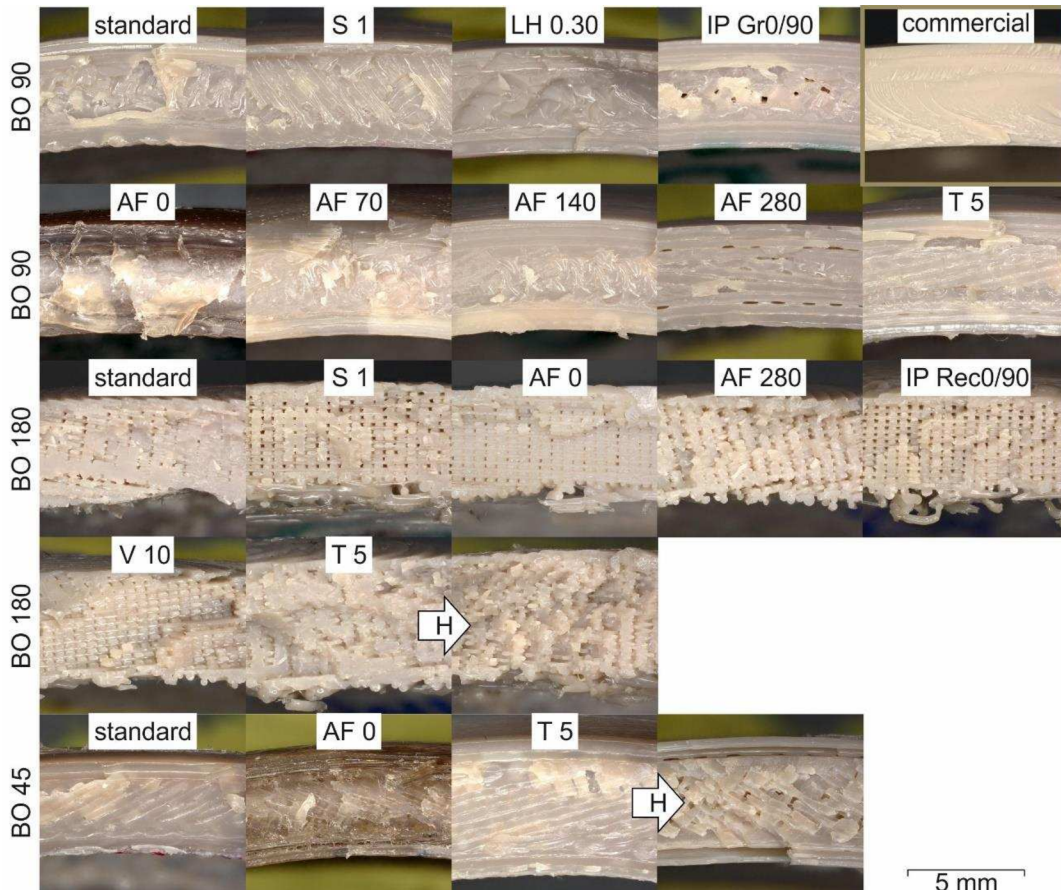


Fig. 9: Microscopy images of the fracture surfaces of a representative PEEK PSCI per printing profile as well as of the milled implant (top right) at a magnification of 20. The images were taken from the middle area of the implants.

2.3. Thermal analyses

The DSC curve of the commercial PEEK implant showed no cold-crystallisation and a melting region which had slightly shifted to higher temperatures compared to 3D printed PEEK (Fig. 10 a). The curves obtained for the different printing profiles were similar to each other except for the samples printed at AF 0, which had a cold-crystallisation peak at approx. 175 °C. For the melting temperature, no trend between the different printing profiles could be observed (Fig. 10 b).

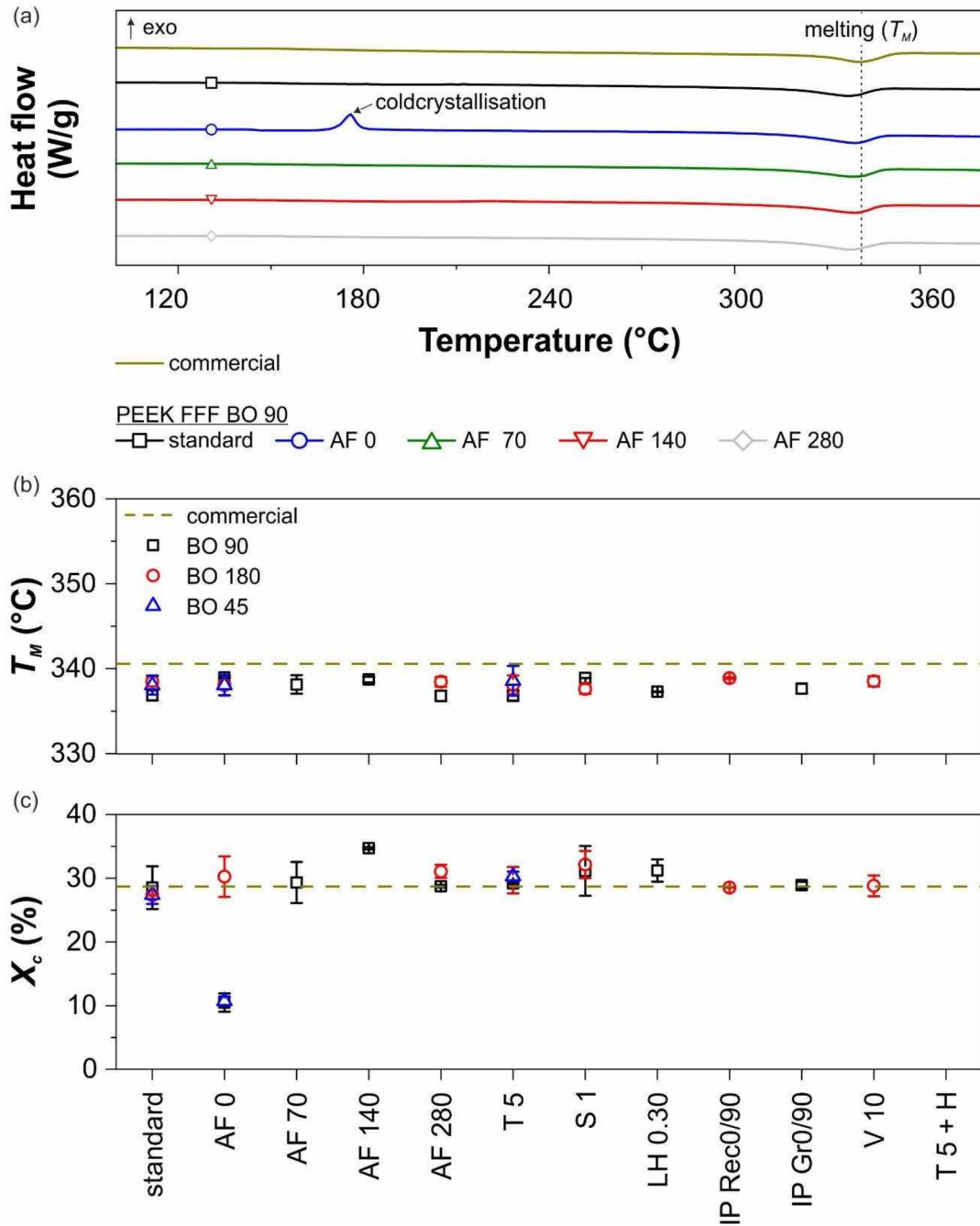


Fig. 10: Representative DSC curves obtained for commercial PEEK in comparison to 3D-printed PEEK at a build orientation (BO) of 90 and different air flow temperatures (AF) (a). Melting temperature (T_M) (b) and degree of crystallinity (X_c) (c) obtained for all analysed printing profiles and the commercial implant (mean and standard deviation of $n=2$ per group).

The degree of crystallinity of the printed implants and the commercial implant were alike (Fig. 10 c). Exceptions were BO 90 and BO 45 manufactured at AF 0, where X_c had significantly decreased, indicating high amorphousness in these implants. The exact values for TM and X_c are summarised in Table A.2. Although implants manufactured with profiles such as BO 90 AF 70 showed a high colour inhomogeneity as well (Fig. 8), differences in the degree of crystallinity were not observed via DSC. This is most likely due to the local nature of the DSC measurement, which was only able to assess a very small sample region where the impactor struck the implant.

2.4. Characterisation of surface quality

The waviness profile of the top and bottom surface of the commercial implant was similar with a low range of fluctuation (Fig. 11). The profiles evaluated for BO 90 were comparable to the profiles evaluated for the commercial implant and show rather small variances between the top and bottom surface. At lower airflow temperatures, the difference between the top and bottom increased.

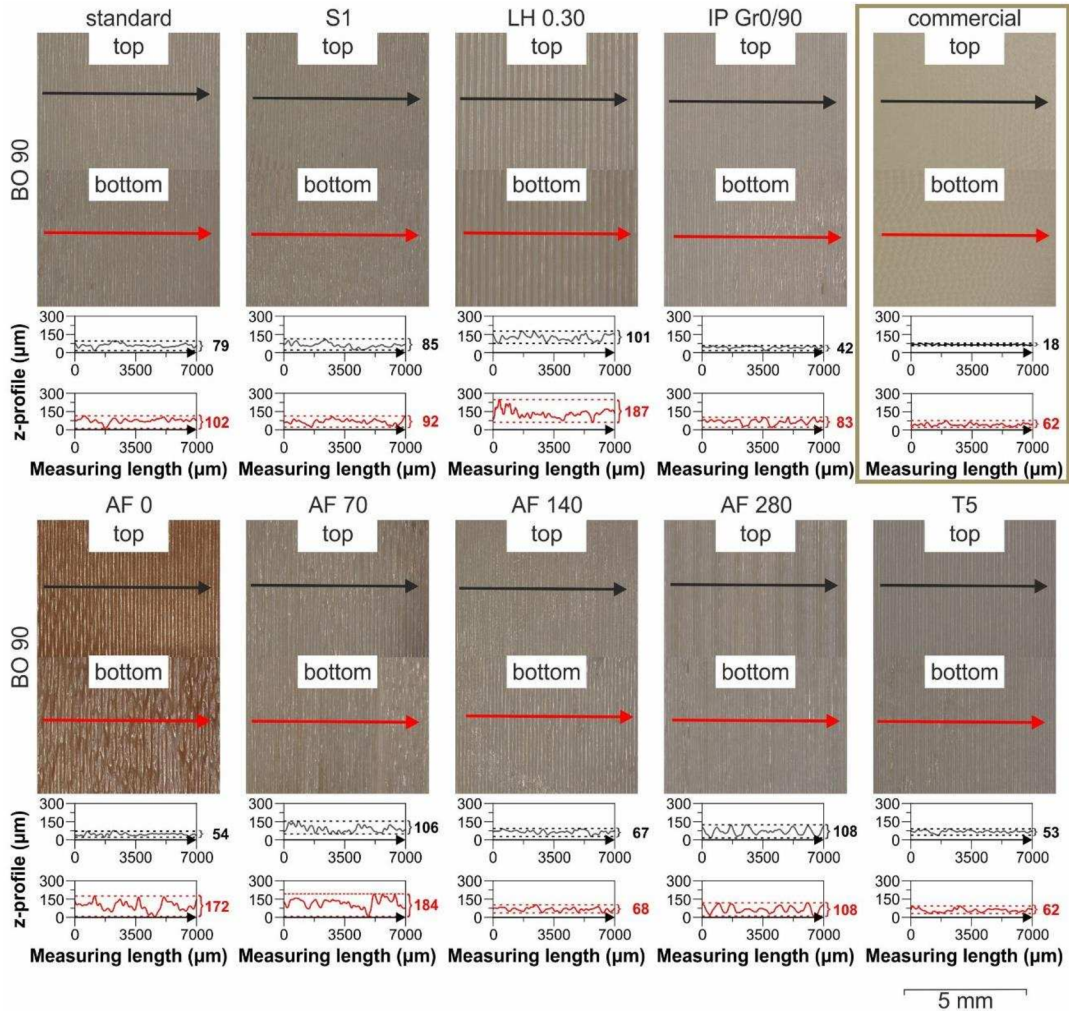


Fig. 11: Microscopy images of top and bottom surface of a representative PEEK PSCI per printing profile at a build orientation of 90 (BO 90), as well as of the milled implant (top right) at a magnification of 40. Underneath the images the waviness profiles for the top (black) and bottom (red) implant surface along the displayed measuring length is given.

For implants manufactured at BO 180, the bottom surfaces show a higher level of waviness compared to the top surface (Fig. 12). The measured waviness profiles varied between the individual printing profiles. This is likely due to the fact that the recorded measurements are local, particularly on the bottom of the implant, which varies in waviness greatly across the build. This phenomenon could be felt with bare hands. Implants printed with one outer shell (S1) recorded the highest waviness values of all prints. This was credited to changes in the print path close to the implant's surface and its associated poorer welding to the rectilinear infill. The waviness profiles of the BO 45

implants were also very similar to those measured for BO 90 specimens, which can be attributed to the comparable printing paths between the two build orientations (Fig. 12, the three at the bottom right).

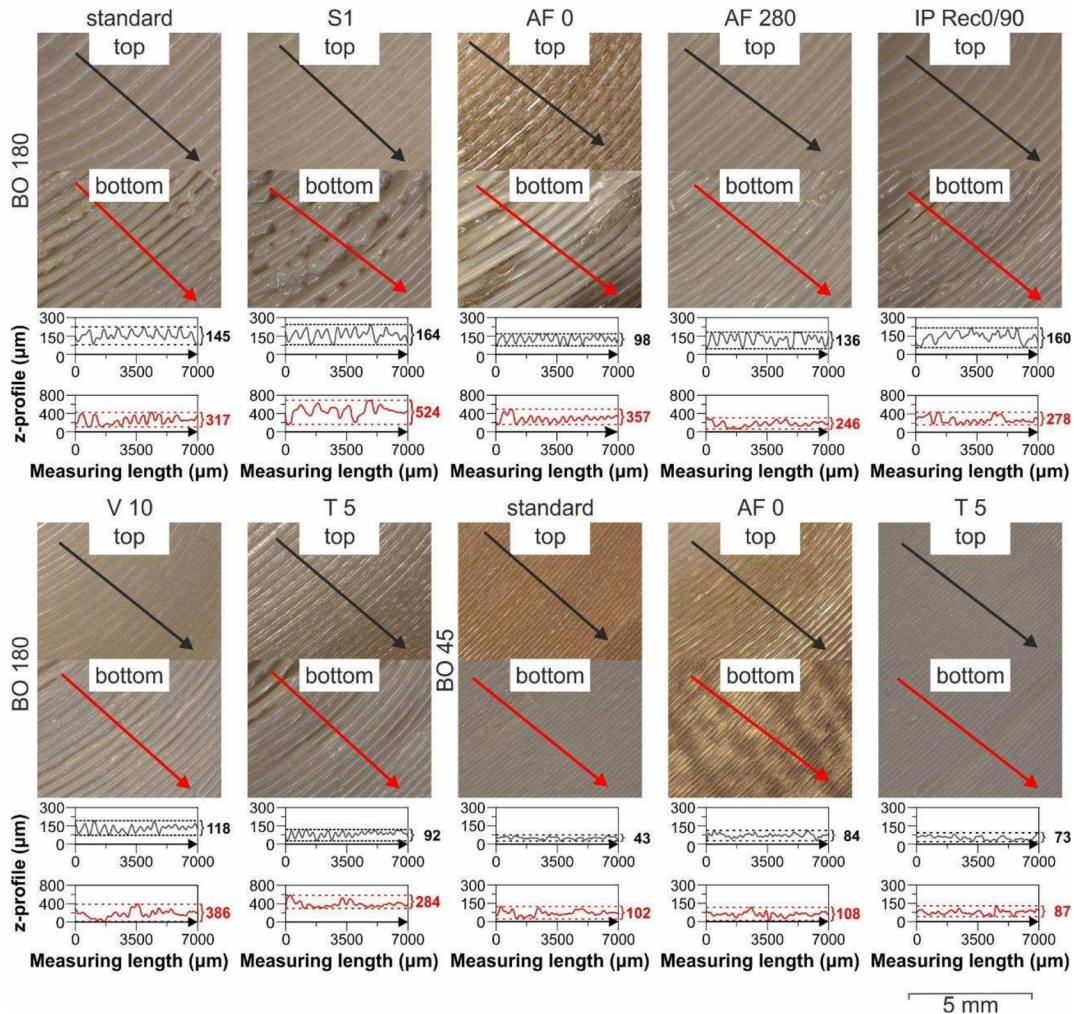


Fig. 12: Microscopy images of top and bottom surface of a representative PEEK PSCI per printing profile at a build orientation of 180 (BO 180) and 45 (BO 45) at a magnification of 40. Underneath the images the waviness profiles for the top (black) and bottom (red) implant surface along the displayed measuring length is given.

The L^* , a^* , b^* coordinates evaluated for commercial PEEK are ~ 74.7 , ~ 0.8 and ~ 10.1 , respectively. For the 3D-printed PEEK implants, L^* ranged from 30.8 to 65.38, a^* from 1.0 to 4.78 and b^* from 1.6 to 11.8. The exact values for the L^* , a^* , b^* coordinates for each printing profile are summarised in Table A.3. Since the values for L^* are high compared to a^* and b^* , the total colour difference is mainly influenced by L^* . Implants printed at BO 90 showed very similar values for ΔE_{ab}^* except for AF 0 and AF 70

(Fig. 13). The results fit very well with the colour distribution of the implants and the high standard deviation for BO 90 AF 70 can be explained by the strongly inhomogeneous colour distribution (Fig. 4). In the case of horizontally manufactured implants (BO 180), ΔE_{ab}^* varied greatly between the different printing profiles, which can also be seen in the photographs of the implants (Fig. 4). The same applied to the implants printed with a 45° inclination (BO 45).

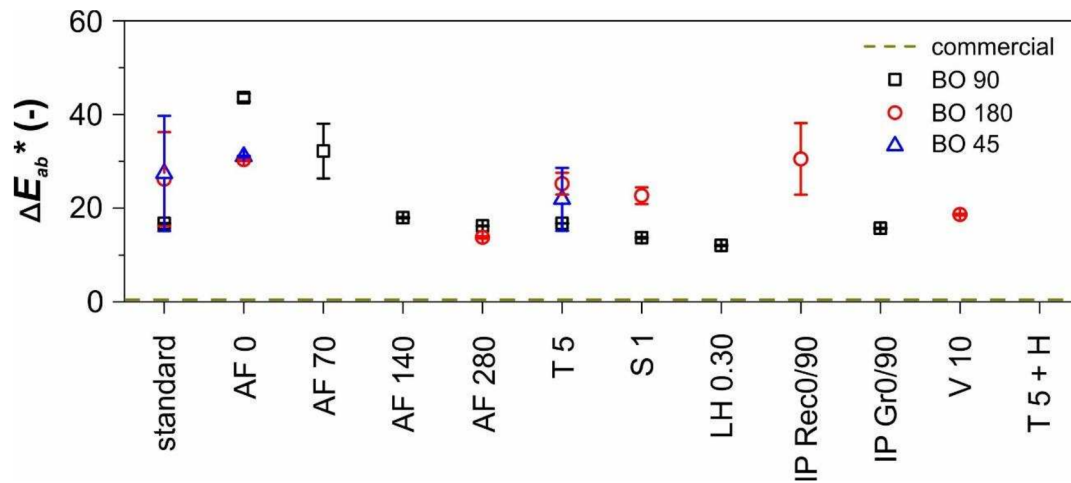


Fig. 13: Total colour differences (ΔE_{ab}^*) calculated for all analysed printing profiles and the commercial PEEK implant (mean and standard deviation of $n=2-4$ per group).

3. Discussion

Implant materials have to meet a variety of requirements such as mechanical performance. However, haptics and appearance also play an important role for surgeons. Therefore, uniformly coloured implants with a smooth surface are preferred. For this reason, amorphous areas are not desirable, even though they can lead to preferred levels of mechanical behaviour. In this study, it was found that lower degrees of crystallinity result in moderate maximum impact forces, high deformations until maximum force – also until final failure – and therefore high energy uptakes until maximum force as well as total absorbed energy values. Notably, the brownish amorphous areas have a positive influence on the fracture pattern, as the individual fragments were still partially connected after impact, due to the plastic deformation of the amorphous regions of the implants (especially with AF 0 BO 180 or B O45; Fig. 8), which prevented splintering of the parts. The fracture behaviour of the printed PSCIs with 2 to 4 fracture pieces is the main advantage over the commercial milled implant, which broke into a larger number of pieces (Fig. 8). Although the arrangement of the individual strands creates welds that weaken the mechanical behaviour perpendicular to the strands, the direction of crack propagation can be defined with the strand orientation [46]. The reduced performance in the z-direction for FFF is well known [47–50] and explains the low impact parameters observed for PSCIs printed at a build orientation of 90 (Fig. 14 a). When the samples are tilted by 45° (BO 45), they still break between the strands in z-direction, but the effective cross-section between the layers is increased (Fig. 14 b). This leads to an improvement in the mechanical properties. The mechanical integrity of the PSCIs can further be enhanced by using a horizontal build orientation, where the load direction is perpendicular to the strands (Fig. 14 c) and the fracture propagates in the direction of imperfections within the part (e.g. cavities). The mechanical behaviour of the commercial PEEK implant ($F_M=2.2$ kN, $l_M=2.6$ mm, $E_M=3.0$ J and $E_T=3.5$ J) could be best approximated with the BO 180 T 5 printing profile ($F_M=2.4\pm 0.7$ kN, $l_M=3.4\pm 0.9$ mm, $E_M=4.2\pm 2.2$ J and $E_T=7.1\pm 0.8$ J). Even after inserting drainage holes according to the commercial implant design, adequate maximum forces could be achieved ($F_M=2.2\pm 0.3$ kN). Liu et al. [51] compared the dimensional accuracy, compression and impact behaviour of powder bed fusion (PBF) and FFF PEEK cranial implants. They found that FFF PEEK implants absorbed more total energy in both compression tests at 0.016 mm/s and impact tests at 2.18 mm/s (3.5 ± 1.1 J and 3.7 ± 1.0 J, respectively) in comparison to PBF PEEK implants (2.6 ± 0.9 J and 2.7 ± 0.5 J, respectively). The corresponding maximum force values for FFF samples are with 1.4 ± 0.1 kN and

1.4±0.3 kN, respectively, comparable to the values evaluated for PBF specimens (1.3±0.0 kN and 1.0±0.0 kN, respectively). In this study, about 1 kN higher impact forces could be achieved, but the values were also obtained at a much higher test speed of 4.43 m/s. The increased test speed could significantly alter the material behaviour since polymers are known to show strain-rate dependent behaviour. In a previous study, an increase in elastic modulus was observed in the tensile test when the crosshead speed was increased from 10⁻³ (3.2±0.2 GPa) to 10³ mm/s (4.8±1.3 GPa) [21]. Furthermore, Liu et al. [51] saw that the FFF implants deformed more before a local fracture occurred in the area where the impactor hit the samples. The PBF samples, on the other hand, broke into several pieces compared to the fracture of the commercial implant presented in this study. This should be avoided in order not to injure surrounding bone or especially soft tissue. In addition to these impact parameters, similar secant and dynamic compliance values were also recorded and compared to the commercial PEEK implant ($C_{sec,5000}=0.204$ mm/10 kg and $C_{dyn,5000}=0.134$ mm/10 kg vs. e.g. $C_{sec,5000}=0.328±0.069$ mm/10 kg and $C_{dyn,5000}=0.132±0.011$ mm/10 kg for BO 180 T 5 printing profile). The compliance generally indicates the ability of a material or structure to give way or deform under load. Since the structure mainly changes with the build orientation, the highest fluctuations were found when the orientation was altered. A comparison with the literature was not possible as no comparable studies could be found.

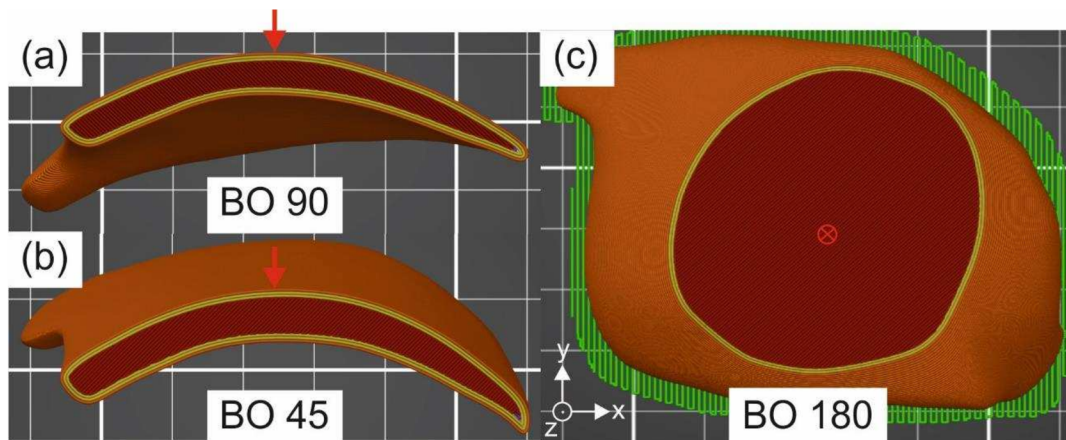


Fig. 14: Direction of impact (red arrow) in relation to a build orientation (BO) of 90 (a), 45 (b) and 180 (c) of the printed PSCIs.

Next, datasets from the PSCIs printed at AF 210 (standard) and AF 0 were pooled together, in order to identify the optimal set of printing parameters to match the performance of the commercially produced implant (Fig. 15).

First the **mechanical integrity** is ranked using the impact parameters force maximum F_M and a relation between total absorbed energy (E_T) and displacement until failure (l_T). Since the dynamic stiffness of all tested implants is in a similar range for all printed implants (slope at very low deformations in the force-displacement curves, Fig. 6) and is rather influenced by the material than by the processing parameters, F_M and E_T / l_T are used for comparison. The 3D-printed implants should behave similarly to the commercial implant, which broke in a brittle manner under high forces and deforms only slightly before failure. It is important that the implant fractures before deforming too much (deformation limit could not be found in the literature), as it might lead to the damage of surrounding soft tissue or bone. Hence, the ratio E_T / l_T is used for comparison, as high energies are preferred, but not if they are accompanied by high values of deformation. Additionally, it is also preferred that the implant fractures before the adjacent bone does (to prevent surgical resection/further complications). Taking a look at F_M , it is found that BO 90, BO 180 and BO 45 implants printed with the 'standard' printing profile all obtain a lot lower values in average compared to the commercial implant. On the other hand, if printed without using an air flow temperature (AF 0), F_M values were increased with average values in the range of the commercial implant. However, the increase in F_M at AF 0 comes along with an increase in deformation and therefore a risk of reaching too high deformations in the target application in the case of an accident. These implants absorb a huge amount of energy before fracturing, but may fracture too late. Especially implants printed at BO 180 AF 0 show a really good energy to deformation ratio (E_T / l_T). In contrast, BO 180 and BO 90 standard show insufficient E_T / l_T ratios by either achieving high energies, but at the cost of too high deformations (BO 180 standard), or by reaching too low force and thus energy levels with low deformations (BO 90 standard). However, depending on the size and geometry, the implant is connected to the bone via several anchors, which on the one hand changes the loading situation and on the other hand makes it unclear whether the implant or the fixation fails first during an accident.

In addition to the mechanical integrity of the implants, haptics and the appearance are key factors for an implant to be applicable. The surface quality in particular is a measure of print quality and is strongly influenced by the print profile used. Furthermore, it also plays an important role in the interaction between the implant and the surrounding soft tissue or bone. For milled implants, the surface quality can be analysed on the basis of their roughness, whereas for 3D printing, the waviness is more relevant, due to the layered structure introduced through the manufacturing process. Hence, the degree of crystallinity (X_c), the range of z-waviness on the bottom surface of the implants (as it is

the more critical value compared to the upper side) and the level of discoloration quantified with the total colour differences (ΔE_{ab}^*) are displayed as measure of the **implant quality**. A high value for X_c , and low values for ΔE_{ab}^* and Δ waviness are to be aimed for. Implants printed at BO 90 and BO 45 with AF 0 show the highest amount of amorphous regions (brown areas, Fig. 4), which correlates with the very low values for X_c (~11%). The degree of crystallinity for all other implants is relatively high (~27-35%), specifically in the measuring range where the impactor hit the sample during impact testing. For injection-moulded PEEK, X_c can be between almost zero and 40%, depending on the cooling behaviour and thus crystallisation kinetics [52]. With regard to injection moulded PEEK samples with less variation of crystallinity in both thickness and length (produced with slow cooling rates due to high mould temperatures of 200 °C), degrees of crystallinity in the range of 30–35% were evaluated.

With respect to waviness values, horizontally printed PSCIs exceeded all other implants. This was credited to increases in offset levels between individual print layers, which were far more prominent vs. their vertical counterparts, which experience tighter welding between adjacent layers as consequence of direct pressure exerted on them by the print nozzle. Furthermore, support structure positioning and volume also contribute to increased levels of waviness, whereby residual debris from their removal form an irregular topology. This was also the case for horizontally printed PEEK implants produced by Sharma et al. [16]. Hence, efforts to optimise support structure removal and surface finish post-build are still under investigation. Surface quality, such as roughness and topography, are important factors in determining the osseous integration of PEEK implants [53]. Han et al. [54] found that the anisotropic texture of FFF-printed surfaces had a stimulating effect on the bioactivity of PEEK samples compared to polished and blasted samples, especially regarding metabolic activity and cells proliferation. Explanation was credited to surface area increases in FFF, which allowed for improved cell attachment, anchorage, growth, migration and proliferation. The waviness values evaluated in this study cannot be compared to the literature, since mostly surface roughness was measured. For example, Baek et al. [55] investigated the surface roughness of FFF PEEK in correlation to nozzle temperature. Increasing the temperature from 360 to 380 °C decreased the surface roughness from 60 to 54 μm , but roughness rose to 67 μm between 380 and 400 °C. The first drop was explained by a reduction in viscosity at higher temperatures, which filled the cavities better, and the subsequent increase by a higher cooling rate, which leads to a faster solidification of the material. Here, too, several factors seem to interact, which in turn is an indication of the complex

crystallisation process behind it. The next measure of implant quality, the discolouration of the samples, is directly related to the crystallinity of the parts. Therefore, implants printed at AF 0 show the greatest deviation from the commercial implant again. On the other hand, the most uniform colour was achieved with BO 90 standard. Colour inhomogeneities in PEEK PSCIs were also observed by Sharma et al. [16] presenting builds with dark-brownish areas that indicated higher amorphousness and lighter areas representing higher degrees of crystallinity. However, they saw lower amounts of amorphous regions for horizontal printed samples compared to vertical ones, whereas in this study the most uniform colour could be achieved for upright printed samples (BO 90). This could be due to the smaller implant size and the smaller amount of support structures used within this study, again leading to different thermal conditions. Generally, colour inhomogeneity results from insufficient time for crystallisation, which could be overcome by annealing the samples after printing [35,56]. For this purpose, a temperature between the measured cold crystallisation (~ 175 °C) and melting temperature (~ 338 °C) should ideally be selected. A similar principle is behind the application of an increased air flow or build chamber temperature, which increases the surrounding temperature. This results in a reduced cooling speed and prolongs the time for crystallisation. In addition, the increased ambient temperature also causes an annealing effect during the printing process.

Lastly the **time to availability** is compared, influencing the lead times and manufacturing costs. As the implants are printed directly in the clinic, the printing time is equal to the time to availability. The horizontal prints (~ 300 min) show about twice the manufacturing time compared to the upright implants, with those tilted at 45° somewhere in between. The air flow temperature does not affect the print time, however, layer height and printing speed do. For example, the print time for BO 180 V 10 PSCIs was 1206 min, which means a nearly quadrupled value at five times slower print speed. Nevertheless, the time for in-house printing together with any post-processing should be comparably less to commercial implant lead times (~ 3 weeks [14]).

For now, the optimal printing profile for PEEK implants was not found. Ideally, the perfect PSCI would combine the mechanical properties of BO 180 T 5, with the surface quality and appearance achieved for BO 90 standard. Moreover, it is also important to test other geometries with the optimal printing profile selected, as changing the geometry will affect the implants thermal history [57] and another printing profile may be more suitable. Therefore, a compromise for different geometries has to be found since each profile has

to be certified in order to guarantee colour homogeneity, adequate print quality and mechanical performance, non-cytotoxicity, etc. [38,58,59].

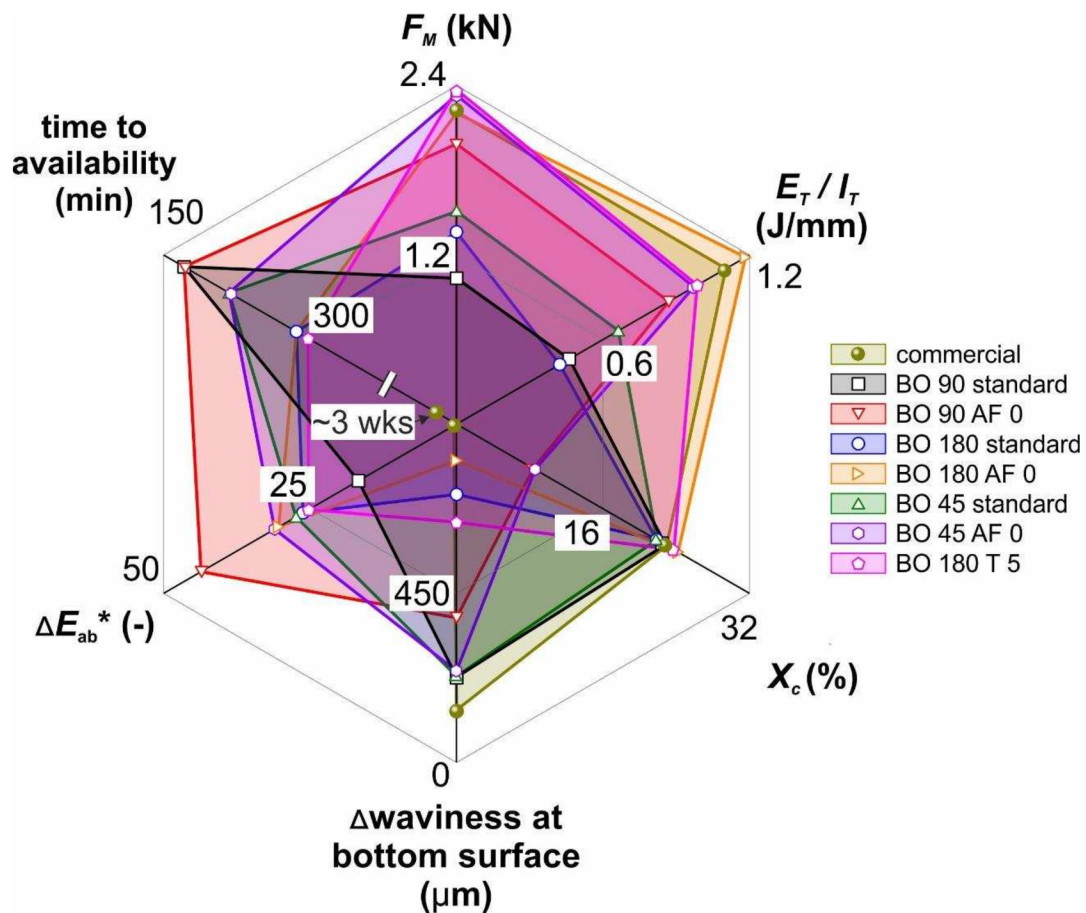


Fig. 15: Comparison of FFF and commercial PEEK cranial implants in terms of their mechanical integrity (maximum impact force - F_M , relation between total absorbed energy - E_T and displacement until failure - I_T), implant quality (degree of crystallinity - X_c , span of waviness at the bottom surface and ΔE_{ab}^* as level of discoloration) and time to availability. Three different build orientations (BO) each at two different air flow temperatures (AF) are displayed (standard = AF 210). Additionally, the 5 mm thick (T 5) BO 180 implant is shown, which mechanically best fits the commercial implant.

4. Conclusions

There is a trend towards the investigation of polyetheretherketone (PEEK) patient specific cranial implants (PSCIs) manufactured via fused filament fabrication (FFF). However, as the correlations between the different process parameters and the resulting properties are not yet fully understood, the optimal process parameters to manufacture PEEK cranial implants have not been found yet. In addition, it is still unclear which implant metrics are to be aimed for, since the values for living bone hardly exist and in its dry state are not truly comparable. Therefore, a commercial PEEK implant was used for comparison in this study, as it is assumed that it has the desired properties necessary for application.

In this study the effects of build orientation (BO) and air flow temperature (AF) among other parameters (layer height, shell number, printing speed, infill pattern) on mechanical integrity (cyclic and impact behaviour), print quality (colour uniformity, surface topography and degree of crystallinity) and the time to availability were examined.

The highest mechanical properties were observed for horizontally printed implants (BO 180), where the load acts perpendicular to the strands, followed by 45° tilted (BO 45) and upright (BO 90) printed parts. On the contrary, the surface quality was best for BO 90 and worst for BO 180 PSCIs, mostly due to residual support structures left on the surface.

In addition, a high AF led to higher degrees of crystallinity and a more uniform colour distribution. Implants printed with no AF showed extensive brown amorphous regions throughout their build, which resulted in high absorbed energies until fracture but at high levels of deformation. Such high deformations during an accident may injure surrounding soft tissue or bone. On the other hand, the implant should not be too brittle that it splinters when failure occurs. Notably, it was observed that the commercial implant broke into several pieces during impact testing, which may be another advantage of 3D-printing, where the fracture path could be specified by the print path.

However, application-driven tests are proposed for future studies, as in real application x-y-deformations are constrained by the adjacent bone and the implant will be surrounded by soft tissue and the scalp, significantly affecting implant loading and the fracture behaviour. Moreover, it is still questionable whether the implant itself fails when unexpected stresses are applied to the skull, or rather the attachments which are needed to fix the implant to the bone.

5. Acknowledgement

This work was supported by the project CAMed (COMET K-Project 871132) which is funded by the Austrian Federal Ministry of Transport, Innovation and Technology (BMVIT) and the Austrian Federal Ministry for Digital and Economic Affairs (BMDW) and the Styrian Business Promotion Agency (SFG). The authors would like to thank Eric Helfer for performing the Vis spectroscopy and the determination of the CIELab colorimetric coordinates.

6. References

- [1] A. Haleem, M. Javaid, Polyether ether ketone (PEEK) and its 3D printed implants applications in medical field: An overview, *CEGH* 7 (2019) 571–577. <https://doi.org/10.1016/j.cegh.2019.01.003>.
- [2] E. Alonso-Rodriguez, J.L. Gebrián, M.J. Nieto, J.L. Del Castillo, J. Hernández-Godoy, M. Burgueño, Polyetheretherketone custom-made implants for craniofacial defects: Report of 14 cases and review of the literature, *J. Craniomaxillofac. Surg.* 43 (2015) 1232–1238. <https://doi.org/10.1016/j.jcms.2015.04.028>.
- [3] D. Garcia-Gonzalez, A. Rusinek, T. Jankowiak, A. Arias, Mechanical impact behavior of polyether–ether–ketone (PEEK), *Compos. Struct.* 124 (2015) 88–99. <https://doi.org/10.1016/j.compstruct.2014.12.061>.
- [4] S.M. Kurtz, J.N. Devine, PEEK biomaterials in trauma, orthopedic, and spinal implants, *Biomaterials* 28 (2007) 4845–4869. <https://doi.org/10.1016/j.biomaterials.2007.07.013>.
- [5] O.B. Searle, R.H. Pfeiffer, Victrex® poly(ethersulfone) (PES) and Victrex® poly(etheretherketone) (PEEK), *Polym. Eng. Sci. (Polymer Engineering & Science)* 25 (1985) 474–476. <https://doi.org/10.1002/pen.760250808>.
- [6] H. Xin, D. Shepherd, K.D. Dearn, Strength of poly-ether-ether-ketone: Effects of sterilisation and thermal ageing, *Polym. Test.* 32 (2013) 1001–1005. <https://doi.org/10.1016/j.polymertesting.2013.05.012>.
- [7] T. Nieminen, I. Kallela, E. Wuolijoki, H. Kainulainen, I. Hiidenheimo, I. Rantala, Amorphous and crystalline polyetheretherketone: Mechanical properties and tissue reactions during a 3-year follow-up, *J. Biomed. Mater. Res. A* 84 (2008) 377–383. <https://doi.org/10.1002/jbm.a.31310>.

- [8] A.D. Schwitalla, T. Spintig, I. Kallage, W.-D. Müller, Flexural behavior of PEEK materials for dental application, *Dent. Mater.* 31 (2015) 1377–1384. <https://doi.org/10.1016/j.dental.2015.08.151>.
- [9] J.S. Stuart Green, A Polyaryletherketone Biomaterial for use in Medical Implant Applications, Rapra Technology Limited, Shawbury, Brussels (2006) UK1–7.
- [10] J.A. Smith, E. Mele, R.P. Rimington, A.J. Capel, M.P. Lewis, V.V. Silberschmidt, S. Li, Polydimethylsiloxane and poly(ether) ether ketone functionally graded composites for biomedical applications, *J. Mech. Behav. Biomed. Mater.* 93 (2019) 130–142. <https://doi.org/10.1016/j.jmbbm.2019.02.012>.
- [11] C. Morrison, R. Macnair, C. MacDonald, A. Wykman, I. Goldie, M.H. Grant, In vitro biocompatibility testing of polymers for orthopaedic implants using cultured fibroblasts and osteoblasts, *Biomaterials* 16 (1995) 987–992. [https://doi.org/10.1016/0142-9612\(95\)94906-2](https://doi.org/10.1016/0142-9612(95)94906-2).
- [12] K.B. Sagomonyants, M.L. Jarman-Smith, J.N. Devine, M.S. Aronow, G.A. Gronowicz, The in vitro response of human osteoblasts to polyetheretherketone (PEEK) substrates compared to commercially pure titanium, *Biomaterials* 29 (2008) 1563–1572. <https://doi.org/10.1016/j.biomaterials.2007.12.001>.
- [13] I.V. Panayotov, V. Orti, F. Cuisinier, J. Yachouh, Polyetheretherketone (PEEK) for medical applications, *J. Mater. Sci.: Mater. Med.* 27 (2016) 118. <https://doi.org/10.1007/s10856-016-5731-4>.
- [14] F. Jalbert, S. Boetto, F. Nadon, F. Lauwers, E. Schmidt, R. Lopez, One-step primary reconstruction for complex craniofacial resection with PEEK custom-made implants, *J. Craniomaxillofac. Surg.* 42 (2014) 141–148. <https://doi.org/10.1016/j.jcms.2013.04.001>.
- [15] S. Singh, C. Prakash, S. Ramakrishna, 3D printing of polyether-ether-ketone for biomedical applications, *Eur. Polym. J.* 114 (2019) 234–248. <https://doi.org/10.1016/j.eurpolymj.2019.02.035>.
- [16] N. Sharma, S. Aghlmandi, S. Cao, C. Kunz, P. Honigmann, F.M. Thieringer, Quality Characteristics and Clinical Relevance of In-House 3D-Printed Customized Polyetheretherketone (PEEK) Implants for Craniofacial Reconstruction, *J. Clin. Med.* 9(9) (2020) 2818. <https://doi.org/10.3390/jcm9092818>.
- [17] Wohlers Associates, Wohlers report 2016: Wohlers Report 2016: 3D Printing and Additive Manufacturing State of the Industry Annual Worldwide Progress Report, Wohlers Associates, Inc, Fort Collins, USA, 2016.

- [18] O.A. Mohamed, S.H. Masood, J.L. Bhowmik, Optimization of fused deposition modeling process parameters: a review of current research and future prospects, *Adv. Manuf.* 3 (2015) 42–53. <https://doi.org/10.1007/s40436-014-0097-7>.
- [19] X. Gao, S. Qi, X. Kuang, Y. Su, J. Li, D. Wang, Fused filament fabrication of polymer materials: A review of interlayer bond, *Addit. Manuf.* 37 (2021) 101658. <https://doi.org/10.1016/j.addma.2020.101658>.
- [20] S. Petersmann, P. Spoerk-Erdely, M. Feuchter, T. Wieme, F. Arbeiter, M. Spoerk, Process-induced morphological features in material extrusion-based additive manufacturing of polypropylene, *Addit. Manuf.* 35 (2020) 101384. <https://doi.org/10.1016/j.addma.2020.101384>.
- [21] S. Petersmann, M. Spoerk, W. van de Steene, M. Üçal, J. Wiener, G. Pinter, F. Arbeiter, Mechanical properties of polymeric implant materials produced by extrusion-based additive manufacturing, *J. Mech. Behav. Biomed. Mater.* 104 (2020) 103611. <https://doi.org/10.1016/j.jmbbm.2019.103611>.
- [22] M.F. Arif, H. Alhashmi, K.M. Varadarajan, J.H. Koo, A.J. Hart, S. Kumar, Multifunctional performance of carbon nanotubes and graphene nanoplatelets reinforced PEEK composites enabled via FFF additive manufacturing, *Compos. B. Eng.* 184 (2020) 107625. <https://doi.org/10.1016/j.compositesb.2019.107625>.
- [23] S. Ding, B. Zou, P. Wang, H. Ding, Effects of nozzle temperature and building orientation on mechanical properties and microstructure of PEEK and PEI printed by 3D-FDM, *Polym. Test.* 78 (2019) 105948. <https://doi.org/10.1016/j.polymertesting.2019.105948>.
- [24] A. El Magri, K. El Mabrouk, S. Vaudreuil, H. Chibane, M.E. Touhami, Optimization of printing parameters for improvement of mechanical and thermal performances of 3D printed poly(ether ether ketone) parts, *J. Appl. Polym. Sci. (Journal of Applied Polymer Science)* 137 (2020) 49087. <https://doi.org/10.1002/app.49087>.
- [25] Haijun Gong, X. Xing, Janske Nel, Impact Strength of 3D Printed Polyether-etherketone (PEEK), in: *Proceedings of the 30th Annual International Solid Freeform Fabrication Symposium, Austin, Texas, USA, 12–14 August 2019*.
- [26] K.M. Rahman, T. Letcher, R. Reese, Mechanical Properties of Additively Manufactured PEEK Components Using Fused Filament Fabrication, in: *Volume 2A: Advanced Manufacturing, Houston, Texas, USA, American Society of Mechanical Engineers, 2015*.

- [27] M. Rinaldi, T. Ghidini, F. Cecchini, A. Brandao, F. Nanni, Additive layer manufacturing of poly (ether ether ketone) via FDM, *Compos. B. Eng.* 145 (2018) 162–172. <https://doi.org/10.1016/j.compositesb.2018.03.029>.
- [28] J.-W. Tseng, C.-Y. Liu, Y.-K. Yen, J. Belkner, T. Bremicker, B.H. Liu, T.-J. Sun, A.-B. Wang, Screw extrusion-based additive manufacturing of PEEK, *Mater. Des.* 140 (2018) 209–221. <https://doi.org/10.1016/j.matdes.2017.11.032>.
- [29] M. Vaezi, S. Yang, Extrusion-based additive manufacturing of PEEK for biomedical applications, *Virtual Phys. Prototyp.* 10 (2015) 123–135. <https://doi.org/10.1080/17452759.2015.1097053>.
- [30] P. Wang, B. Zou, S. Ding, L. LI, C. HUANG, Effects of FDM-3D printing parameters on mechanical properties and microstructure of CF/PEEK and GF/PEEK, *CJA* 34 (2021) 236–246. <https://doi.org/10.1016/j.cja.2020.05.040>.
- [31] P. Wang, B. Zou, H. Xiao, S. Ding, C. HUANG, Effects of printing parameters of fused deposition modeling on mechanical properties, surface quality, and microstructure of PEEK, *J. Mater. Process. Technol.* 271 (2019) 62–74. <https://doi.org/10.1016/j.jmatprotec.2019.03.016>.
- [32] Y. Wang, W.-D. Müller, A. Rumjahn, F. Schmidt, A.D. Schwitalla, Mechanical properties of fused filament fabricated PEEK for biomedical applications depending on additive manufacturing parameters, *J. Mech. Behav. Biomed. Mater.* 115 (2021) 104250. <https://doi.org/10.1016/j.jmbbm.2020.104250>.
- [33] W.Z. Wu, P. Geng, J. Zhao, Y. Zhang, D.W. Rosen, H.B. Zhang, Manufacture and thermal deformation analysis of semicrystalline polymer polyether ether ketone by 3D printing, *Mater. Res. Innov.* 18 (2014) S5-12-S5-16. <https://doi.org/10.1179/1432891714Z.000000000898>.
- [34] W. Wu, P. Geng, G. Li, Di Zhao, H. Zhang, J. Zhao, Influence of Layer Thickness and Raster Angle on the Mechanical Properties of 3D-Printed PEEK and a Comparative Mechanical Study between PEEK and ABS, *Materials (Basel)* 8 (2015) 5834–5846. <https://doi.org/10.3390/ma8095271>.
- [35] C. Yang, X. Tian, D. Li, Y. Cao, F. Zhao, C. Shi, Influence of thermal processing conditions in 3D printing on the crystallinity and mechanical properties of PEEK material, *J. Mater. Process. Technol.* 248 (2017) 1–7. <https://doi.org/10.1016/j.jmatprotec.2017.04.027>.
- [36] A.R. Zanjanijam, I. Major, J.G. Lyons, U. Lafont, D.M. Devine, Fused Filament Fabrication of PEEK: A Review of Process-Structure-Property Relationships, *Polymers (Basel)* 12 (2020). <https://doi.org/10.3390/POLYM12081665>.

- [37] F. Zhao, D. Li, Z. Jin, Preliminary Investigation of Poly-Ether-Ether-Ketone Based on Fused Deposition Modeling for Medical Applications, *Materials (Basel)* 11 (2018). <https://doi.org/10.3390/ma11020288>.
- [38] P. Honigmann, N. Sharma, B. Okolo, U. Popp, B. Msallem, F.M. Thieringer, Patient-Specific Surgical Implants Made of 3D Printed PEEK: Material, Technology, and Scope of Surgical Application, *BioMed Res. Int.* 2018 (2018) 4520636. <https://doi.org/10.1155/2018/4520636>.
- [39] L. Jin, J. Ball, T. Bremner, H.-J. Sue, Crystallization behavior and morphological characterization of poly(ether ether ketone), *Polymer* 55 (2014) 5255–5265. <https://doi.org/10.1016/j.polymer.2014.08.045>.
- [40] T.L. Conrad, D.J. Jaekel, S.M. Kurtz, R.K. Roeder, Effects of the mold temperature on the mechanical properties and crystallinity of hydroxyapatite whisker-reinforced polyetheretherketone scaffolds, *J. Biomed. Mater. Res. B* 101 (2013) 576–583. <https://doi.org/10.1002/jbm.b.32859>.
- [41] N. Sharma, S. Aghlmandi, F. Dalcanale, D. Seiler, H.-F. Zeilhofer, P. Honigmann, F.M. Thieringer, Quantitative Assessment of Point-of-Care 3D-Printed Patient-Specific Polyetheretherketone (PEEK) Cranial Implants, *Int. J. Mol. Sci.* 22 (2021). <https://doi.org/10.3390/IJMS22168521>.
- [42] Davide Sher, World's first surgery with PEEK 3D printed implants made in-hospital, 2021. <https://www.3dprintingmedia.network/worlds-first-surgery-with-peek-3d-printed-implants-made-in-hospital/> (accessed 26 February 2022).
- [43] E. Nout, M.Y. Mommaerts, Considerations in computer-aided design for inlay cranioplasty: technical note, *Oral Maxillofac. Surg.* 22 (2018) 65–69. <https://doi.org/10.1007/s10006-017-0668-4>.
- [44] A.A. Mehmet-Alkan, J.N. Hay, The crystallinity of poly(ether ether ketone), *Polymer* 33 (1992) 3527–3530. [https://doi.org/10.1016/0032-3861\(92\)91116-J](https://doi.org/10.1016/0032-3861(92)91116-J).
- [45] International Commission on Illumination, Colorimetry - Part 4: CIE 1976 L*a*b* colour space (ISO/CIE Standard No. 11664-4:2019) (2019).
- [46] C. Waly, S. Petersmann, F. Arbeiter, Multimaterial Extrusion-Based Additive Manufacturing of Compliant Crack Arrester: Influence of Interlayer Length, Thickness, and Applied Strain Rate, *Adv. Eng. Mater. (Advanced Engineering Materials)* (2022) 2101703. <https://doi.org/10.1002/adem.202101703>.
- [47] M. Erylidiz, Effect of Build Orientation on Mechanical Behaviour and Build Time of FDM 3D-Printed PLA Parts: An Experimental Investigation, *Eur. Mech. Sci.* 5 (2021) 116–120. <https://doi.org/10.26701/ems.881254>.

- [48] H. Gonabadi, A. Yadav, S.J. Bull, The effect of processing parameters on the mechanical characteristics of PLA produced by a 3D FFF printer, *Int. J. Adv. Manuf. Technol. (The International Journal of Advanced Manufacturing Technology)* 111 (2020) 695–709. <https://doi.org/10.1007/s00170-020-06138-4>.
- [49] S.-H. Ahn, M. Montero, D. Odell, S. Roundy, P.K. Wright, Anisotropic material properties of fused deposition modeling ABS, *Rapid Prototyp. J.* 8 (2002) 248–257. <https://doi.org/10.1108/13552540210441166>.
- [50] Q. Li, W. Zhao, B. Niu, Y. Wang, X. Wu, J. Ji, Y. Li, T. Zhao, H. Li, G. Wang, 3D printing high interfacial bonding polyether ether ketone components via pyrolysis reactions, *Mater. Des.* 198 (2021) 109333. <https://doi.org/10.1016/j.matdes.2020.109333>.
- [51] Y. Liu, N. Yi, R. Davies, P. McCutcheon, O. Ghita, Powder Bed Fusion Versus Material Extrusion: A Comparative Case Study on Polyether-Ether-Ketone Cranial Implants, *3D Print. Addit. Manuf.* (2022). <https://doi.org/10.1089/3dp.2021.0300>.
- [52] B.I. Oladapo, S.A. Zahedi, S.O. Ismail, F.T. Omigbodun, 3D printing of PEEK and its composite to increase biointerfaces as a biomedical material- A review, *Colloids Surf. B Colloid Surface B* 203 (2021) 111726. <https://doi.org/10.1016/j.colsurfb.2021.111726>.
- [53] Z. Schwartz, B.D. Boyan, Underlying mechanisms at the bone-biomaterial interface, *J. Cell. Biochem.* 56 (1994) 340–347. <https://doi.org/10.1002/jcb.240560310>.
- [54] X. Han, N. Sharma, Z. Xu, L. Scheideler, J. Geis-Gerstorfer, F. Rupp, F.M. Thieringer, S. Spintzyk, An In Vitro Study of Osteoblast Response on Fused-Filament Fabrication 3D Printed PEEK for Dental and Cranio-Maxillofacial Implants, *J. Clin. Med.* 8(6) (2019) 771. <https://doi.org/10.3390/jcm8060771>.
- [55] I. Baek, O. Kwon, C.-M. Lim, K.Y. Park, C.-J. Bae, 3D PEEK Objects Fabricated by Fused Filament Fabrication (FFF), *Materials (Basel)* 15 (2022). <https://doi.org/10.3390/ma15030898>.
- [56] A. Das, C.A. Chatham, J.J. Fallon, C.E. Zawaski, E.L. Gilmer, C.B. Williams, M.J. Bortner, Current understanding and challenges in high temperature additive manufacturing of engineering thermoplastic polymers, *Addit. Manuf.* 34 (2020) 101218. <https://doi.org/10.1016/j.addma.2020.101218>.
- [57] J. Zhang, B. van Hooreweder, E. Ferraris, T4F3: temperature for fused filament fabrication, *Prog. Addit. Manuf. (Progress in Additive Manufacturing)* (2022). <https://doi.org/10.1007/s40964-022-00271-0>.

- [58] Acosta-Vélez G. F., Wu B. M., 3D Pharming: Direct Printing of Personalized Pharmaceutical Tablets, *Polym. Sci. (Polymer science)* 2(1) (2016). <https://doi.org/10.4172/2471-9935.100011>.
- [59] International Organization for Standardization, Medical devices - Quality management systems — Requirements for regulatory purposes (ISO Standard No. 13485:2016) (2016).

Appendix A. Supplementary material

Table A.1: The secant ($C_{sec,500}$) and dynamic ($C_{dyn,500}$) compliance after 500 cycles, the maximum impact force (F_M), the displacement until F_M (I_M), the energy uptake until F_M (E_M) and the total absorbed energy (E_T) obtained through cyclic and impact tests on PEEK implants manufactured using different printing profiles in comparison to a commercial implant (mean and standard deviation of $n=3$ per group; except for commercial implant).

Build orientation	Printing profile	$C_{sec,500}$ (mm/10kg)	$C_{dyn,500}$ (mm/10kg)	F_M (kN)	I_M (mm)	E_M (J)	E_T (J)
BO 90	standard	0.225±0.011	0.123±0.005	1.0±0.2	2.6±0.4	1.4±0.4	4.5±1.7
	AF 0	0.397±0.216	0.132±0.006	2.0±0.7	14.1±3.9	11.9±3.5	17.6±5.5
	AF 70	0.355±0.065	0.133±0.004	0.8±0.0	2.5±0.2	1.6±0.1	7.2±1.0
	AF 140	0.257±0.114	0.128±0.003	0.8±0.0	2.3±0.2	1.0±0.1	5.6±2.3
	AF 280	0.270±0.073	0.154±0.008	0.8±0.0	2.7±0.5	1.4±0.4	3.1±0.2
	T 5	0.266±0.084	0.122±0.003	1.0±0.0	2.2±0.0	1.3±0.1	3.5±0.2
	S 1	0.197±0.017	0.128±0.002	0.9±0.0	2.2±0.3	1.2±0.2	4.1±1.0
	LH 0.30	0.211±0.029	0.127±0.001	0.9±0.0	2.3±0.1	1.3±0.1	3.4±0.9
BO 180	IP Gr0/90	0.231±0.055	0.136±0.005	0.8±0.0	3.1±0.5	1.7±0.3	3.6±1.2
	standard	0.345±0.097	0.145±0.005	1.4±0.2	2.2±0.1	1.5±0.1	4.7±0.9
	AF 0	0.326±0.012	0.222±0.002	2.2±0.0	6.6±0.3	8.9±0.4	37.0±7.9
	AF 280	0.326±0.098	0.174±0.006	1.5±0.2	2.8±0.5	2.1±0.9	4.3±2.2
	T 5	0.328±0.069	0.132±0.011	2.4±0.7	3.4±0.9	4.2±2.2	7.1±0.8
	S 1	0.382±0.007	0.194±0.006	1.3±0.0	2.4±0.0	1.4±0.1	4.7±0.6
	IP Rec0/90	0.329±0.051	0.185±0.006	1.5±0.1	2.3±0.1	1.5±0.2	3.8±1.7
	V 10	0.289±0.068	0.198±0.029	1.6±0.0	3.6±0.1	3.1±0.4	12.7±2.2
BO 45	T 5 + H	0.305±0.010	0.194±0.011	2.2±0.3	4.1±0.6	4.7±1.4	9.6±2.4
	standard	0.309±0.067	0.135±0.003	1.5±0.2	3.1±1.4	2.4±1.2	11.0±1.5
	AF 0	0.347±0.092	0.168±0.003	2.3±0.1	5.6±0.5	7.7±1.1	22.2±4.7
	T 5	0.246±0.097	0.112±0.003	1.7±0.2	1.9±0.1	1.6±0.2	9.9±3.2
Commercial		0.204	0.134	2.2	2.6	3.0	3.5

*Only deviations from the standard values of AF 210 – S 3 – LH 0.15 – V 50 – IP Rec±45 – T 4 are indicated in the implant designation (BO...build orientation, AF...air flow temperature in °C, S...number of shells, LH...layer height in mm, V...printing speed in mm/s, IP...infill pattern, T...average implant thickness in mm, H...drilled holes).

Table A.2: The melting temperature (T_M), the specific enthalpy of fusion (ΔH) and the degree of crystallinity (X_c) obtained through DSC for the different printing profiles and the commercial PEEK implant (mean and standard deviation of $n=2$ per group).

Build orientation	Printing profile	T_M (°C)	ΔH (J/g)	X_c (%)
BO 90	standard	336.9±0.6	35.3±0.8	28.5±3.4
	AF 0	339.0±0.0	33.0±1.0	10.5±1.4
	AF 70	338.1±1.1	35.0±1.0	29.3±3.2
	AF 140	338.7±0.3	39.1±0.2	34.7±0.2
	AF 280	336.8±0.6	32.3±0.2	28.7±0.2
	T 5	336.8±0.6	32.8±0.0	29.2±0.0
	S 1	338.9±0.0	35.1±4.4	31.2±3.9
	LH 0.30	337.3±0.0	35.1±2.0	31.2±1.7
	IP Gr0/90	337.6±0.6	32.5±0.6	28.9±0.5
BO 180	standard	338.5±	30.7±0.0	27.3±0.0
	AF 0	338.1±	34.0±3.6	30.2±3.2
	AF 280	338.5±	35.0±1.2	31.1±1.0
	T 5	338.1±	33.4±2.3	29.7±2.1
	S 1	337.6±	36.2±2.4	32.1±2.1
	IP Rec0/90	338.9±	32.1±0.0	28.5±0.0
	V 10	338.5±	32.4±1.8	28.8±1.6
	T 5 + H	same as for T 5		
BO 45	standard	338.1±1.1	34.1±3.0	27.4±1.4
	AF 0	338.1±1.2	31.7±0.4	10.7±0.7
	T 5	338.6±1.7	34.1±0.8	30.3±0.7
	T 5 + H	same as for T 5		
commercial		340.6±0.0	32.3±2.2	28.7±1.9

*Only deviations from the standard values of AF 210 – S 3 – LH 0.15 – V 50 – IP Rec±45 – T 4 are indicated in the implant designation (BO...build orientation, AF...air flow temperature in °C, S...number of shells, LH...layer height in mm, V...printing speed in mm/s, IP...infill pattern, T...average implant thickness in mm, H...drilled holes).

Table A.3: The L^* , a^* , b^* coordinates (L^* - lightness of colour; a^* - position between red and green; b^* - position between yellow and blue) obtained through UV-Vis spectroscopy for the different printing profiles and the commercial PEEK implant (mean and standard deviation of $n=2 - 4$ per group).

Build orientation	Printing profile	L^* (-)	a^* (-)	b^* (-)
BO 90	standard	60.0±0.1	1.2±0.0	2.2±0.2
	AF 0	31.6±0.7	4.3±0.2	7.3±0.9
	AF 70	42.9±6.1	3.8±0.9	6.6±2.3
	AF 140	58.2±0.5	1.4±0.1	3.2±0.9
	AF 280	60.6±0.1	1.8±0.1	2.3±0.2
	T 5	60.0±0.2	1.7±0.1	2.2±0.5
	S 1	63.3±0.2	1.2±0.0	2.6±0.0
	LH 0.30	65.0±0.4	1.2±0.1	3.1±0.3
BO 180	IP Gr0/90	61.5±0.2	1.0±0.0	1.6±0.0
	standard	49.0±10.7	3.1±1.4	8.0±2.8
	AF 0	44.5±0.3	3.4±0.3	9.4±0.7
	AF 280	61.9±0.4	1.8±0.0	5.2±0.4
	T 5	49.6±2.3	3.3±0.6	10.3±1.2
	S 1	52.2±1.7	3.6±0.5	10.6±0.9
	IP Rec0/90	44.4±7.6	4.3±0.5	10.2±0.2
	V 10	56.2±0.2	2.6±0.1	9.7±0.4
BO 45	T 5 + H	same as for T 5		
	standard	48.6±13.5	2.9±2.0	5.7±4.6
	AF 0	43.8±0.2	3.6±0.4	11.2±0.8
	T 5	53.7±7.6	2.6±1.0	6.0±3.1
commercial	T 5 + H	same as for T 5		
	commercial	74.7±0.6	0.8±0.0	75.4±0.5

*Only deviations from the standard values of AF 210 – S 3 – LH 0.15 – V 50 – IP Rec±45 – T 4 are indicated in the implant designation (BO...build orientation, AF...air flow temperature in °C, S...number of shells, LH...layer height in mm, V...printing speed in mm/s, IP...infill pattern, T...average implant thickness in mm, H...drilled holes).